

NASA-CR-136069) ANALYSIS AND DESIGN OF  
A CAPSULE LANDING SYSTEM AND SURFACE  
VEHICLE CONTROL SYSTEM FOR MARS  
EXPLORATION (Rensselaer Polytechnic  
Inst.) 175 p HC \$10.75

N74-11077

Unclas  
15616

CSCI 13F

G3/11



R.P.I. Technical Report MP-35

A Progress Report for  
July 1, 1972 to June 30, 1973

ANALYSIS AND DESIGN OF A CAPSULE  
LANDING SYSTEM AND SURFACE VEHICLE  
CONTROL SYSTEM FOR MARS EXPLORATION

National Aeronautics and Space  
Administration

Grant NGL 33-018-091

Submitted by the Special Projects Committee

D.K. Frederick  
P.K. Lashmet  
G.N. Sandor  
C.N. Shen  
E.J. Smith  
S.W. Yerazunis

School of Engineering  
Rensselaer Polytechnic Institute

# ABSTRACT

Investigation of problems related to the design and control of a mobile planetary vehicle to implement a systematic plan for the exploration of Mars has been undertaken. Problem areas receiving attention include: vehicle configuration, control, dynamics, systems and propulsion; systems analysis; terrain modeling and path selection; and chemical analysis of specimens. The following specific tasks have been under study: vehicle model design, mathematical model of vehicle dynamics, experimental vehicle dynamics, obstacle negotiation, electromechanical controls, remote control, collapsibility and deployment, construction of a wheel tester, wheel analysis, payload design, system design optimization, effect of design assumptions, accessory optimal design, on-board computer subsystem, laser range measurement, discrete obstacle detection, obstacle detection systems, terrain modeling, path selection system simulation and evaluation, gas chromatograph/mass spectrometer system concepts, chromatograph model evaluation and improvement.

These tasks are defined in detail and the progress which has been achieved during the period July 1, 1972 to June 30, 1973 is summarized.

# TABLE OF CONTENTS

	Page
INTRODUCTION.....	1
DEFINITION OF TASKS.....	1
A. Vehicle Configuration, Control, Dynamics, Systems and Propulsion.....	1
B. General Systems Analysis.....	2
C. Surface Navigation and Path Control.....	2
D. Chemical Analysis of Specimens.....	2
SUMMARY OF RESULTS.....	8
DETAILED SUMMARIES OF PROGRESS.....	8
A. Vehicle Configuration, Control, Dynamics, Systems and Propulsion.....	8
A.1. Vehicle Design.....	8
A.1.a. Design, Construction, and Evaluation of 0.4 Scale Model.....	17
A.1.b. Vehicle Dynamics.....	18
A.1.c. Obstacle Negotiation.....	19
A.1.d. Radio Control.....	21
A.2. Collapsibility and Deployment.....	41
A.3.a. Wheel Tester and Grouser Design.....	42
A.3.b. Wheel Analysis.....	51
B. System Analysis.....	59
B.1. System Modeling and Design Optimization.....	59
B.2. Sensitivity of Optimal Design.....	61
B.3. Time Simulation of Vehicle Performance.....	66
B.4. Specification of an Integrated MRV Controller.....	67
C. Surface Navigation and Path Control.....	68
C.1.a. Laser Rangefinder: Pulse Amplification.....	68
C.1.b. Laser Scan Methods and Phase Comparison Rangefinder..	90
C.2.a. Error Analysis and Stochastic Fit for Gradients.....	97
C.2.b. Gradient Estimates from Stereo Measurements.....	107

C.3.	Path Selection System Evaluation.....	123
D.	Chemical Analysis of Specimens.....	136
D.1.	GC/MS System Concepts.....	136
D.1.a.	Mass Spectrometer System Characteristics.....	136
D.1.b.	Carrier Gas Generation and Removal.....	140
D.2.	Chromatographic System Analysis.....	149
D.2.a.	Multicomponent Chromatography.....	149
D.2.b.	Chromatograph Model Improvement.....	156
REFERENCES.....		166
EDUCATIONAL CONSIDERATIONS.....		169

Analysis and Design of a Capsule Landing System  
and Surface Vehicle Control System for Mars Exploration

I. Introduction

Current national goals in space exploration include a detailed study and examination of the planet Mars. The effectiveness of Mars exploration missions would be enhanced according to the extent to which the investigative devices which are landed are mobile, to the range of their mobility, and to the ability to control their motion. In order to achieve basic mission objectives, and beyond that, to maximize the return on the commitment of resources to the mission, formidable technical problems must be resolved. The major factor contributing to these problems is the round trip communications time delay between martian and earth control stations which varies from a minimum of about 9 minutes to a maximum of 25 minutes. This time delay imposes stringent requirements on the vehicle, on its control and communication systems and on those systems included on board to make the scientific measurements, in terms of their ability to function autonomously. These systems must be able to operate with a high degree of reliability and must be capable of calling for earth control under appropriate circumstances.

A number of important problems originating with these factors and relating directly the basic mission objectives of an unmanned exploration of Mars have been and are currently being investigated by a faculty-student project team at Rensselaer Polytechnic Institute with the support of NASA NGL-33-018-091.

This progress report describes the tasks which have been undertaken and documents the progress which has been achieved in the interval July 1, 1972 to June 30, 1973.

II. Definition of Tasks

The delay time in round trip communication between Mars and Earth gives rise to unique problems relevant to martian and/or other planetary explorations. All phases of the mission from landing the capsule in the neighborhood of a desired position to the systematic traversing of the surface and the attendant detection, measurement, and analytical operations must be consummated with a minimum of control and instruction by earth based units. The delay time requires that on board systems capable of making rational decisions be developed and that suitable precautions be taken against potential catastrophic failures. Four major task areas, which are in turn divided into appropriate sub-tasks, have been defined and are listed below.

- A. Vehicle Configuration, Control, Dynamics, Systems and Propulsion. The objective of this task is the design of a roving vehicle for the exploration of Mars. This design includes the aspects of vehicle configuration, collapsibility for launch configuration, deployment, dynamics, motion and attitude control, capability definition, and performance evaluation. The efforts of this task are made within the text of the mission definition and delivery system constraints. The ultimate goal is the development of a vehicle capable of operating within the constraints of the Mars mission, but flexible in design, to insure reliability with respect

to the unknowns of Mars, and to accommodate the alterations in the mission as a result of information gathered during the exploration.

- B. General Systems Analysis. The objective of this task is to develop a framework within which decisions in design involving conflicting requirements can be made rationally and in the context of the whole system and mission. Relationships between alternative mission profiles and specifications and weight, energy and space allocation and management will be sought.
- C. Surface Navigation and Path Control. Once the capsule is landed and the roving vehicle is in an operational state, it is necessary that the vehicle can be directed to proceed under remote control from the landing site to specified positions on the martian surface. This task is concerned with the problems of terrain sensing, obstacle detection, terrain modeling, path selection and navigation between the initial and terminal sites when major terrain features precluding direct paths are to be anticipated. On board decision making capability must be designed to minimize earth control responsibility except in the most adverse circumstances.
- D. Chemical Analysis of Specimens. A major objective of martian surface exploration will be to obtain chemical, biochemical or biological information. Many experiments proposed for the mission require a general duty, gas chromatograph-mass spectrometer for chemical analysis. The objective of this task is to generate fundamental data and concepts required to optimize this chemical analysis system.

### III. Summary of Results

#### Task A. Vehicle Configuration, Control, Dynamics, Systems and Propulsion

This broad task has been divided into the following subtasks: vehicle model design, construction and evaluation; mathematical modeling of vehicle dynamics; experimental dynamics analysis; obstacle negotiation; electromechanical control systems and remote control; collapsibility and deployment; wheel testing apparatus; and wheel analysis. A brief summary of the progress achieved in the prior interval in each of these areas follows below.

##### A.1. Vehicle Design

The fundamental features of a "third-generation design" vehicle have been developed and are shown to meet collapsibility, capsule limitation, and launch configuration requirements. A deployment scheme which is reliable and requires no special terrain for landing has been developed. The present design allows for an emergency maneuver in which the vehicle can, in fact, reverse itself and provide the means for the vehicle to extricate itself from an impossible situation. A conservative estimate of the payload fraction of this vehicle is shown to be equivalent to that estimate for a six wheel vehicle. A 0.2 scale vehicle has been built to demonstrate these capabilities.

##### A.1.a. Design, Construction and Evaluation of 0.4 Scale Model

Construction of a 0.4 scale model of the RPI-MRV has been

essentially completed. The proposed deployment concept has been implemented and shown to be effective. This model has been used for preliminary dynamic studies, the results of which are expected to modify the design detail. It is intended that this vehicle will be fully automated and be tested dynamically on appropriate terrains by remote control during the coming year.

A.1.b. Vehicle Dynamics

Equations describing the dynamic behavior of the RPI-MRV using the bicycle configuration have been developed and are in the process of being solved by digital computation. In addition, an analytical model describing a three-dimensional three degree of freedom model is under development. The 0.4 model has been tested on an electromagnetic shaker and the experimental results which have been obtained are being used to modify the detailed design of the vehicle. These mathematical studies combined with the experimental studies are intended to provide a sound basis for modifying the 0.4 model and at the same time permitting extension of the design to a prototype.

A.1.c. Obstacle Negotiation

A digital computer program has been developed to model a two dimensional vehicle operating in a vertical plane as it traverses steps, slopes and crevasses. The program provides knowledge on energy requirements to overcome frictional and static torques. In addition, the program includes a stability factor which indicates under what obstacle circumstances the vehicle's stability may become marginal. These calculations and others to be made in the future will provide a basis for sizing the motors for the vehicle.

A.1.d. Radio Control

The objective of this task is to design, construct and implement a remote control capability for the 0.4 scale model. The manual input device, command encoder, radio link and command decoder have been designed, built and tested with the exception of the clocks required at the transmitter and receiver to synchronize the data reception with the data transmission. Progress has been made on the control system in the areas of speed control, command storage, and conversion to analog levels. To complete the systems, sensors must be placed in the vehicle and their output incorporated into the control systems. The radio link and motor controls systems have been interfaced and used to control the vehicle motors at three output speed levels in both the forward and reverse directions. As a first step, it is planned that the complete radio system be installed to permit open loop manual control of the vehicle. This will be expanded first to close loop control and ultimately to computer operation.

A.2. Collapsibility and Deployment

A solution for the problem of stowage of the RPI-MRV in the Viking capsule and its subsequent deployment on Mars has been developed. The vehicle is folded in such a manner as to locate the center of the payload fraction on the centerline of the capsule, and to locate the wheels in appropriate positions. The deployment concept



is such as to permit deployment on relatively difficult terrains. Furthermore, the particular configuration which has been developed allows the vehicle to reverse itself, if necessary, to avoid an impossible obstacle situation.

#### A.3.a. Wheel Tester and Grouser Design

A wheel tester system has been designed, built and used to test the RPI toroidal wheel and alternative grouser designs. Slip and power tests have been performed and evaluated for five alternative grouser designs.

#### A.3.b. Wheel Analysis

Existing mathematical models for the design of the toroidal wheel have been appraised and evaluated. A new iterative mathematical analysis has been developed and has been applied to experimental data. Comparison with experimental data and predicted results for concentrated loads have proved to be favorable. Future work will be directed to the problem of distributed loads.

#### Task B. General Systems Analysis

This major task is subdivided into four subtasks: system modeling and design optimization; sensitivity of optimal designs; time simulation of vehicle performance; and specification of an integrated MRV controller.

##### B.1. System Modeling and Design Optimization

During the past year, the objectives set for this subtask have been achieved. Optimal designs have been identified and the implications of these results have been investigated for three major alternative models, i.e. four-wheeled vehicle with direct earth link, six-wheeled vehicle with direct earth link and a four-wheeled vehicle with an orbiter-earth link. These optimal designs specify values of the parameters of the system, e.g., weight and power allocations to the vehicle subsystems and subsystem performance levels (communications data rate, vehicle velocity, science time, etc.). It is believed that the overall approach to the system analysis problem which has been developed represents a contribution to the design methods for large aerospace systems.

##### B.2. Sensitivity of Optimal Designs

The method for the linear approximation of effects of forced perturbation of one of the parameters of a design from its optimal value has been derived. The sensitivity of the optimal rover designs which have been obtained are being investigated by this method.

##### B.3. Time Simulation of Vehicle Performance

A simulation program that allows the investigation of the performance of designs determined under B.1. in real-time has been written. It is planned that these optimal designs be studied in the real-time sense to determine their feasibility. The objective is to analyze the performance of the designs identified under B.1. with differing mission profiles and stochastic inputs, (terrain slopes, emergencies, etc.).

#### B.4. Specification of an Integrated MRV Controller

The objective of this subtask is to investigate the performance requirements and candidate designs for the MRV on-board computer. A queuing theory structure has been developed for determining the type of computer architecture appropriate for a given set of requirements.

#### Task C. Terrain Sensing, Terrain Modeling, Obstacle Detection and Path Selection

This task deals with problems of terrain sensing, terrain modeling, obstacle detection and path selection for an autonomous roving vehicle. Specific tasks receiving active effort include: the design of a laser rangefinder for terrain sensing; design of a laser scan system; stochastic estimation of gradient; stereo and non-stereo obstacle detection systems; and path selection systems evaluation.

##### C.1.a. Laser Rangefinder Design: Pulse Amplification

Various systems by which a laser may be used for ranging purposes in the range of 3-30 meters have been analyzed and evaluated. Optical focusing, timed pulse and phase comparison techniques were compared. It has been concluded that a pulse amplification technique or a hybrid system combining the timed pulse and phase comparison concepts are most promising. Of these two systems, pulse amplification appear to be more suited for rapid terrain scanning. A preliminary design of a rangefinder based on pulse amplification has been completed and some of the required electronic components have been constructed and tested.

##### C.1.b. Laser Scan Systems and Laser Rangefinder Design: Phase Comparison

Alternative laser scan systems have been considered and an alternative utilizing digital deflection optics or a matrix of laser diodes and a vibrating detector mirror which can meet the rapid scan requirement has been developed. This scan system can support a pulse amplification rangefinder system such as that described under C.1.a. above, or a system based on phase comparison as proposed under this task.

A design of a laser rangefinder based on phase comparison has been developed and construction and testing of some of the electronic components has been completed. Unfortunately critical components could not be constructed during this past period and a decisive appraisal of the feasibility of the phase comparison method will have to be deferred to the future.

#### C.2. Terrain Modeling and Obstacle Detection

##### C.2.a. Error Analysis and Stochastic Fit for Gradients

An analysis of the effect of measurement errors, i.e., range and elevation and azimuthal angles, on the gradient of terrain in the 3-30 meter range has been undertaken. It is found that measurement errors originating with vehicle motion, (i.e. roll, pitch and heave) result in very large errors in estimating the in-path and cross-path slopes and the gradient. It is concluded that a rapid

scan system should be used to eliminate these errors. Assuming a rapid scan system obviating vehicle motion effects, the relationships between the standard deviation of gradient as a function of range and of the standard deviation range and elevation and azimuthal error for a horizontal flat plain have been determined. The standard deviation of gradient varies from less than  $1^\circ$  to about  $8^\circ$  depending on the measurement errors of up to a standard deviation of 10 cm in range and for a data spacing corresponding to elevation and azimuthal angle increments of 1 minute. Data spacing as determined by elevation and azimuthal angle increments has a major effect on the gradient error. As the spacing is increased, the gradient error is reduced. Unfortunately large data spacing also implies increased loss of information. A trade-off between data spacing and gradient error will be necessary. The effect of an inclined terrain has also been determined.

As this effort more completely relates the effect of measurement errors on the reliability of terrain model interpretation, specification for a terrain sensing system can be defined more rationally.

#### C.2.b. Gradient Estimates Based on Stereo Measurements

The method of calculating a stochastic estimate of the gradient has been applied to two stereo-measurement systems and compared to the non-stereo range-angle system. Instrumentation accuracy requirements to meet a 2 degree gradient standard deviation have been determined for each alternative. The non-stereo system is shown to be superior to both the stereo-range and stereo-angles alternatives and indeed is the only system which can be conceivably implemented with only modest improvements in the state of the art of laser range measurement.

#### C.3. Path-Selection System Evaluation

The principal efforts have been devoted to improving the realism of the digital computer simulation program developed in the previous year and in using the program for system evaluation purposes. Specifically, simulation of an emergency backup mode, non-zero vehicle dimensions, and indices for safety and obstacle detection errors have been incorporated into the program. In addition, the program has been used to compare two different mounting arrangements for the range-measuring sensor used by the path-selection system. The two configurations compared have the plane of the sensor beam fixed relative to the vehicle and fixed relative to the local planet vertical.

#### Task D. Chemical Analysis of Specimens

This task is concerned with developing the fundamental concepts which will be required to optimize a gas chromatograph-mass spectrometer analysis system. Topics receiving active effort include mass spectrometer characteristics, carrier gas generation and removal, multicomponent chromatography, and chromatograph model improvement.

##### D.1. Gas Chromatograph/Mass Spectrometer System Concepts

#### D.1.a. Mass Spectrometer System Characteristics

The mass spectrometer studies are intended to characterize the major properties of the instrument, the resulting relations being suitable for investigation of system power, weight, and volume requirements. Relations involving mass resolution for single and double focussing instruments have been developed. Preliminary studies showed the theoretical analysis of instrument sensitivity to be beyond the scope of this project, and empirical relations are being sought. Investigation of the effect of major design variables upon power requirements was begun. Preliminary analysis of the characteristics of the ionization chamber filament was completed.

#### D.1.b. Carrier Gas Generation and Removal

Preliminary analysis of high-pressure gas storage as a source of carrier gas has been completed. Use of filament-reinforced construction will provide storage capacity for one year's operation of the chromatograph within a volume of about one or two liters and a weight of about 2 kgm. The concept appears competitive with a previously proposed electrolytic gas generator. Engineering analysis of carrier gas removal by diffusion through a palladium alloy tubing began. A system containing only carrier gas and no sample was successfully modeled. Future work with the model will incorporate the effect of the nondiffusing sample.

#### D.2. Chromatographic Systems Analysis

##### D.2.a. Multicomponent Chromatography

Data for the system n-pentane/n-heptane on porous Chromosorb-102 adsorbent were obtained at 150, 175, and 200° C for mixtures containing zero to 100% n-pentane by weight. Prior results showing limitations on superposition of pure component data to predict multicomponent chromatograms were verified. A nonporous adsorbent failed to separate the system because of large input sample dispersions. Modifications to the system to improve sample injection are being considered. An automated data processing scheme involving magnetic tape recording of the detector signals and processing by a minicomputer was rejected because of resolution limitations of the available A/D converters. Preliminary studies on porosity and pore size distribution of the adsorbents were begun.

##### D.2.b. Chromatograph Model Improvement

Intraparticle diffusion and rates of adsorption were incorporated into the mathematical model of the chromatograph to improve representation of the experimental data. Moment analysis of the resulting system of equations showed the model to be capable of representing more adequately the spreading of experimental data. It appeared an analytical solution of the model was not realizable, and numerical solution methods are being investigated. Criteria for substituting a finite boundary condition required for numerical solution in place of an infinite boundary condition used in prior analytical work were developed. Computational schemes based on finite differences were shown to be inefficient, so the method of weighted residuals with orthogonal collocation is being investigated.

#### IV. Detailed Summaries of Progress

##### Task A. Vehicle Configuration, Control, Dynamics, System and Propulsion

This broad task is concerned with all aspects of the design of a roving vehicle for Mars exploration. Included within this major effort are the following subtasks: vehicle model design, construction and evaluations; mathematical model of the vehicle dynamics; experimental dynamic analysis; obstacle negotiation; electromechanical control systems and remote control systems; collapsibility and deployment; wheel testing apparatus; wheel analysis; and payload design.

Progress made in these areas during the past interval is summarized in the sections which follow.

##### A.1. Vehicle Design

Student Group Leader: J. Almstead  
Faculty Advisor: Prof. G. N. Sand

The objective of this task is to develop the concepts of the RPI-MRV and evaluate these concepts relative to the rover mission requirements. Efforts during the past year have been directed toward making the fundamental features of this "third-generation design" meet the collapsibility, capsule space limitation and launch configuration requirements, developing a deployment scheme which is reliable and requires no special landing terrain, and refining the emergency maneuver to better protect the instrumentation when executed. While satisfying these three areas of requirements, the design had to remain as simple as possible to keep structure weight minimized and reliability maximized.

Figures 1 through 8 show the vehicle concept which was developed. It has the capability of collapsing to fit in the Viking capsule. When in the capsule, the payload is centered and attached to the mounting ring in the capsule bottom. The frame is locked in place and braced to the capsule walls. The wheels are compressed slightly to act as mounts in the closed capsule, and provide a positive force for the separation of the capsule.

Deployment on Mars requires only three vehicle motions which can be done as long as the vehicle has landed safely and the payload is stable on the ground. Because the wheels are raised above the ground, deployed, and then placed on the ground, the limitations on the terrain at the landing site are minimized. The three vehicle motions involved in the deployment are rear strut deployment, frame unfolding, and front axle swing-over. The details of the deployment were reported in Ref. 1.

The emergency maneuver, also described in Ref. 1, permits the RPI-MRV to escape from situations which would otherwise terminate the mission. The vehicle is now able to execute the maneuver without having to use the payload as a skid as did the second generation version. With symmetry, the vehicle is able to switch front for rear and rear for front, and drive away from the danger.

A first approximation of the payload fraction was made. It defined payload fraction to be:  $(\text{Total permitted weight-vehicle})/(\text{Total permitted weight})$ , or effectively:  $(\text{payload weight})/(\text{total permitted weight})$ .

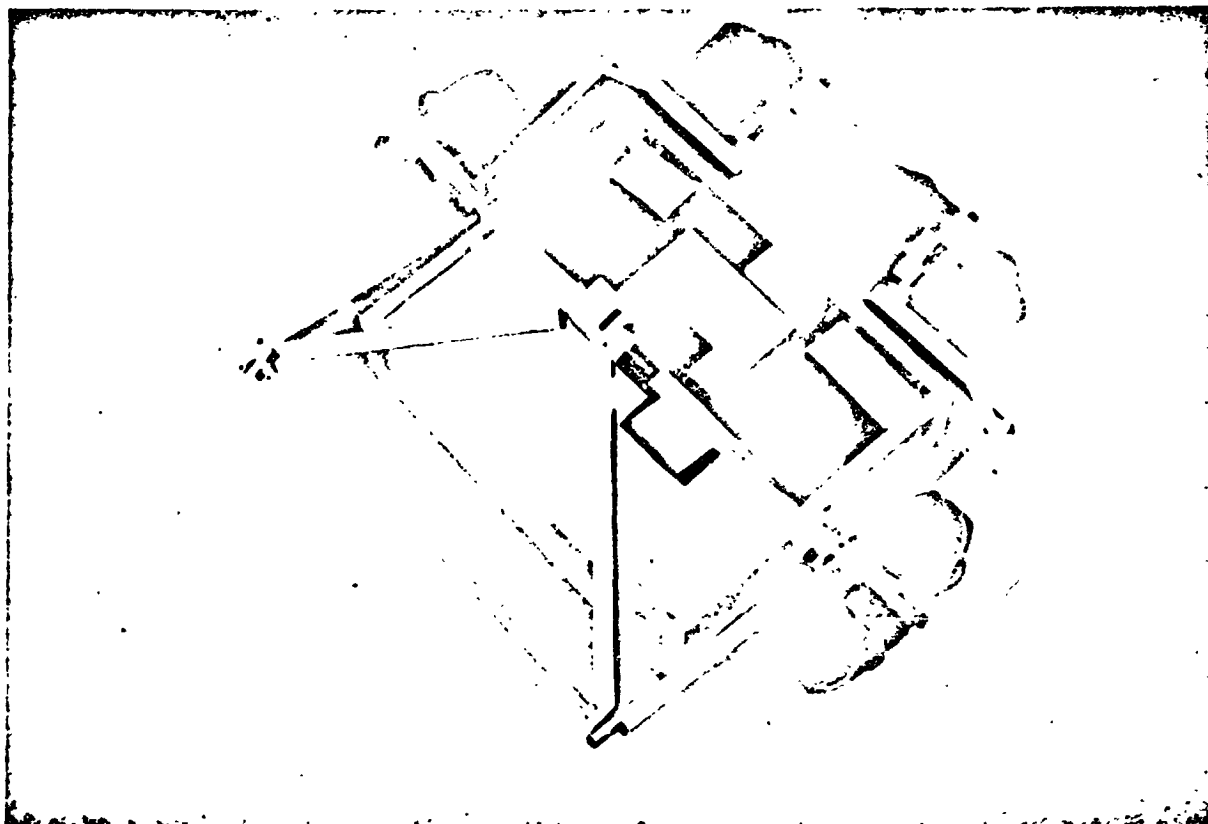


**Fig. 1.** The RPI-MRV in collapsed launch/land configuration.  
This 0.184 scale model fits into a similar scale  
model of the Viking capsule.

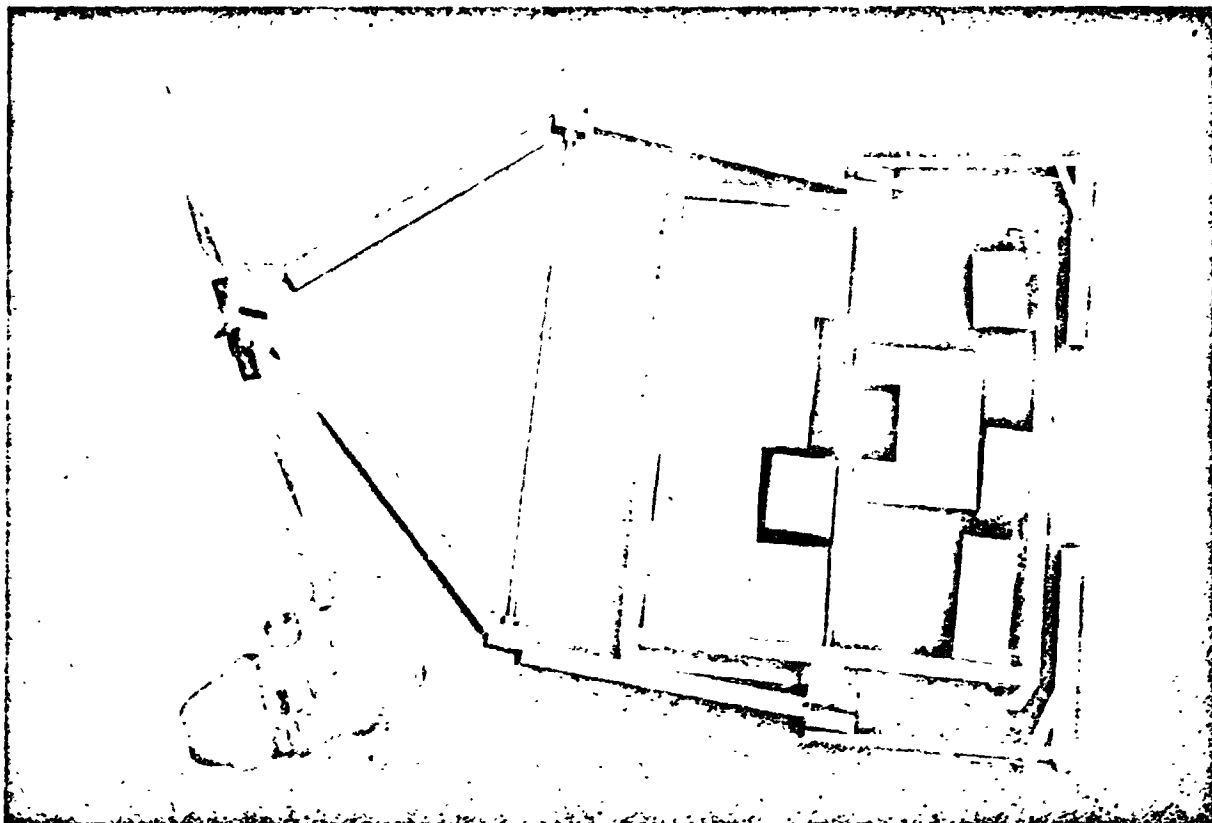


Figure 2. After landing, with the payload package still resting on the ground, the front frame and wheel structure deploy.



Figure 3. With payload package still on the ground, and the front structure and wheel's deployed, the rear wheels begin to unfold.



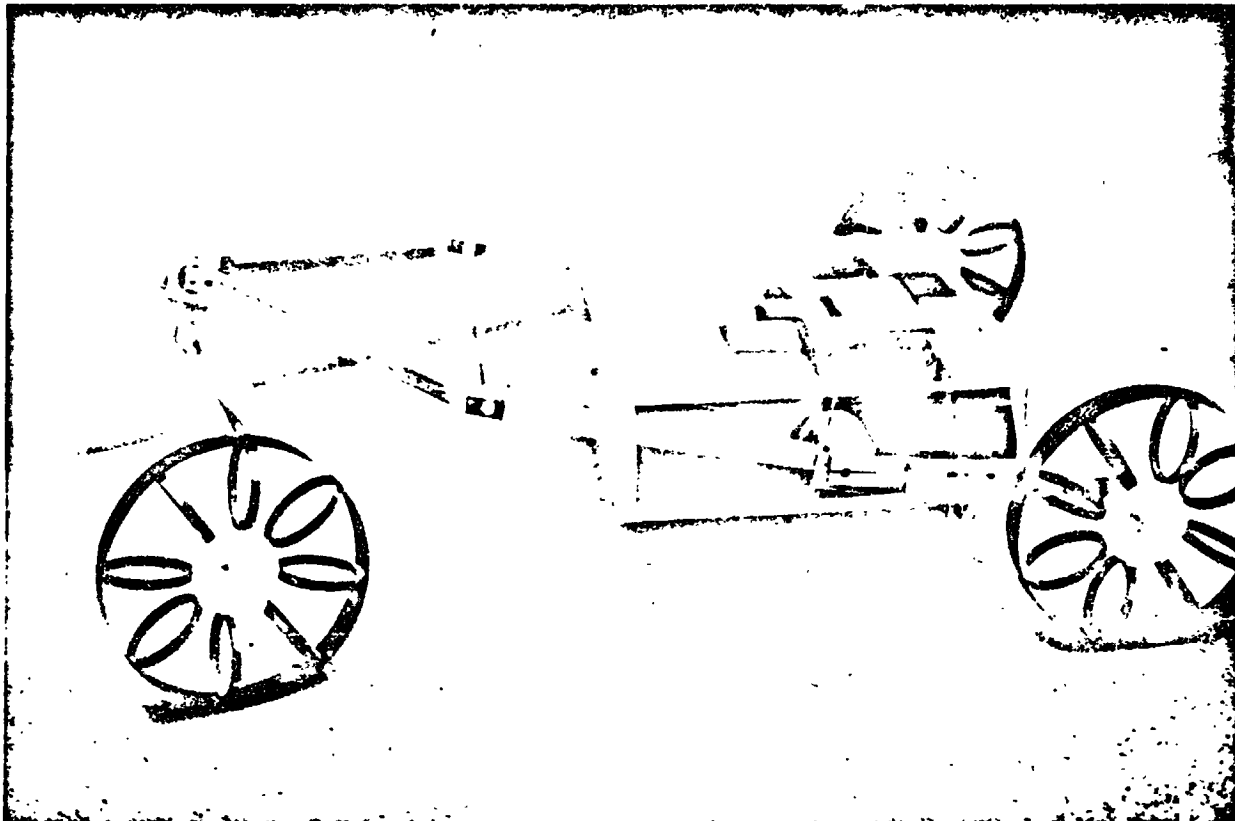


Figure 4. With all four wheels deployed, the payload is raised off the ground to the desired height.

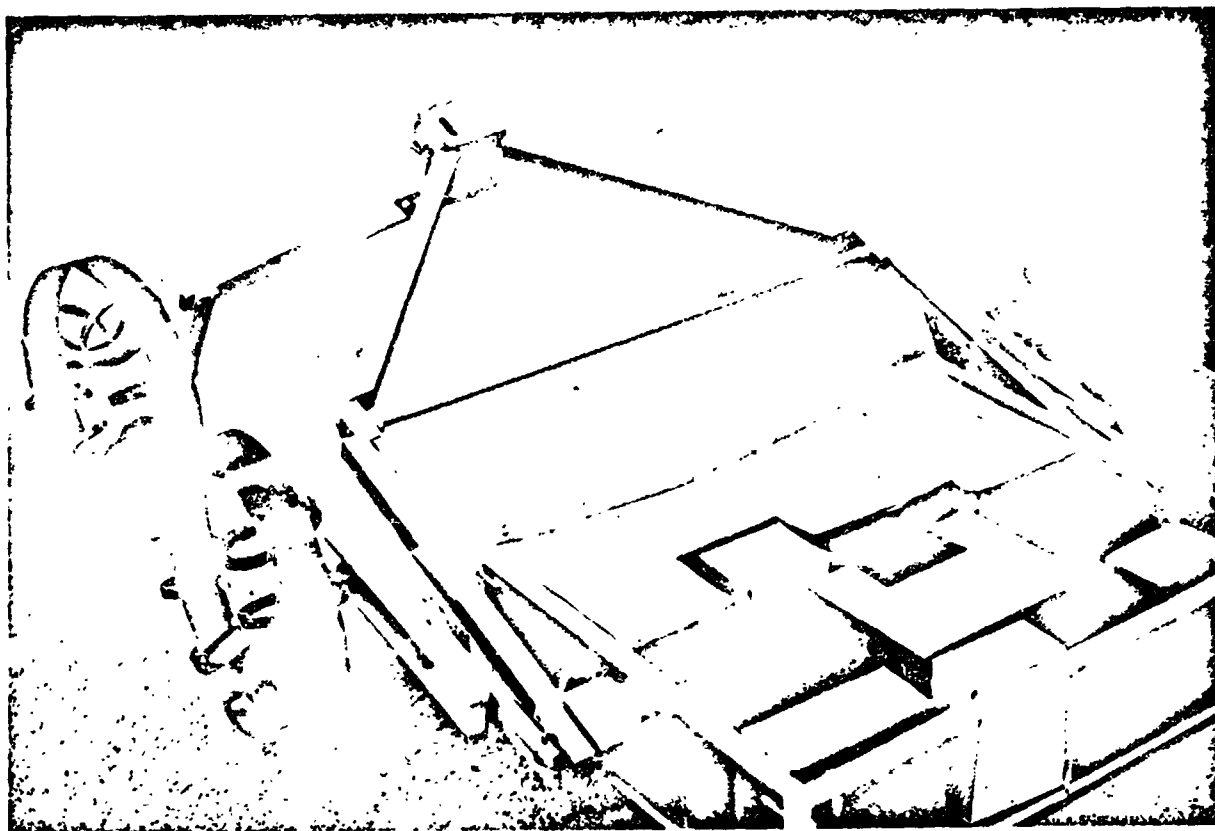


Figure 5. Emergency Maneuver of the RPI-MRV

Should the front wheel become entrapped in an obstacle, the payload is lowered to the surface and the rear wheels are swung over  $180^{\circ}$  around the central torsion bar which runs across the payload.

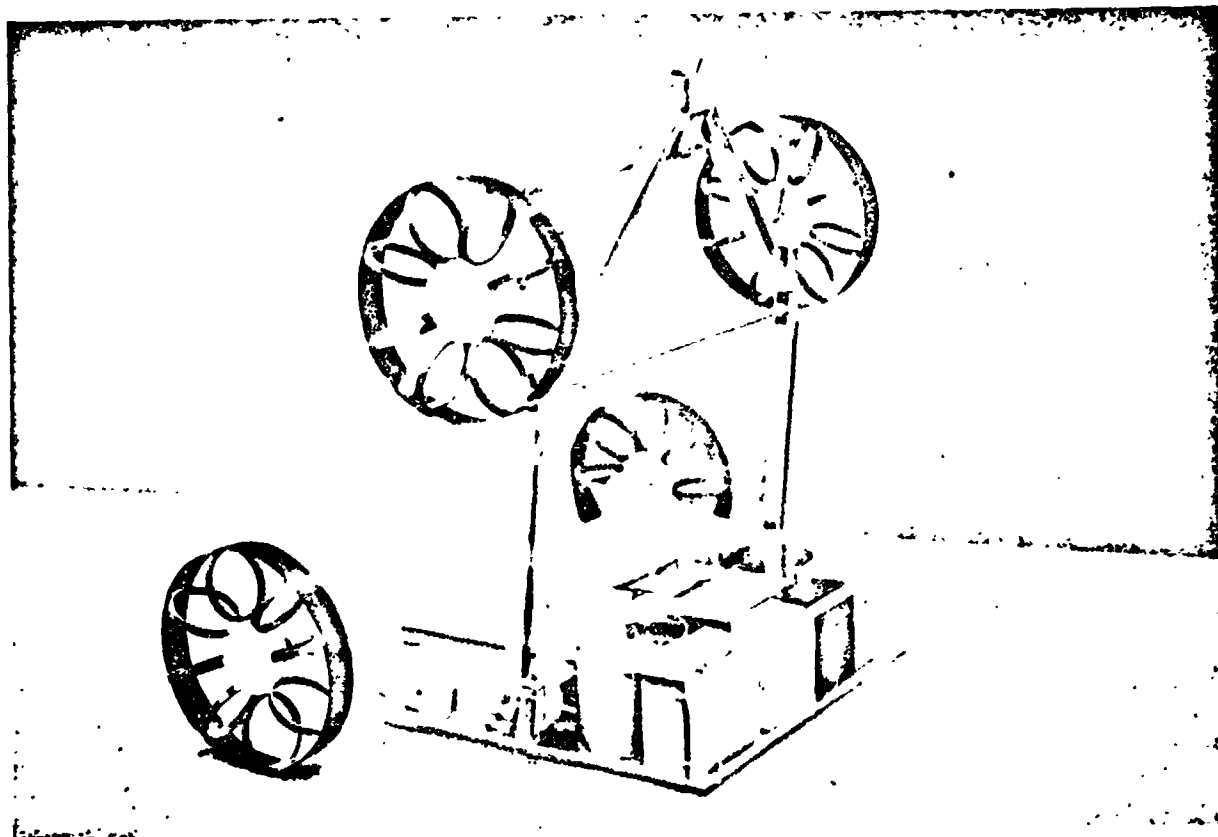


Figure 6. With the payload still on the ground and the rear wheels rotated, the front frame and wheels are swung to the opposite side of the payload, clearing all antennas and vertical extensions of the payload.

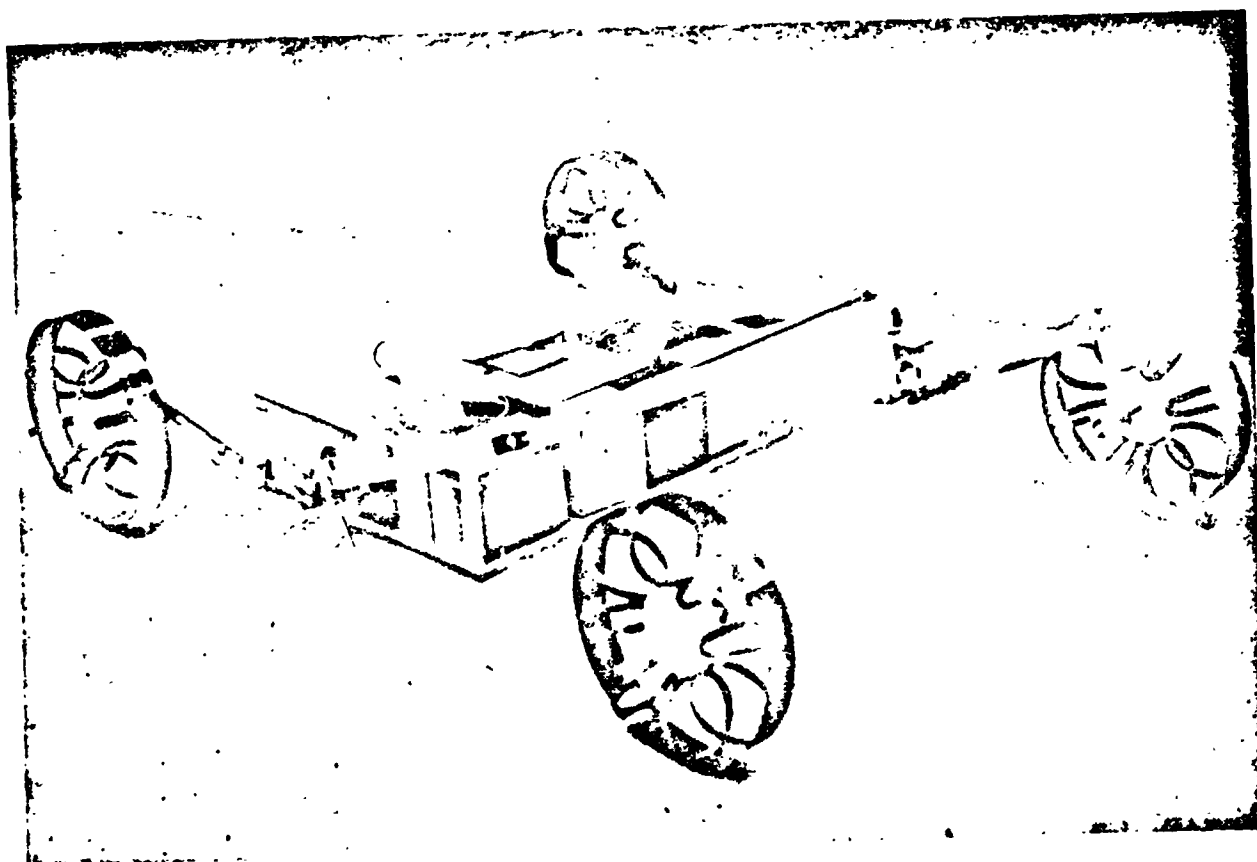


Figure 7. The front wheels touch ground 'n the rear of the payload. Note the payload configuration relative to the new front and rear wheel locations.

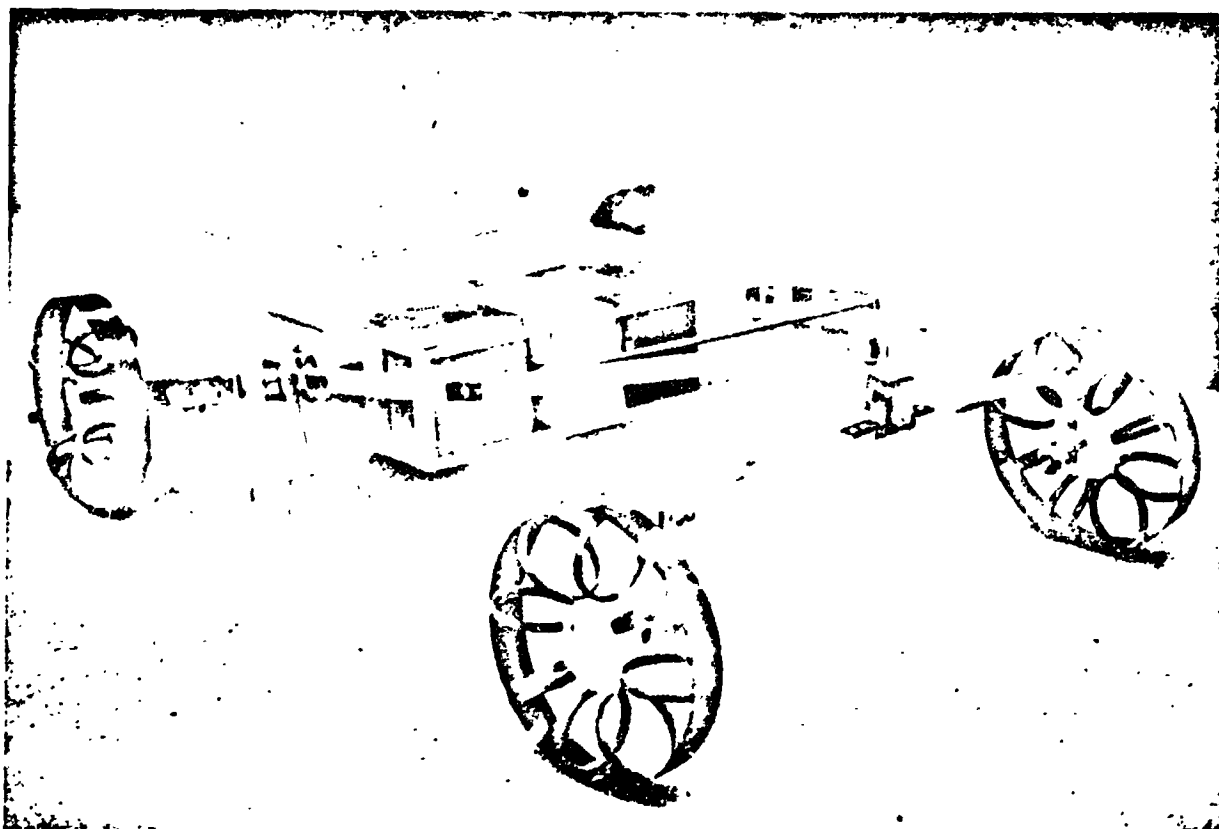


Figure 8. With all four wheels again on the surface, the payload is raised to desired height, and the RPI-MRV drives away from the obstacle.

Included for the calculation of the vehicle weight are estimates of the frame weight, motor weight and frame link weight. The results indicated that the greatest contribution to the vehicle weight was due to the motors. Those weights were conservative estimates, which included the motor, motor mounting and gearing weights. The motor weight estimate was 65% of the total vehicle weight estimate. The calculated payload fraction was 0.585. The indication is that even with the very conservative motor weight estimates, the payload fraction of the RPI-MRV is equivalent to the payload fraction estimation made for the six wheel vehicle, Ref. 2.

A 0.2 scale vehicle and capsule model has been built to demonstrate the vehicle capabilities. The basic design concepts are well established for the RPI-MRV. What remains is to evaluate the vehicle design relative to the mission requirements.

In the finalizing of the vehicle design, the areas of concern are: evaluation and testing of existing mechanisms, design of locking and deployment actuation mechanisms, physical damper designs and investigation of operating parameters, such as power and torque requirements, structural components, payload fraction and science package operation.

A.1.a. Design, Construction, and Evaluation of 0.4 Scale Model - W. Embleton  
Faculty Advisor: Prof. G. N. Sandor

Construction of a 0.4 scale model of the RPI-MRV has reached a stage which will accommodate the first tests and evaluations of the larger scale vehicle. This modelling has indicated the need for additional design work in the areas of lateral stiffness of the wheel, front suspension and motor mounts. It has also provided information on the constraints associated with the hinges, joints and locking mechanisms for collapsibility and deployment. While bringing to light problems in the areas mentioned, the scaling up to the 0.4 scale has reinforced the RPI-MRV concept as a plausible candidate for the rover mission.

The requirements for the structure of the 0.4 model were determined by area-moment analysis. Materials were selected to minimize the frame weight. Once constructed, it was found that the section used for the frame was inadequate because of its response to shaker inputs, contributing to the oscillations of the vehicle. Also, the frame provided insufficient support for the frame pivot. It was changed, the new frame being more rigid with the frame pivots removed to accommodate the shaker testing. This frame is temporary. When complete, the 0.4 scale model will have the required pivots and locking mechanisms for implementation of the collapsibility and deployment scheme as well as the emergency maneuver.

The problem of the lateral softness of the wheel was noted during the shaker tests. The vertical input to the front was resulting in a significant horizontal response of the rear of the vehicle. An investigation is presently underway which will evaluate the lateral softness problem and make recommendations as to the most effective approach to increasing lateral stiffness of the wheel while retaining its radial compliance and minimal weight.

The front suspension originally on the 0.4 scale model proved to be too soft when the vehicle was tested on the shaker unit. It was replaced with a rigid axle. The shaker data taken in both conditions will be compared to indicate the effects of a soft axle versus a stiff axle on vehicle response.

The motor mounts and motor locations will depend on the kind of motors used to control the vehicle functions. Presently, an effort is being made to locate appropriate DC motors for the 0.4 model.

Future work will be directed to designing, constructing and evaluating frame pivots and locking and deployment actuators and to providing the propulsive power and control systems required to evaluate the performance of the vehicle. Efforts to optimize the design will continue.

A.1.b. Vehicle Dynamics - Mark C. Rodamaker, Alan Ryder  
Faculty Advisor: Prof. G. N. Sandor

The objective of this task is to provide a mathematical model and computer simulation of the vehicle to: 1) aid in the basic design of the full scale vehicle, and 2) optimize the full scale design by predicting the dynamic response of the vehicle to various inputs. Two approaches to the development of the analytical model are currently being studied. Both approaches are described below.

The first analytical approach assume the vehicle to be of a bicycle configuration. Equations for this six-degree-of-freedom planar model have been derived using a complementary virtual work method. This allows the inputs to be displacements rather than forces as required in classical Newtonian methods. An analog simulation of the model was attempted. However, technical problems resulting from the mating of more than one analog computer forced this method to be abandoned. A digital computer package "DYNAMO" (DYNAMIC Models) is currently being used in an attempt to solve the derived equations.

The second, more recent analytical model considers a three-dimensional, three-degree-of-freedom model (see Fig. 9). Equations have been developed for a moving reference frame as follows:

$$\begin{aligned} y &= \text{vertical translation} \\ \theta_x &= \text{rotation about longitudinal axis (roll)} \\ \theta_z &= \text{rotation about lateral axis (pitch)} \end{aligned}$$

With these, the equations of motion take the form:

$$\begin{aligned} m_r \ddot{y} &= -y(2K_1 + Z_r + Z_f) + \theta_x(l_2 K_1 - l_1 K_1) - \theta_z(bZ_r - aZ_f) \\ I_{xx} \ddot{\theta}_x + I_{yy} (-\dot{\theta}_x \dot{\theta}_z) &= y(K_1 l_1 - K_1 l_2) + \theta_x(-l_1^2 K_1 - l_2^2 K_1 + w_r h) \\ I_{zz} \ddot{\theta}_z + I_{xy} (\dot{\theta}_x)^2 &= y(bZ_r - aZ_f) + \theta_z(-b^2 Z_1 - a^2 Z_f + w_r h) \end{aligned}$$

where:

- $Z_r$  = rear suspension mechanical impedance (in the vertical direction)  
 $Z_f$  = front suspension mechanical impedance (in the vertical direction)  
 $K_1$  = mechanical impedance of side suspension (in the vertical direction) (front-rear wheel combination)  
 $m_r, w_r$  = mass, weight of sprung vehicle  
 $h$  = height of center of mass of sprung vehicle above horizontal plane of unsprung center of mass  
 $l_1, l_2, a, b$  = dimensions locating center of sprung mass, Figure 9.

These simultaneous equations remain to be linearized and solved.

Actual physical testing of the 0.4 model has been conducted. A capacitance-displacement measurement system has been used to measure responses. An electro-magnetic shaker unit has provided oscillatory inputs to the model. Three dimensional front end frequency responses have been measured, in addition to step response data for the front end. Rear frequency responses have been practically determined. Vehicle characteristics (mass, spring rates, damping coefficients, moments of inertia) have been measured.

This will serve as the background for analyzing the measured dynamic responses in order to:

- 1) evaluate and refine the analytic models
- 2) determine the source of undesirable response characteristics.

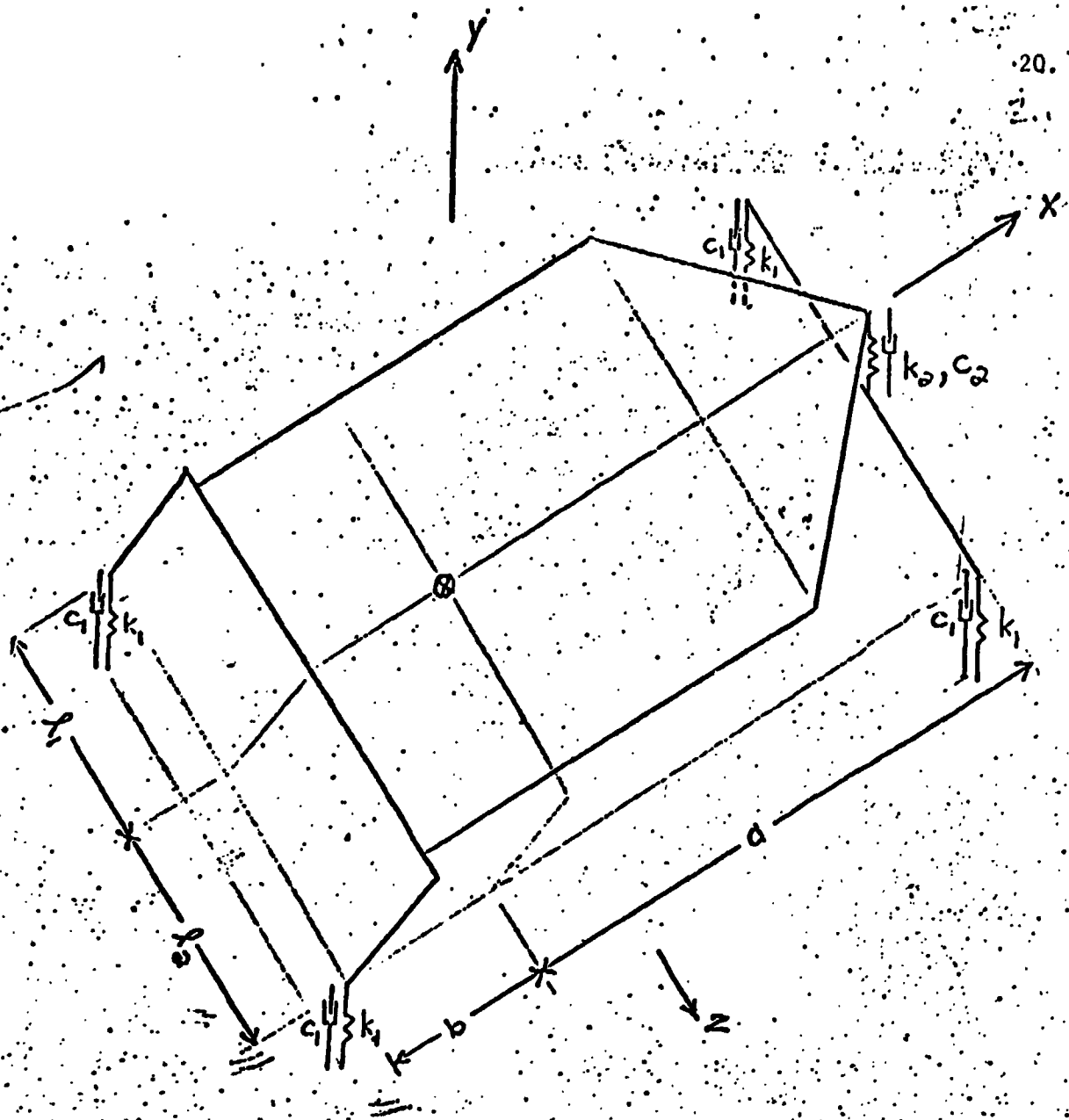
In the future, it is proposed that the three-dimensional mathematical dynamic modelling of the 0.4 scale model be extended to include additional degrees of freedom. Computations will be compared with experimental results to verify the mathematical analysis. The analysis will then be used to determine the spring and damping coefficients to be put on the experimental 0.4 scale model.

In the development of the bicycle model, the next stage involves modeling of terrain features. This is necessary to calculate the dynamic pitch and heave response of the RPI-MRV to "typical" Martian surface inputs. This terrain model will later be applied to the extension of the bicycle model: a three-dimensional multi-degree-of-freedom dynamic model. Loading, calculated from the three-dimensional analysis, will be used to size the structural members of the RPI-MRV. Analysis of the structurally sized vehicle will permit reliability and payload fraction analysis.

A.1.c. Obstacle Negotiation - Larry Mabius  
 Faculty Advisor: Prof. G. N. Sandor

The objectives of this task were to extend the obstacle negotiation study to include the variability of the vehicle center of gravity, a stability factor for the vehicle condition, a generalization of the obstacles to a series of straight lines in a plane, and background provision for the eventual extension of the obstacle negotiation modeling to three dimensions.





Consider 3 degrees of freedom:  
 translation:  $y$   
 rotation:  $\theta_x$  (roll)  
 $\theta_z$  (pitch)

Figure 9. Schematic Model.

A digital computer program was developed to model a two dimensional vehicle operating in a vertical plane as it traversed steps, slopes and crevasses. The geometric technique used in earlier studies was abandoned in favor of the more general force and moment equation, which simplified the analysis and accommodates the inclusion of an adjustable payload height as an additional model parameter. The study indicated that by lowering the cg. of the vehicle, (at the same time lengthening the vehicle and placing a greater percentage of weight on the front wheels) the rear wheel drive torque required to drive the front wheels up a simple obstacle increased. This was expected, because of the increase in loading of the front wheels while lowering the center of gravity. The rear wheel drive torque required for simple step, crevasse and slope obstacles decreased as the cg. was lowered. The model confirmed what had been expected. This means that, if needed, an advantage may be gained by reducing the rear wheel torque required to traverse an obstacle by cg. height adjustment. The torque requirements calculated are based on static equilibrium, not including friction or soil-wheel interaction.

The program was extended to include a stability factor. The intent was to have this factor serve as an indicator of how close the center of support (vertical projection of cg.) came for some attitude and configuration to the wheels (the vehicle support points). This will then give, some indication of the magnitude of disturbance the vehicle could tolerate before becoming unstable. (Instability is here defined as the vertical projection of the cg. being outside the quadrangle of wheel contacts on the ground).

A friction term was also included in the model by indicating a torque necessary to overcome the rolling friction of the vehicle. As data becomes available, this term will be altered to increase its realism for the vehicle. Presently it is included as a constant, but could be made a variable dependent upon vehicle life, speed, soil conditions, and wind velocities and direction.

Energy requirement calculations were made based on the frictional and static torques. This should be extended to energy calculations which include the effects of factors of terrain, soil conditions (including slip), relative wind velocities, and vehicle speed.

Additional work in this area will be aimed toward developing an extension of the planar two-dimensional vehicle and obstacle field to a three-dimensional vehicle and obstacle field. This extension should include the testing of combinations of obstacles which the vehicle could negotiate individually but possibly not in combination. From this will develop information which will define terrain conditions which pose to the vehicle true obstacles for reasons of stability, power or torque requirements. An extension of this work will include soil-wheel traction parameters. This would define completely the terrain conditions and permit calculation of the vehicle ability to negotiate or not negotiate the indicated combinations of terrain geometry and conditions.

A.1.d. Radio Control - Mark Rinaldi, Mike Wolf  
Faculty advisor: Prof. G. N. Sandor

The objective of this task is to design and build remote control capability for the 0.4 scale model. This involves establishing a radio

link between the operator and the vehicle. The purpose of this remote capability is twofold. The first is that of observing the vehicle behavior under varying conditions for identical sets of instructions. The second is to provide a test bed for sensing and operating systems. These objectives will ultimately require computer control of the vehicle through the radio link.

The initial stage is the development of a manual input system. Additional features will be added, and refinements made until closed loop computer control is achieved. Incorporated in this task, and undergoing parallel development is the vehicle function control. The received radio signal must be converted to a meaningful command to which the vehicle functions must respond.

The parameters of the radio link system have been defined and the system functional blocks designated. Flexibility in the design of the system and its components has been stressed to accommodate additions and changes to the vehicle and the commands desired.

The task of creating equipment designs for the functional blocks has begun. Designs for the manual input device, command encoder, radio link and command decoder are complete. They have been built and tested, with the exception of the "clocks" required at the transmitter and receiver to synchronize the data reception with the data transmission.

Significant progress was made toward realizing only the first of the above objectives. After some thought it was decided that a digital communications system would be most appropriate, especially to simplify interfacing problems with the computer.

From the several types of digital modulation available, Frequency Shift Keying (FSK) was chosen, primarily for its high noise immunity and ease of implementation. FSK can only be used for low data rates, but since high speed was not a primary concern, a data rate of 106 bits/sec. was chosen.

Another factor in selecting a data rate of 106 bits/sec was selection of walkie-talkies to provide the necessary radio link. While their small band width limits them to slow data speeds, their advantages include their low cost, high flexibility, and the ability to use them in a two-way communications link.

The time from September 1972 to January 1973 was spent in developing general design objectives and system requirements. Decisions concerning signal type, modulation type, transmitter type and initial design considerations were made during this time.

Most of this effort was centered around the construction of the Command Encoder, a block diagram of which is shown in Fig. 10. The function of the Command Encoder is to select data from either the manual controller or the digital computer and arrange it in a format that is suitable for radio transmission. The two major "blocks" in the Encoder are:

1. **CONTROL LOGIC**, takes the input data and arranges it in a suitable digital format and generates the necessary timing signals for the transmission of the data.

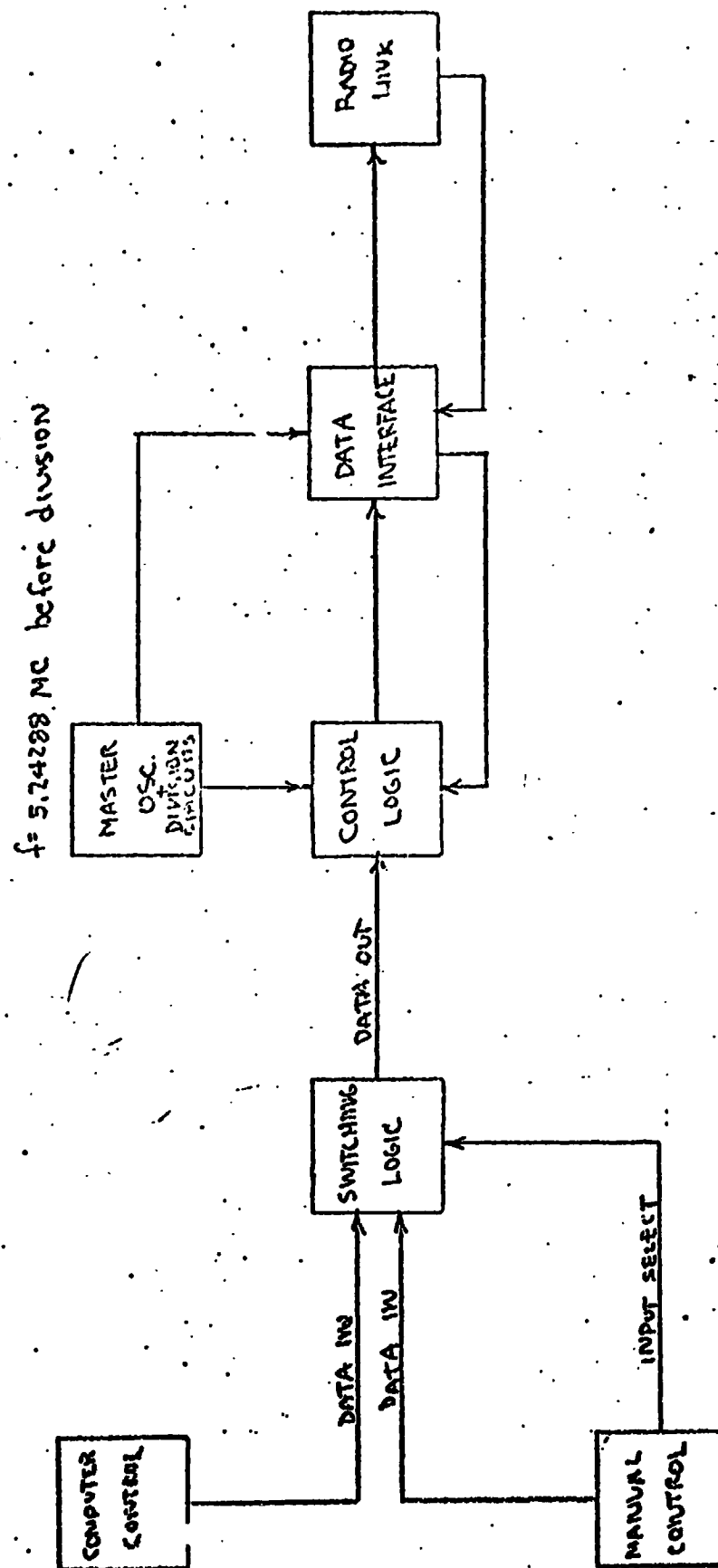


Figure 10. Command Encoder - Block Diagram

2. DATA INTERFACE, converts the digital output of the Control Logic into the corresponding FSK tones.

The Control Logic, Data Interface, manual control panel and the FSK detection circuitry which reconverts the FSK tones back into digital data have been designed and constructed. A more detailed discussion of these devices follows.

#### Summary of Work

The biggest problem encountered was the design of the Control Logic. The data format chosen consists of a 8-bit serial for each command transmitted. Since the computer provides data in this form, this choice was most convenient. The structure of the command work is as follows (see Fig. 11):

1. The first bit, called the flag, is always a logical one and is used to mark the beginning of a word.
2. Bits 2-7 are data bits comprising the command.
3. The eighth bit is a parity bit. Even parity is maintained and is used for error detection purposes.

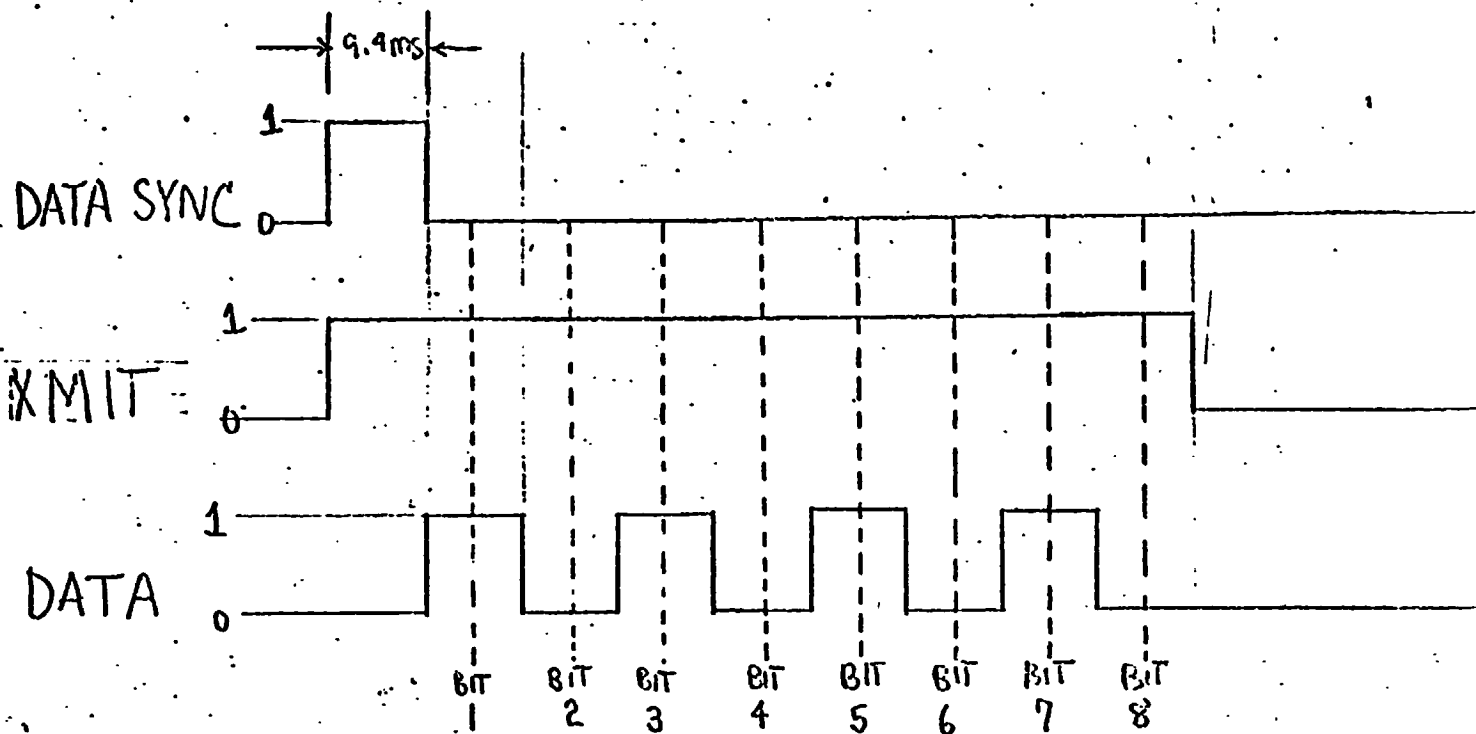
As shown in Fig. 11, the bit length is 9.4 ms. In addition, a 9.4 ms. timing signal called DATA SYNC precedes every command work and is used to synchronize the vehicle clock with the incoming data. A complete schematic of the control logic appears in Fig. 12.

#### Definition of input symbols:

1. DATA VALID - a high (logical 1) on this line indicates that the vehicle has accepted a transmitted command.
2. M.R. - Master Reset - a low here resets all systems in the Command Encoder.
3. COMPUTER CONTROL - a high level indicates that the system is under computer control. All input data comes from the computer output. A low level enables manual control of the vehicle.
4. MAN. XMIT (a&b) - the transmit command from the manual controller is entered here.
5. CLOCK - a 106khz square wave derived from the 5.26 mhz master clock is used to clock data through the system.
6. DATA IN - data is entered here from either the manual controller or the computer depending on the state of the COMPUTER CONTROL input line.

#### Definition of output symbols:

1. CLEAR - a zero level indicates system clear. (not to be confused with clear for individual counters or flip-flops)



DATA SYNC: frequency = 1310 HZ.

DATA; logical "1": frequency = 2620 HZ.

logical "0": frequency = 2048 HZ.

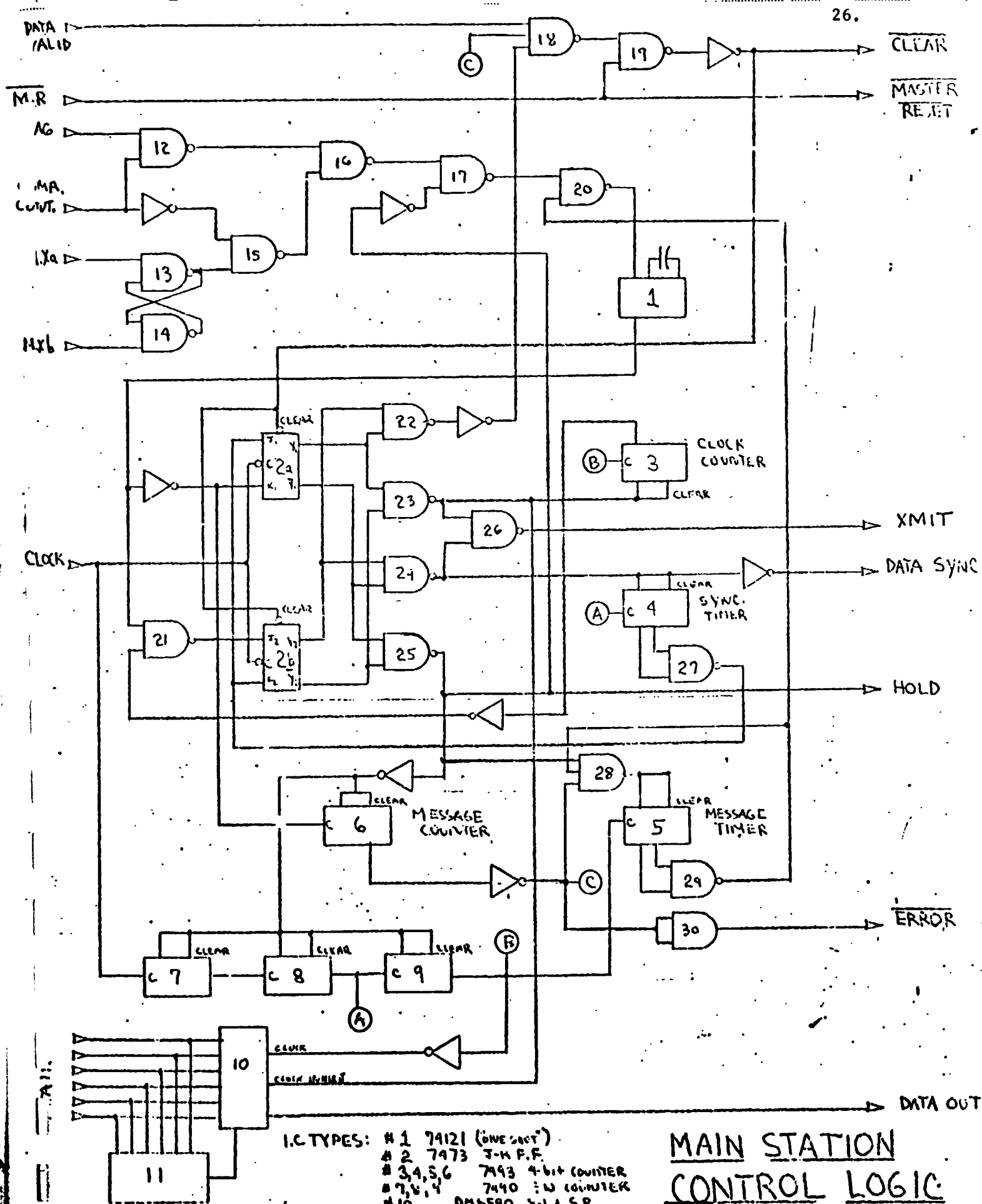
BIT 1 - FLAG BIT, USED TO INDICATE BEGINNING OF MESSAGE

BITS 2-7 - MESSAGE BITS, CONTAIN COMMAND INFORMATION

BIT 8 - PARITY BIT (EVEN PARITY)

Figure 11: Waveforms - Control Logic

REPRODUCIBILITY OF THE ORIGINAL PAGE IS POOR.



I.C. TYPES: # 1 74121 (ONE SHOT)  
 # 2 7473 J-K F.F.  
 # 3, 4, 5, 6 7493 4-bit COUNTER  
 # 7, 8, 9 7490 10 COUNTER  
 # 10 DM6590 8-bit S.R.  
 # 11 74150 PARITY GEN.  
 ALL OTHERS AS SHOWN

**MAIN STATION  
 CONTROL LOGIC**  
 FIG. 13.

2. XMIT - a one indicates that the system is transmitting and switches the walkie-talkie to the transmit mode.
3. DATA SYNC - explained previously.
4. HOLD - a one indicates that the system is processing a command. In the computer control mode it will instruct the computer to hold any new data until the system is cleared.
5. ERROR - a zero indicates that there is a communications problem and the vehicle refused to accept commands.
6. DATA OUT - eight 9.4 ms. bits that comprise a command word.

The control logic was built and tested and after some troubleshooting it met its design specifications. Having completed the control logic, the next goal was the construction of the DATA INTERFACE.

Three frequencies had to be selected to represent logical one, logical zero, and DATA SYNC. The frequencies were chosen to be well within the pass band of the walkie-talkies and yet far enough apart to allow for efficient filtering. All three frequencies were derived from the 5.42 mhz master oscillator, (see Fig. 13).

A block diagram for the DATA INTERFACE appears in Fig. 14. The digital waveforms from the control logic enables one of the three output lines (2048 hz, 2620 hz or 1310 hz) on which appear 0-5 volt square waves of the corresponding frequency. The low pass filter is used to eliminate some of the higher harmonics. The high pass filter eliminates the d.c. component and, the new symmetrical signal, is fed to a buffer amplifier and finally to the walkie-talkie. The 4-volts peak to peak output signal is reduced to about 200 mv at the walkie-talkie. A complete schematic of the Data Interface is shown in Fig. 15 and typical waveforms are shown in Fig. 16.

The next task that was undertaken was the construction of a COMMAND DECODER to reconvert the FSK tones back into a digital signal. The most important part of the Command Decoder is the tone detector circuitry, the block diagram of which appears in Fig. 17. A complete schematic appears in Fig. 18. The operation of the tone detector is relatively simple.

An amplifier of gain 10 is used to boost the input signal (IC 1) and a high pass filter removes the dc component. IC 2 is a buffer amplifier used to provide a low source impedance for the filters.

The active filters (IC's 3, 4, 5) are of the multiple feedback bandpass type with  $Q = 10$ . Trim pots R1, R2, R3 provide center frequency adjustment for each filter.

Following each filter is a peak detector the output of which is proportional to the amplitude of the input sinusoid.

IC's 7, 8, and 9 are voltage comparators used as threshold detectors. Trim pots R4, R5, R6 provide adjustable threshold levels for each of the detectors. The DATA and SYNC outputs are TTL and DTL compatible.



# MASTER OSCILLATOR AND DIVISION CIRCUITS

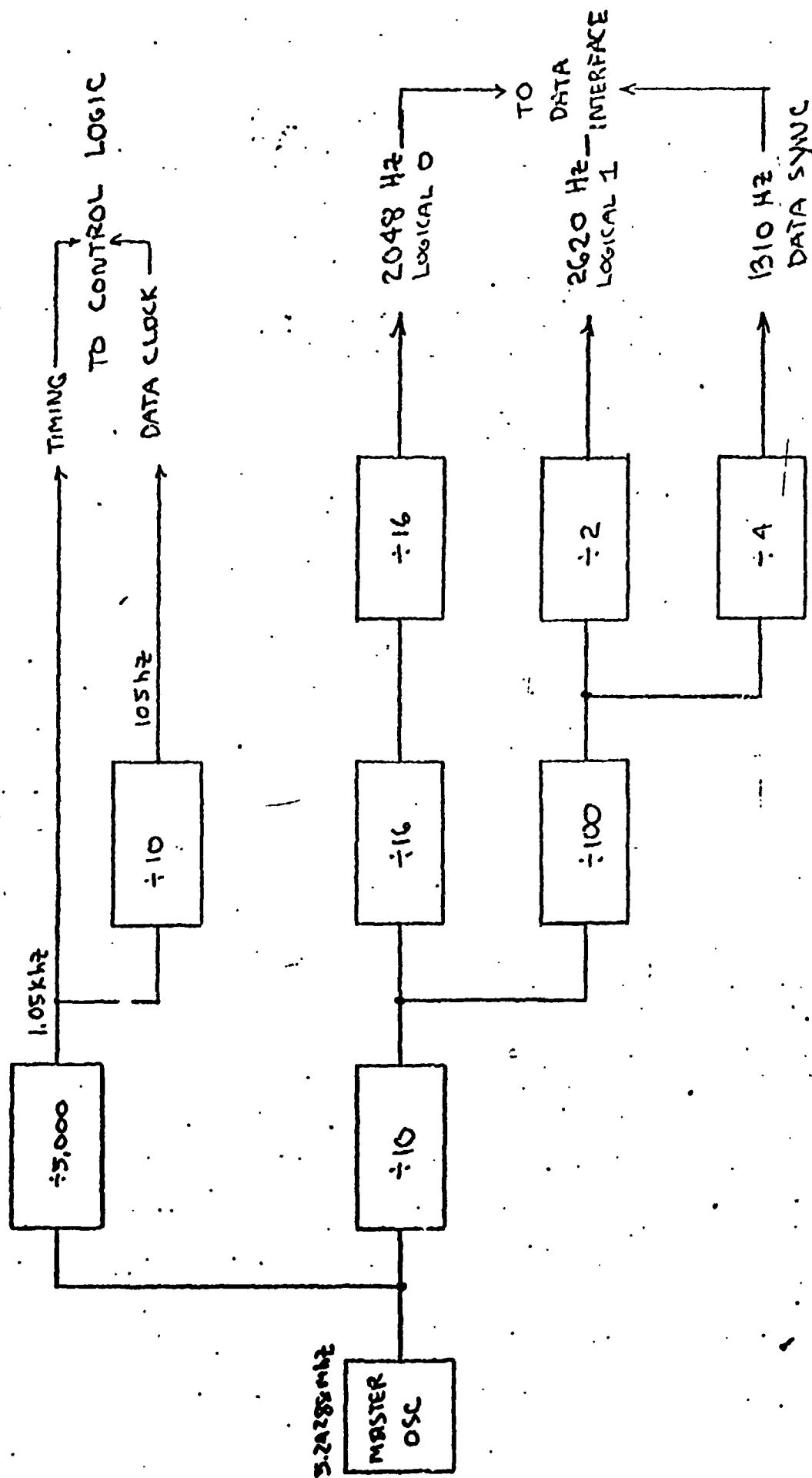


Figure 13.

# DATA INTERFACE

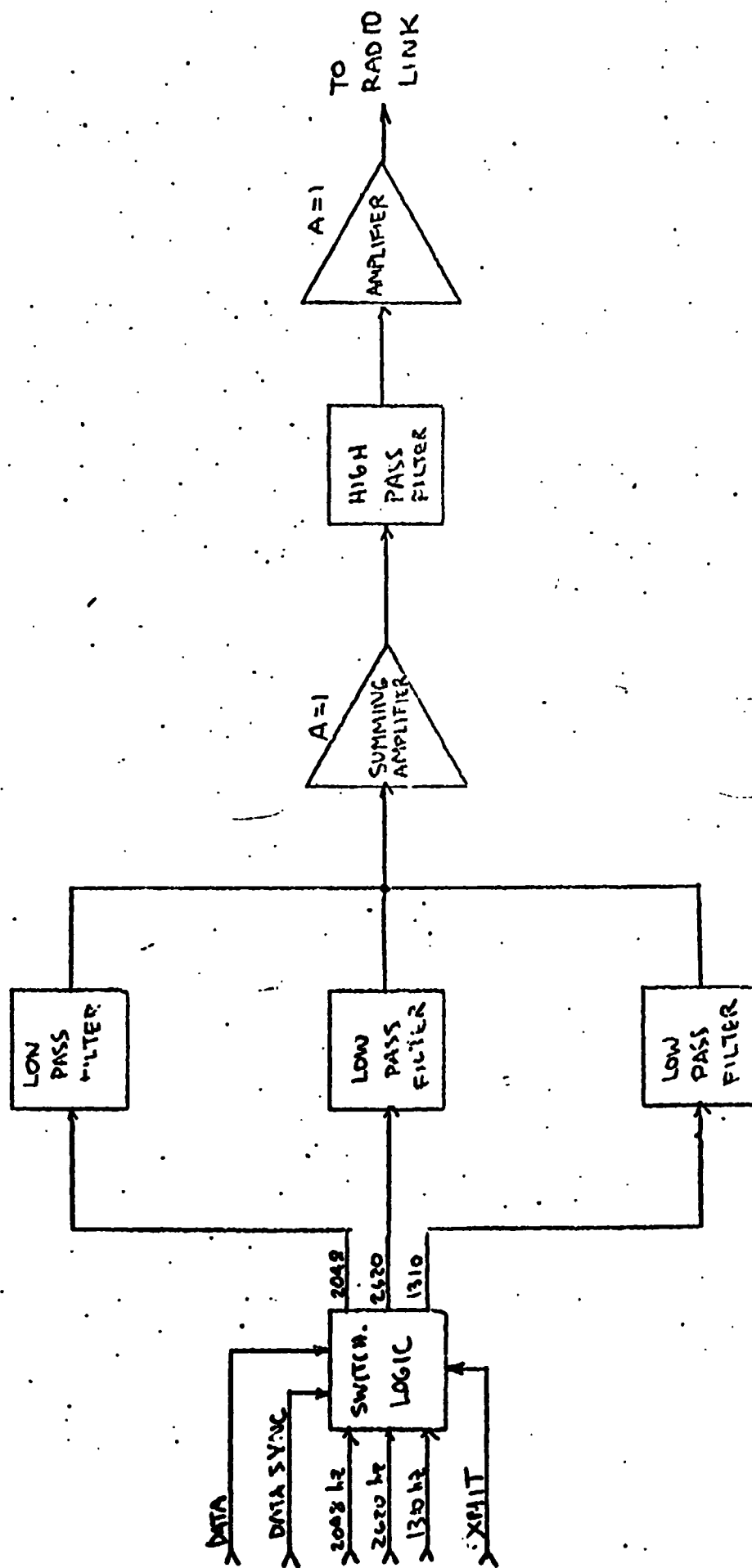


Figure 14.

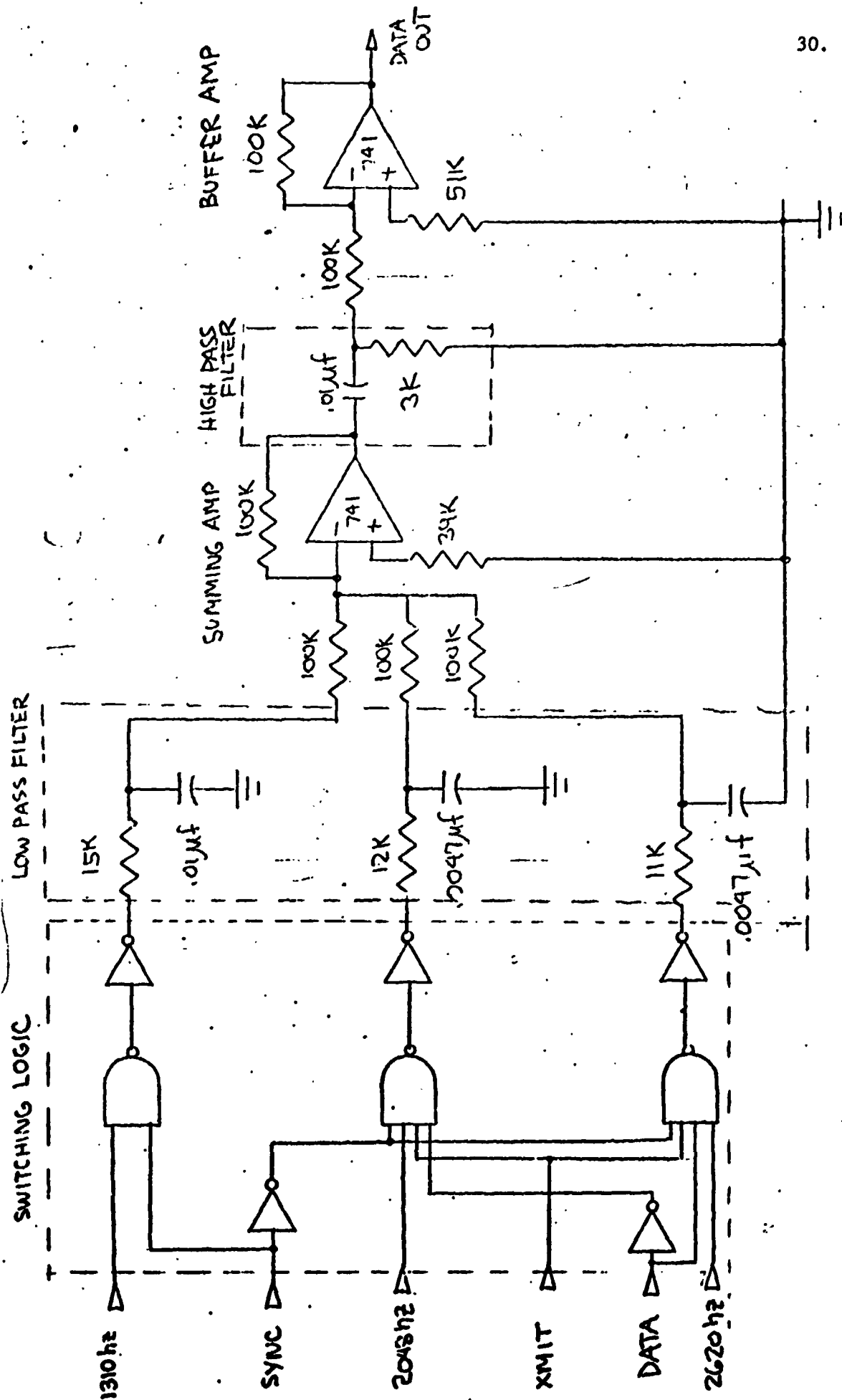


Figure 15. Transmit Data Interface

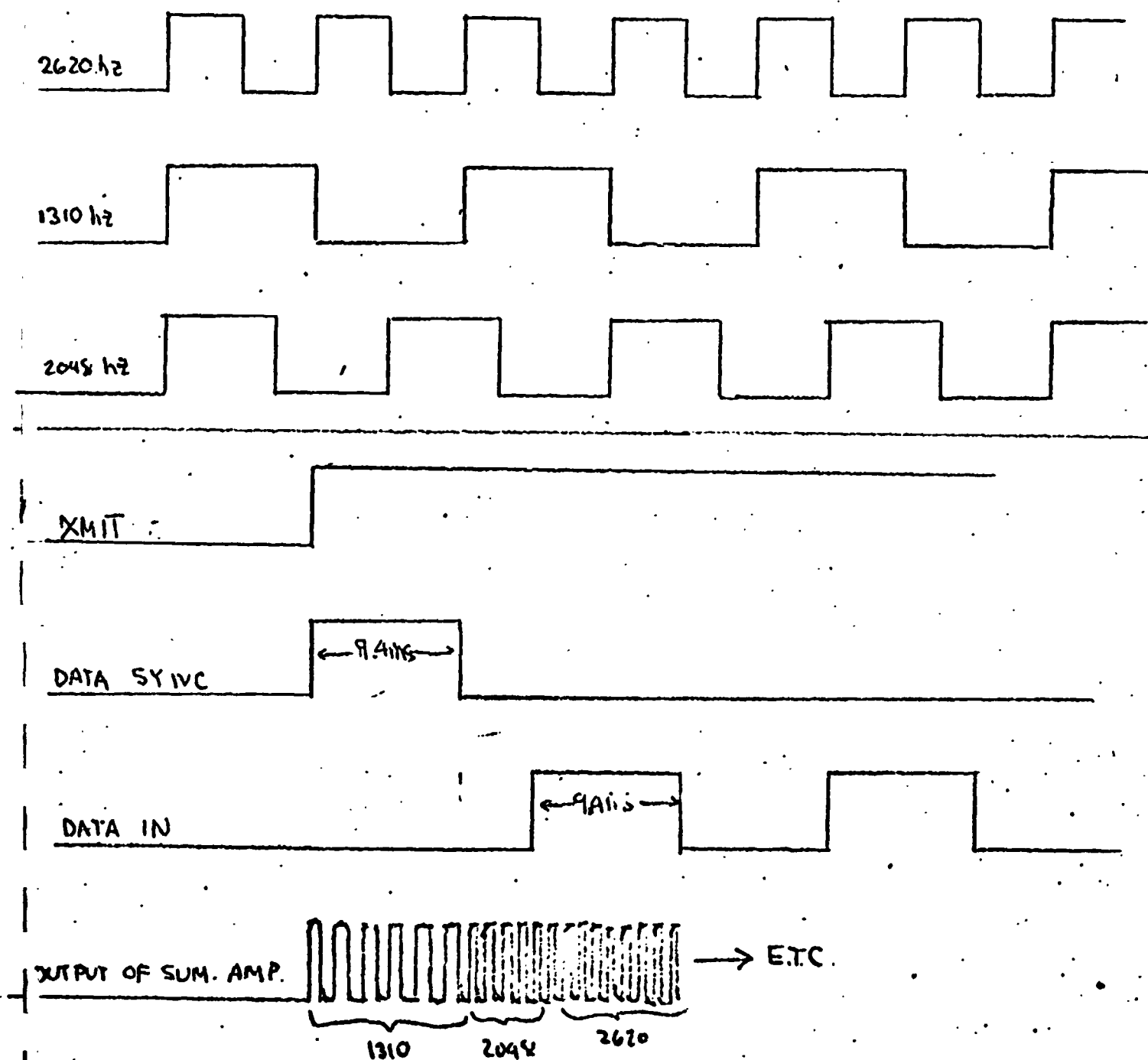


Figure 16. Data Interface - Waveforms

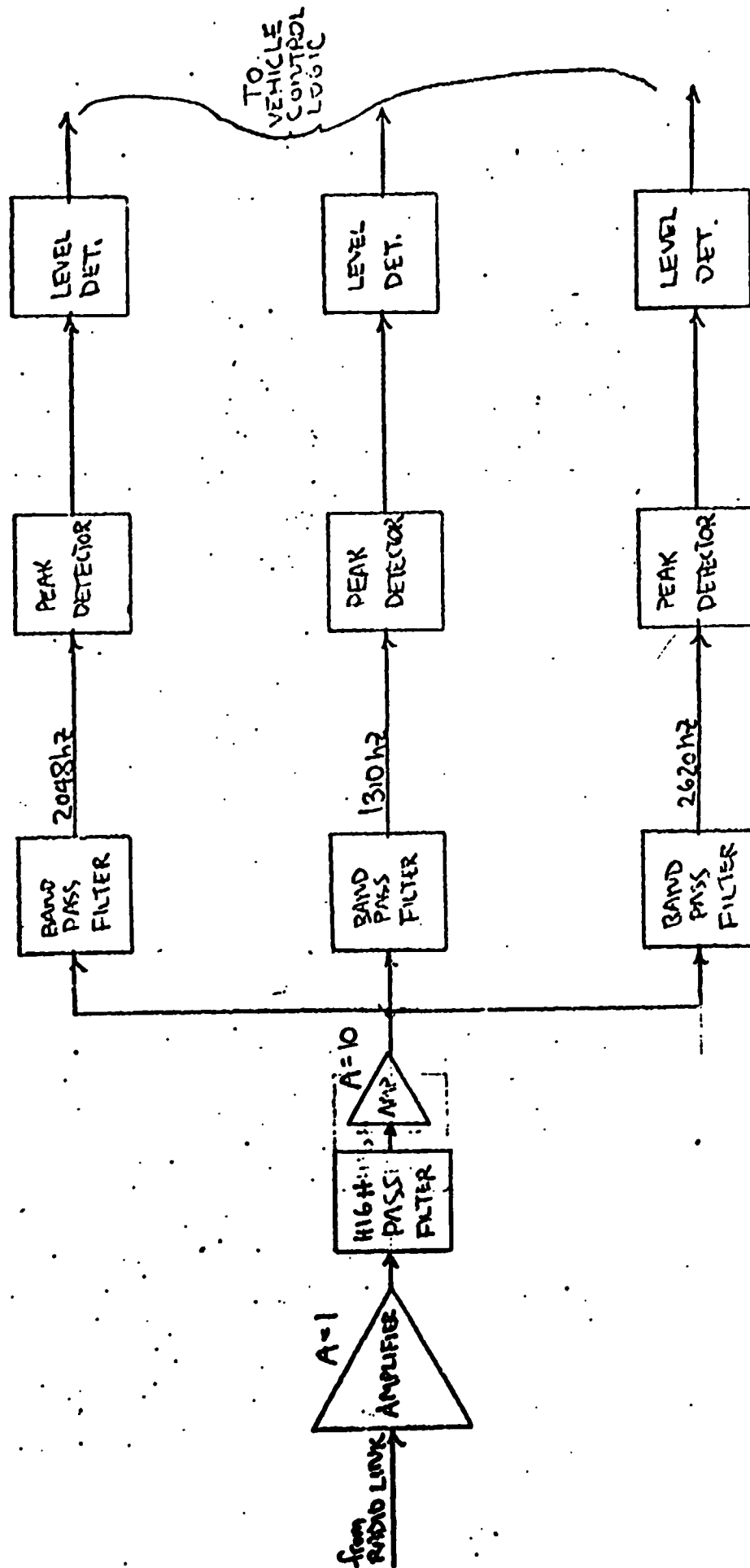


Figure 17. Block Diagram - Tone Detector



**Figure 18.**

### Summary of Radio Link

With regard to the work completed so far, the major problem was receiver noise. To ensure proper operation of the vehicle, a low data error rate is essential. Although FSK provides good noise immunity, walkie-talkies are very noisy devices. Initial tests were disappointing, showing poor system noise immunity. After some adjustment of the threshold levels and better shielding techniques the performance improved significantly and is satisfactory.

Major accomplishments during the past year were the completion of the COMMAND ENCODER including the manual controller. The construction of the tone detector and subsequent testing showed that the system is capable of transmitting relatively error-free data. In addition, the present system incorporates enough flexibility to allow for many changes in system requirements.

The problem of converting the received command into action by the vehicle was considered in conjunction with, but separate from the radio link. The system decided upon has a discrete command format, with the vehicle being self reliable (an open loop system). The received and decoded command is stored and then converted to a speed reference in accordance with which the drive power is supplied. Figure 19 shows the functional block diagram of the motor control system. The system provided three areas of concern: a time base, a motor speed reference, and a motor driver circuit.

The design of the motor driver circuit settled on a class "D" modulated pulse-width amplifier. This was selected because negligible energy is dissipated in the output devices since they operate as common-emitter switches.

### Summary - Control System

Progress has been made on the control system in the areas of speed control, command storage and conversion to analog levels. The system was designed to be an all purpose one which could be duplicated for control of each of the vehicle's four motorized functions. To complete the system reference, sensors must be placed on the vehicle and their output incorporated into the control system. The radio link and motor control system were linked together and used to control the states of a vehicle motor.

The mated systems were able to produce three output speed levels in both forward and reverse directions. Control was done remotely from the manual control panel. The clocks for this were signal generators which will be replaced by individual receiver and transmitter clocks when they have been built and tested.

The test showed the feasibility of the radio control system in the actual control of motor states. While much remains to be done before the system is complete, initial strides have been made.

The time-base for the pulse generator was driven from the master clock in the receiver decoder logic. This was divided down to approximately 600 hz. This, was then fed to a one-shot multivibrator that reset

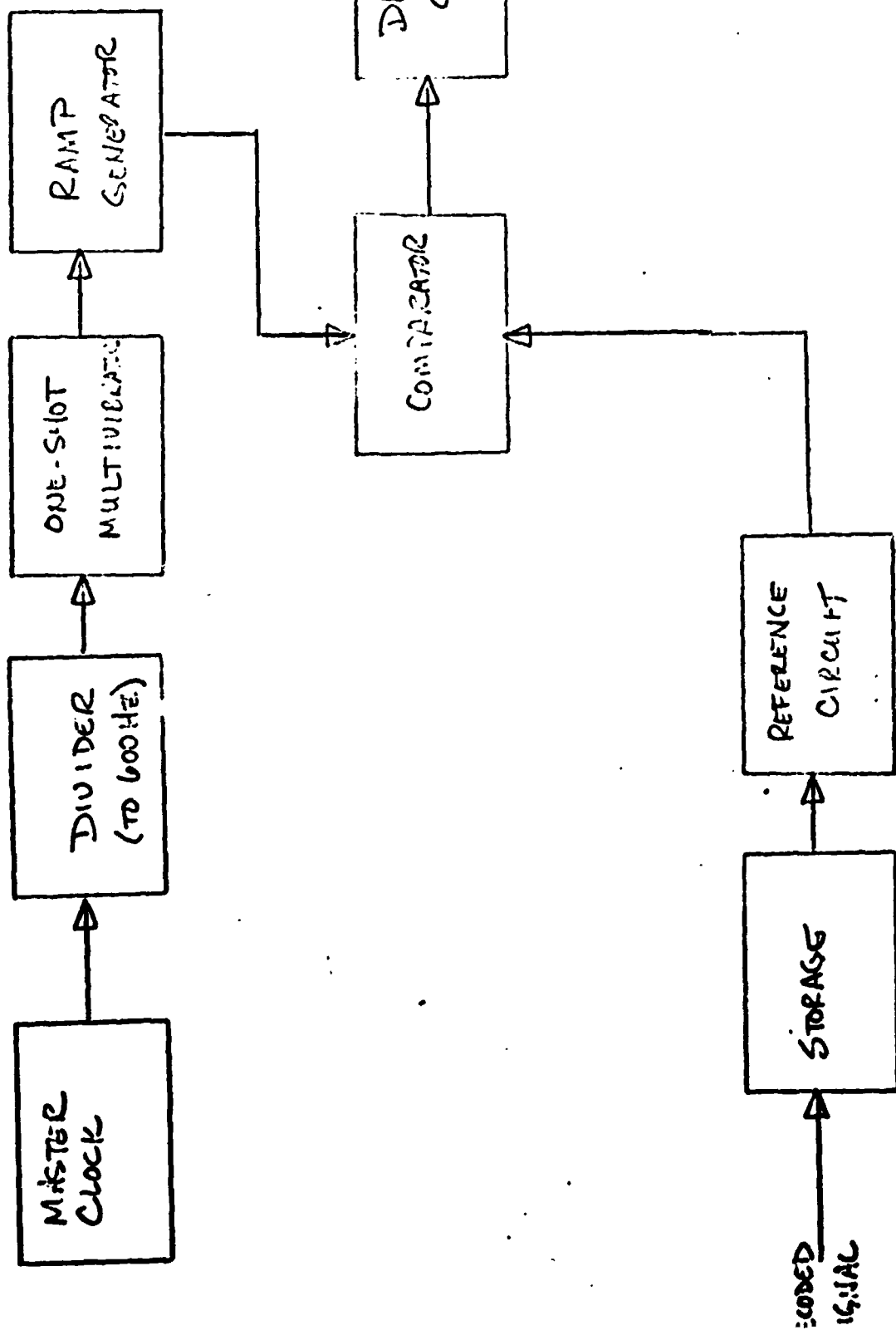


Figure 19. Functional Block Diagram



the ramp generator periodically. The voltage ramp was generated using a constant-current source transistor charging a capacitor. The voltage rises as a ramp since:

$$V_{cap} = \frac{1}{C} \int_0^t I_{charge} dt$$

with  $I_{charge}$  constant. Components of the ramp generator (Fig. 20) were picked so that the ramp could reach 5 volts before being reset by the discharge transistor. Two ramps were made available by the operational amplifiers: the first used as a buffer amplifier with a gain of ten, and the second as an inverting amplifier. The ramp outputs were sent to the comparators in the driver circuit, (Fig. 21). With a zero reference level the outputs were +12 for one and -12 for the other. Since the ramp did not reset to zero exactly, a dead-band exists which gives a stop level for the motors.

Once power control was established, a reference level was needed, Fig. 22. The data was to be provided by the radio link, and a separate storage register was necessary to hold the commands. The only commands were speed magnitude and direction. Output from the J-K flip-flops were routed to the appropriate summing resistors via the two input and gates. The operational amplifier acted as a scaling adder in which the reference resistors provided several magnitudes of current to the amplifier inputs. The circuit was a simple digital-to-analog converter shown in the table below.

Ex.	BINARY	ANALOG
	0 0 0	0.00
	1 1 1	+ 5.00
	1 1 0	+ 3.34
	1 0 1	+ 1.67
	0 0 1	- 1.67
	0 1 0	- 3.34
	0 1 1	- 5.00
Storage	4 5 6	

This analog output was then sent to the comparators in the driver circuit. The pulsewidth was determined by the length of time the ramp stayed below the reference level (above the reference for the negative driver comparator), Fig. 23. A shift of reference voltage would therefore alter the width of the pulses and generate a change of speed.

For the future, the completion of the first stage will be the installation of the complete radio system for open-loop manual control. This will be extended first to closed-loop control, and then to computer operation. The on-board motor controller will be completed for all of the motorized vehicle functions. Once the control of the vehicle has been proven with basic command inputs (i.e., forward, reverse, turn thirty degrees), a function controller algorithm will be prepared to respond to complex commands (i.e., turn from heading of 300 degrees to a heading of 200 degrees).

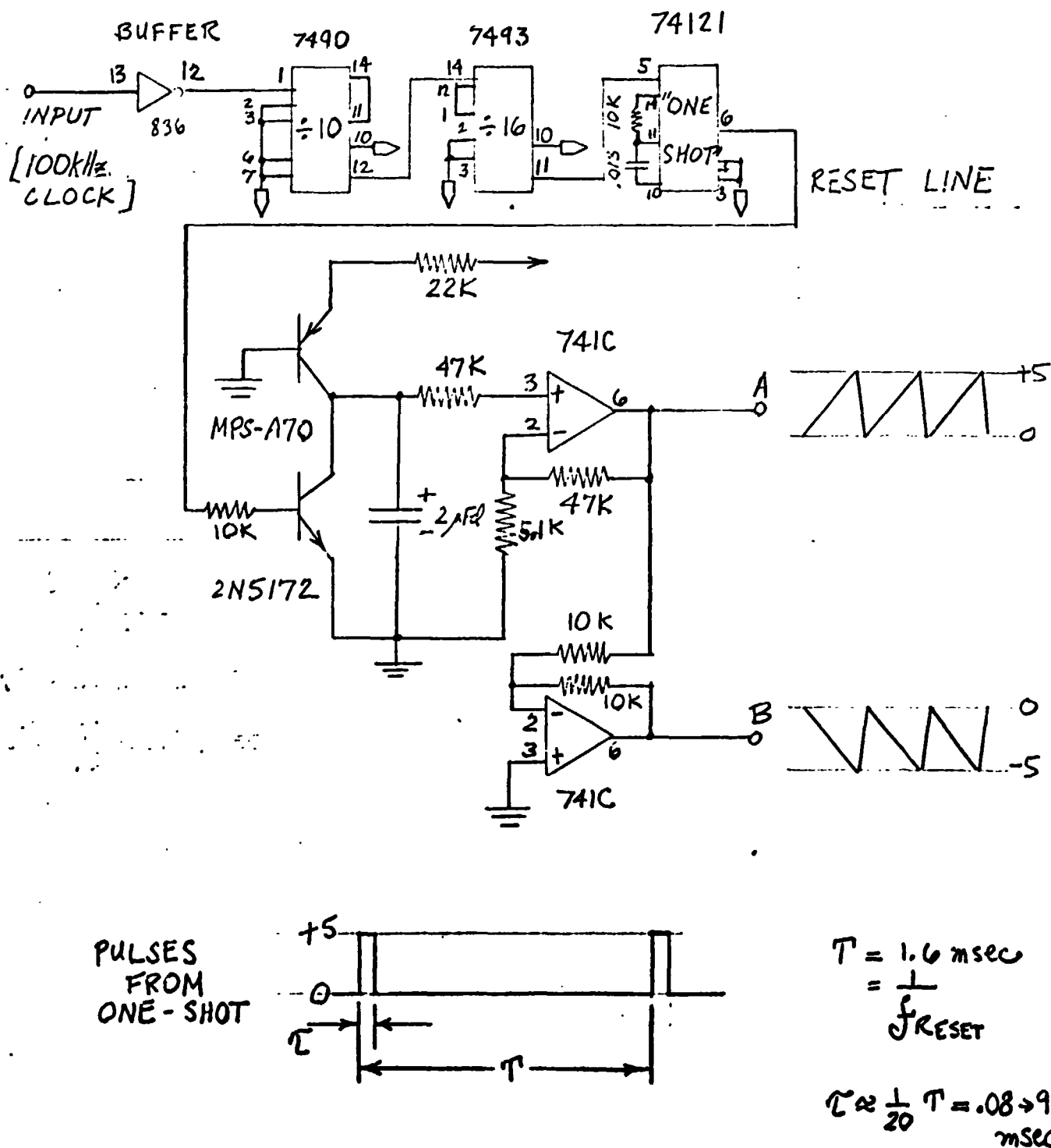


Figure 20. Ramp Generator

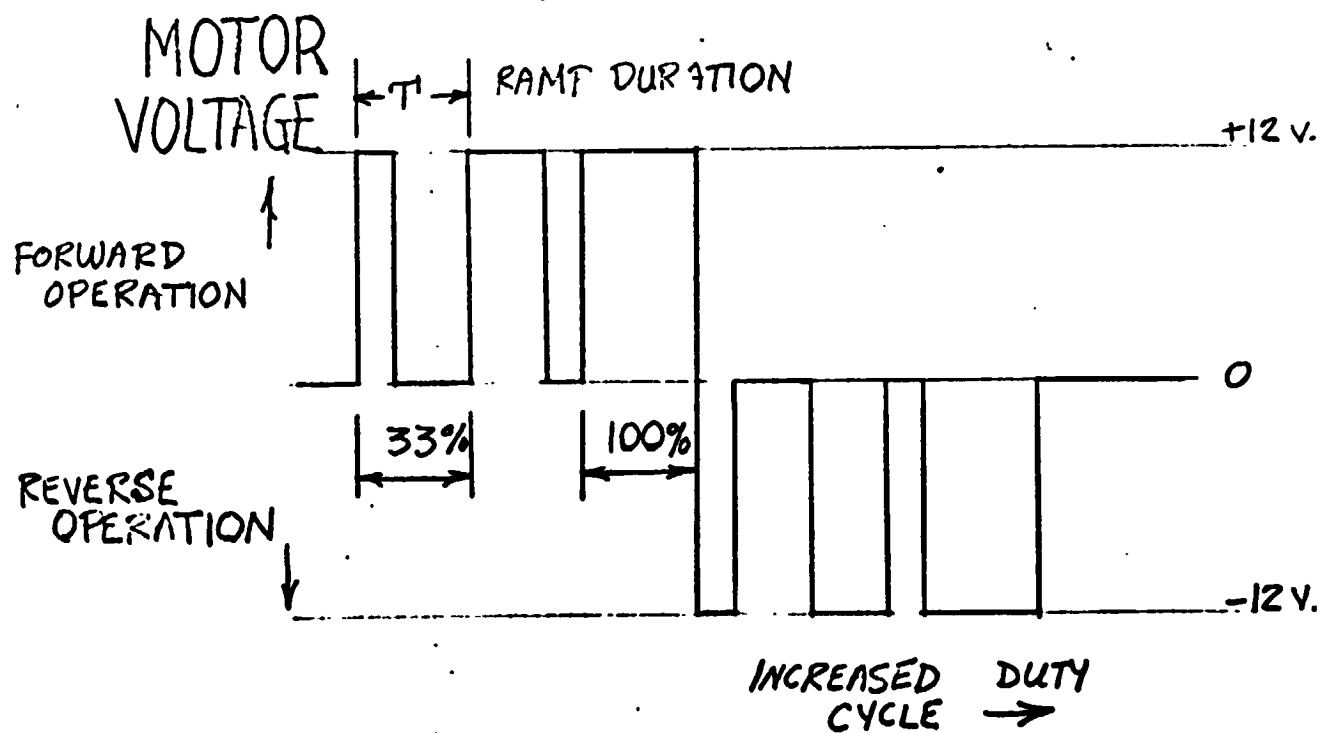
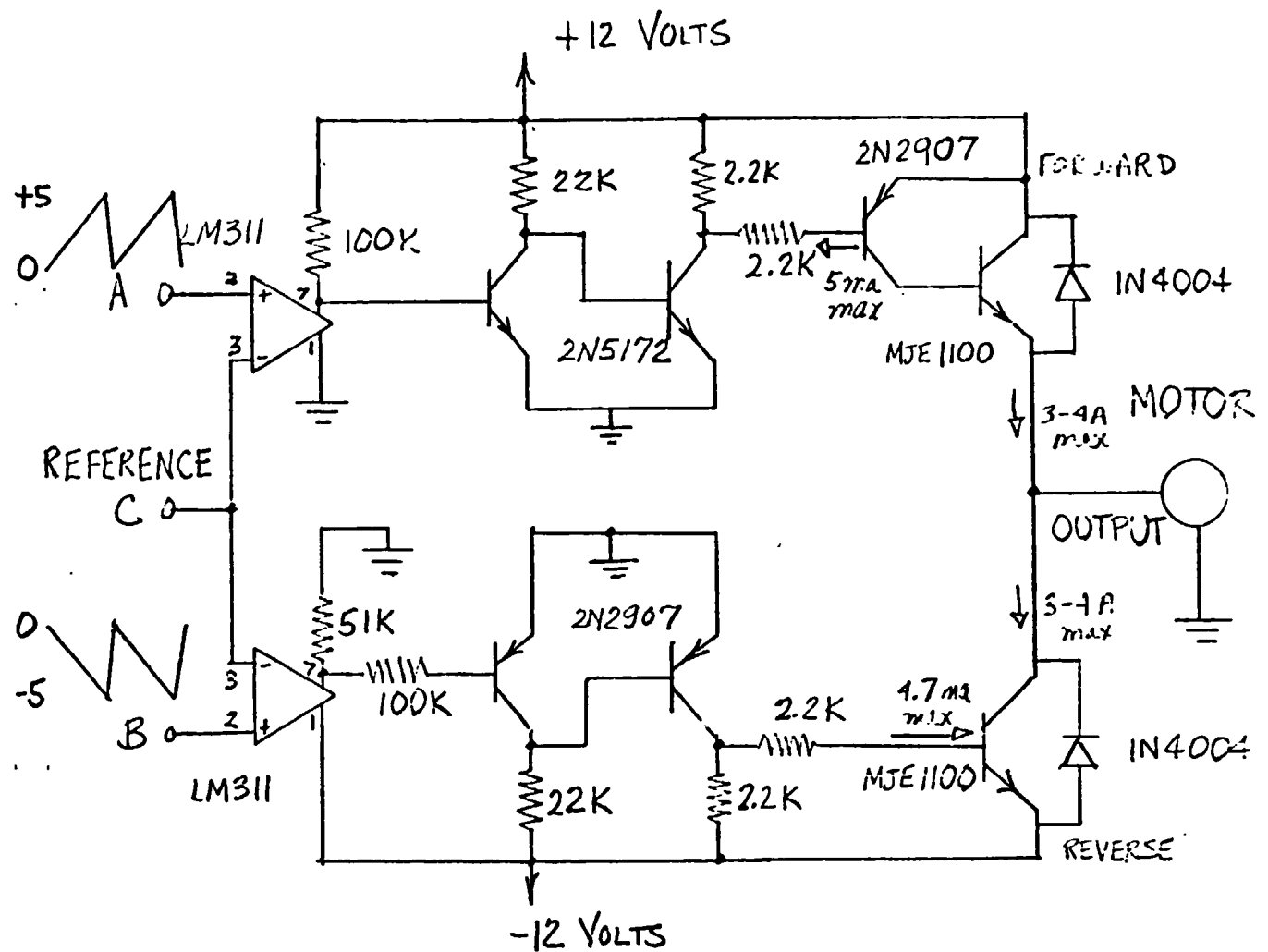


Figure 21. / Motor Driver

BITS FROM  
DECODER-DRIVER INTERFACE

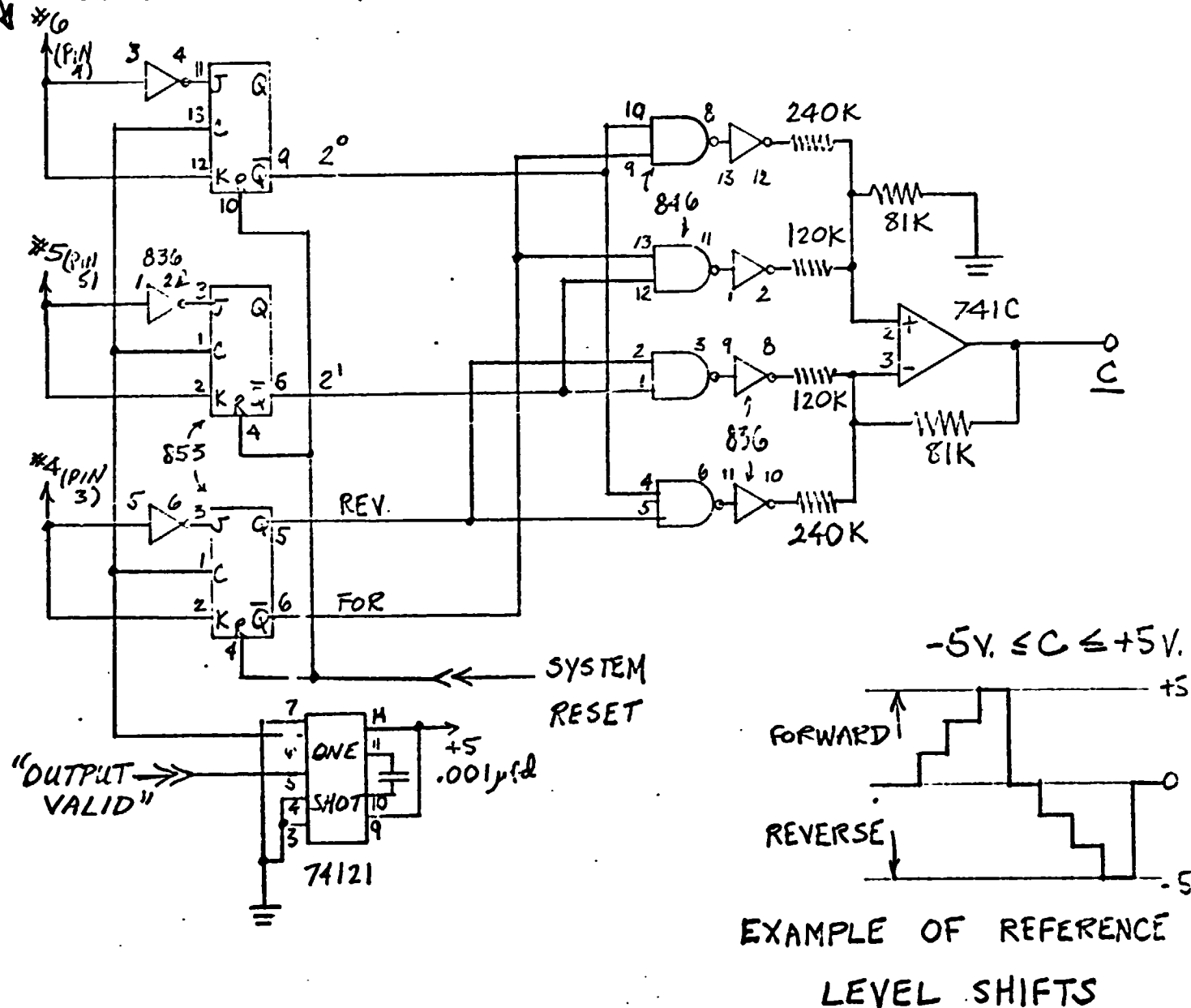


Figure 22. Motor Speed Reference Circuit

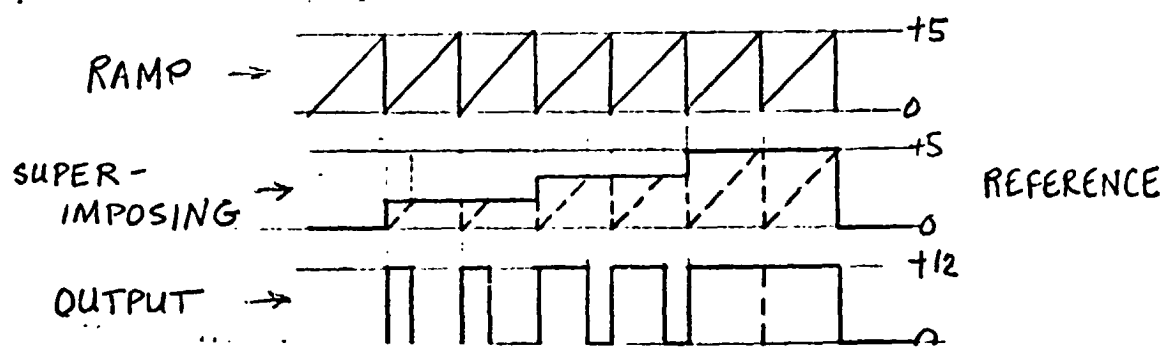


Figure 23.

A.2. Collapsibility and Deployment - John Almstead  
Faculty Advisor: Prof. G. N. Sandor

A solution for the problem of stowage of the RPI-MRV in the Viking capsule, and its subsequent deployment on Mars, has been found. The third generation design had as one of its criteria, to fit in the Viking capsule and to deploy with the greatest degree of simplicity and reliability possible.

The vehicle is "folded" in such a way as to locate the center of the payload package on the centerline of the capsule, and to deploy by use of the front pivot, frame pivot and rear strut pivots as described in the following paragraphs and Figures 1 through 8.

The front frame articulation pivot is to be used for collapsibility and deployment only. Once the vehicle has landed on the Martian surface and has been deployed to its operational configuration, the front frame articulation pivot will be fixed. The folded frame will most likely be deployed by some form of stored energy, such as springs at the pivot points. Collars placed around the overlapping frame sections will make the frame structure rigid.

The rear strut pivot and lengthening will be accomplished by a four bar linkage. The linkage was developed through the use of the complex-number technique of linkage synthesis for three precision points and specified fixed pivot positions. A computer program was written based on this technique and used interactively on a graphic time sharing terminal to synthesize and analyze the four bar mechanism that can be used to deploy the rear wheels. Analysis of the linkage transmission angles insured easy and positive deployment which can be accomplished by a stored energy system such as a spring. Once the rear wheels have been deployed and locked with a collar or clamp arrangement, they will remain in the operational configuration for the remainder of the vehicle life.

The front axle-frame connection has been designed to permit collapsibility and deployment, minimize weight, and provide for vehicle symmetry. The front axle and wheels may be rotated at the front axle-frame connection to bring the front wheels and axle above the frame. This maneuver is accomplished by the same motor used to steer the vehicle, and permits vehicle symmetry about the plane of the vehicle frame. This allows the vehicle to perform the "emergency maneuver". Without moving the vehicle body, the forward frame is brought over the vehicle to the rear, and vice-versa, clearing antennas, scanners and the like. Thus reversed, the vehicle can drive away from a condition from which it could not have backed away.

These three mechanisms required for collapsibility and deployment are being designed, implemented and tested on both the 0.2 scale model and 0.4 scale model.

Evaluation of the collapsibility deployment scheme is necessary with reference to the requirements for operation. In the near future, it is expected that requirements of the rear strut and of the forward frame for unfolding and locking the linkages in operating position will be investigated. The collapsibility scheme will be evaluated relative to reliability and the operation of the RPI-MRV. The method of deployment will be fully implemented on the 0.4 scale model.

A.3.a. Wheel Tester and Grouser Design - J. Ozimek and P. Morino  
Faculty Advisor: Prof. G. N. Sandor

The purpose of this phase of the project is to determine the performance aspects of the wheels of the Martian roving vehicle. The project was divided into four related segments discussed below. Basic equipment consisted of a 24' long plywood box 1' high and 1' wide. A test vehicle held the wheel and a drive motor arrangement. When the box was filled with sand, the wheel was driven on the sand, pulling the test vehicle which rode rails mounted on the box.

Sand Preparation: It was desirable to simulate the soil conditions which the wheel would encounter over a year's span on Mars. This means that all possible combinations of soil conditions could exist, from fine loose sand to hard bedrock. From the traction standpoint, loose sand represents one of the extreme conditions. For testing purposes, sand between two and sixty microns was obtained from a local creek bed. The sand was dried to as nearly zero percent moisture content as was feasible under room conditions.

The experimental soil conditions could have been varied by the addition of moisture and by compaction, as well as the addition of various rock sizes. However, since there exist few published results against which experimental results could have been compared, the soil conditions were not varied. It was felt that dry sand representing the worst condition, would yield conservative results. More significantly, the desired result of a comparison of the various wheel parameters, i.e. grouser design, is more readily discernable if the surface conditions are maintained constant.

Instrumentation: Initially a sophisticated arrangement was proposed in order to perform slip tests. After spending considerable time evaluating various techniques, a simpler scheme was settled upon without affecting the results to be gathered.

To obtain information about the pulling ability of the wheel and the amount of power required by the wheel, a weight and pulley system was made. Weights, suspended out a window, were connected to the test vehicle with a cord and pulley arrangement. A wattmeter was used to measure the input power to the wheel drive motor. This was compared to the theoretical power required to raise the weights.

Wheel rotation speed and cart translatory speed were also measured. Both the circumference of the test wheel axle and a cart wheel were segmented into conducting and non-conducting segments with tape strips. Brushes were installed on each. When electrical signals were sent through the brushes, the nonconducting portions produced a series of pulses which were printed on a strip chart recorder. The resulting plot was easily translated to determine the wheel's rotation speed and the cart's translatory speed. Relative slip was easily determined from these results.

It was also desirable to measure the retarding force necessary to cause the wheel to slip. To determine this, the cart was affixed to the end of the test box via a linear spring. The spring deformation was then easily translated into the retarding force.

Grouser Design: Few actual formulas or guidelines exist for the design of grousers; most design has been accomplished by use of empirical formulas or off the shelf designs. These formulas give only qualitative ideas of how grousers will perform under various conditions.

The actual material used for the grousers was old tire rubber. Initially the pattern of Figures A.3.a-1 and 2 was cut. The .3" thick lugs were glued to the rim surface, covering 90 percent of the surface. A second design removed every other grouser lug resulting in 45 percent of the rim surface being covered. The third design consisted of attaching the removed lugs on top of the remaining lugs. This resulted in the pattern of design #2 with a lug height of 0.6 inches. A fourth design used a lug of the pattern as shown in Figure 26, covering 60 percent of the rim surface. On recent lunar missions, this pattern proved to be effective in use with lunar roving vehicle wheels. A fifth design merely doubled the fourth design lug height from 0.3" to 0.6". The lug to surface ratio was not altered.

Testing Procedures: Two types of tests, slip test and power test, were performed for the five grouser designs:

Slip Tests: A linear spring attached to the test cart provided the pulling force. For six variac settings (i.e. wheel rotation speeds), pulling force readings were taken for initial wheel slip, and total wheel stall. Two surfaces: 1) deep dry sand and 2) wood, were used. Power readings were also taken simultaneously with all tests.

Power Tests: Weights suspended out the window were connected to the cart via the pulley arrangement. Runs from nine to thirteen feet for load weights of zero to two pounds were performed. Input power readings were taken in all cases.

Results: Figure 27 summarizes slip tests on the deep dry sand surface. Types 1, 4, and 6 yield fairly similar results. Type 2, although showing poorer characteristics at low speeds, proves to be superior at speeds likely in the desired operating range (approximately 2 mph). As can be seen in Figure 28, type 2 again proves to be slightly superior on a hard surface.

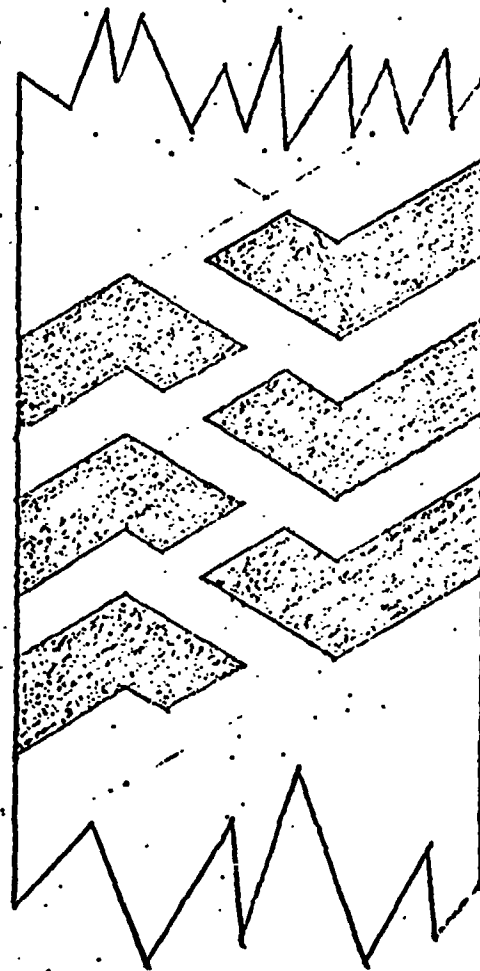
Stall slip results are summarized in Figure 29. Under equal loading types 1, 4, and 5 dig into the sand to a depth of one to two inches at stall slip. Types 2 and 3 penetrate to a depth of up to 4 or 5 inches. Type 2 proved to be the best of the five designs tested.

Figures 30 and 31 show cart speed characteristics versus power input for both a no vertical load and a two pound vertical load\* test. Since experimental error may account for some of the differences, it appears that the different grouser designs vary little in efficiency. All designs exemplify linear speed-power characteristics.

Conclusions: 1) Grouser thicknesses greater than 0.3 inches (for the 6.85 inch radius wheel) will not perform well. Although type 2 generally proved to be the superior of the five designs, other basic designs should be tested.

\*Zero vertical load means that the wheel supports only its own weight and the weight of its support lever and drive.



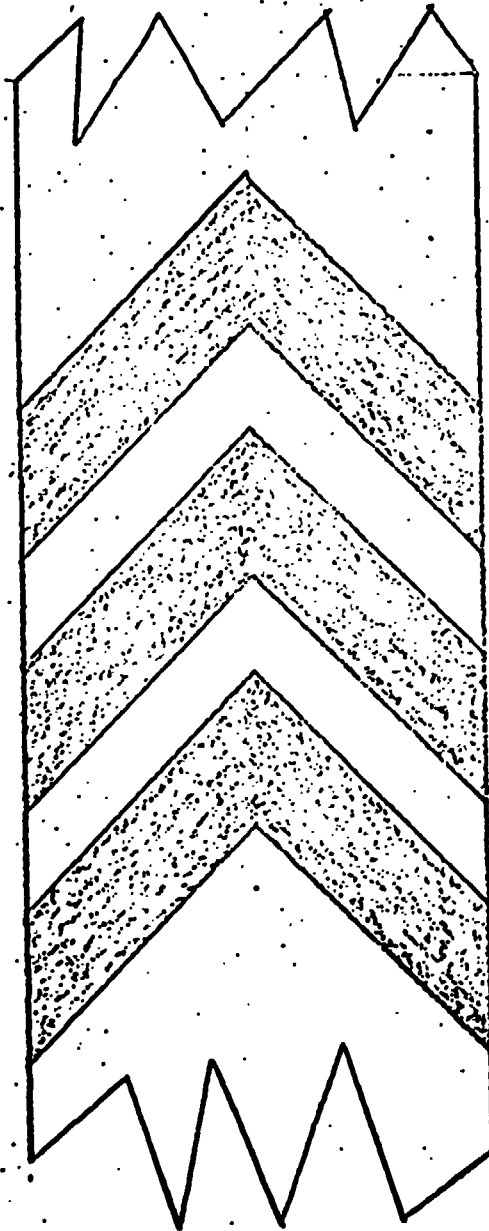


SCALE 1" = 1"

Figure 24. HASH GROUSER DESIGN



Figure 25. RPI-MRV 0.4 Scale Toroidal All-Metal-Elastic Wheel on RPI Test Rig, with 0.3" Thick 45° "Hash" Grousers



SCALE: 1" = 1"

Figure 26. CHEVRON GROUSER DESIGN

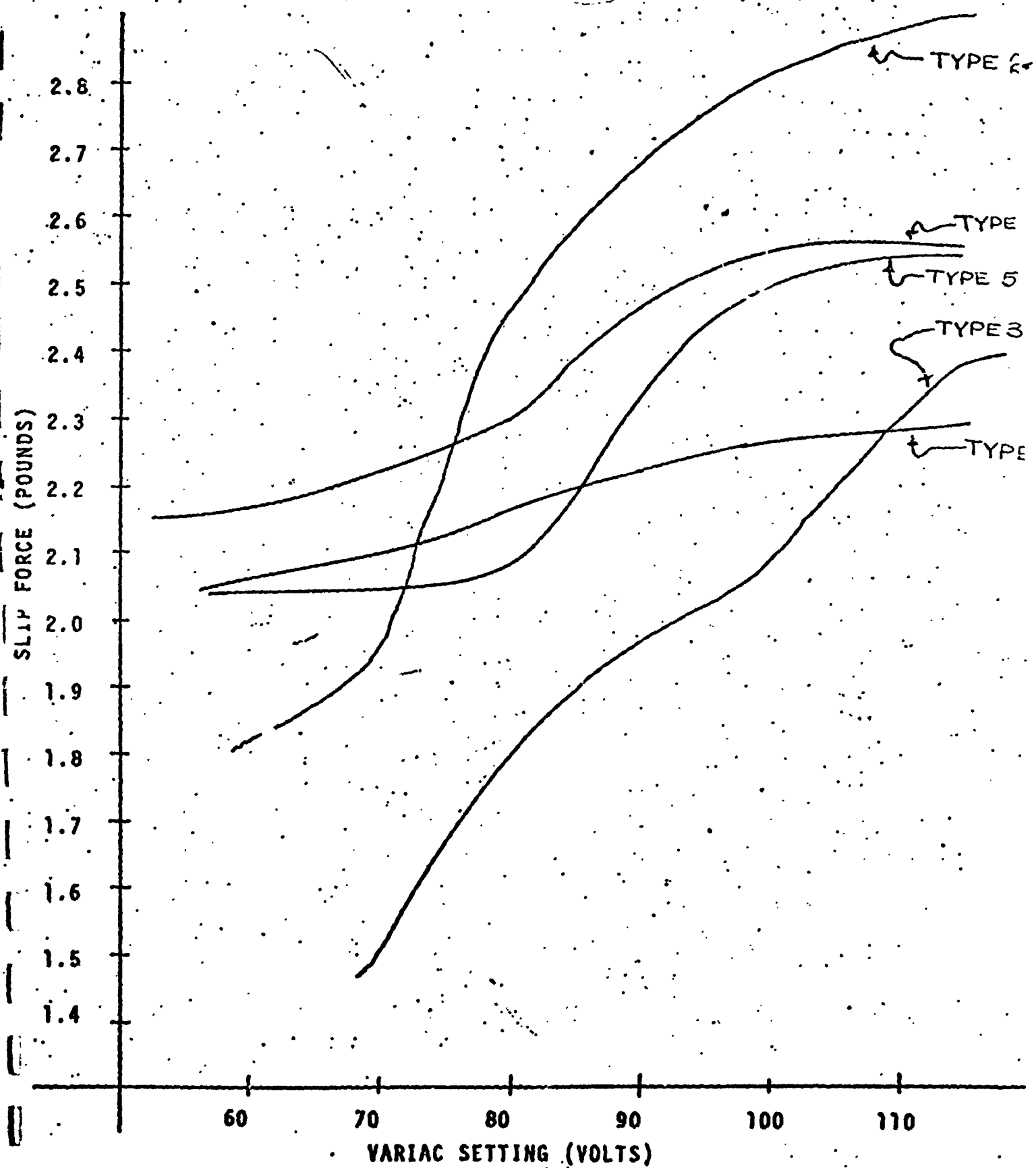


Figure 27. Slip on Sandy Surface

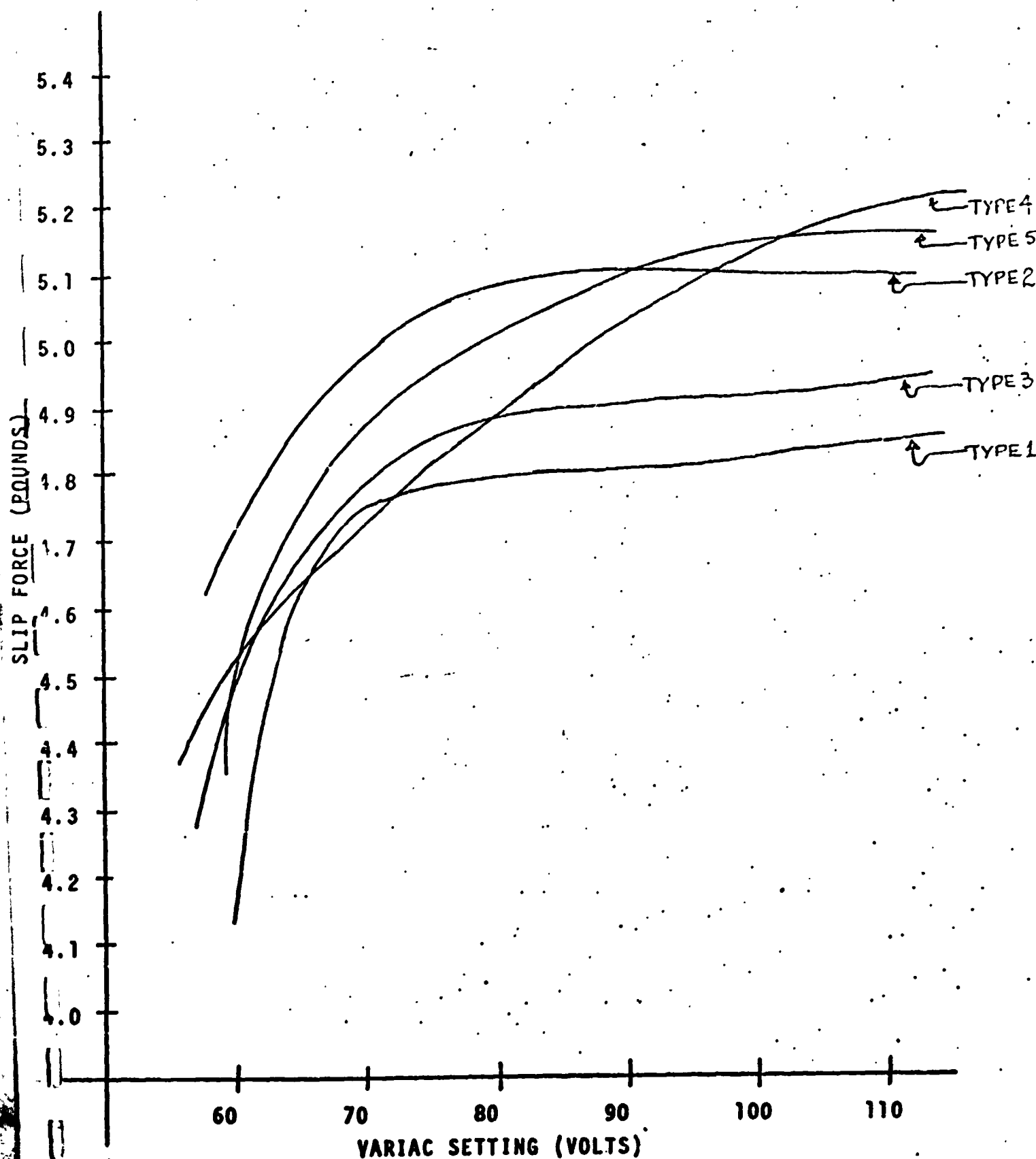


Figure 28. Slip on a Hard Surface

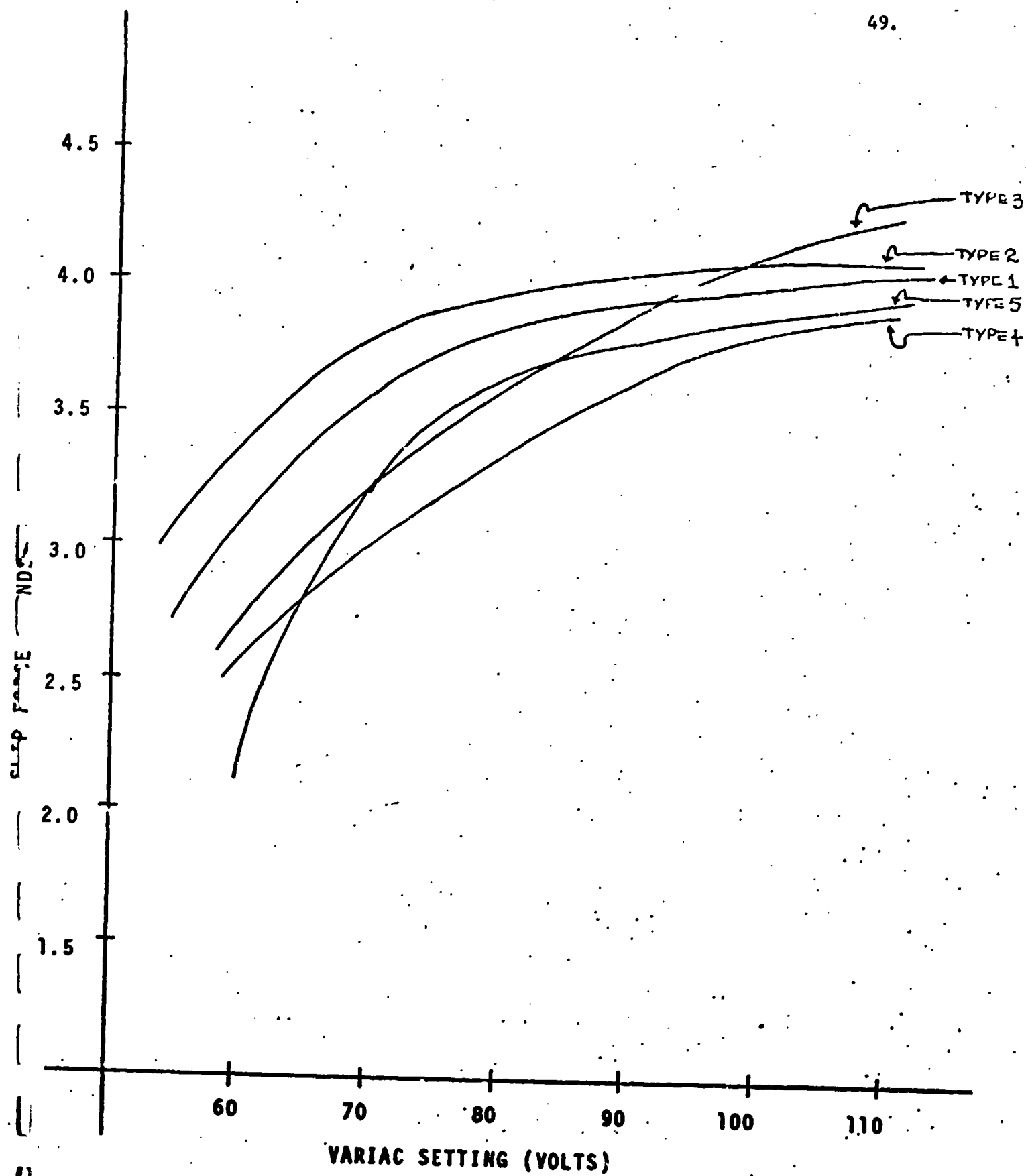


Figure 29. Stall Slip

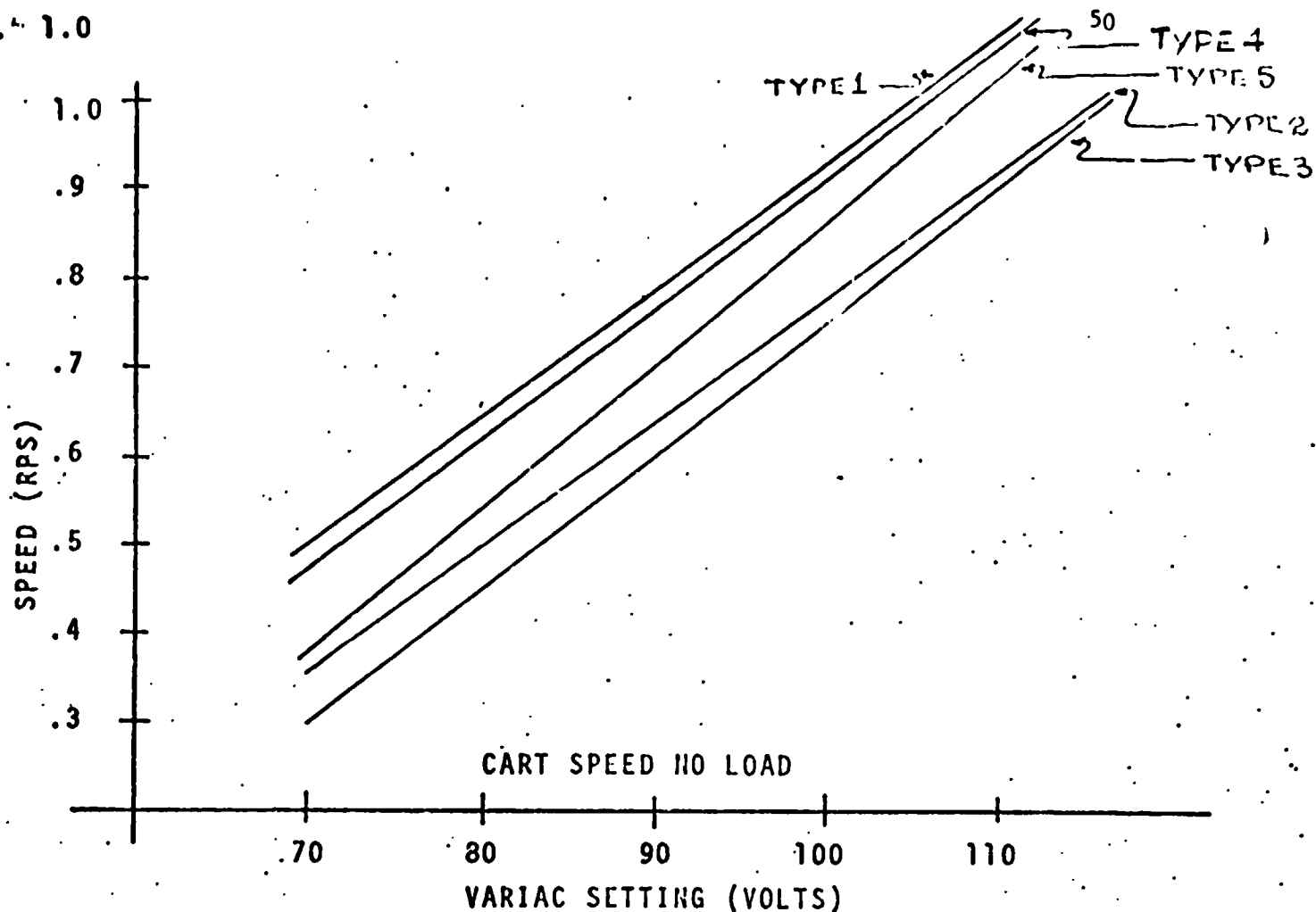
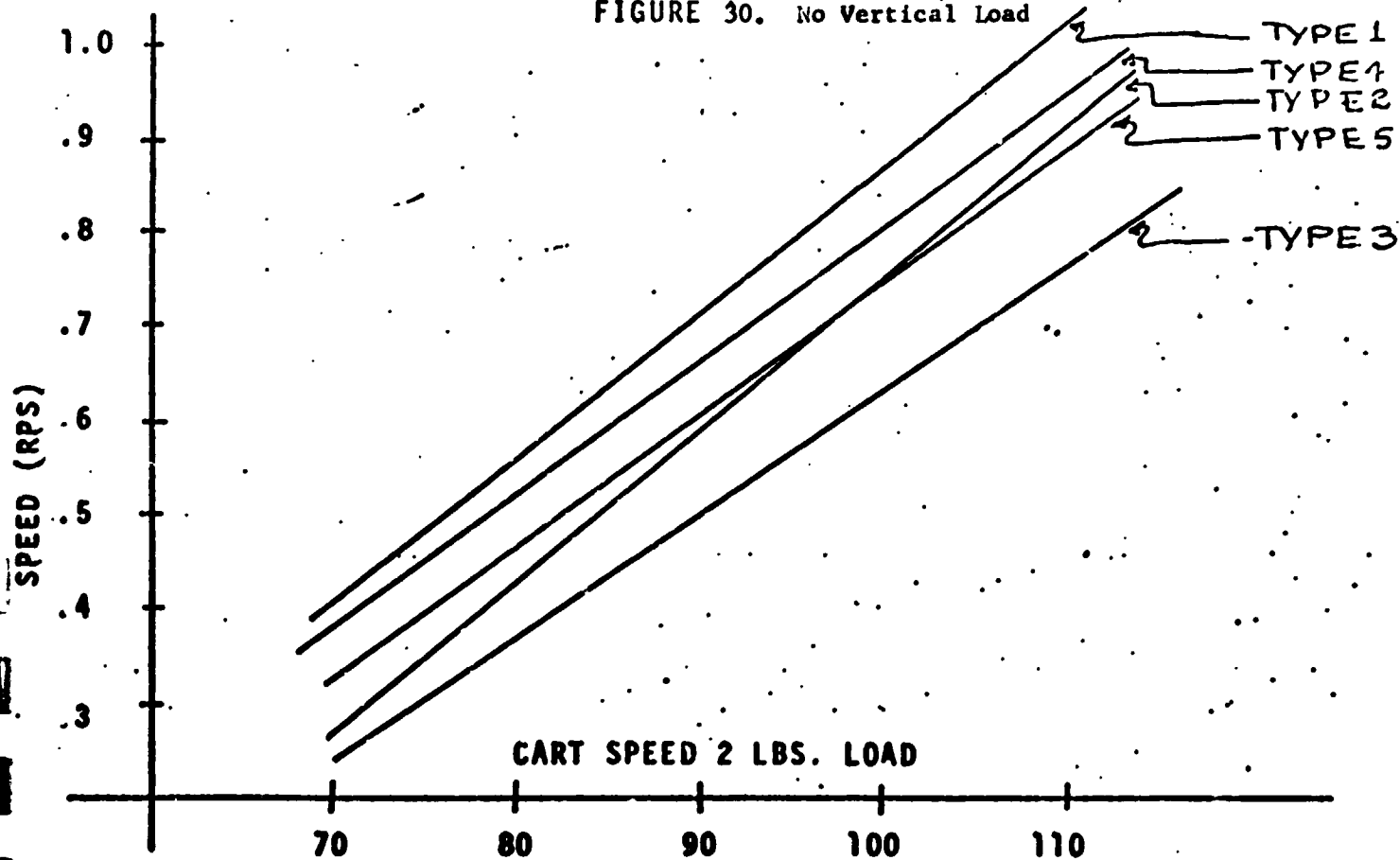


FIGURE 30. No Vertical Load



VARIAC SETTING (VOLTS)  
Figure 31. Two Pound Vertical Load

2) The wheel shows excellent flotation. Even carrying a 28 pound load (comparable in scale to actual weight), the rim does not penetrate below the sand surface except when slip occurs.

Proposed Future Work: Since this test facility produces only results which can be compared only on a relative basis with other wheels tested in the same facility, it will be necessary to test other proposed wheel designs to determine how the RPI wheel design ranks relative to other wheel concepts. Additional testing will be required and should include variation of soil parameters, by, for example, increasing the moisture content of the test soil and running the tests over a hard surface. The solid state tachometers will be perfected to make the output of the tests more easily reduceable.

The ultimate objective is to optimize the RPI-MRV Toroidal Wheel/Grouser Design.

A.3.b. Wheel Analysis - W. Embleton  
Faculty Advisor: Prof. G. N. Sandor

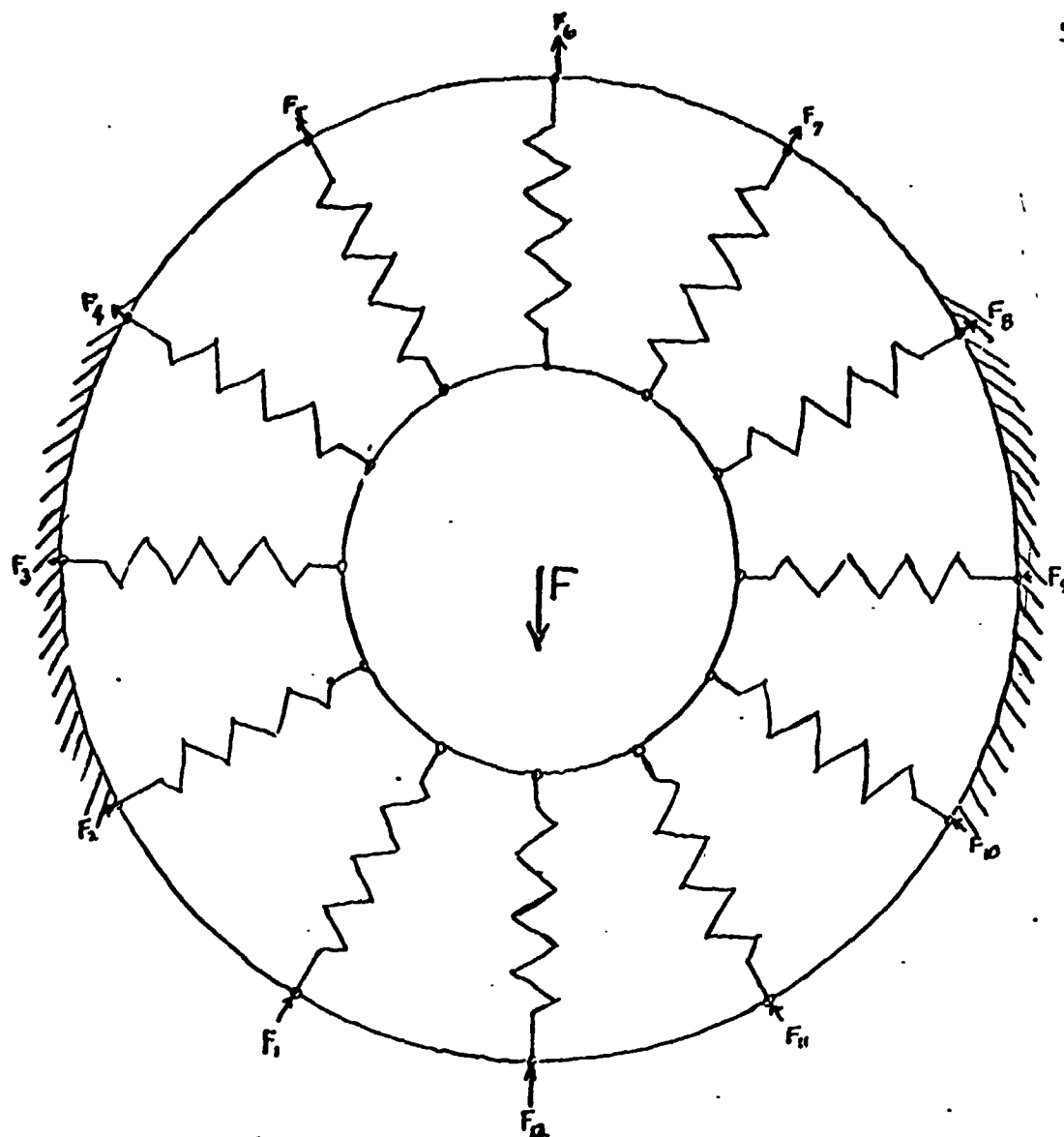
The task of developing reliable methods for analyzing and designing wheels for the Mars mission has been pursued for several years, and a number of computer programs have been developed. However, none of the programs correlate effectively the experimental data for the 0.184 scale, 0.4 scale, or full-size models of the RPI torsional wheel. The objective of this task is to obtain an effective analysis method which can represent accurately the behavior of the wheel. An effective method will provide a rational basis for the design of wheels for defined specifications.

Previous analytical methods considered a finite pin-jointed rim, neglecting the bending moments of the curved rim. Current analysis regards the rim as a continuous deformable member. Deflection characteristics for a concentrated point load are considered.

Initially an iterative procedure was developed. The wheel was visualized as two separate configurations: (1) System "A", Fig. 32, with an inelastic rim and a series of radial linear springs (the hoop "spokes"), and (2) System "B", Fig. 33, with an elastic rim with the "spokes" replaced with radial forces. The basic iterative procedure developed as follows:

1. Apply an initial load to system "A".
2. Determine the resultant radial spring forces from "A" and substitute for the radial forces of system "B".
3. Determine deflection of "B" and proportionally deform the corresponding points of "A".
4. Re-evaluate the resultant radial forces of "A".
5. Repeat steps (2) through (4) until the vertical force components are "sufficiently small."

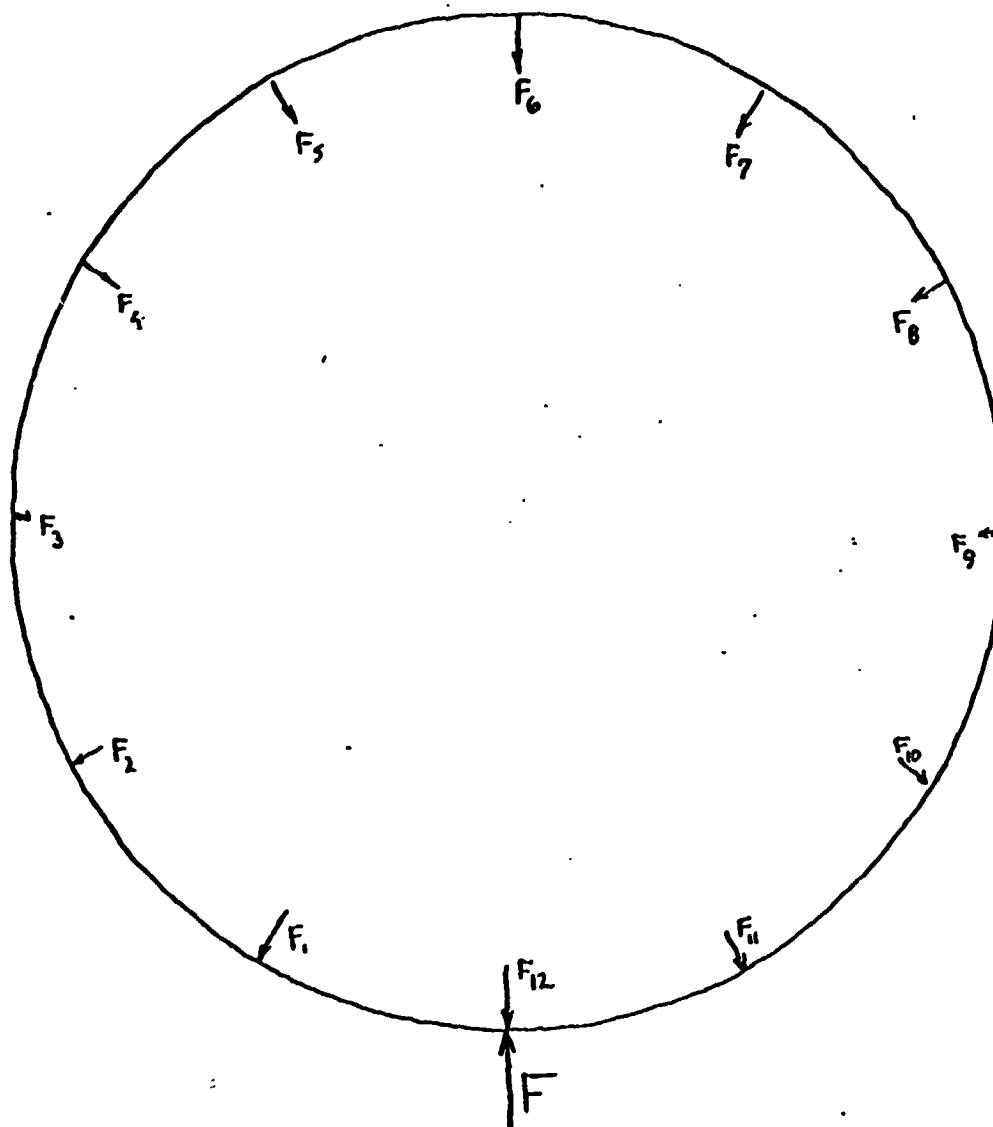




1. Solid inelastic rim
2. System of radial linear springs
3. External force applied at center
4. System of radial reaction forces

SYSTEM "A"

FIGURE 32. System "A"



1. Elastic rim
2. System of forces
3. System of deflections due to system of forces

SYSTEM "B"

FIGURE 33. System "B"

This iterative procedure was programmed and deflections for various load forces were solved on a digital computer. Results were compared with experimentally determined results for the 0.4 and full scale wheels. As Figures 34 through 37 indicate, the analysis closely predicts deflections for small loads. However, large deflection analysis is of little value. As a result, a new analytical technique was sought.

The analytical model described above predicts the deflection of the rim to be symmetric about the horizontal center line of the wheel cross section. Experimental results showed that the lower wheel half deflects considerably more than the upper half for both concentrated and distributed loads. The symmetric deflection is a result of the analysis of system "A". Therefore, the current analysis utilizes system "B" with the linear springs of system "A". The forces applied to the elastic rim of system "B" are transformed into an initial reaction at the base of the rim and a system of forces which depend upon the system of deflections. The final expression relating the point load and the resultant rim deflection is as follows:

$$y_i = K \left[ \sum_{j=1}^n \delta(\phi_i - \alpha_j) y_j + \frac{P_F}{C} \delta(\phi_i - \alpha_F) \right]$$

where  $y_i$  = rim deflection to  $i^{\text{th}}$  point

$n$  = number of spring spokes

$P_F$  = reaction force due to initial load

$\alpha_F$  = angle on the rim where  $P_F$  is applied

$P_j$  = forces applied to the rim

$\phi_i$  = angle on the rim where deflection  $y_i$  occurs

$c$  = spring constant of spring spokes

$E_R$  = Young's modulus for rim material

$I_R$  = second

$r$  = radius of the rim

$K = (Cr^3)/(\pi E_R I_R)$

$P_j = Cy_j$

$$\delta(\phi_i - \alpha_j) = \sum_{K=2}^{\infty} \{ [\cos K(\phi_i - \alpha_j)] / (K^2 - 1)^2 \}$$

This expression yields a system of linear equations of the form

$$\Delta Y = B$$

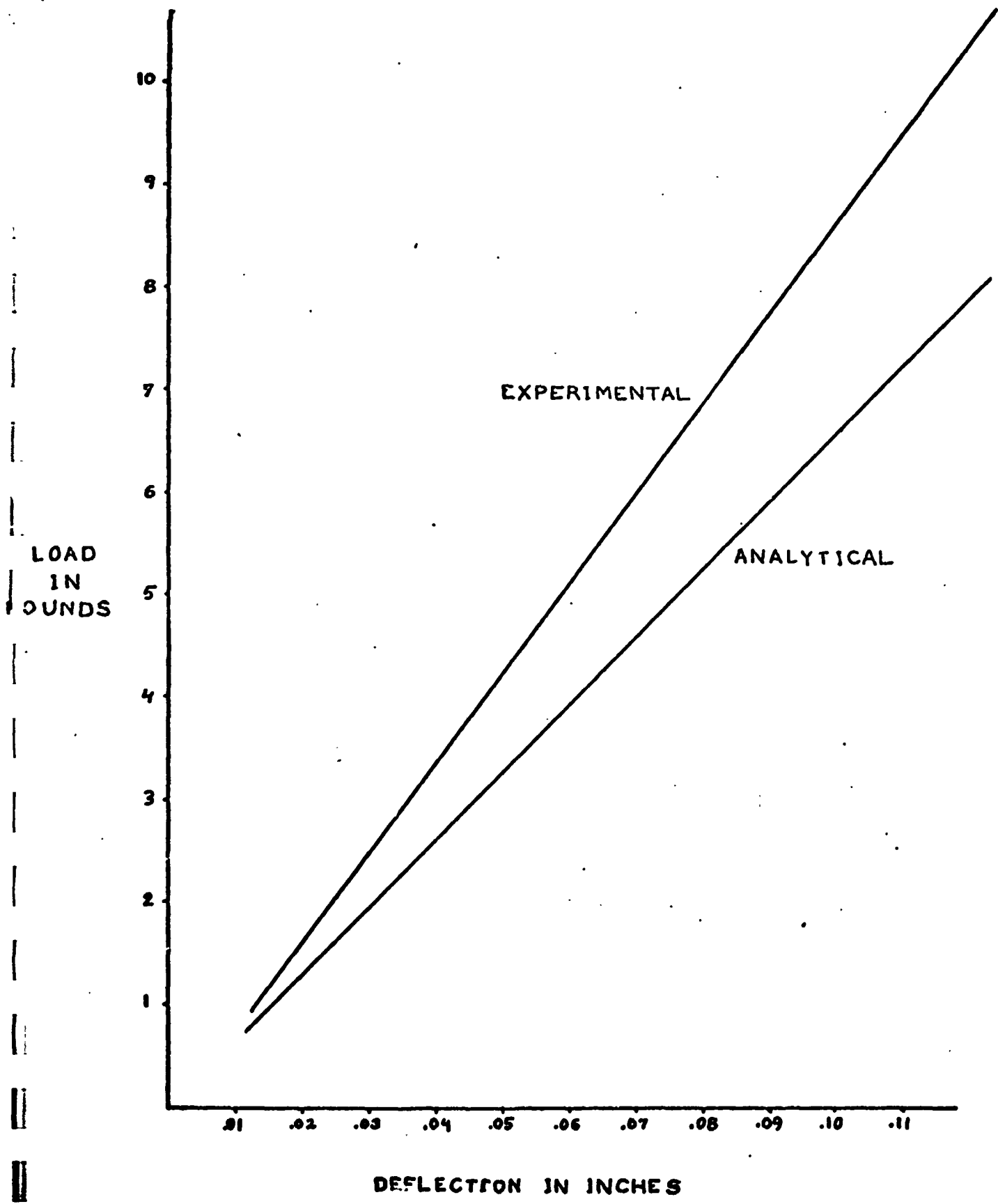


Figure 34. LOAD VS. DEFLECTION FOR 0.4 WHEEL  
-SMALL LOADS

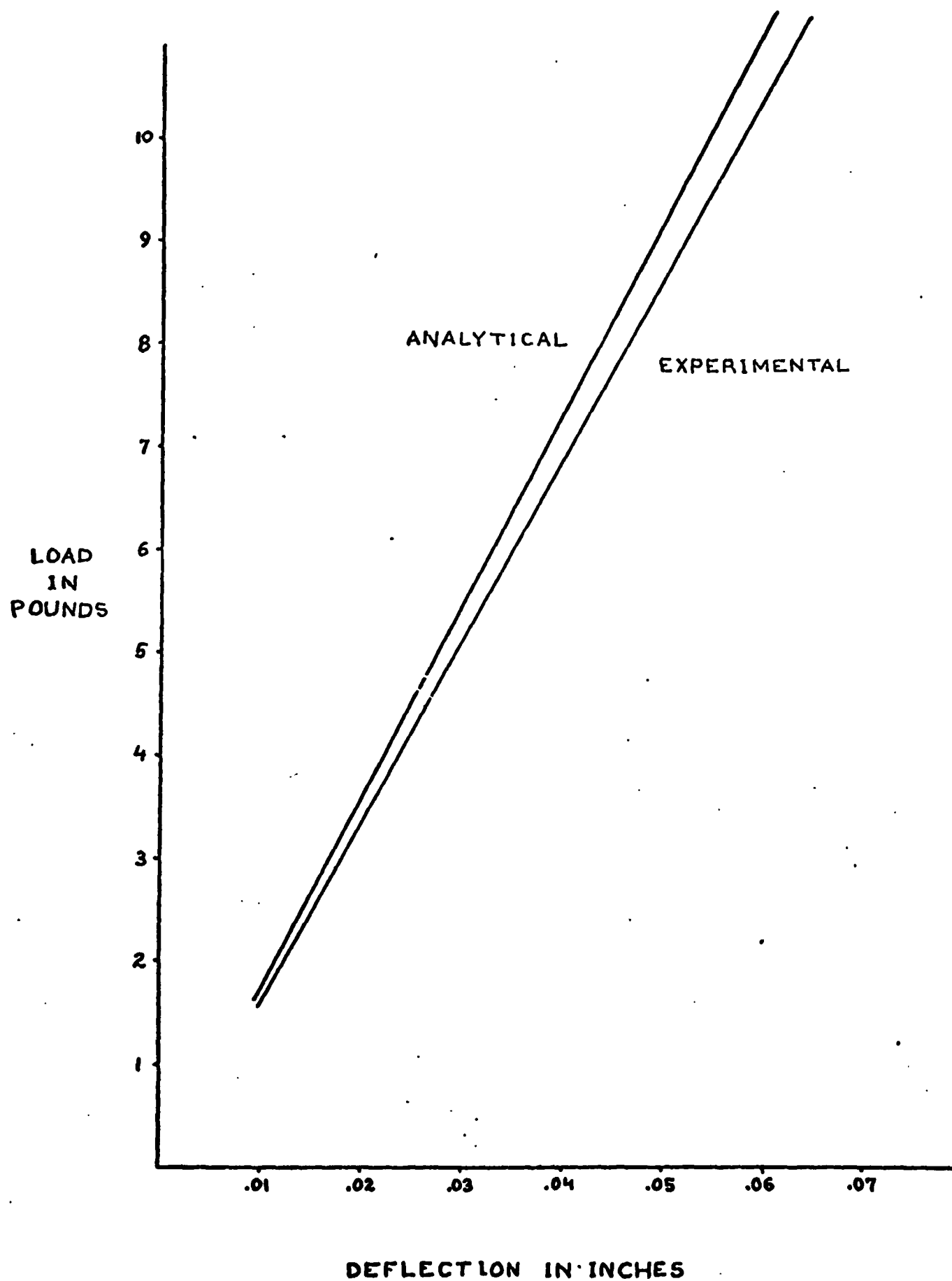
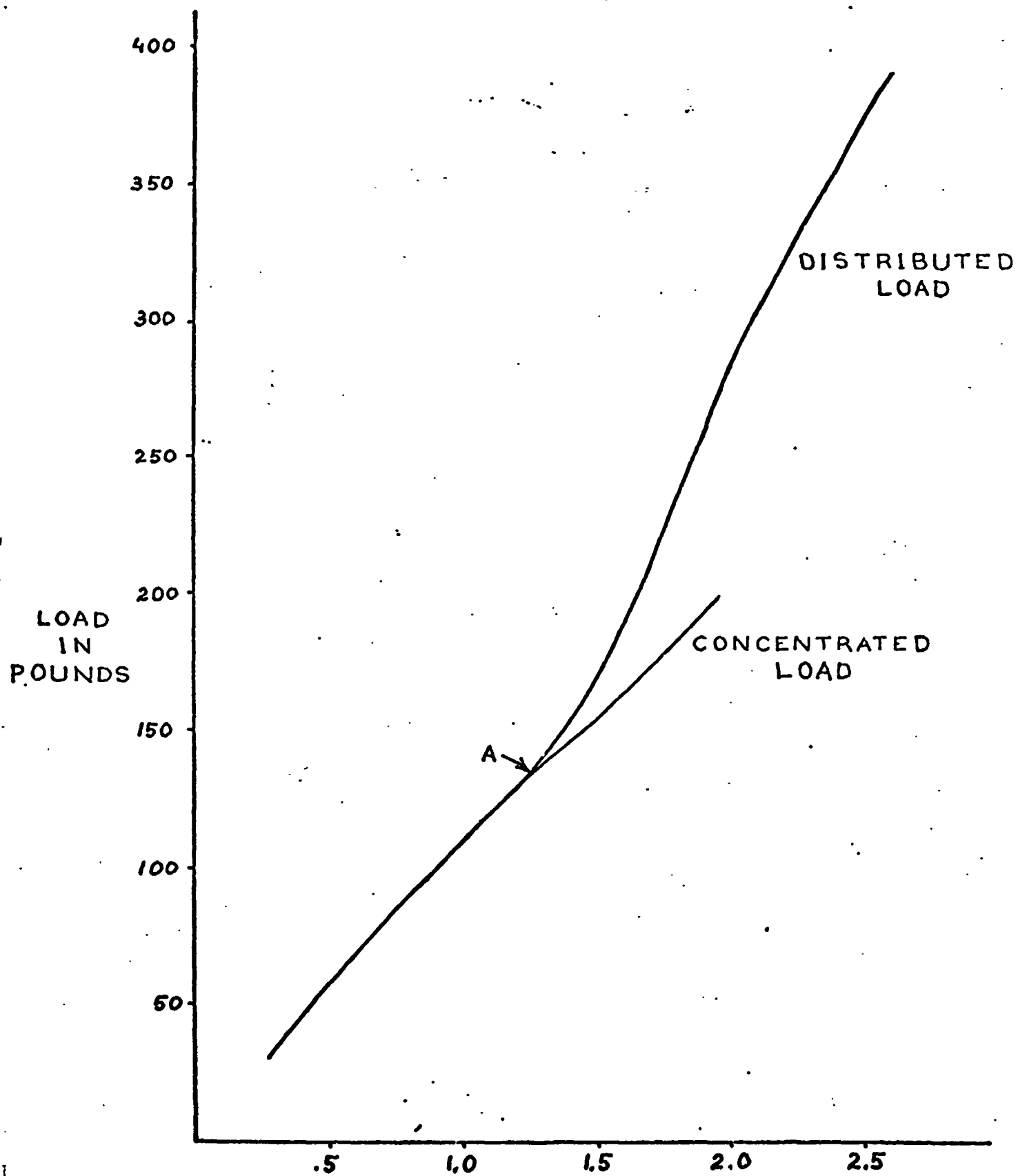


Figure 35.  
LOAD VS. DEFLECTION FOR 1.0 WHEEL SMALL DEFLECTION



DEFLECTION IN INCHES

Figure 36. Experimental Large Load Deflection

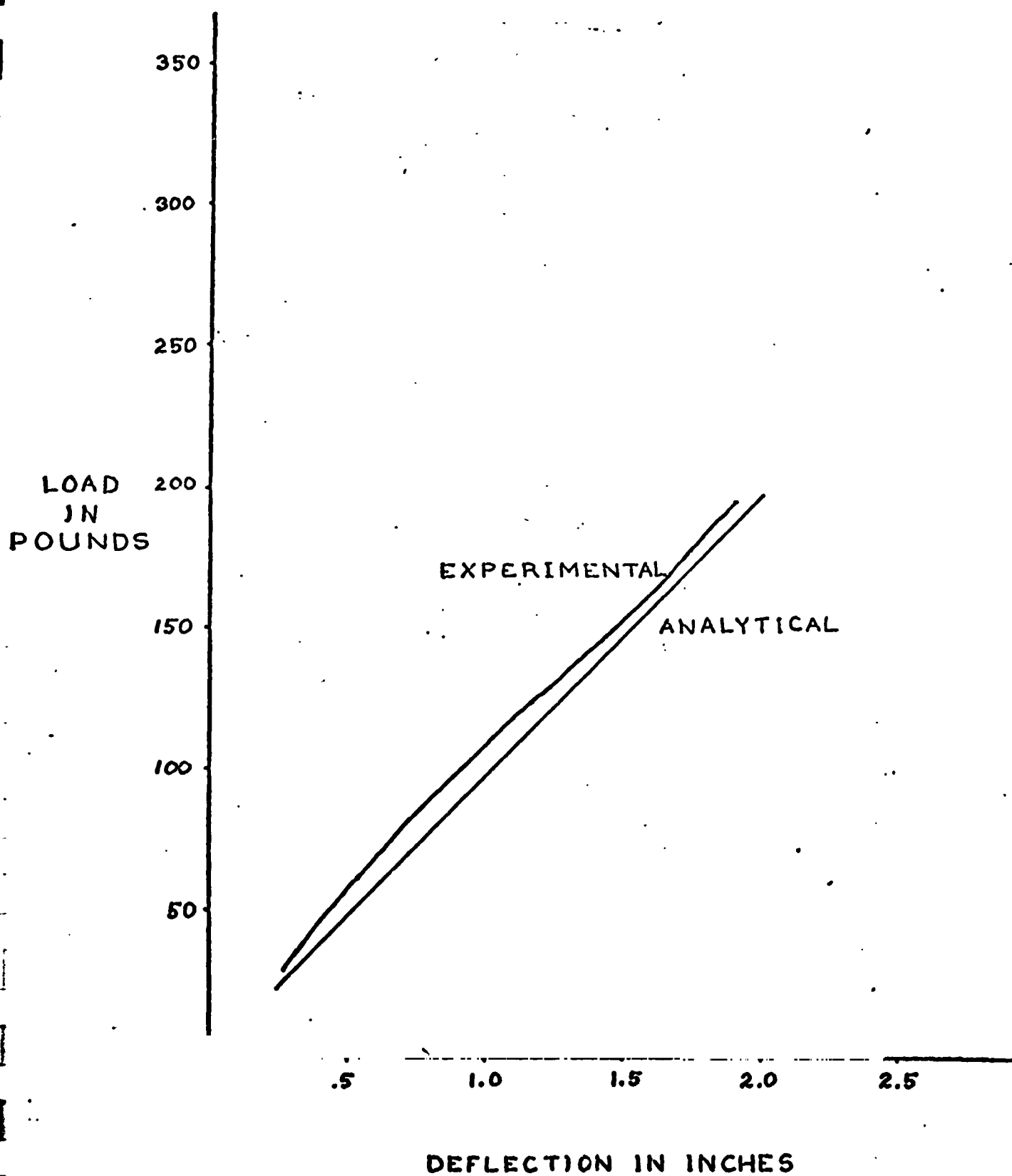


Figure 37. Load vs. Deflection for 1.0 Wheel Large Loads

This system was programmed on the digital computer, and the results compared with the experimental large load deflections. Figure 37 indicates that this current math model will be a valuable tool in future wheel synthesis.

The current analysis now must be expanded to include the application of distributed loads. This may be accomplished by segmenting the lower portion of the wheel, and considering the contributions individually from each segment. If the segments are made sufficiently small, distributed loads may be approximated.

Proposed Future Work: The extension of this work will be in the investigation of modelling the wheel with a distributed load on the rim, calculation of the resulting footprint and of the pressure distribution on the footprint. Once this is completed, the design parameters for the wheel will have been determined. The tools for design of the wheel, in its present configuration, to meet specific requirements will then be available.

#### Task B. System Analysis

The objective of this task is to develop a framework within which design decisions involving conflicting requirements can be made, and to use this framework to identify desirable and non-desirable features of a roving vehicle design. Progress for the academic year included identification of optimal vehicle system designs, an analysis of the sensitivity of some of these designs, a start on a program to observe the operation of these designs in real time, and an analysis of the MRV computer as a queue server.

Progress achieved is described in detail under the following subtasks:

1) System Modeling and Design Optimization, 2) Sensitivity of Optimal Designs, 3) Time Simulation of Vehicle Performance, and 4) Specification of an Integrated MRV Controller. Finally, a projection of activities for the next period is included.

##### B.1. System Modeling and Design Optimization M. O'Callaghan, C. Pavarini, F. Stolen Faculty Advisor: Prof. E. J. Smith

The method of investigating properties of Mars-roving vehicle designs is covered in past progress reports, and specifically in Ref. 3. Briefly, the method involves three major steps:

1. Identification of static system models for 3 cases
  - a. 4-wheeled, direct communicating rover
  - b. 6-wheeled, direct communicating rover
  - c. 4-wheeled rover, communicating via a Mars orbiter relay link
2. Establishing a system evaluation function in terms of the model parameters (in this case, the product of science time and straight-line distance roved),
3. Nonlinear programming optimization with varying limits on vehicle velocity, slope thresholds, internal temperature, etc.



The optimization process for the design of a moderately high order system, such as the Mars roving vehicle (MRV), is a process of specifying the information required by the subsystem designers. This information consists of the operating requirements to be met by the subsystem, and all of the constraints under which the designer must work. For example, the designer of the communications subsystem would be given the information on the maximum weight, maximum power available and the required data transmission rate for a pulse coded modulation subsystem.

Previous work in the systems analysis area has determined a reasonably good model for the MRV, Ref. 3. This model was refined and used to obtain several optimal designs for different operational restrictions. These operational considerations include such considerations as the frequency of science stops and safety considerations such as the constraints on speed and slope which the rover would traverse. It should be noted that the model used includes not only the modeling for the subsystems but also includes the design tradeoffs and interrelationships between the subsystem. Although these interrelationships are mostly of the form of power and weight distributions, internal heat dissipation is also included in the considerations for the thermal control subsystem.

The major area in which the final model differs from the previous model, Ref. 3, is in the thermal control subsystem model. In particular, it was decided that heat pipes were inadequate to maintain the internal temperature at  $300^{\circ} \pm 5^{\circ}\text{K}$  and hence a compressor type of active cooling system was included in the model. Another change in the modeling was in the manner in which the batteries would be used. Previously it was thought that the batteries would be used as long as the MRV was moving. In the present model, the batteries are used only when the rover exceeds a slope such that the radio-isotope thermoelectric generators (RTSs) can not provide enough power for the rover's motors and accessory equipment.

Once the model was refined to include the changes noted above, the equations which constitute the model were rearranged to allow the design states to be represented as combinations of a few state variables and all other factors which go into a design to be represented as functions of the state variables. Once this rearrangement was done, it was relatively easy to put the problem into a form such that the techniques of mathematical programming could be used to optimize the design of the vehicle according to some design criterion. There was some rearrangement and elaboration of the chosen design criterion in order to put it into a form which was applicable to the chosen state variable form of the model.

Since not all designs would be acceptable, a reasonable set of constraints had to be placed upon the design states and upon selected functions of the states. Most of the constraints were of the form of non-negativity of various elements of the design. An example of this type of a constraint is one that requires the weight of the communications subsystem to be positive. There are also other constraints on the system which are of the form of "total system" constraints and an example of which is that the vehicle and all equipment be less than the launch weight. Once all of the proper constraints are placed upon the design

process, the modeling is complete enough for the mathematical programming techniques of optimization.

The routine used for the optimization was Fiacco and McCormick's Sequential Unconstrained Minimization Technique (SUMT). This was obtained from the Hartford Graduate Center of RPI in the summer of 1971. After some reprogramming of the subroutines which constitute SUMT, it was compiled under Fortran H and installed on disk. The routine works using first and second partial derivatives or, with some degradation of efficiency, the first derivatives only or no derivatives at all using numerical differencing methods to approximate derivatives in the latter two cases.

During the past academic year, the system optimization process has been completed for all three cases, yielding 36 designs for differing assumptions. To best illustrate the type and uses of the results, an example will be given.

For a 4-wheeled, direct communicating rover with a slope threshold of  $20^\circ$ , velocity limit of 1.5 m/sec, internal temperature bonds of  $295\text{--}305^\circ$  Kelvin, and antenna diameter limited to 2 meters, the design determined appears in Table I.

The complete set of designs will be covered in a Technical Report to be issued in September 73.

No further work is projected along these lines in the immediate future. In the long range, however, it is expected that the method would be applied to the RPI-MRV as its design is advanced.

B.2. Sensitivity of Optimal Designs - C. Pavarini, M. Ryan  
Faculty Advisor: Prof. E. J. Smith

Consider the case where an optimal design has been determined for a given mathematical model of a system, and a given evaluation function, as in Task B.1. Suppose that one or more of the components of this design must be perturbed when the system is constructed. This perturbation(s) may be due to factors not considered in the system model:

1. Although modeling equations are continuous, perhaps only certain discrete values are feasible (e.g., it is probably infeasible to design a communications system with a bit rate of 1.38762 K, but 1.5 K might be acceptable.)
2. Perhaps another constraint is added, a posteriori (e.g., it may be decided to reduce the slope threshold as a safety consideration)
3. Perhaps some off-the-shelf hardware can be used, but its parameters do not coincide exactly with the optimal values.

Then, it would be desirable to know how to change the other components of the optimal design to maintain the optimal property of the design,

TABLE 1. EXAMPLE OPTIMAL DESIGN

62.

<u>SUBSYSTEM</u>	<u>WEIGHT (KG)</u>	<u>POWER (WATTS)</u>
SCIENCE	70.1	26.0
COMMUNICATIONS	139.7	176.8
POWER GENERATION	105.9	-
THERMAL CONTROL	29.9	DAY=220.1, NIGHT=395.8
NAVIGATION	15.0	6.0
OBSTACLE AVOIDANCE	5.0	15.0
COMPUTATION, DATA	46.8	90.0
VEHICLE STRUCTURE	197.5	-

OTHER DESIGN PARAMETERS:

COMMUNICATIONS DATA RATE	14.847	KBITS/SEC
BATTERY ENERGY	7.60	WATT-HRS
RTG POWER OUTPUT	545.4	WATTS
INSULATION THICKNESS	0.028	M
PROPULSION POWER	165.1	WATTS
VEHICLE WHEELBASE	3.12	M
PATH-LENGTH RATIO	2.18	
DISTANCE BETWEEN SCIENCE STOPS	3.9	KM
NUMBER OF RECHARGES/DAY	1.0	(AVERAGE)

subject to what is, in effect, a new constraint. This new solution has been termed the "perturbed-optimal solution," and methods for the solution of this problem have been investigated over the past two report periods. During the past academic year, the mathematical development of the method of solution has been completed, and application to the MRV designs has begun.

The mathematical analysis work included several parts. First, the existence of a unique, continuously differentiable trajectory, parameterized by the initial perturbation, that solves the sensitivity problem was proved. Second, a first-order approximation to the general nonlinear solution was developed. Third, error-bounds on this approximate solution, and methods to improve the accuracy of the solution were obtained.

The mathematical results to date will be presented briefly here. Consider the nonlinear programming (NLP) problem

$$\begin{array}{ll} \text{minimize } f(x) \\ \text{subject to } g_i(x) \geq 0 & i = 1, \dots, m \\ h_j(x) = 0 & j = 1, \dots, p \end{array}$$

where  $x$  is an  $n$ -vector and  $f$ , and the  $g_i$  and  $h_j$  functions are nonlinear scalar functions of the elements of  $x$ . At the solution to NLP,  $x^*$ , there exist two other vectors (an  $m$ -vector,  $u^*$ , and a  $p$ -vector  $w^*$ ) such that

$$\begin{array}{ll} h_j(x^*) = 0 & j = 1, \dots, p \\ u_i^* g_i(x^*) = 0 & i = 1, \dots, m \\ g_i(x^*) \geq 0 & i = 1, \dots, m \\ u_i^* \geq 0 & i = 1, \dots, m \end{array}$$

$$\text{and } \nabla \mathcal{L}(x^*, u^*, w^*) = \nabla f(x^*) - \sum_{i=1}^m u_i^* \nabla g_i(x^*) + \sum_{j=1}^p w_j^* \nabla h_j(x^*) = 0$$

where  $\nabla$  is the gradient operator with respect to  $x$ .

A "perturbed-optimal solution" problem is generated from (NLP) by forcibly perturbing one of the components of  $x^*$  and seeking the solution to this new problem. The solution to the perturbed-optimal solution is denoted  $x'$  and can be found from

$$x' = x^* + \delta x$$

where the  $K$ th component of  $x'$  ( $x'_k$ ,  $k$  fixed,  $1 \leq k \leq n$ ) is now fixed prior to solving this new problem by writing

$$x'_k = x_k^* + \delta x_k$$

When

- a) the functions  $f$ ,  $(g_i)$ ,  $(h_j)$  are twice continuously differentiable

- b) the solution  $(x^*, u^*, w^*)$  satisfies certain sufficiency conditions for (NLP)
- c) the vectors  $\nabla f(x^*), \nabla g_i(x^*)$  for  $i$  such that  $g_i(x^*) = 0, \nabla h_j(x^*), j = 1, \dots, p$ , and  $e^k$  (an  $n$ -vector of zeroes except for a '1' in the  $k$ th place) are linearly independent
- d)  $g_i(x^*) = 0$  implies  $u_i^* > 0$ ,

a linear approximation to the perturbed-optimal solution can be found. That is

$$x' = x^* + \delta x \approx x^* + \eta^k \delta x_k$$

(where  $\eta^k$  is a variable vector except for a '1' in the  $k$ th place) where  $\eta^k$  is solved from

$$\begin{vmatrix} \nabla^2 \mathcal{L}(x^*, u^*, w^*) - G^* H^{*T} & e^k \\ U^* G^{*T} & \text{diag}(g_i^*) & 0 & 0 \\ H^{*T} & 0 & 0 & 0 \end{vmatrix} \begin{vmatrix} \eta^k \\ \frac{du}{dx_k} \\ \frac{dw}{dx_k} \\ \frac{dr}{dx_k} \end{vmatrix} = 0$$

where  $U^* = \text{diag}(u_i^*)$ ,  $G^* = (\nabla g_1(x^*), \dots, \nabla g_m(x^*))$  and  $H^* = (\nabla h_1(x^*), \dots, \nabla h_p(x^*))$ .

The conditions a through d above apply to the MRV system design problem and model. The results generated to date are values of the "perturbation coefficients", the vector in the equation immediately above, which indicate the sensitivity of the optimal design to the perturbed parameter.

The application to the MRV design problem will be shown by example. Place the optimal design (unperturbed) in a vector  $x^*$ . Then, mathematically, the new (perturbed) design can be written

$$x = x^* + \eta^k \delta x_k$$

where  $\eta^k$  is the perturbation coefficient vector, and  $\delta x_k$  is the magnitude of the perturbation in the  $k$ -th component. Table II shows results for an initial perturbation in science weight. An interpretation of these results indicates that the optimal way to increase (decrease) the weight of the science package is to increase (decrease) the insulation thickness on the equipment package, thereby decreasing (increasing) the thermal control power required. This change can be reflected into a decrease (increase) in RTG power required and thus a corresponding savings (expenditure) in weight, which can be put toward the change in science weight. Note that the solution accounts for the weight change in increasing (decreasing) insulation thickness, thus taking into account the coupling in the system design. It should be noted that these results hold only for the case described in detail in B.1, and thus not only are there many perturbed-optimal solutions problems for each design (a new solution for each value of  $k$ ), but that each different design has

TABLE II  
THE PERTURBED-OPTIMAL SOLUTION FOR A PERTURBATION IN WEIGHT  
OF THE SCIENCE PACKAGE

x =	EXPERIMENTAL SCIENCE TIME TOTAL SCIENCE WEIGHT TOTAL SCIENCE TIME COMM. POWER COMM. ANTENNA SIZE COMM. DATA RATE RTG POWER VEHICLE VELOCITY SLOPE THRESHHOLD THERMAL CONTROL POWER BATTERY ENERGY MOVING TIME/DAY WHEELBASE EQUIPMENT PACKAGE AREA INSULATION THICKNESS HEATER POWER % TERRAIN IMPASSABLE PATH-LENGTH RATIO SCIENCE STOPS/METER RECHARGE TIME LARGE SLOPE FACTOR*	, $\eta^k =$	35.75 1.0 35.75 0.0 0.0 0.0 -7.27 0.77E-02 0.81E-19 -7.55 0.252 0.082 0.75E-04 -0.62E-02 0.55E-03 -7.27 -0.15E-05 -0.39E-05 -0.16E-04 0.67E-03 0.78E-03
-----	---	--------------	---

\* Large slope factor is the inverse of the percentage of time the vehicle spends on slopes the slope threshold (the optimal value is 51.3)

its own set of solutions. A limited number of cases have been solved as of this date. All results will appear in detail in a September 73 technical report.

No further work on this task is expected in the near future. In the long run, it may be applied to the RPI-MRV as its design is more completely developed.

B.3. Time Simulation of Vehicle Performance - R. Gallerie, T. Mans  
Faculty Advisor: Prof. E. J. Smith

As the system models derived are static, they consider many effects in their average or worst-case sense. This subtask is an attempt to investigate these effects in time (or equivalently, in their time-varying sense), by simulating the performance of the vehicle designs in real (scaled) time. Some of the effects to be considered in this manner include slopes the vehicle will traverse, failures of the long-range obstacle avoidance subsystem, such alternative concepts as regenerative braking, etc. In addition, the performance of the designs under more comprehensive and varied earth command can be investigated.

The progress for this academic year has been limited to the development of a general purpose Monte-Carlo simulation program to allow this type of simulation. This has been accomplished since this subtask was initiated in February 73. The program includes the system models derived in B.1. modified to run "in time", and is modular in its construction to allow easy expanding of its capabilities.

This program simulates the operation of a Mars roving vehicle, with particular attention being given to power consumption. The system model is an adaptation of the system model used in Ref. 3.

The model looks at the rover operation on an instantaneous level, where the model of Ref. 3 was an average type model. The program keeps a running account of time, power being used, energy level of auxiliary batteries, and distance traveled. It also calculates the total time spent on science experiments, the total time spent stopping to recharge the batteries, the total time spent in direct communication, and the total ideal distance traversed.

The program consists of the main program and four subroutines. The main program reads the inputs, calculates any design parameters not on the input list, initializes all variables, and prints out the results. It also creates a boulder distribution on the sample roving grid, which will be explained in detail later. The program finally directs the coded commands to the proper subroutines. Each subprogram is a distinct mode of operation of the vehicle. The first subroutine is the recharge subroutine. It is called whenever the battery level is lower than a specified level. This recharge subroutine is the only mode which is not started by direct command. The second subprogram is the science subroutine. It is called by direct command whenever the vehicle is to stop and take pictures. It is not used for communication dealing with transmission other than pictures because the power consumption is not as great. The final subprogram, the one of most interest, is the rove subroutine. In this subroutine, the actual roving is simulated. The vehicle roves about on a "sample" Mars terrain.

During its rove, the vehicle searches for obstacles, picks the "best" path, and travels the desired distance, meanwhile keeping an account of the power and energy consumption. The most critical power loads are used at this time. This subroutine is also called by direct command.

The Mars "terrain" consists of a two dimensional grid, 100 meters by 100 meters, over which the vehicle travels back and forth. The distance between grid points represents one meter. The obstacles are actually dimensionless points, located on the grid by a two dimensional coordinate system which is supplied by input data. The obstacles are given dimension by the CLEAR input parameter. This parameter specifies the distance by which the vehicle must avoid the obstacle point. Larger obstacles are created by placing two or more obstacle points adjacent to each other. Boulder obstacles and crater obstacles are not differentiated on the grid. The obstacle profile of the grid has an impassable area comparable to an average Mars terrain; however, it may be changed by input data cards. The profile considers any boulder over .5 meters high as being impassable. The profile of small rocks (under .5 meters high) and slopes is not time invariant. Although it changes with time, it is repeatedly determined by equations representing the actual slope and boulder distribution of Mars.

The equations governing power requirements are adapted from Ref. 3. An equation calculating the power to rove over small boulders is a second order polynomial approximation for the data from a program developed under Task A.1.c. This program calculates power requirement as a function of boulder size for a Mars roving vehicle. This program assumes that the power to traverse slopes and the power to travel over rocks can be superimposed.

The program features a special recharge option which is controlled by the input parameter NOPT. If NOPT equals one, any surplus power produced by the RTG's will be used to recharge the auxiliary batteries. If NOPT equals zero, this recharge option is not used.

It is planned that continued effort on the time-simulation of vehicle performance be applied with the objective of gaining additional knowledge regarding design trade-offs, and the relationships between static system optimal designs and the performance of these designs in time.

B.4. Specification of an Integrated MRV Controller  
C. Boroughs, F. Samuel, J. Zeitlin  
Faculty Advisor: Prof. E. J. Smith

It is the objective of this subtask to describe in detail the principal tasks the computer must perform when it is roving on the surface of Mars and to estimate the performance requirements of the computer imposed by these tasks. In addition, this group provides support for the remote control of the RPI-MRV under Task A.1.d.

A statistical approach using queuing theory and random variables was chosen because the main object of the study was the average behavior of the computer-vehicle system rather than a second-by-second study of the vehicle behavior. The roving mode was chosen as the object of study



because of the major computing requirements imposed by the obstacle avoidance and guidance functions as well as the strict time constraints due to the desire for efficient roving.

Of course, at this stage in the development of the MRV there are many unanswered questions concerning the implementation of various functions in the roving mode. Thus, while some systems such as the laser rangefinder have been well defined, others, such as the path selection and obstacle avoidance algorithms are still in the early stages of development. Still, some estimates can be made concerning the amount of computer processing required. The goal is to give subsystem designers of such software-bound subsystems as obstacle avoidance and path selection a kind of bound on the computational capability available to them.

The computer-vehicle system interaction was modeled by assuming the computer could be viewed as a queue server, servicing "customers" on two queues, the fixed queue (containing normal ongoing functions) and an interrupt queue. By queuing theory, it was determined how the timing of service to various tasks constrains the cycle time of the computer. Tables III, IV, and V list operation timings, fixed queue tasks and timings, and interrupt queue tasks and timings, respectively. Results using these assumptions have not been fully evaluated as of this date, but indications are that for this model, a cycle time under 50 microseconds should suffice in the roving mode for the cases listed in Table VI. Further analysis of results will be completed by August '73.

Support has also been provided to the vehicle group responsible for Task A.1.d. in defining the communication system for remote open-loop control and ultimate closed-loop computer control.

It is intended that both thrusts of this task will be continued in the future. Performance requirements on on-board computer will be refined as more reliable subsystem requirements are obtained and analyzed through queuing theory. The interface with the RPI-MRV group will be maintained and particular attention will be given to the implementation of remote control with the ultimate objective of achieving autonomous roving closed-loop control with a remote mini-computer.

**Task C.1.a. Laser Rangefinder: Pulse Amplification - D. Palumbo**  
**Faculty Advisor: Prof. C. N. Shen**

There have been five requirements placed on a laser Rangefinder used for Martian Terrain Measurements.

1. Range  $\pm$  .05 meters
2. Angle  $\pm$  10 arc seconds
3. Fast scan rate, on the order of 1 m sec.
4. Low weight
5. Low power consumption

The first two requirements are to assure meaningful calculation of terrain data when determining the in-path slope. To simplify the calculations, a complete scan of the terrain should be made in about 1 m sec to eliminate error due to vehicle pitch and yaw, which leads to the third requirement. The last two requirements originate with the intended use on a space vehicle.

TABLE III  
OPERATION TIMINGS FOR THE MRV COMPUTER

Definition of timing variables

$t_c$	computer cycle time - variable
$t_a$	subsystem access delay - variable
$t_{ss}$	laser range-finder settling delay - 1.1 mil.
$t_{as}$	analog sensor settling time - 20 microsec.
$t_{ds}$	digital sensor settling delay - negligible

Instruction timing

Register-Register Instructions (Add Register, etc.)	$1t_c$
Register-Storage Instructions (Load from storage, etc.)	$2t_c$
Multiply (floating point or integer)	$6t_c$
Divide (floating point or integer)	$12t_c$
Sine, Cosine Tangent	$100t_c$

TABLE IV  
FIXED QUEUE TASKS AND TIMINGS

1. ENG      Gather and encode engineering data  
time=  $611t_c + 2t_a$
2. POWER    Monitor subsystem power consumption  
Time=  $970t_c + 32t_c + 320\text{usec}$
3. TEMP     Monitor subsystem temperature  
time=  $582t_c + 32t_a + 320\text{usec}$
4. SCAN     Update terrain array  
time=  $3266t_c + 1446t_a + 522,500\text{usec}$
5. ANNAL    Analyse array and find path  
time=  $110,711t_c$
6. GENER    Generate path commands  
time=  $107t_c + 4t_a$
7. SCIENCE   Perform science monitoring  
time=  $72t_c + 4t_a + 120\text{usec}$

TABLE V  
INTERRUPT QUEUE TASKS AND TIMINGS

<u>Interrupt</u>	<u>Function</u>	<u>Exec Time</u>	<u>Arrival Rate</u>
1. FCOM	Fetch earth command	$119t_c + 2t_a$	35.0
2a. TWARN	Thermal warning	$253t_c + 8t_a + 20$	0.0017
2b. BWARN	Battery warning	$209t_c + 10t_a + 40$	0.0083
2c. PWARN	Power warning	$253t_c + 8t_a + 20$	0.017
3a. OSTOP	Stop for obstacle	$535t_c + 9t_a$	0.035
3b. SSTOP	Stop for slope	$537t_c + 11t_a$	0.035
4a. NTIMER	Normal request for path command	$522t_c + 9t_a$	1.0
4b. STIMER	Special request after a reverse	$56,590t_c + 638t_a +$ 296,000	0.07
5. DCOM	Down link ready for data	$82t_c + t_a$	1.0

TABLE VI  
LIST OF TEST CASES FOR THE MRV COMPUTER MODEL

1. Standard run - subsystem access time ( $t_a$ ) is 10 cycles,  
computer waits during scan
2. Standard run -  $t_a$  is assumed 1 cycle, computer still  
waits during scan
3. Standard run -  $t_a = 10$  cycles, computer is assumed to  
execute other tasks without waiting during  
scanning
4. Standard run -  $t_a = 1$  cycle, computer does not wait  
during scanning
- 5 - 8. Runs 5 through 8 correspond to runs 1 through 4  
except that all task processing times were doubled.  
That is, the number of processing cycles were  
doubled, but the number of subsystem accesses  
and sensor delays remained unchanged.

Previously, only the "Phase Comparison" method offered accuracies meeting the first requirement. However, this technique uses a heterodyning process which requires prolonged focus on a single point. Semi-conductor lasers cannot be pulsed over .2 microseconds leaving gas lasers such as Helium-Neon for use. The phase comparison method then may not meet fast scan assumptions and will be heavier and more power consuming than a method using a semi-conductor laser.

The timed pulse method uses a GaAs laser and can be made to yield a .05 m accuracies if pulse expanding techniques are used. Pulse expansion is used on commercially available counters claiming .1 nano second resolution. Such a system has been designed and is proposed.

The time pulse method is shown in Figure 38. The operation of the system is simpler than the phase comparison method, but, unfortunately, not as accurate. Initial investigations showed that .25 naosecond time resolution is needed when measuring the elapsed time of flight in order to achieve  $\pm 5$  cm. accuracy, Ref. 4. The system shown in Figure 38 was suggested by W. Kuriger, Ref. 5, and is reported to be capable of  $\pm 10$  cm. accuracy under laboratory conditions. Some modifications can be made to improve Kuriger's design.

The range is determined by monitoring a ramp generator (most likely with an A/D converter). The amplitude that the ramp reaches is proportional to the length of time it is on. The ramp begins on a signal from the pulse generator and stops on signal from the returning laser beam.

Figure 39 contains the modified circuit diagram. One important design change concerns triggering the electronics with on board and returning laser beams. Lasers have an indefinite delay time between pulse application and onset of the lasing mode. Triggering with a split laser beam will eliminate the error due to this time lag. The processing begins on signal from the storage-averaging branch. A two ma. pulse triggers the power supply to drive the laser. The time delay between on board and returning laser pulses is recorded by the detector and output as a pulse of width, T. This pulse width is expanded and timed. The count resulting from the timing is used as a memory address for read only memories (ROM's). The range is output from the ROM's and stored to await averaging. The pulse generator is then signaled for another range beginning the cycle over. The number of ranges to be averaged depends on how much time is allowed under the 1 msec. scan requirement.

The pulse width, T, proportional to the beam time of flight is produced by an exclusive or gate as shown in Figure 40. The beams are detected by photodiodes, amplified and applied to the gate. The on board beam will be stronger and require less amplification, thus  $A_2$  will be greater than  $A_1$ . The function of the gate as shown in the truth table is to produce the pulse length. Since the gate triggers at a specific voltage, 5 volts, the pulse length will also depend on the slope of the leading edge of the input pulse. This won't disturb the operation of the on-board circuit, but will affect the timing of the reflected circuit since the shape of this pulse will depend on distance traveled and type of terrain encountered. This has been investigated, Ref. 4, and it was shown that

$$dt = T^1/(S/N)/2$$

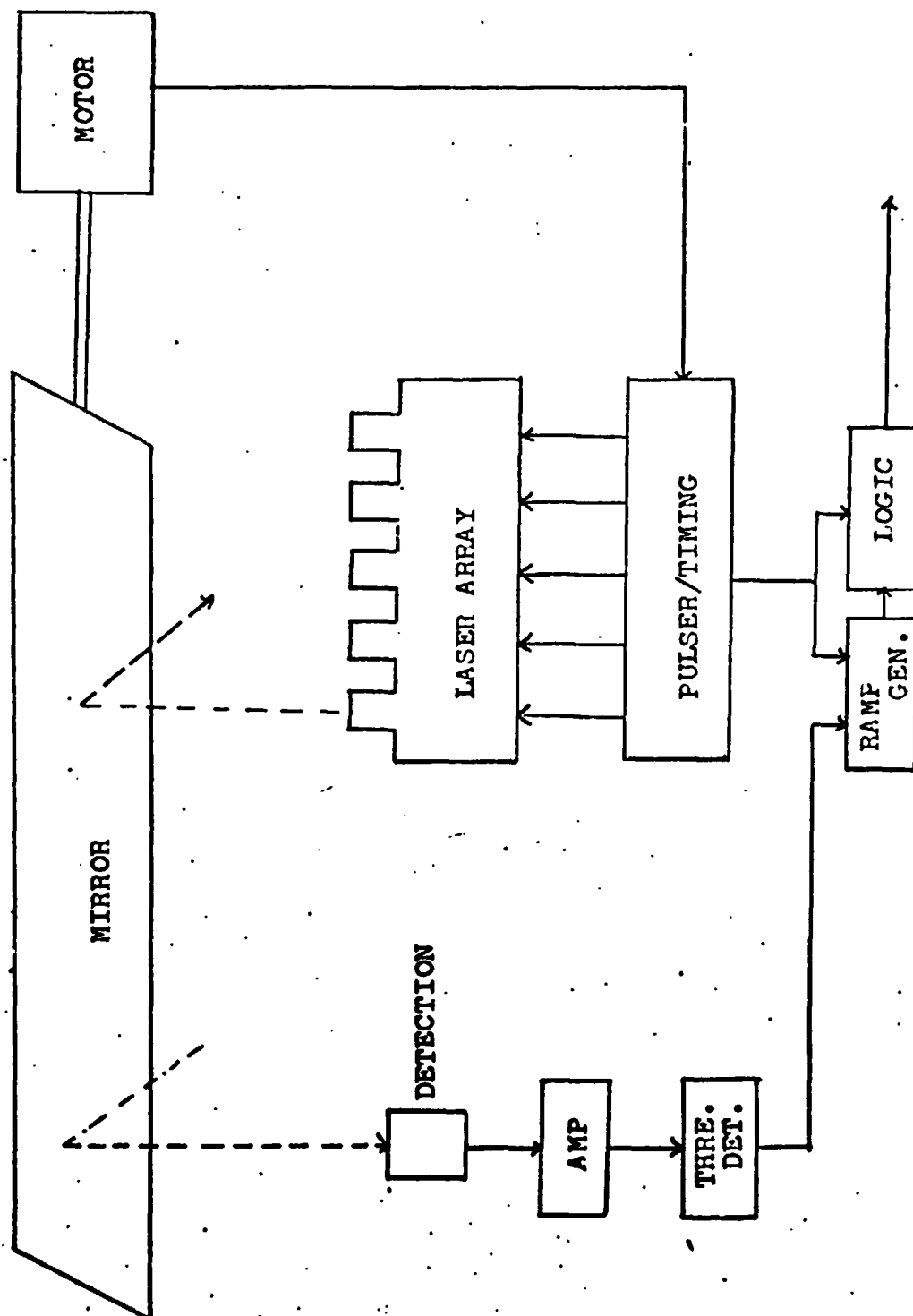


FIGURE 38.

TIMED PULSE

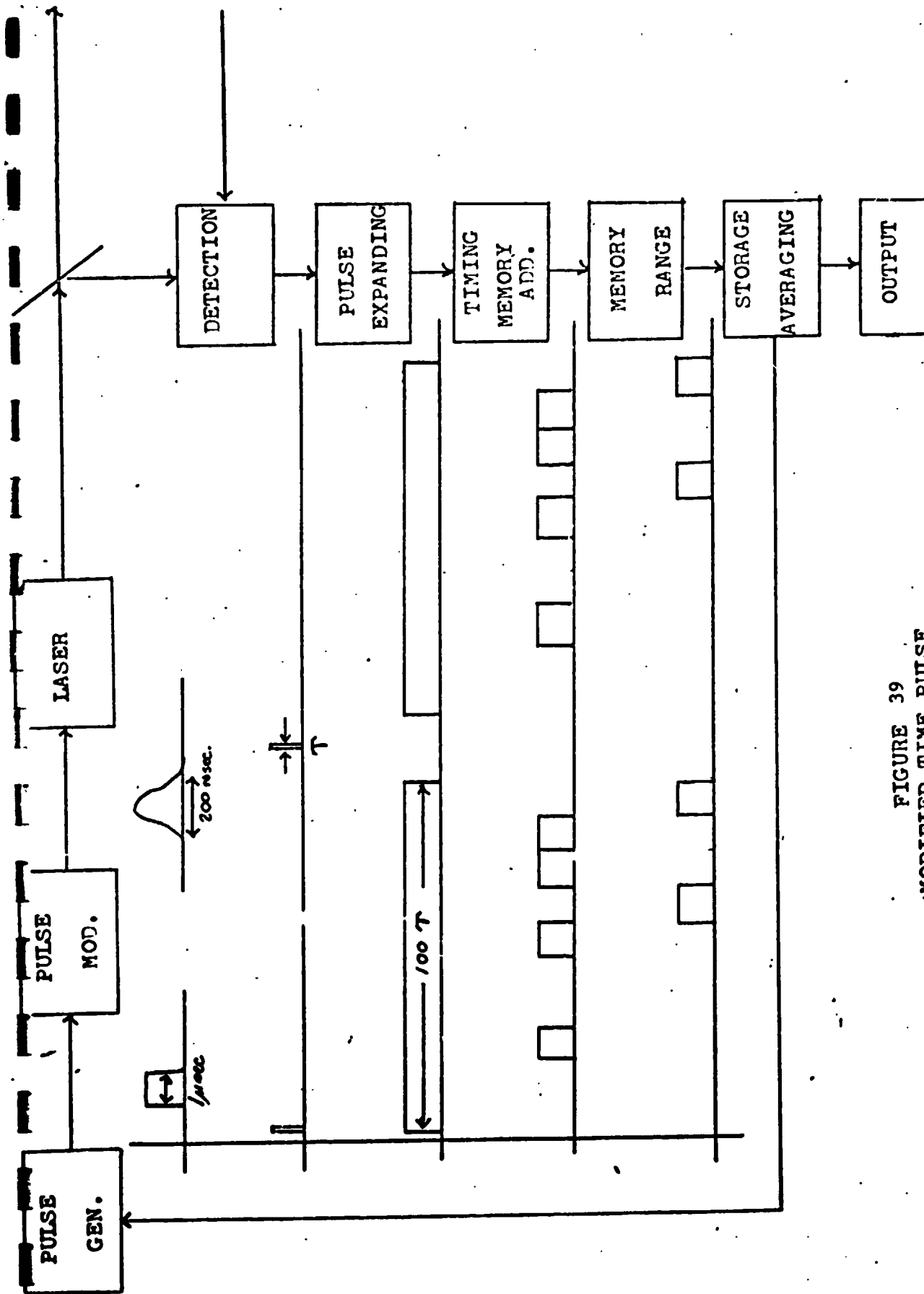


FIGURE 39  
MODIFIED TIME PULSE



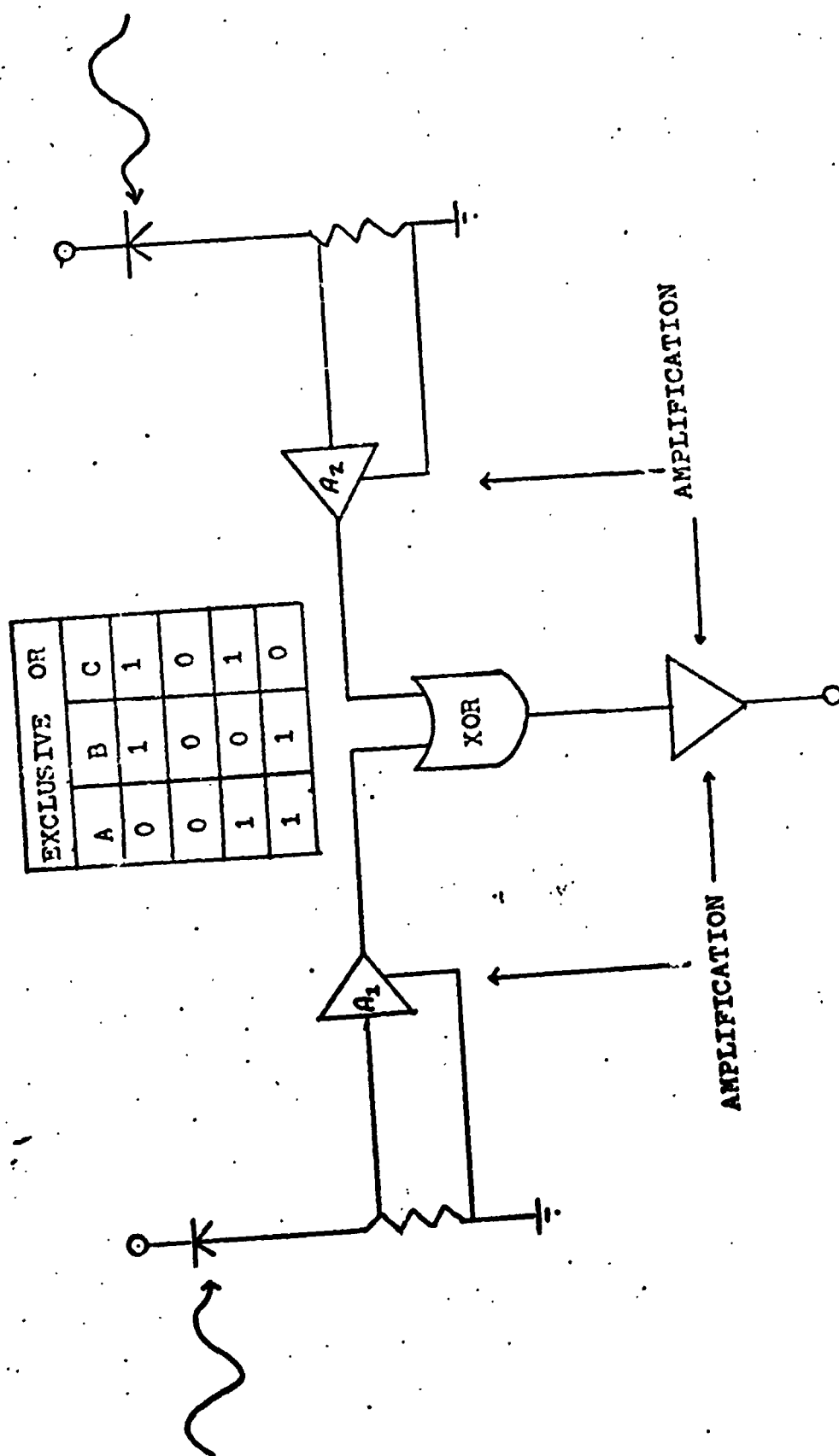


FIGURE 40

DETECTION CIRCUIT

where  $dt$  is the timing error,  $T^1$  the pulse length, and  $S/N$  the signal to noise ratio. Using nominal values, a maximum error of 3.75 cm. is calculated. Since this is 75% of the allowable error, every effort must be made to minimize it. Although the reflected pulse shape won't be identical to the output pulse shape, it certainly will depend on it. The laser output pulse shape must be as square and as powerful as possible.

The problem of extracting centimeter accuracy from the timed pulse method may be approached as follows, assuming rounded numbers for ease of calculation. The range depth of field,  $R$ , will be from 3 to 30 meters and can be related through the speed of light,  $c$ , to the time field by  $T_1 = 2R/c$ . Accordingly  $T_1$  must be between 20 and 200 n sec. If a range resolution of 03 meters is required, a time resolution of .2nsec. is necessary. As stated earlier, soon to be available counters will have resolutions of 10 nsec. (100Mhz.). A minimum magnification of 50 x is required for proper resolution.

The combination  $R_b$ ,  $T$ , and  $C$  constitute a ramp generator similar to Kuriger's design. The difference here is the method of output. A large resistor is placed across the capacitor with the result shown in Fig. 41.  $V_{in}$  is the pulse input from the detector and is width modulated depending on range. Using a capacitor of .01 microfarads and a resistor of 470K ohms, the transfer function of Figure 42 was obtained. The slope, or magnification, of the system is 1300 for the first part of the curve, and 300 for the second part. Note both slopes are well over one hundred. The resistor,  $R$ , may be replaced by a high input impedance schmitt trigger shown in Figure 43. The function of the circuit is to provide triggering at predetermined voltages, producing a square wave output which is more suitable for timing. Figure 43 shows the input and output wave shapes along with the circuit's transfer function. The transfer function shows the hysteresis exhibited by the circuit, allowing precise wave shaping and timing.

Figure 44 shows the expander with  $R'$  replaced by a transistor circuit. The two transistors are driven by pulses  $V_1$ , from the detection branch, and  $V_2$ , a pulse generator triggered by  $V_1$ .  $V_1$  charges the capacitor as before, but now the charge is metered out at a constant current determined by the transistor. As before

$$Vc_1 = I_1 T_1 / C$$

If the stored charge  $I_1 T_1$  is metered out at current  $I_2$ ,

$$Vc_1 = I_2 T_2 / C$$

Then simply

$$I_1 / I_2 = T_2 / T_1$$

The capacitor would supply a constant current until it's voltage dropped to the point where the transistor saturated. The discharge would then be exponential (see V.). Little time was available to be spent on this circuit, but it shows promise for development in the future.

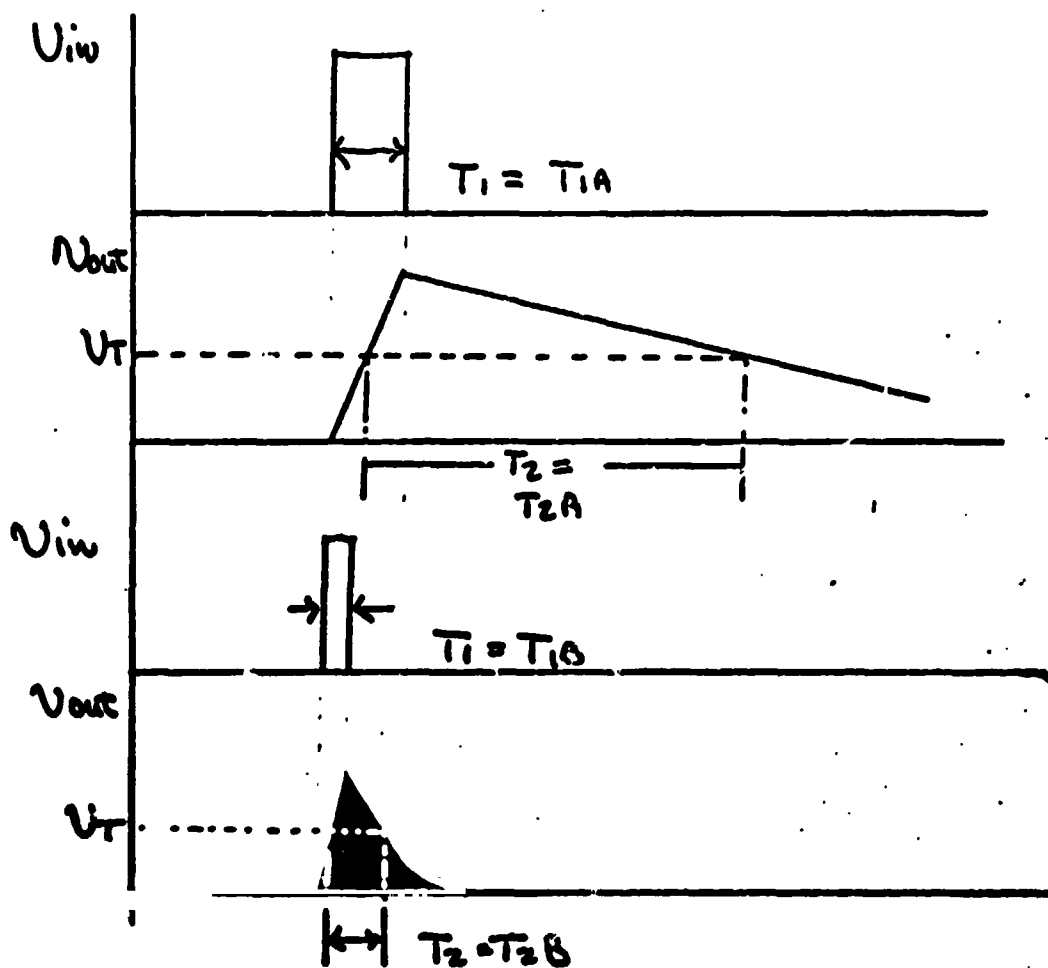
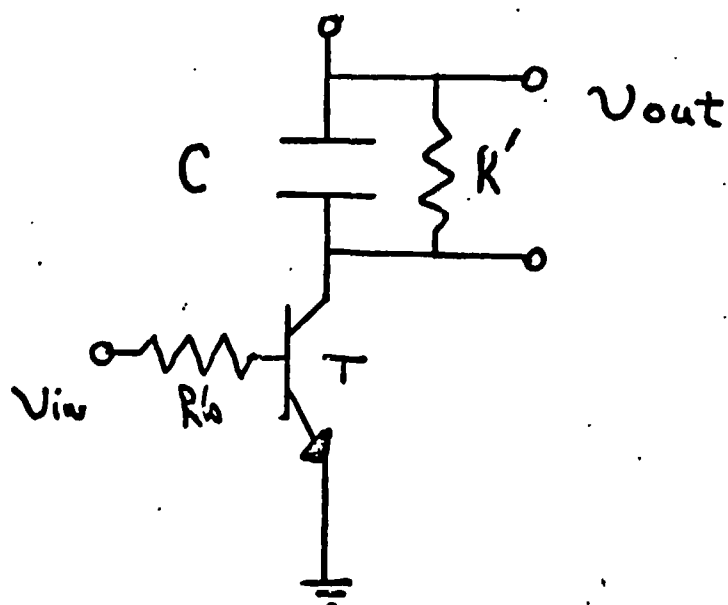


FIGURE 41 - PULSE EXPANDER - FREE RINGING

$T_2 \uparrow$   
ms

6.0

5.0

4.0

3.0

2.0

1.0

slope = 1000 ←

①

②

$C = .01 \mu\text{fd}$   
 $R = 470\text{K}\Omega$

79.

8.0

7.0

6.0

5.0

4.0

3.0

2.0

1.0

$T_1 \mu\text{sec} \rightarrow$

FIGURE 42. PULSE EXPANDER TRANSFER FUNCTION

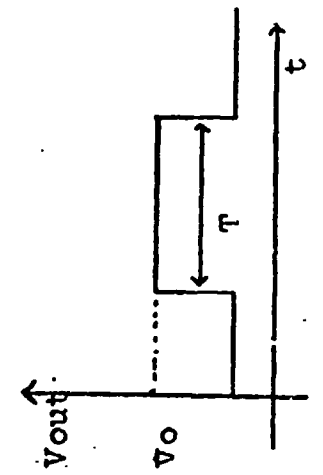
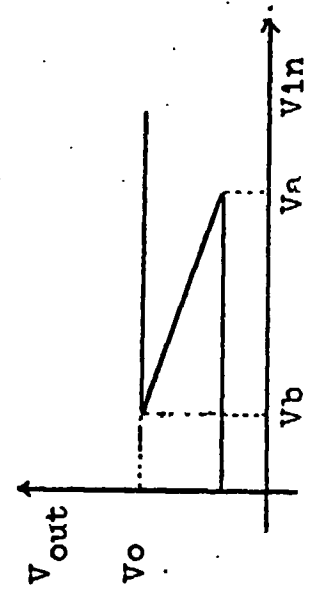
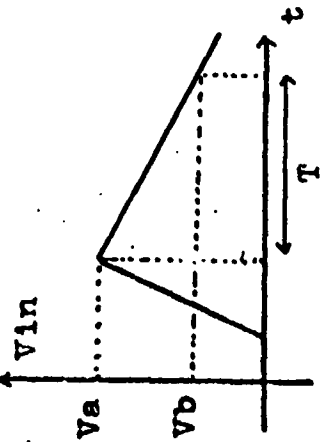
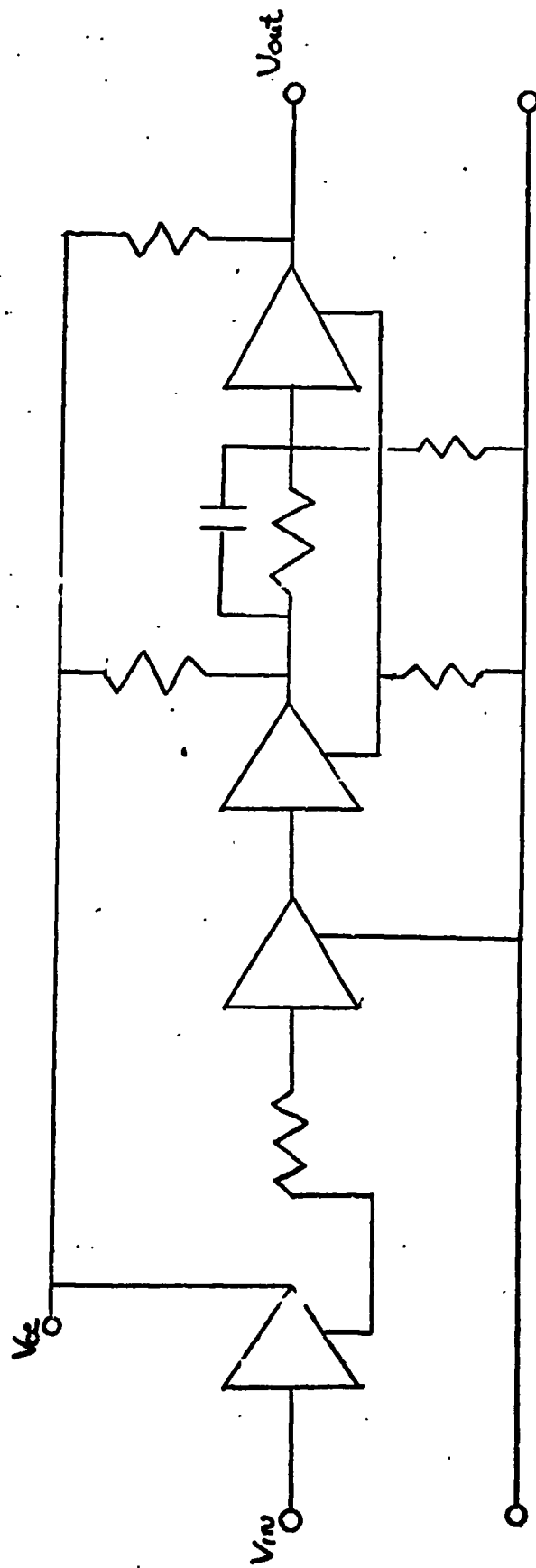
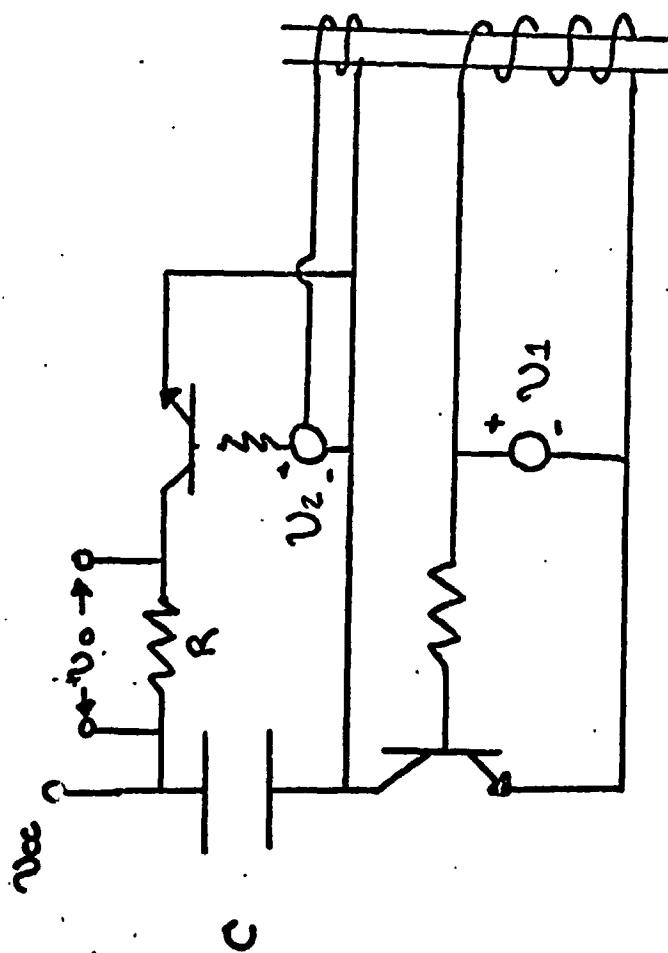


FIGURE 43. - SCHMITT TRIGGER



TRANSFORMER GIVES DC  
ISOLATION, WHILE ALLOW-  
ING EXTERNAL TRIGGERING.

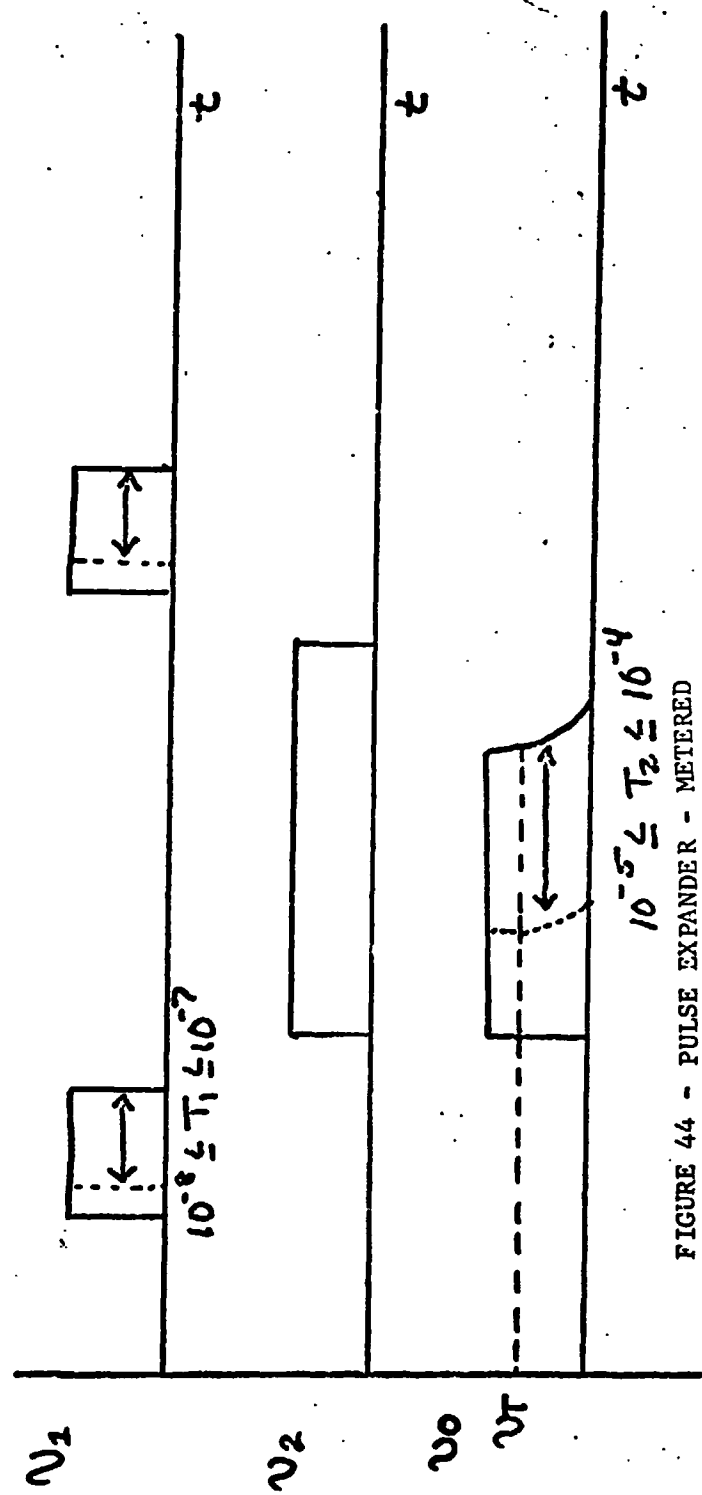


FIGURE 44 - PULSE EXPANDER - METERED

Up till now the concern has been producing a pulse width dependent on range and long enough to allow proper resolution. It is clear from Figure 42 that the pulse expander's transfer function is not linear, and computation of range from timing the pulse width would require extensive calculation. However, the pulse can be timed and hardwired to produce a memory address corresponding to the correct range.

Since  $T_1$ , the unexpanded pulse width, is related to the range by  $T_1 = 2R/c$ , the field of  $T_1$  will be

$$20 \leq T_1 \leq 200 \text{ nsec}$$

and

$$T_{\max.} - T_{\min.} = 180 \text{ nsec.}$$

If the range is to be known within  $\pm .03$  meters, a differential element of range,  $dR = .06$  meters, would correspond to a differential time of

$$dT_1 = 2dR/c = .4 \text{ nsec.}$$

The number of unique time values needed to define the field is then

$$N = 180/dT_1 = 450$$

If a portion of the pulse expander's transfer function, say with slope = 100, was blown up, the relation would be similar to Figure 45. If  $T_1 = 60 \text{ nsec.}$ , the differential element would be from 59.8 to 60.2 nsec. as shown. This transfers to  $T_2$  as mean time  $T_2 = 6 \text{ microsec.}$  and differential element from 5.98 to 6.02 microsec. If a 10 nsec. clock is used, 4 pulses will fit into  $T_2$ .

$T_{2\max.}$  will be given by  $100 \times T_{1\max}$  or 20 microsec. With a clock period of 10 nsec., this transforms to a maximum count of 2000 at  $T_{2\max.}$  The number of binary digits necessary to handle this count is 12. For the case being considered here, with  $T_2 = 6 \text{ microsec.}$ , the count will be 600. Notice that any count from 597 to 604 is representative of the same elapsed time,  $T_1$ , and the corresponding range since all are within the differential time element  $dT_2$ , see Figure 45.

The memory address is produced from the count by hardwired logic gating, Figure 46. A count of 600 is shown in the register. This corresponds to an elapsed time of 60 nsec. or a range of 9 meters. This range would correspond ideally to a memory address of 150. When the count is anywhere from 597 to 604, 150 should appear in the memory address register through similar gating. If the entire transfer function is calibrated in this manner, a unique memory address will be produced for any elapsed time  $T_1$  within the differential limits.

The memory component is the least complicated of the system. It's purpose is to store 450 values of range for processing. Since the maximum range has been assumed to be 30 meters or 3000 centimeters, a 12 bit memory word length will be necessary, the whole memory consisting of 450 words.

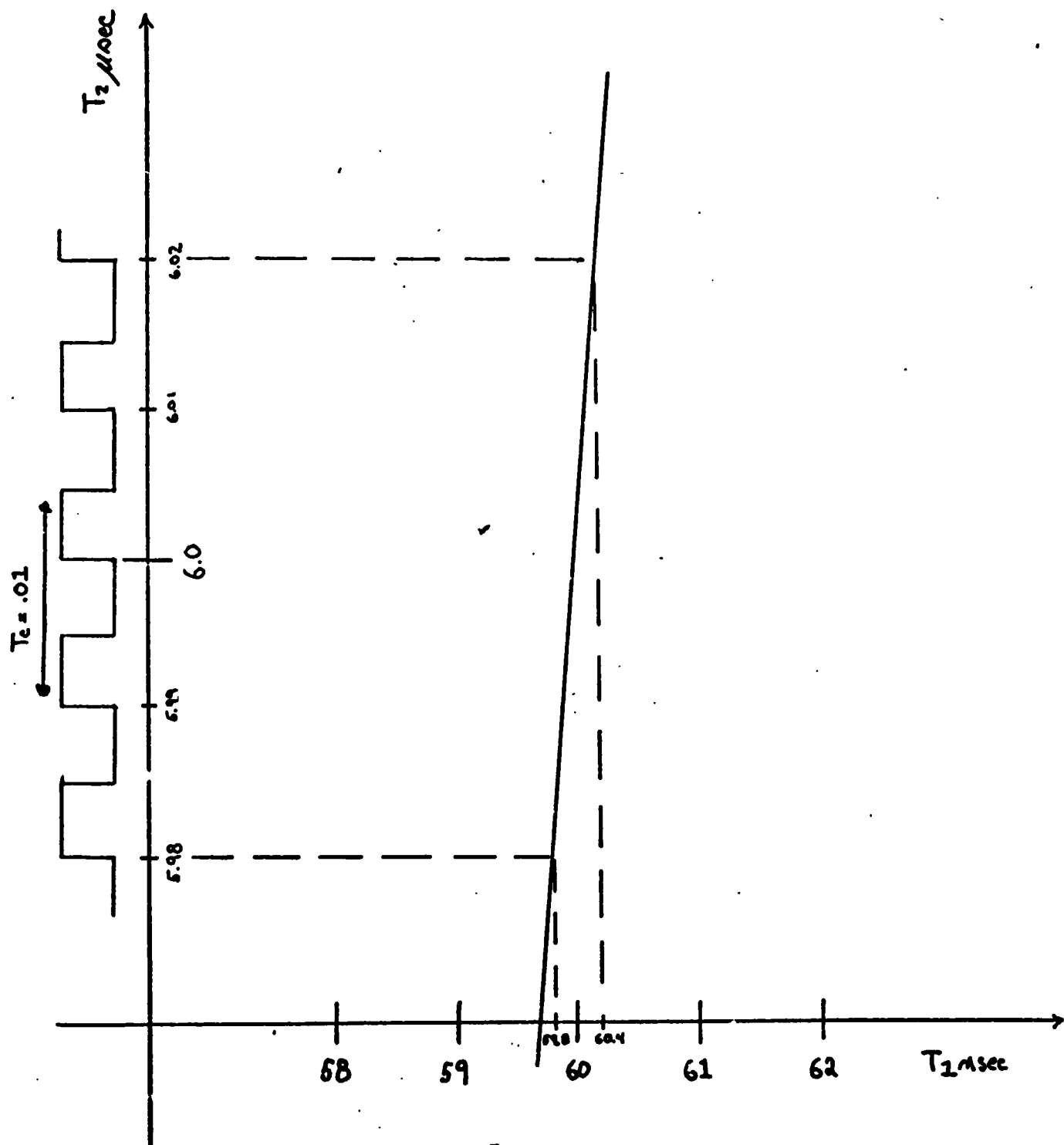


Figure 45  
Blown-up Portion of  
Transfer Function



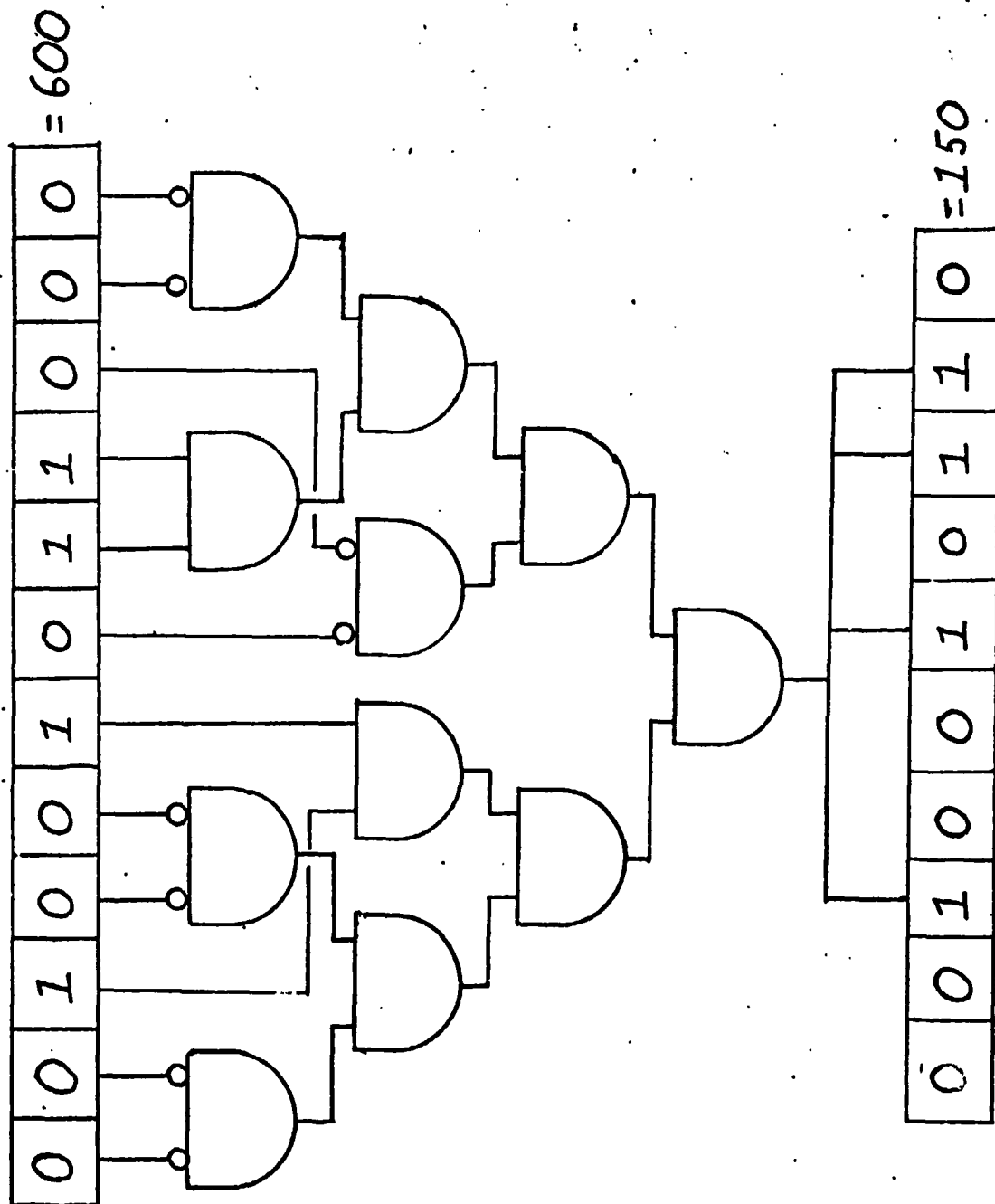


Figure 46

Memory Address Fabrication

As far as the averaging process is concerned, every logic gate has associated with it a delay time. This time is constant and if accounted for will not hamper operation. The typical delay time for a gate is 10 nsec. The data access time from memory is 100 nsec. Notice that the maximum output from the pulse expander will be 20 microsec., and if 100 gates plus memory have to be passed, the delay from pulse expander to range will be 21.1 microsec. A safe figure for the total figure would be about 25 microsec. Since a GaAs laser is to be pulsed for 100 nsec. (maximum) at a duty factor of .1%, the minimum period allowable for laser operation is 100 micro sec. This can be lowered easily to 50 microsec. by shortening laser 'on' time, but clearly the laser is the dragging foot. At a period of 50 microsec., 4 points will be averaged 10 times in 2msec. meeting pitch and yaw assumptions.

The major features of a power supply for laser operation are the high current needed for onset of lasing (10 amps) and the narrow pulse width necessary to avoid burn out. At first a supply was designed for use with the phase difference method. The current pulse must have a flat top if the laser output is to be modulated. Transistor 2N5262 was chosen for its speed and current capabilities. The final design is shown in Figure 47 with 15 transistors in parallel to supply 45 amps to the laser. The circuit was never constructed because 2N5262 could not be obtained. The circuit would have been ideal for experimentation allowing low current (non-lasing) pulses of long length for heterodyning experimentation and short, high current pulses for time pulse experiments. When it became obvious that 2N5262 would not arrive, an alternate design was chosen.

Figure 48 shows a power supply and the current waveform it produces. The operation is to charge the storage capacitor through the transistors until the capacitor voltage reaches  $V_{cc}$ . SCR GA201 is triggered to allow discharge through the laser diode. This pulser was built with the waveform resulting shown in Figure 49. Note, this is not the current waveform, but the signal waveform received at the photodiode. The rise time of the pulse (100 nsec.) is far from the current rise time given for the circuit (20 nsec), Ref. 6 and 7.

Recalling the requirements placed on the rangefinder, they are:

1. Range  $\pm .05$  meters
2. Angle  $\pm 10$  arcsec.
3. Fast scan rate
4. Low weight
5. Low power consumption

The timed pulse method meets all requirements and is recommended for further development in two main areas of study: the laser power supply with related detector electronics, and the modified pulse expander including counters and registers.

Supplying 40 amps to the laser becomes a problem, but can be solved by eliminating all unnecessary components and wire lengths in the laser's circuit. Figure 50 shows a suggested power supply scheme to eliminate the 3 IN914's as an example of power supply improvement. The detection may be improved by adding a differentiating op-amp, Ref. 8, to eliminate received pulse rise time and the error introduced by this rise time.

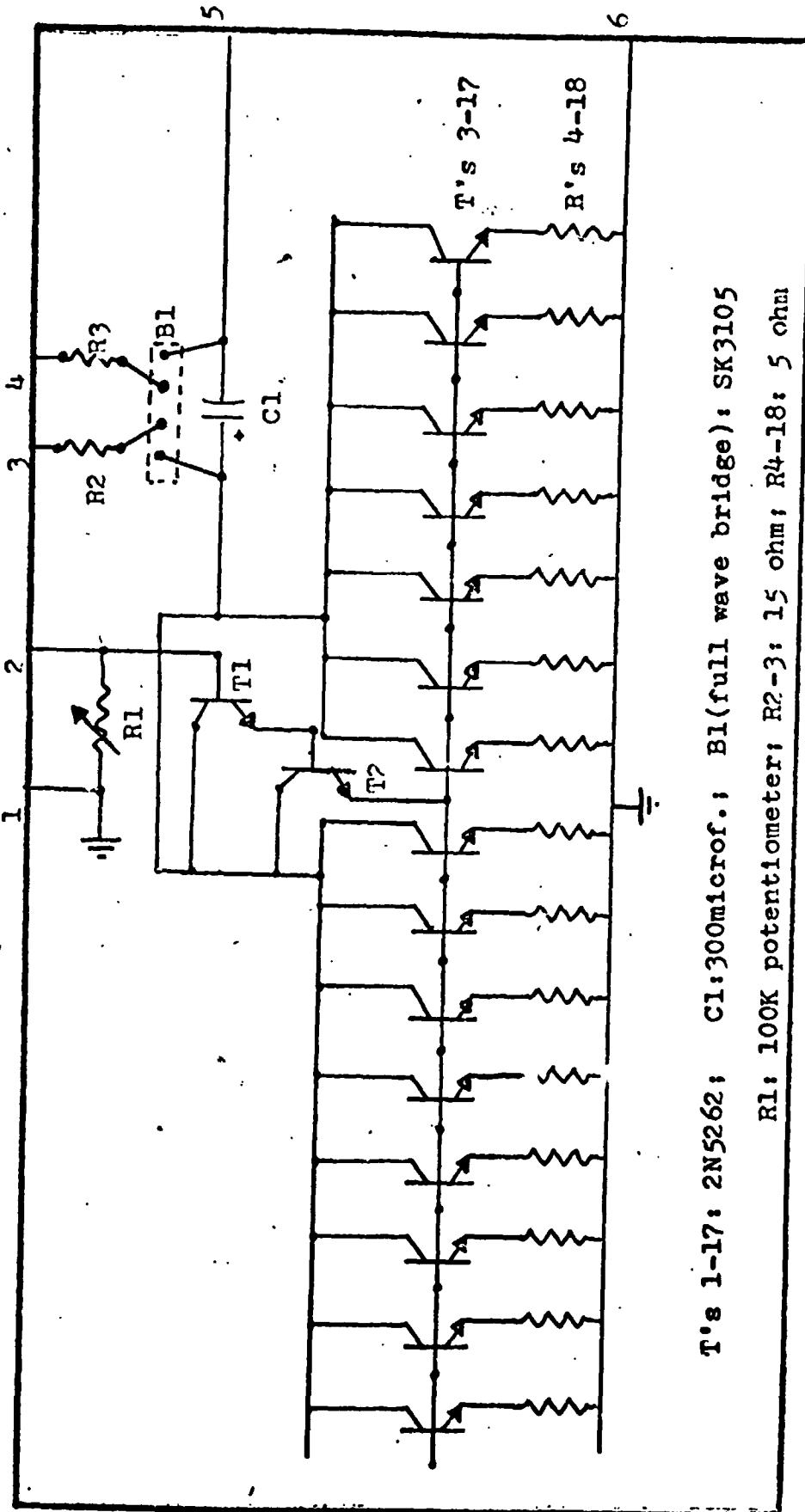


Figure 47  
 Pulse Current Amplifier for GaAs Laser

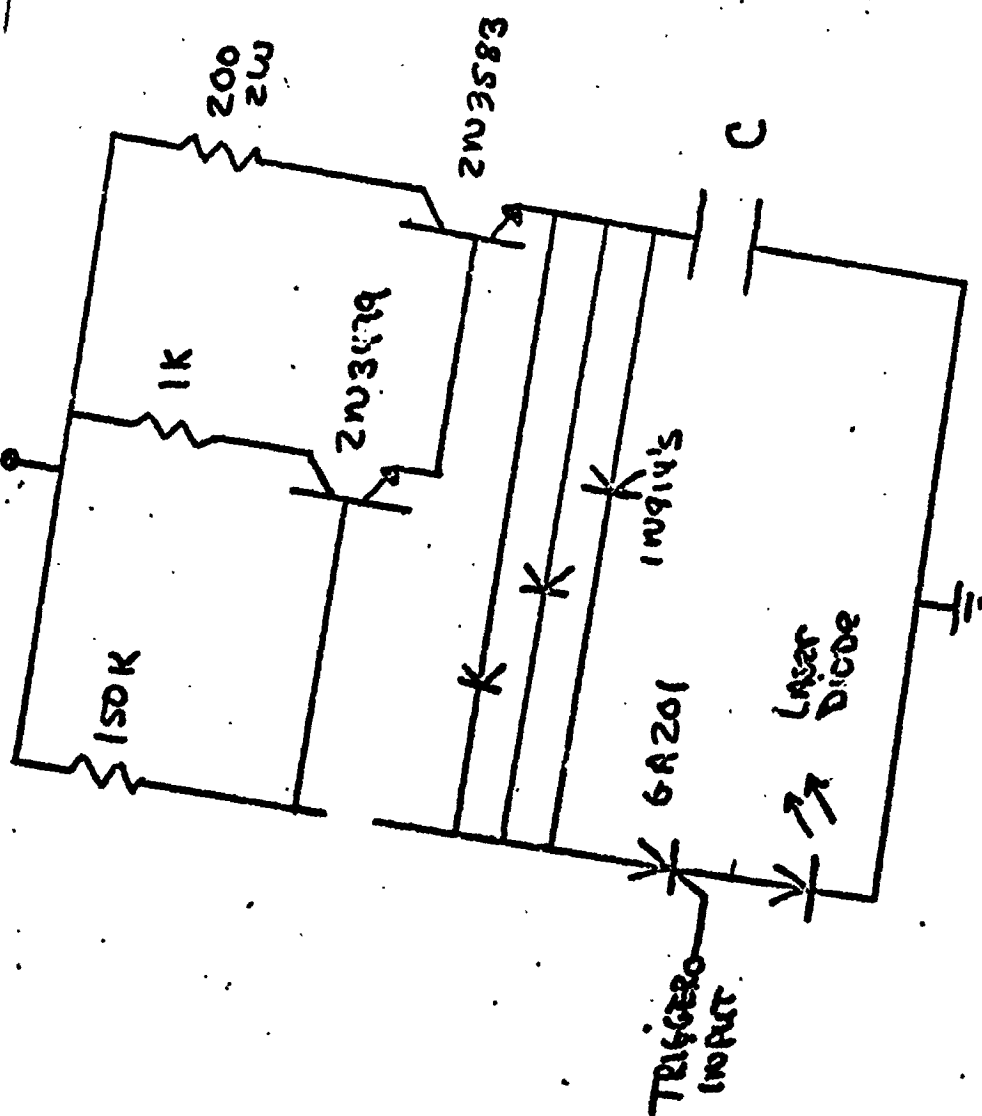
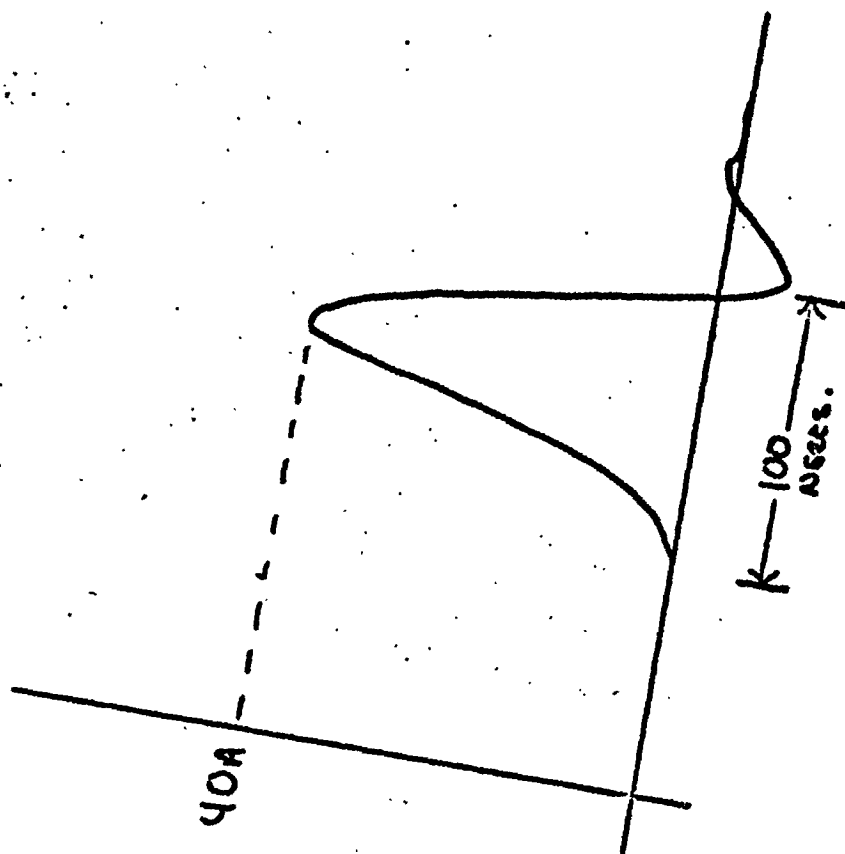


Figure 48

Conventional power supply  
and output waveform



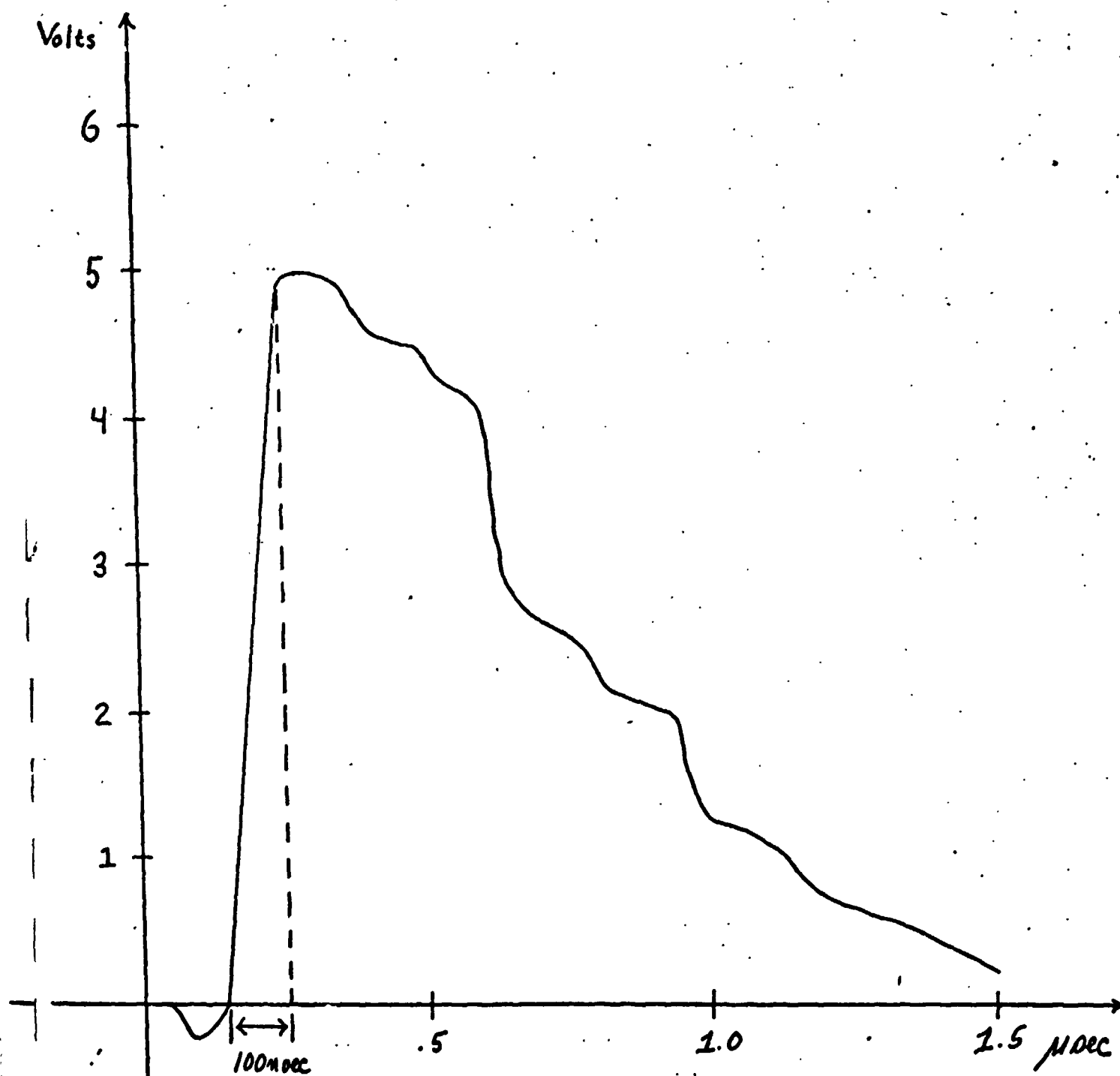


Figure 49  
Received signal waveform

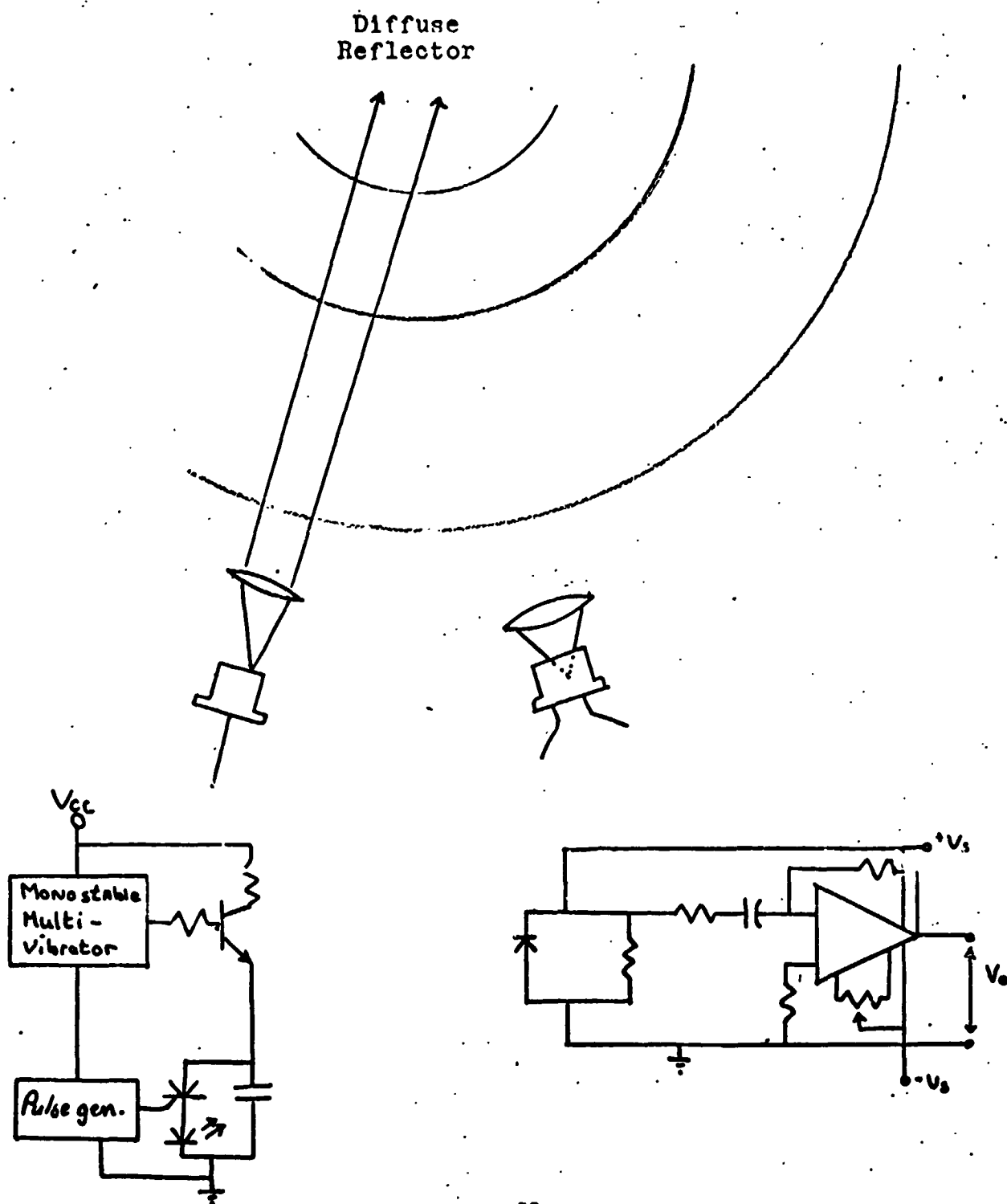


FIGURE 50

Proposed Power Supply and  
Detection Circuitry

The modified pulse expander is not a unique design. Hewlett-Packard counters model numbers 5360 and 5379 boast .1 nsec. resolution and use pulse expanding techniques. They cost around \$6,000.00. Therefore further research into the modified expander is recommended towards a possible linear transfer function to simplify processing. If the pulse expanding technique can be debugged and made practical, the timed pulse method, as described, is a laser rangefinder for terrain sensing measurements for Mars application.

It is planned to continue the design, construction and evaluation of this laser rangefinder alternative during the coming year.

Task C.1.b. Laser Scan Methods and Phase Comparison Rangefinder - G. Herb  
Faculty Advisor: Prof. C. N. Shen

This task addresses two areas of study: (1) a laser scanning system, and (2) the range finder electronics and methods.

If the terrain data is to be collected as the vehicle is moving, the rocking and rolling of the vehicle as it travels the uneven terrain can be a large source of error. To attempt to reduce this error, the laser scan methods considered here are of a block scanning nature. That is, the entire field of view of the rover is scanned out very rapidly so that the rock and roll error between points is negligible and all points in the field may be considered to have been obtained simultaneously.

The criterion for such a system are:

1. No or few moving parts
2. An angle incremented scan (i.e. point spacings vary with distance from vehicle)
3. Scan requirements - scan angle  $40^\circ - 60^\circ$   
range angle  $40^\circ$

A rapid scanning laser range finder meeting these requirements was shown to be a feasible system. A non-mechanical laser scanner using either digital deflection optics or a modulated semiconductor laser diodes was found to be the most promising method. A complete range finder scanning system was proposed around this type of rapid scan. The proposed system is highly accurate because it does not use analog signals to determine the angles at which a laser pulse is transmitted. All directions have binary labels which correspond to angles which can be known to a high degree of accuracy.

The problem of phase blur due to the incident spot from the laser beam being distorted due to the beam's shallow angle of incidence was found to cause negligible errors compared with the accuracies desired for a reasonable range of beam diameter.

A design for a phase comparison, modulated laser range finder has been developed which appears to provide a very promising way of achieving the desired  $\pm 1$  centimeter accuracy at mid-range (= 15 to 20 meters).

A section of the design was bread-boarded and tested. Although the tests were in good agreement with predicted results, additional work will

be necessary to complete the laboratory testing of the entire system.

Details of the progress are provided in the following sections on scanning systems and rangefinder system.

### Scanning Systems

One possible system, the dual vibrating mirror scan, was investigated but proved to be inappropriate for a rapid scan system. Here, two more systems will be introduced which attempt to alleviate the problems of the dual mirror approach.

Kuriger, Ref. 5, has worked on and proposed a hybrid scan system using a vibrating mirror for a vertical scan and a line of laser diodes to accomplish the horizontal scan. His rangefinder system is not capable of producing the necessary accuracy, but his scanning system does have some advantages. Kuriger's system is presented with some minor modifications in Figure 51. The "pulse transmitted detector" has been added to conform with the information needed in one of the rangefinding schemes currently under study. In this system both the transmitter and the detector use the same vertical scan mirror. The diodes provide the horizontal scan, while the receiver looks at the entire horizontal scan area via the cylindrical lens. The use of the same scan mirror assures synchronization between transmitter and receiver, and the narrowing of the detector's field of view to only one horizontal row at a time increases the signal to noise ratio. Further advantages of this system are its compactness and small number of components. But although the horizontal transmitted angle is known exactly, the vertical angle determination relies on the same type of mirror position detection as does the dual mirror system and suffers the same problems.

An alternative system which seems to avoid all the major scan problems is proposed. Figure 52 shows the proposed system using digital deflection optics, but a matrix of laser diodes could be substituted just as well.

The detection system used is similar to Kuriger's except the detector section is mechanically a separate entity from the transmitter. When the mirror drive starts its vertical sweep, the synch (start) circuit detects this and initiates the transmitter's scan. The transmitter's vertical scan is approximately synchronized to the mirror, but the detector is given a wide enough field of view to compensate for a slight mis-match. Any mis-match which does occur does not continue to accumulate since the transmitter and detector are re-synchronized at the beginning of each vertical scan.

The advantages of this system are many-fold. First, the actual laser scanning is completely solid state. Also the transmitted angles are known exactly, with each pair of horizontal and vertical having its own binary code label. Finally, although a hybrid detector scheme is used, data point accuracy is extremely improved because we are not relying on the mirror position to give point location, only to narrow the detector's field of view to the approximate azimuthal scan line of the transmitter. This system then seems to have the potential for extremely accurate transmitted angle information while maintaining a reasonable signal to noise ratio at the detector by narrowing its field of view.



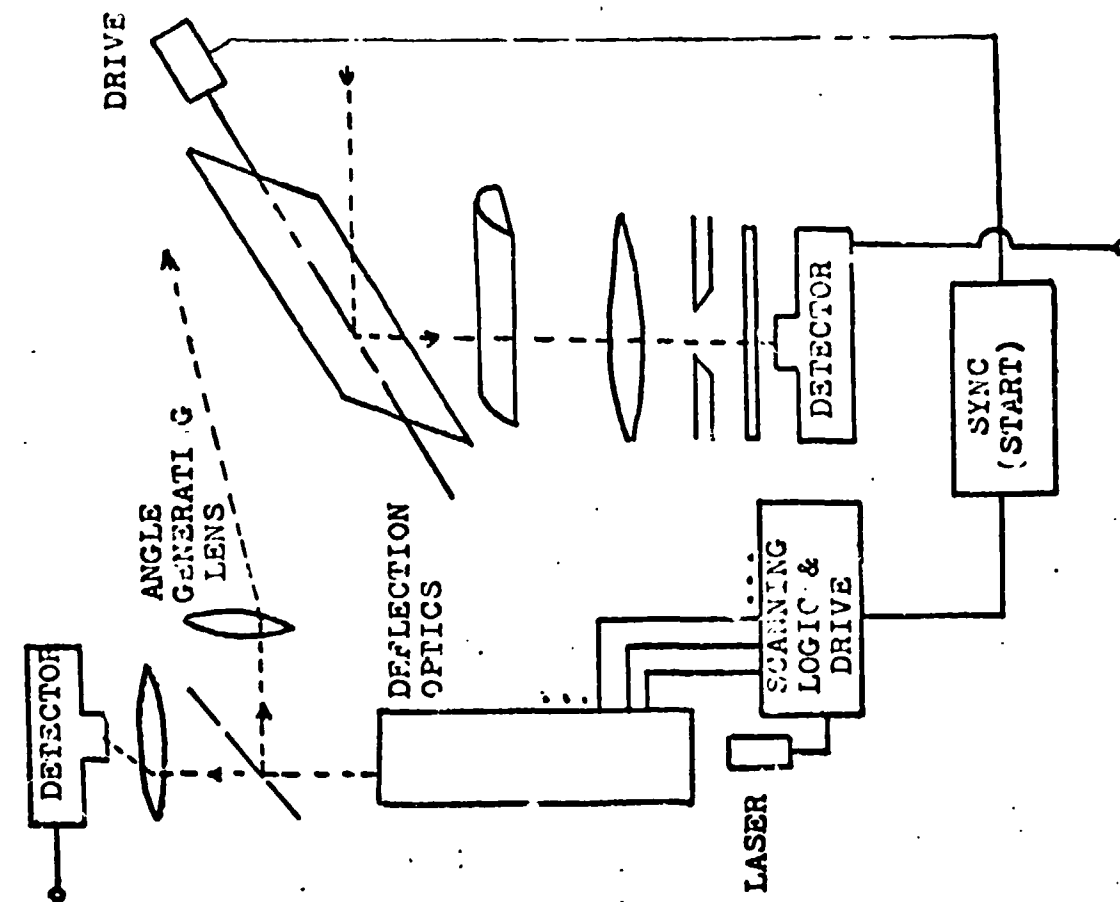


FIGURE 52  
PROPOSED SCANNING SYSTEM

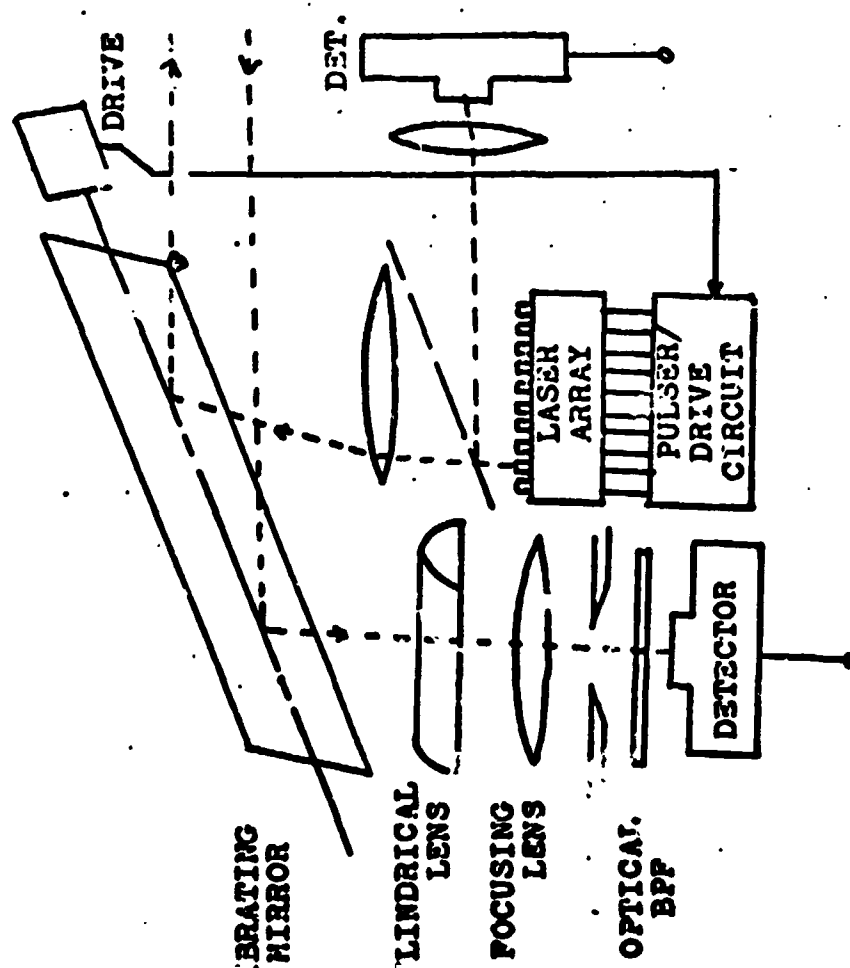


FIGURE 51  
KURIGER SCANNING SYSTEM

One problem with all the angular scan methods is the incident spot distortion at the terrain. Since a collimated beam is transmitted at an angle, the actual shape and size of the spot will be distorted when it strikes all surfaces other than those to which it is normal (see Figure 53). This is most severe at the maximum ranges. As can be seen from the figure

$$W = \frac{d}{\sin \theta} \quad \begin{array}{l} \text{for horizontal terrain} \\ \text{(i.e. in the plane of the river)} \end{array}$$

Therefore, at 30 meters ( $\theta = 5.7^\circ$ ) a 2.5 cm beam diameter (= 1 inch) would produce a spot length of 25 cm. This effect worsens for negative in-path slopes and improves up to a point for positive in-path slopes.

This distortion results in different rays within the beam traveling different total paths. Thus a ray on the top of the beam in Figure 53 would travel a total round trip distance of  $2(\Delta L/2)$  or  $\Delta L$  more than a ray on the bottom of the beam. This distribution of path lengths within a single beam will cause a time of flight ambiguity at the rangefinder's detector. In the case of a modulated beam type rangefinder which is described more fully in the following section, the phase of the modulating frequency on the returning beam relative to the outgoing beam is what supplies the range information. Spot distortion will cause a phase blur of a magnitude proportional to the amount of distortion. Referring to Figure 53 and taking the speed of light to be  $3 \times 10^8$  meters/second

$$\Delta \phi = .024 f_m (w^2 - d^2)^{\frac{1}{2}}$$

where  $\Delta \phi$  = peak to peak phase blur in degrees

$w$  = incident spot length in cm.

$d$  = beam diameter in cm.

$f_m$  = modulating frequency in Mhz

But since

$$\phi = (\Delta t) f_m 360^\circ$$

where  $\phi$  = relative receiver to transmitter phase of modulating frequency

$\Delta t$  = beam ideal round trip transit time in microseconds

The error introduced by the phase blur is

$$\frac{\Delta \phi}{\phi} = \frac{.024 (w^2 - d^2)^{\frac{1}{2}}}{360 \Delta t}$$

and is independent of  $f_m$ . Therefore, the phase blur error is independent of the beam's modulating frequency and can be fixed by other constraints.

Table VII shows values of  $\Delta \phi / \phi$  as a function of range in front of

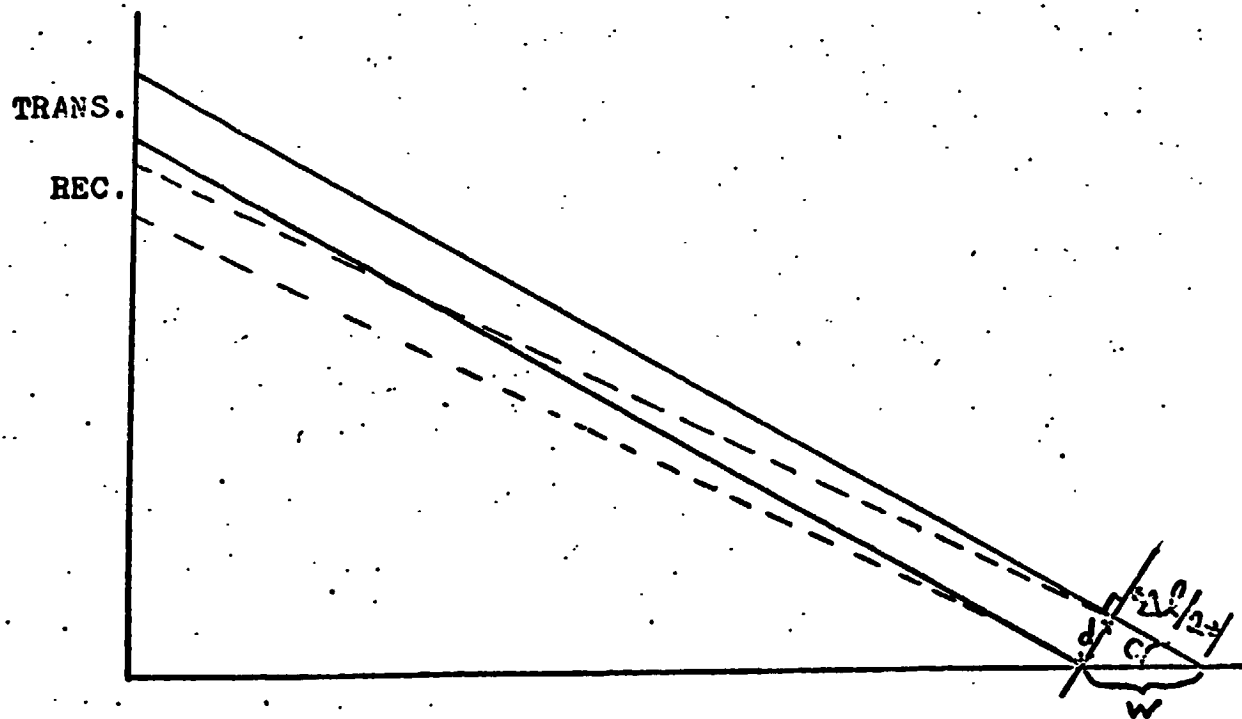
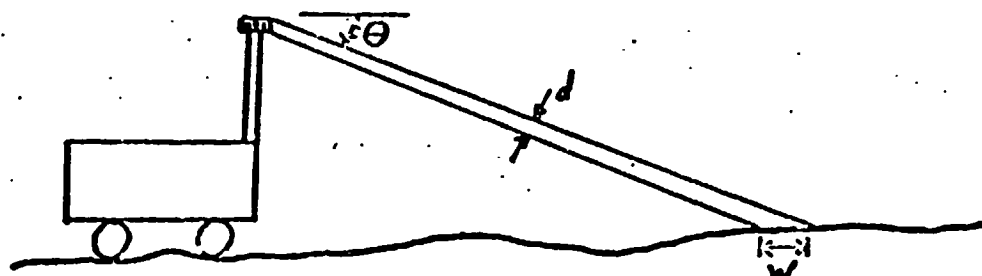


FIGURE 53. INCIDENT SPOT DISTORTION

the vehicle, R, and beam diameter, d.

TABLE VII

R	$\Delta\phi/\phi$ in %		
	$d = .5$	$d = 1$	$d = 2$
3	.0131	.0262	.0524
5	.0158	.0317	.0635
10	.0178	.0355	.0709
20	.0183	.0366	.0732
30	.0134	.0368	.0737

This can be done since R is a function of  $\Theta$  and w is a function of d and  $\Theta$ . Note that the errors introduced by spot distortion on a flat terrain are negligibly small over a large range of d.

#### A Rangefinder System

A modulated laser - phase comparison rangefinder was proposed and appears in block diagram form as Figure 54. The benefit of this type of system is that since the returned signal will be a sine wave of a specific frequency in noise, it can be put through a very narrow band pass filter to increase its signal to noise ratio.

Heterodyning techniques (frequency translating) are used as a method of increasing resolution. A constant phase angle is maintained in a heterodyning procedure. Therefore a  $45^\circ$  phase lag at 1 MHz corresponds to a lag of 125 nanoseconds. After heterodyning down to 10 KHz, the  $45^\circ$  phase lag is maintained, but a  $45^\circ$  lag at 10 KHz corresponds to 12.5 microseconds. Thus a frequency decrease of 100 times has given a time expansion of 100. The proposed system also averages several cycles of phase differences to further increase the range accuracy. A complete description of this system can be found in Ref. 9.

The phase detection section of the rangefinder was bread-boarded in the laboratory to check its operation. Due to equipment problems the heterodyning section could not be simulated. Without the frequency translating section, the phase comparator had to be checked with a lower frequency. The time expansion feature was also lost. Phase delays of sufficient magnitudes for the comparator to resolve thus had to be artificially produced. These phase differences therefore represented no actual range measurements, but were for test purposes only.

Since this self contained system had no significant noise, the Schmitt triggers were set at the more easily implemented threshold of zero with zero hysteresis. In the actual system, more realistic values of the thresholds should be chosen. The most logical place to locate this threshold voltage at first glance, is at the point of maximum slope of the signal, since this would reduce the sensitivity of the trigger to premature or late switching due to noise spikes close to the threshold. However, for sinusoids this point is at zero voltage which eliminates the hysteresis region and it is the hysteresis that reduces the sensitivity to premature CFF

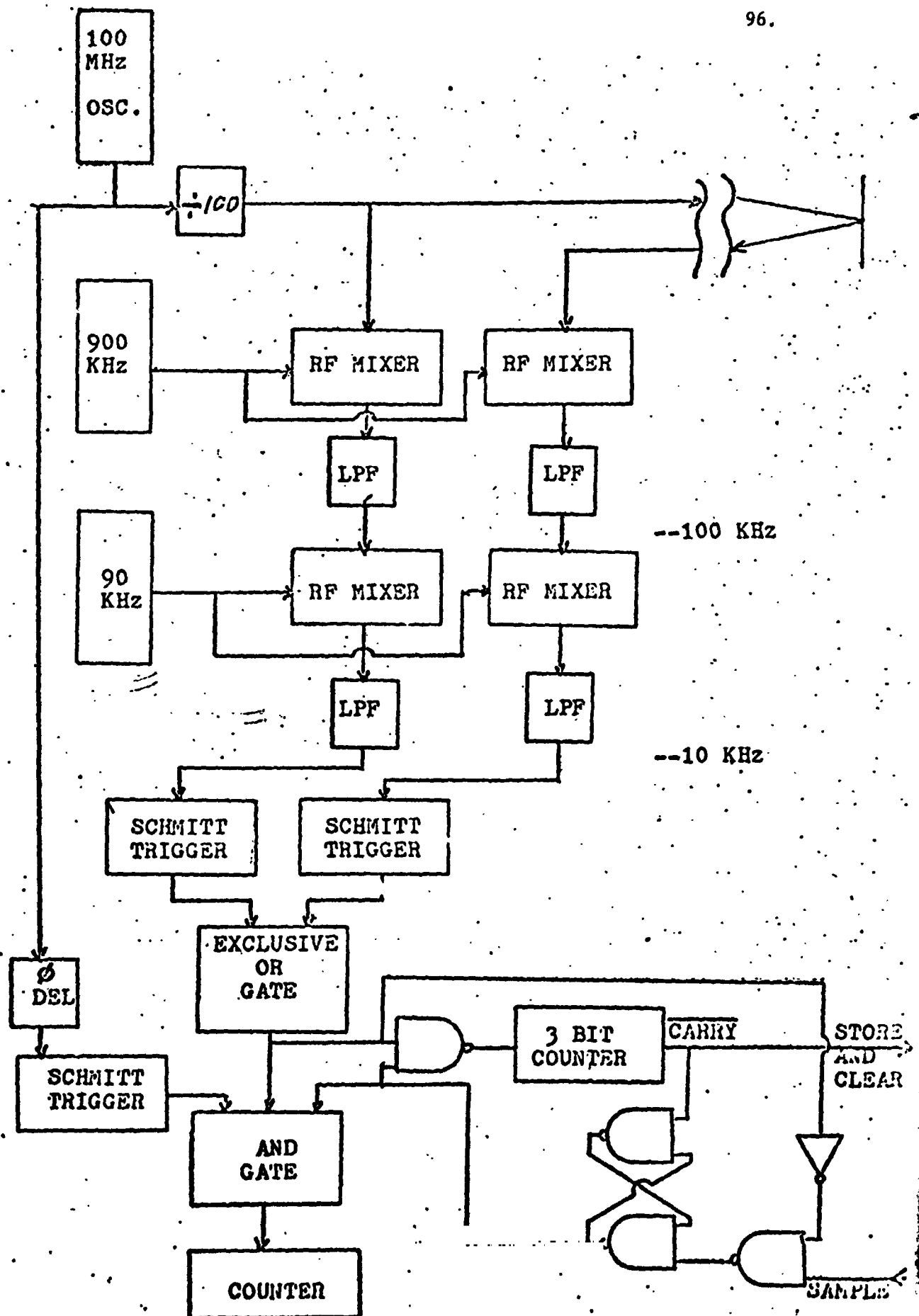


FIGURE 54. PROPOSED RANGEFINDER

switching of the trigger after it has just crossed the ON threshold and vice versa (see Figure 55). Thus the actual hysteresis, and therefore thresholds, should be set as a function of the most probable noise amplitude of the processed signal.

As for the system under test, all sections worked as expected. The output wave closely resembled Figure 56 (with the exclusive OR envelope missing of course). Since NAND logic was used, however, the wave forms were inverted. With the SAMPLE command held high, the clocked phase pulses were grouped into the appropriate number of samples for averaging. Varying the phase angle of the input signals varied the phase pulse width, and therefore the number of pulses in the output count, by a proportional amount.

It is planned to continue laboratory development of the phase comparison alternative and to compare its feasibility with the pulse amplification system described under Task C.1.a.

Task C.2.a.     Error Analysis and Stochastic Fit for Gradients - P. Burger  
Faculty Advisor: Prof. C. N. Shen

Because of the round trip communication delay of between nine and twenty-five minutes, it is essential that a Mars roving vehicle be equipped with autonomous terrain modeling and path selection systems. The objective of this task is to determine the effects of terrain sensing instrumentation errors on the estimation of terrain features, specifically slopes and gradients, and to evaluate the feasibility of employing a stochastic fit for gradients. These results can assist in defining terrain sensor instrumentation specifications on the one hand and can guide the development of path selection systems on the other.

The terrain sensor system being appraised, Figure 57, involves a rangefinder which is aimed along azimuthal and elevation angles to a point on the terrain. It is assumed that a scanning system based on increment in the elevation and azimuthal angles, Figure 58, will cover the interest of region in front of the vehicle. It has been determined that such a scanning and rangefinding system can be used to estimate the local gradient of the terrain. However, because of the sensor errors in range and pointing angles, the estimated gradient will differ from the actual gradient depending on the magnitude of the sensor errors. It has been determined that the standard deviation of the gradient will be in the range of one to eight degrees for standard deviations in rangefinding of 0.01 to 0.1 meters and elevation and azimuthal standard errors of one minute. The standard deviation of the gradient is also dependent on the gradient of the terrain, on the distance of modeled plane from the vehicle and the data point spacing. In this analysis, it has also been assumed that a rapid scan is used so that errors due to the pitch and roll of the vehicle can be neglected.

Complete details of the analysis and interpretation are presented in Ref. 16.

#### Mathematical Analysis

The quantities  $R$ ,  $\Theta$ , and  $\phi$  are measured with respect to the coordinate system  $h''$ ,  $a''$ , and  $b''$ , fixed to the vehicle, Figure 57. With

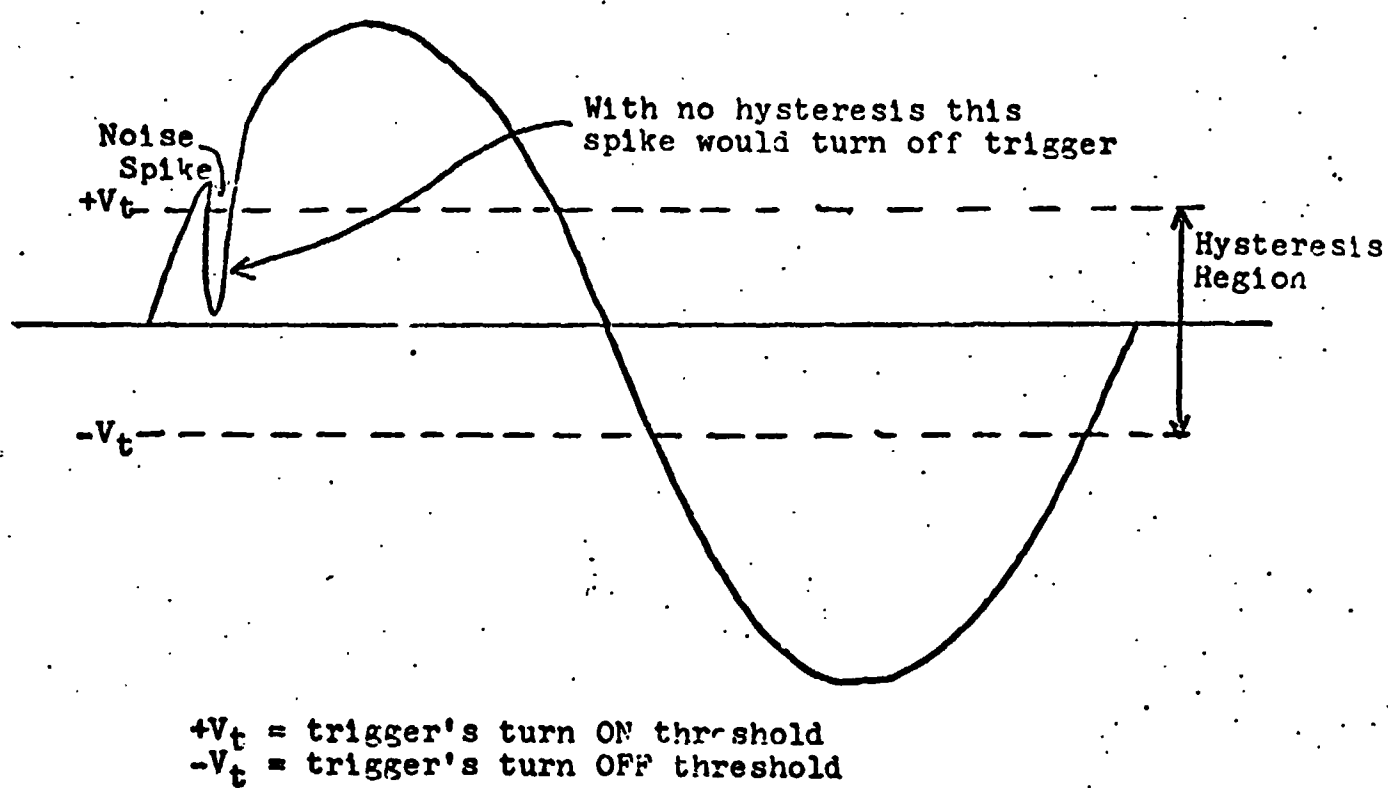


FIGURE 55. EFFECT OF SCHMITT TRIGGER ON NOISEY INPUT

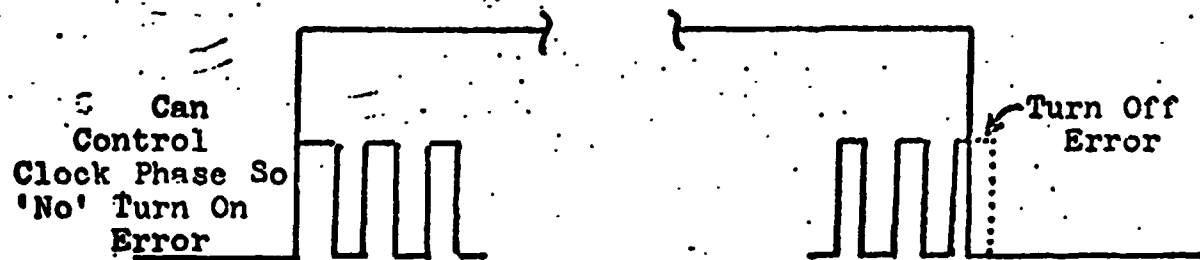
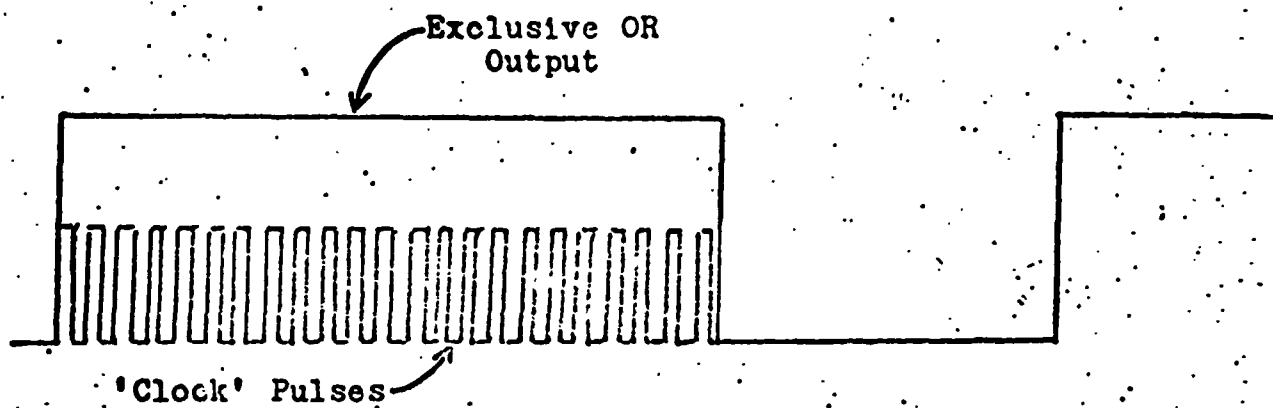


FIGURE 56. RANGEFINDER OUTPUT WAVEFORM



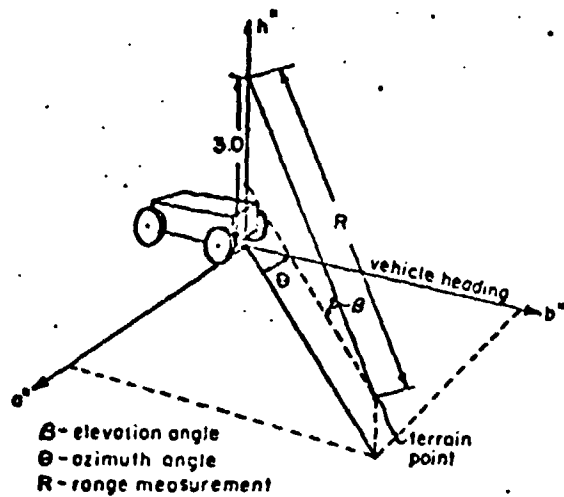


Figure 57. VEHICLE COORDINATE SYSTEM

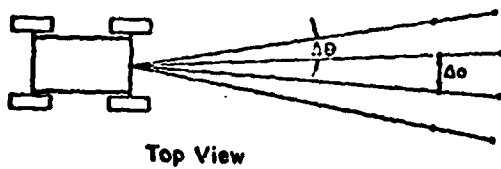
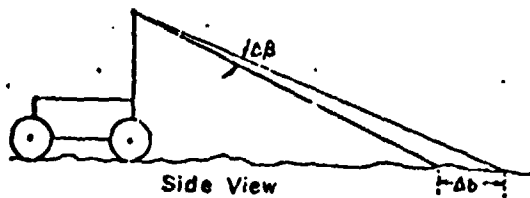


Figure 58. SPLIT BEAM LASER

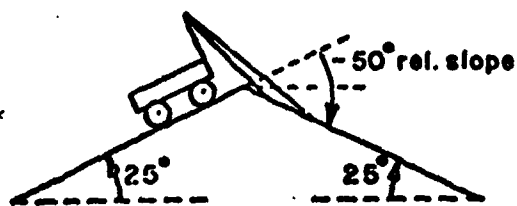
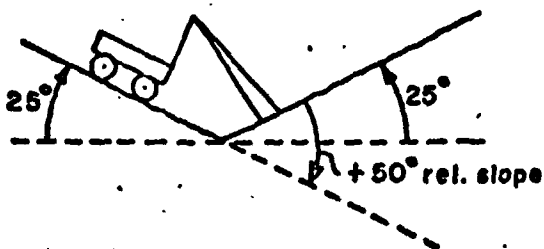


Figure 59. RELATIVE IN-PATH SLOPES

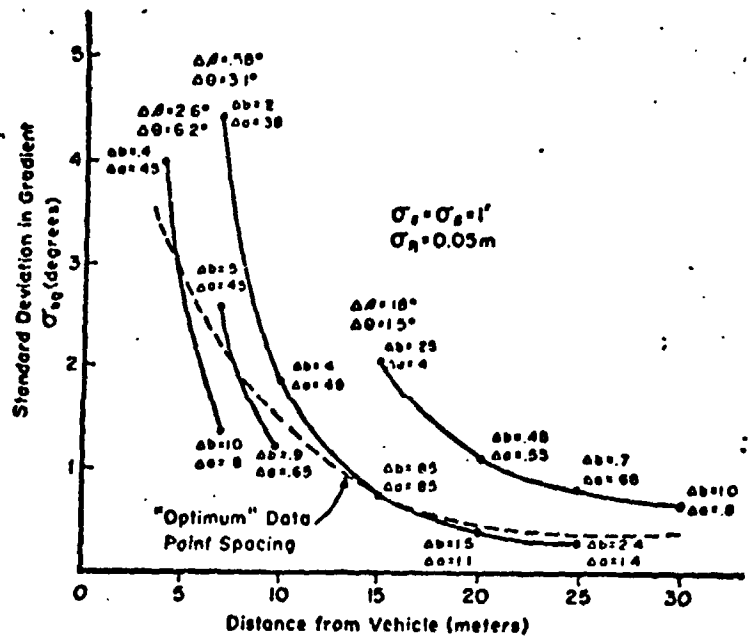


Figure 60. STANDARD DEVIATION IN GRADIENT VS. DISTANCE FROM VEHICLE ON FLAT SURFACE

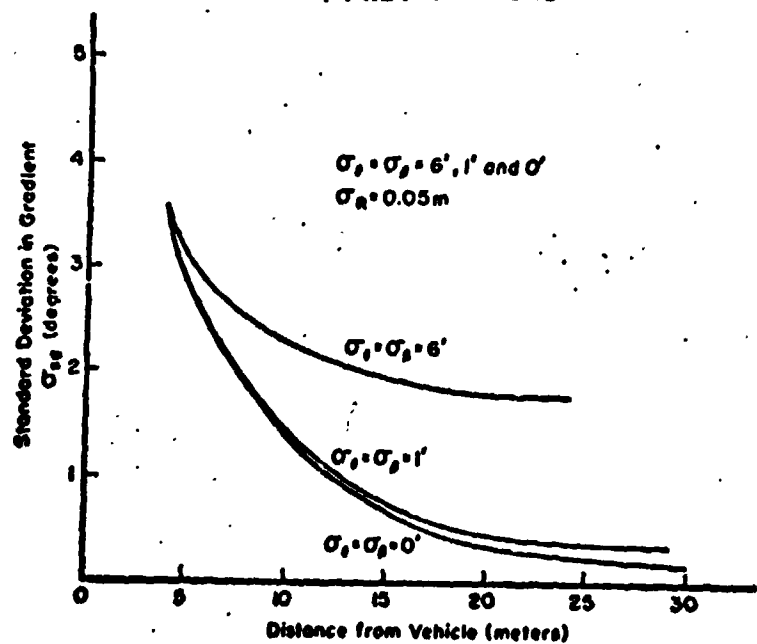


FIGURE 61. STANDARD DEVIATION IN GRADIENT VS. DISTANCE FROM VEHICLE FOR "OPTIMUM" DATA POINT SPACING ON FLAT SURFACE

With laser height at 3 meters

$$h'' = 3 - R \sin \beta \quad (1a)$$

$$a'' = R \cos \beta \sin \Theta \quad (1b)$$

$$b'' = R \cos \beta \cos \Theta \quad (1c)$$

The body-bound axis rolls with the angle  $\phi$  and pitches through an angle  $\xi$  about a reference frame  $h$ ,  $a$ , and  $b$  formed by the local vertical and an axis in a plane containing the heading and the local vertical. The coordinate transformation, Ref. 10, is:

$$\begin{bmatrix} h \\ a \\ b \end{bmatrix} = C(\phi) B(\xi) \begin{bmatrix} h'' \\ a'' \\ b'' \end{bmatrix} \quad (2)$$

where  $C(\phi)$  and  $B(\xi)$  are the roll and pitch transformation matrices respectively.

#### Determination of Slopes and Gradient

A number of measurement points within a certain small area of surface, say 0.5m by 0.5m, can be used to determine a plane in space, which may be written as:

$$h = ax_1 + bx_2 + x_3 \quad (3)$$

where  $x_1$  is the cross path slope and  $x_2$  is the in-path slope, which are the two constant parameters to be determined, Ref. 11 and 12. The corresponding gradient of the plane, which is defined as the gradient of the terrain in that small region on the planet's surface, is

$$Sg = (x_1^2 + x_2^2)^{1/2} \quad (4)$$

If the slope is less than a predetermined criterion, it is considered to be safe for the vehicle to travel ahead.

In order to locate the plane by a number of measurement points, one may rewrite Eq. (3) as

$$h_i = a_i x_1 + b_i x_2 + x_3 \quad (5)$$

where  $h_i$ ,  $a_i$ , and  $b_i$  are found from  $R_i$ ,  $\Theta_i$ , and  $\beta_i$  in Eqs. (1) and (2) for each  $i$ th point. Theoretically, three points determine a plane ( $i=1,2,3$ ). For greater accuracy however, more than three measurements ( $i=1,2,3,\dots,n$ ) probably  $n=4$  or  $6$ ) are needed to determine the slopes. A complete picture of the terrain in front of the vehicle can be constructed by modeling numerous adjacent planes, each covering a small area of surface.

#### Perturbation of the Variables

If  $a_i = \bar{a}_i$  and  $b_i = \bar{b}_i$  are assumed to be true in Eq. (5) a least square error estimate can be performed which minimizes

$$\sum_{i=1}^n (\hat{h}_i - \bar{h}_i)^2 \quad (6)$$

where  $\bar{h}_i$  is the actual measured height and  $\hat{h}_i$  is the corresponding height in the modeled plane.

In matrix-vector notation, Eq. (5) is:

$$\bar{h} = \bar{A}x \quad (7)$$

The least square estimate of the parameter  $x$ , Ref. 13, becomes

$$x = (\bar{A}^T \bar{A})^{-1} \bar{A}^T \bar{h} \quad (8)$$

### Perturbation of the Variables

The least square estimate above assumes the matrix  $A$  to be completely deterministic, Ref. 14. In reality, however, there is error involved in the determination of  $a$ ,  $b$ , and  $h$ , due to the errors in our measured values of  $\phi$ ,  $\xi$ ,  $R$ ,  $\beta$  and  $\theta$ .

If the symbol  $\delta$  denotes a perturbation, then  $\delta h$ ,  $\delta a$ , and  $\delta b$  in terms of  $\delta\phi$ ,  $\delta\xi$ ,  $\delta R$ ,  $\delta\beta$ , and  $\delta\theta$  are:

$$\begin{bmatrix} \delta h \\ \delta a \\ \delta b \end{bmatrix} = D(h'', a'', b'', \phi, \xi) \begin{bmatrix} \delta\phi \\ \delta\xi \end{bmatrix} + C(\phi)B(\xi)G(R, \beta, \theta) \begin{bmatrix} \delta R \\ \delta\beta \\ \delta\theta \end{bmatrix} \quad (9)$$

### Covariance Matrix of the Variables

The covariance matrix of the variables can be defined, Ref. 15, as

$$M = E \left\{ \begin{bmatrix} \delta h \\ \delta a \\ \delta b \end{bmatrix} \begin{bmatrix} \delta h & \delta a & \delta b \end{bmatrix} \right\} \quad (10)$$

where  $E$  denotes expected value.

If  $\delta\phi$ ,  $\delta\xi$ ,  $\delta R$ ,  $\delta\beta$  and  $\delta\theta$  are not correlated, then with the aid of Eq. (9)

$$M = D \begin{bmatrix} E(\delta\phi)^2 & 0 \\ 0 & E(\delta\xi)^2 \end{bmatrix} D^T + CBG \begin{bmatrix} E(\delta R)^2 & 0 & 0 \\ 0 & E(\delta\beta)^2 & 0 \\ 0 & 0 & E(\delta\theta)^2 \end{bmatrix} G^T B^T C^T \quad (11)$$

From Eqs. (10) and (11) the standard deviations of  $h$ ,  $a$ , and  $b$ , can be computed in terms of those of  $\phi$ ,  $\xi$ ,  $R$ ,  $\beta$  and  $\theta$  for each point. These are known quantities that depend upon the accuracy of the measuring devices.

### Covariance Matrix of the Slopes

Eq. (5) can be written as

$$h = Ax \quad (12a)$$

With  $h = \bar{h} + \delta h$ ,  $A = \bar{A} + \delta A$ , and  $x = \bar{x} + \delta x$

and Eq. (7) the covariance matrix of the slopes is

$$E[\delta \hat{x} \delta \hat{x}^T] = F \{ E[\delta h \delta h^T] - E[\delta A x \delta h^T] - E[\delta h (\delta S x)^T] + E[\delta A x (\delta A x)^T] \} F^T \quad (15)$$

This equation utilizes the least square estimate of the parameter  $x$  from Eq. (8) and the elements of the covariance matrix of the variables for each point, which are determined from Eq. (11).

#### Variance of the Gradient

If the symbol  $\sigma_{sg}$  denotes the standard deviation of the gradient,  $S_g$ , then from Eq. (4)

$$dS_g = (x_1^2 + x_2^2)^{-1/2} x_1 dx_1 + (x_1^2 + x_2^2)^{-1/2} x_2 dx_2$$

The variance of the gradient is:

$$\sigma_{sg}^2 = \frac{\bar{x}_1^2}{\bar{x}_1^2 + \bar{x}_2^2} \sigma_{x_1}^2 + \frac{\bar{x}_2^2}{\bar{x}_1^2 + \bar{x}_2^2} \sigma_{x_2}^2 + 2 \frac{\bar{x}_1 \bar{x}_2}{\bar{x}_1^2 + \bar{x}_2^2} \sigma_{x_1 x_2}^2 \quad (16)$$

where  $\sigma_{x_1}^2 = E(\delta \hat{x}_1)^2$ ,  $\sigma_{x_2}^2 = E(\delta \hat{x}_2)^2$ , and  $\sigma_{x_1 x_2}^2 = E(\delta \hat{x}_1 \delta \hat{x}_2)$

The covariances  $\sigma_{x_1}^2$ ,  $\sigma_{x_2}^2$ , and  $\sigma_{x_1 x_2}^2$  can be found from Eq. (15).

The value of  $\sigma_{sg}$  is a measure of the estimation of the gradient. In general, there is a 68% probability that the actual gradient lies between the values of  $S_g + \sigma_{sg}$  and  $S_g - \sigma_{sg}$  and a 95% probability that the actual gradient lies between the values of  $S_g + 2 \sigma_{sg}$  and  $S_g - 2 \sigma_{sg}$ .

#### Minimum Variance Estimate

A generalized form of Eq. (7) is:

$$v = A\bar{x} \quad (17)$$

where  $v$  is the noise due to measurement of  $h$  and  $A$  in Eq. (5). If the expected values of Eq. (17) are

$$E(h) = \bar{h}, \quad E(A) = \bar{A} \quad (18)$$

$$\text{then } E(v) = \bar{v} = \bar{h} - \bar{A}\bar{x} = 0 \quad (19)$$

by virtue of Eq. (12c). Subtracting Eq. (19) from Eq. (17), with the aid of the definitions of Eq. (12b), one obtains:

$$v \approx \delta h - \delta A \bar{x} \quad (20)$$

Thus the covariance of  $v$  becomes

$$\begin{aligned} R = E[vv^T] &= E[(\delta h - \delta A \bar{x})(\delta h - \delta A \bar{x})^T] \\ &= E[\delta h \delta h^T] - E[\delta A \bar{x} \delta h^T] - E[\delta h (\delta A \bar{x})^T] + E[\delta A \bar{x} (\delta A \bar{x})^T] \quad (21) \end{aligned}$$

which is the same as those terms inside the bracket in Eq. (17).

The cost function  $J$  can be expressed as

$$\begin{aligned} J &= \mathbf{v}^T \mathbf{R}^{-1} \mathbf{v} = (\mathbf{h} - \mathbf{A}\bar{\mathbf{x}})^T \mathbf{R}^{-1} (\mathbf{h} - \mathbf{A}\bar{\mathbf{x}}) \\ &= \mathbf{h}^T \mathbf{R}^{-1} \mathbf{h} - \bar{\mathbf{x}}^T \mathbf{A}^T \mathbf{R}^{-1} \mathbf{h} - \mathbf{h}^T \mathbf{R}^{-1} \mathbf{A} \bar{\mathbf{x}} + \bar{\mathbf{x}}^T \mathbf{A}^T \mathbf{R}^{-1} \mathbf{A} \bar{\mathbf{x}} \quad (22) \end{aligned}$$

The minimum variance estimate of  $\bar{\mathbf{x}}$  can be obtained by taking the minimum of  $J$  with respect to  $\mathbf{x}$ .

$$\text{Min}_{\bar{\mathbf{x}}} J = \frac{\partial J}{\partial \mathbf{x}} = -2\mathbf{A}^T \mathbf{R}^{-1} \mathbf{h} + 2\mathbf{A}^T \mathbf{R}^{-1} \mathbf{A} \bar{\mathbf{x}} = 0 \quad (23)$$

Thus the minimum variance estimate  $\bar{\mathbf{x}}$  becomes

$$\bar{\mathbf{x}} = (\mathbf{A}^T \mathbf{R}^{-1} \mathbf{A})^{-1} \mathbf{A}^T \mathbf{R}^{-1} \mathbf{h} \quad (24)$$

where  $\mathbf{R}$  can be obtained from Eq. (21).

The minimum variance estimate given by Eq. (24) is a weighted least square estimate. It will provide a better estimate of the gradient than the standard least square estimate of Eq. (8) because it gives correct weight to the individual measurement points.

However, the numerical results in the example computed from Eq. (24) is very close to the results given by Eq. (17) because the weighting factor in the covariance matrix  $\mathbf{R}$  is nearly proportional to an identity matrix. That is to say, the weighting factors in the diagonal terms of  $\mathbf{R}$  are equal. This is equivalent to an unweighted least square estimate.

### Numerical Results

It is assumed the rover will use a split beam where  $\Delta\beta$  is the difference in the elevation angle between the two beams and  $\Delta\theta$  is the difference in azimuth angle between any two laser pulses as shown in Fig. 58.

The values of  $\beta$  and  $\theta$  for each data point, along with the magnitude of the cross-path and in-path slopes of the terrain, determine the data point spacing and the distance of the data points from the vehicle. After a number of data points are measured, they are transformed to the non-rotating reference system by Eqs. (1a to 2c). Then a least square estimate of the slopes is obtained by Eq. (8). This least square estimate depends directly upon the values of  $h$ ,  $a$ , and  $b$  for each measurement point. Utilizing the value of the vector  $\hat{\mathbf{x}}$  found in Eq. (8), the values of  $\phi$ ,  $\xi$ ,  $R$ ,  $\beta$ , and  $\theta$  for each data point, and the standard deviations of these quantities, the magnitude of the gradient and its variance can be calculated.

The standard deviation in gradient,  $\sigma_{\text{sg}}$ , can be determined by utilizing Eqs. (11), (14), (15), and (16). The variance of the gradient depends upon the cross-path and in-path slopes of the terrain, the roll

and pitch angle of the vehicle, the data point spacing, the distance of the data points from the vehicle, and the accuracy of the measuring devices.

If the rangefinder scan rate is on the order of milliseconds, which is perfectly feasible with electronic scanning, then each set of 4 adjacent data points is measured practically instantaneously since the rover motion is on the order of seconds and all 4 points will retain the same relative position to each other when they are transformed from the vehicle coordinate system to the fixed system. Consequently, the rover can model the planes in the vehicle coordinate system, and then transform the planes to the non-rotating frame. Since the maximum positive or negative slope that the vehicle can navigate is  $\pm 25^\circ$ , relative slopes might be as high as  $\pm 50^\circ$  and still be navigable, Fig. 59.

Also due to rapid scan, the error introduced by setting  $\sigma_\gamma = \sigma_\xi = 1^\circ$  (which is a reasonable estimate of these quantities due to the constant rock and roll of the vehicle as it traverses the surface) will be consistently between  $1^\circ$  and  $2^\circ$  because it only involves the error in transforming the already modeled plane from the vehicle system of reference to the fixed system. Consequently, the effects of  $\sigma_\gamma$  and  $\sigma_\xi$  are not considered in the analysis.

If a flat terrain is assumed,  $\sigma_\theta = \sigma_\beta = 1'$  and  $\sigma_z = 5$  cm, and  $\Delta\theta$  and  $\Delta\beta$  (and consequently the data point spacing) are varied for each set of 4 points, the graphs shown in Fig. 60 are obtained. Each solid line represents constant values for  $\Delta\theta$  and  $\Delta\beta$ .  $\Delta b$  and  $\Delta z$  are the data point spacings along the in-path and cross path directions respectively. For any constant value of  $\Delta\beta$  and  $\Delta\theta$ , the data point spacing decreases very rapidly as the scan approaches the vehicle and consequently the error in gradient rises very rapidly.

In choosing an 'optimum' data point space it must be noted that an increase in the spacing decreases the error in gradient. However, this renders the data less meaningful, as more terrain has been overlooked. At the 30 meter range, a general picture of the terrain with a spacing of 2-3 meters is sufficient. At close range, (4-7 meters) the points should be at least as close as 0.66 meters because this is the width of the widest navigable crevice. In Fig. 60, the dotted line represents  $\sigma_{sg}$  vs. distance from the vehicle for such a scheme, where the data point spacing varies from about 0.5 meters at a distance of 4 meters from the vehicle to about 3 meters at a distance of 30 meters from the vehicle.

Each of the plots in Figs. 61 and 62 utilize the same optimum scheme as the dotted line in Fig. 60. Once again flat terrain is assumed for all the data points. In Fig. 61,  $\sigma_z$  is kept at 5 cm and  $\sigma_\beta$  and  $\sigma_\theta$  are set to 0, .017 (1'), and .1 (6'). The error in gradient is markedly reduced by decreasing  $\sigma_\beta$  and  $\sigma_\theta$  from 6' to 1' but any further increases in accuracy will result in bulkier and heavier equipment which is not very beneficial. By comparing the plots for  $\sigma_\beta = \sigma_\theta = 1'$  and  $\sigma_\beta = \sigma_\theta = 0^\circ$  it is seen that a standard deviation in  $\sigma_\beta$  and  $\sigma_\theta$  of 1' has very little effect on the error in gradient.

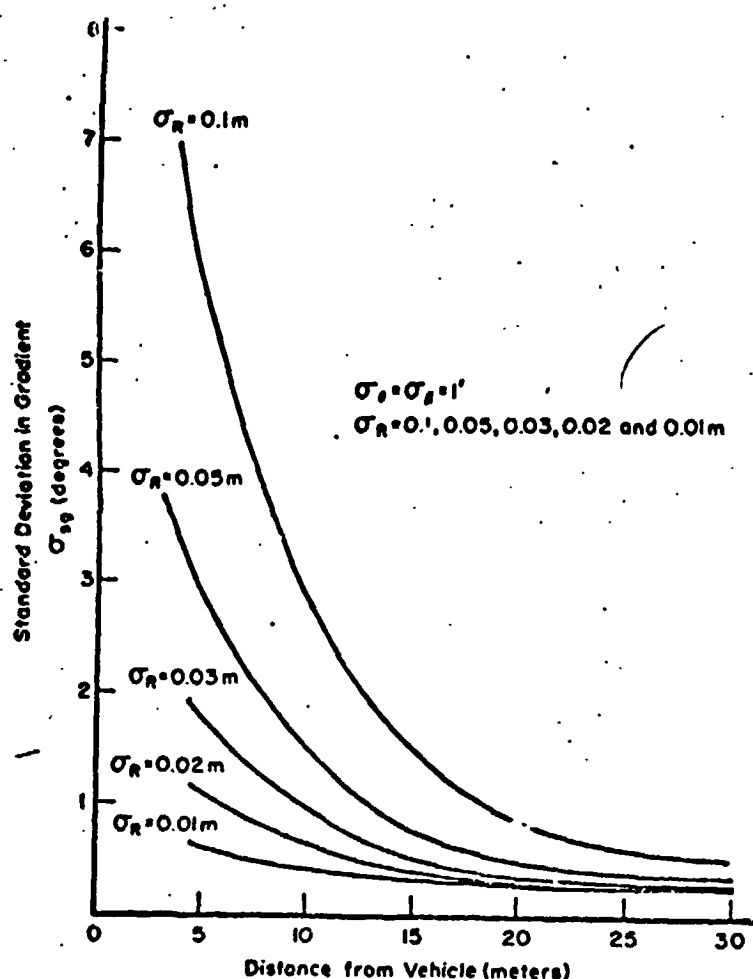


Figure 62. Standard Deviation in Gradient vs Distance from Vehicle for "Optimum" Data Point Spacing on Flat Surface

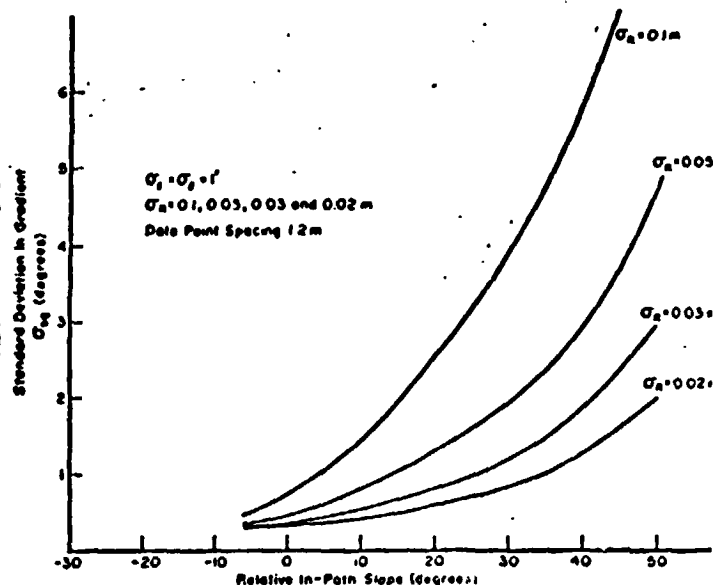


Figure 64. Standard Deviation in Gradient vs Relative In-Path Slope at 20m from the vehicle

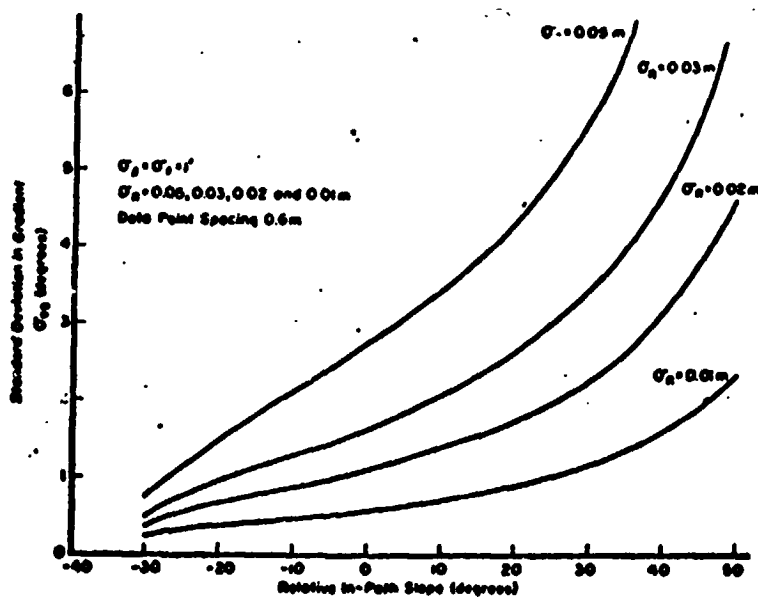


Figure 62. Standard Deviation in Gradient vs Relative In-path Slope at 4m from the Vehicle

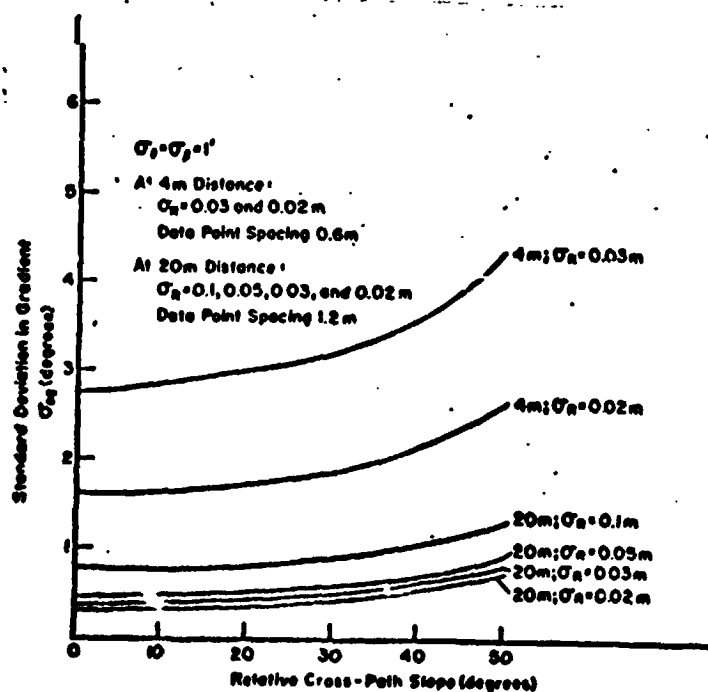


Figure 65. Standard Deviation in Gradient vs Relative Cross-Path Slope at 20m from the Vehicle

In Fig. 62,  $\sigma_R$  is varied from 1 cm to 10 cm while  $\sigma_\beta$  and  $\sigma_\theta$  are kept constant at 1' (.017). The error in gradient increases rapidly at close range for each value of  $\sigma_R$ .

Fig. 63 plots  $\sigma_{sg}$  vs relative in-path slopes of from  $-30^\circ$  to  $+50^\circ$  at 4 meters from the vehicle. In all cases, the cross-path slope of the measured plane is  $0^\circ$  and there is at least 1 data point with a height  $h$  of 0 meters in each group of 4 points. The graph only extends to  $-30^\circ$  because the rangefinder beam cannot 'see' over a negative in-path slope greater than this value at 4 meters distance. With  $\sigma_\beta = \sigma_\theta = 1'$ ,  $\sigma_R$  is varied from 1 cm to 5 cm. A data point spacing of .6 meters is assumed. Fig. 64 plots  $\sigma_{sg}$  vs relative in-path slopes of from  $-6^\circ$  to  $+50^\circ$  at 20 meters from the vehicle. All the other conditions are the same as in Fig. 63 except that the data point spacing is 1.2 meters instead of 0.6 meters. Finally, Fig. 65 plots graphs of  $\sigma_{sg}$  vs relative cross-path slopes of from  $0^\circ$  to  $50^\circ$  for distances of 4 meters and 20 meters from the vehicle. In this case, the in-path slopes are set to  $0^\circ$ . Once again  $\sigma_\beta = \sigma_\theta = 1'$  and  $\sigma_R$  is varied from 2 to 10 cm. The data point spacing at 20 meters from the vehicle is 1.2 meters and the spacing at 4 meters from the vehicle is 0.6 meters.

From Figs. 63 to 65, it can be noted that the higher the relative in-path or cross-path slope, and the closer the data points are to the vehicle, the larger the error in gradient. All other factors considered equal, the error in gradient is larger for a given in-path slope than for a cross path slope of the same magnitude. It is obvious in Fig. 63 that  $\sigma_R$  should be as close to 1 cm as possible in order that  $\sigma_{sg}$  will be within  $2^\circ$  at 4 meters distance and high values of relative in-path slopes.

This analysis, which is summarized in Ref. 17, leads to 3 very important conclusions. First, the very large error due to the motion of the vehicle can be eliminated by utilizing a rapid scan rangefinder. Secondly, if  $\sigma_\beta$  and  $\sigma_\theta$  are reduced below 1 arcminute, no significant reduction in error is obtained. Finally, most of the error in gradient estimation is due to  $\sigma_R$ . The variance of the gradient should be as low as possible, but if an upper bound of  $2^\circ$  is set, then  $\sigma_R$  must be as low as 1 cm.

Due to surface irregularity, data points will not fall at regular intervals as they would on a flat plane, but will be scattered about unevenly. A procedure must be developed to determine how each group of 4 points is to be chosen prior to the modeling procedure. Another question that should be investigated is whether the modeling procedures for terrain at the 20 - 30 meter range should be modified so that the rover can model hills and craters as well as flat planes. More generally the problem is one of determining a complete picture of the terrain from an array of different sized and shaped planes, each of whose gradients have a different magnitude and direction.

**Task C.2.b. Gradient Estimates from Stereo Measurements - W. J. Pfeifer**  
**Faculty Advisor: Prof. C. N. Shen**

The method of calculating a stochastic estimate of the gradient of the terrain in the path of the Martian vehicle, Task C.2.a. has been applied to two stereo measurement systems. One system, called stereo angles, uses three angular measurements in elevation and azimuth to



locate a terrain point. Another system, called stereo range uses three range measurements. These two systems are compared with the non-stereo system, Task C.2.a. and Ref. 16, and with the limits of present laser rangefinder technology.

The standard deviation in the four point estimate of the gradient depends on the distance of the four points from the vehicle, the positions of the terrain points in relation to each other, the gradient of the terrain and the measurement errors. Vehicle motion effect on the standard deviation in gradient has been reduced to an additive factor as a result of the assumption of a rapid-scan laser.

The effects of the above factors on the standard deviation gradient are shown in Figures 68-71 for a stereo angles measurement system which uses 3 angular measurements and in Figures 72-74 for a stereo range system which uses 3 range measurements. A desired maximum allowable standard deviation in gradient has been set at  $2^\circ$ . These results are summarized and compared with the non-stereo system which uses one range and two angular measurements, Ref. 16 and 17, in Table VIII.

Within the limits of present technology, the non-stereo system appears much more practical than the stereo range system. Laser rangefinder technology has not yet reduced range standard deviation  $\sigma_R$  below 0.01 meter. In fact, a more reasonable expectation for range standard deviation may be from 0.02 to 0.05 m. The results for stereo range have been presented in anticipation of improvements in rangefinder accuracy.

At longer range the non-stereo system is better than the stereo angles system. At close range, stereo angle may be comparable to non-stereo if the standard deviation in the transmitter-receiver separation  $\sigma_L$  can be reduced to 0.001m. This conclusion is also based on the assumption that angle standard deviation will be about one minute of arc.

#### Mathematical Analysis

The basic method of estimating gradient from four terrain point measurements is outlined in Ref. 16. For this application, the following modifications were made.

##### a) Stereo Angles

The elevation angles  $\alpha$  and  $\beta$ , and the azimuthal angle  $\theta$  are measured with respect to the coordinate system  $h''$ ,  $a''$ ,  $b''$  fixed to the vehicle as shown in Figure 66. A laser is located at point T which is 3 meters in height. The elevation angle  $\beta$  of the transmitted light beam is measured at T from the horizon to the terrain point U. The elevation angle  $\alpha$  of the received beam is measured at a point L meters from the top of the mast. Some type of scanning detector is assumed in the measurement of the angle  $\alpha$ . The angle  $\theta$  is the azimuthal angle of the transmitted beam.

From the geometry, with a sensor mast height of 3 meters, the terrain point coordinates  $h''$ ,  $a''$ ,  $b''$  are found in terms of  $\alpha$ ,  $\beta$ ,  $\theta$ , and L.

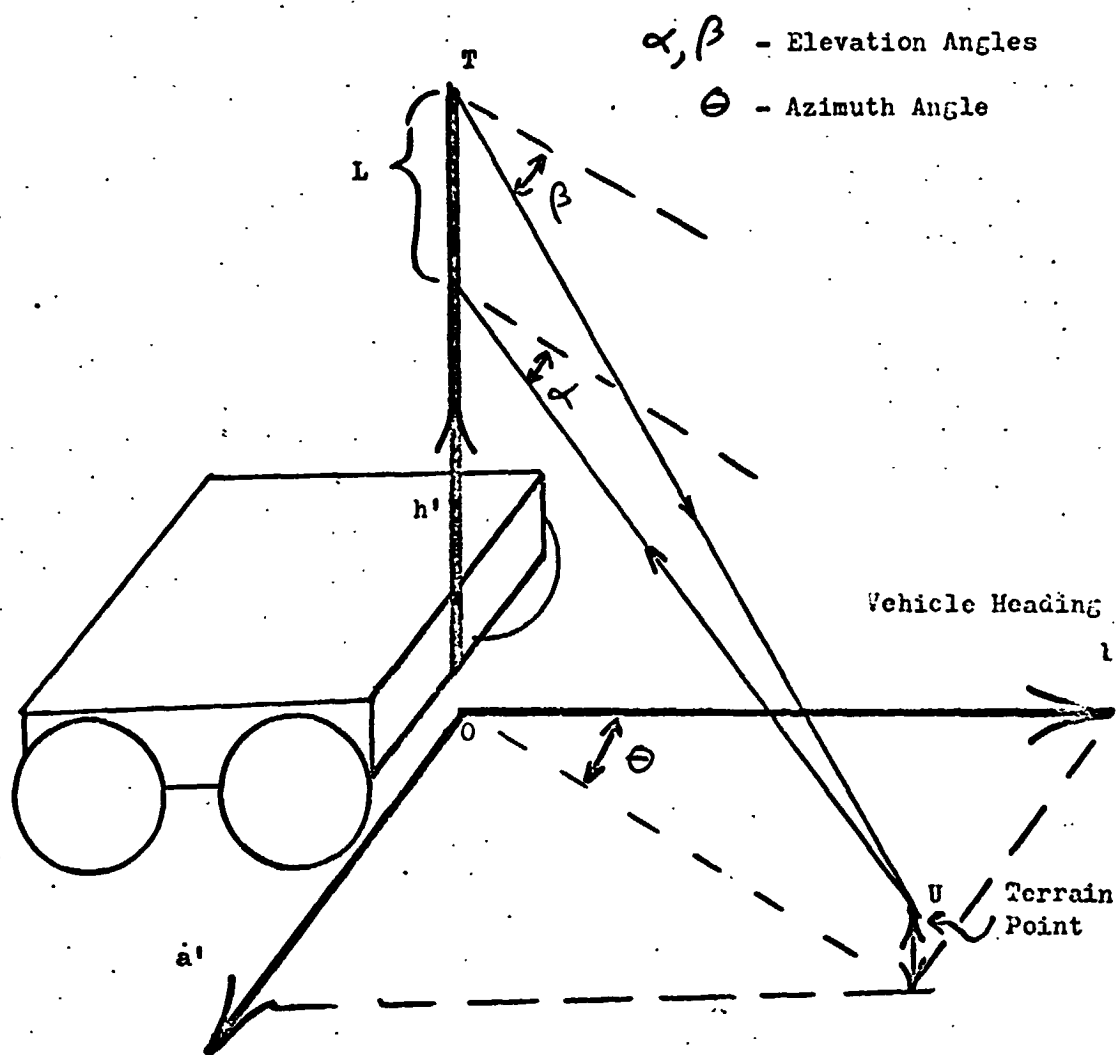


Figure 66. Stereo Angles System Coordinates

$$h'' = 3 - \frac{L \tan \beta}{(\tan \beta - \tan \alpha)} \quad (1a)$$

$$a'' = \frac{L \sin \theta}{(\tan \beta - \tan \alpha)} \quad (1b)$$

$$b'' = \frac{L \cos \theta}{(\tan \beta - \tan \alpha)} \quad (1c)$$

The coordinates  $h''$ ,  $a''$  and  $b''$  are fixed to the vehicle and may be transformed to the  $h$ ,  $a$ ,  $b$  reference system as shown in Eq. (2), Task C.2.a.

b) Stereo Range

The quantities  $M$ ,  $N$  and  $K$  are measured with respect to the coordinate system  $h''$ ,  $a''$ ,  $b''$  which is fixed to the vehicle as in Fig. 67. The measurement  $M$  is twice the range to the terrain point  $U$  from the transmitter and receiver at  $T$  on top of the sensor mast.

$$M = 2 R \quad (2a)$$

The measurement of  $N$  is the sum of the ranges from the transmitter to the terrain point  $U$  and from this point back to a receiver at a vertical distance  $L$  meters from the transmitter.

$$N = R + P \quad (2b)$$

The measurement  $K$  is the sum of the ranges from the transmitter at  $T$  to the terrain point  $U$  and from this point back to another receiver at a horizontal distance  $J$  meters from the transmitter.

$$K = R + Q \quad (2c)$$

From the geometry the coordinates of the terrain points are found in terms of  $M$ ,  $N$ ,  $K$ ,  $L$  and  $J$ .

$$h'' = 3 - \frac{L}{2} + \frac{N(N-M)}{2L} \quad (3a)$$

$$a'' = \frac{K(N-K)}{2J} + \frac{J}{2} \quad (3b)$$

$$b'' = \left[ \frac{M^2}{4} - \frac{L^2}{4} - \frac{J^2}{4} + \frac{N(N-M)}{2} - \frac{K(N-K)}{2} \right]^{\frac{1}{2}} - \left[ \frac{K^2(N-K)^2}{4J^2} - \frac{N^2(N-M)^2}{4L^2} \right]^{\frac{1}{2}} \quad (3c)$$

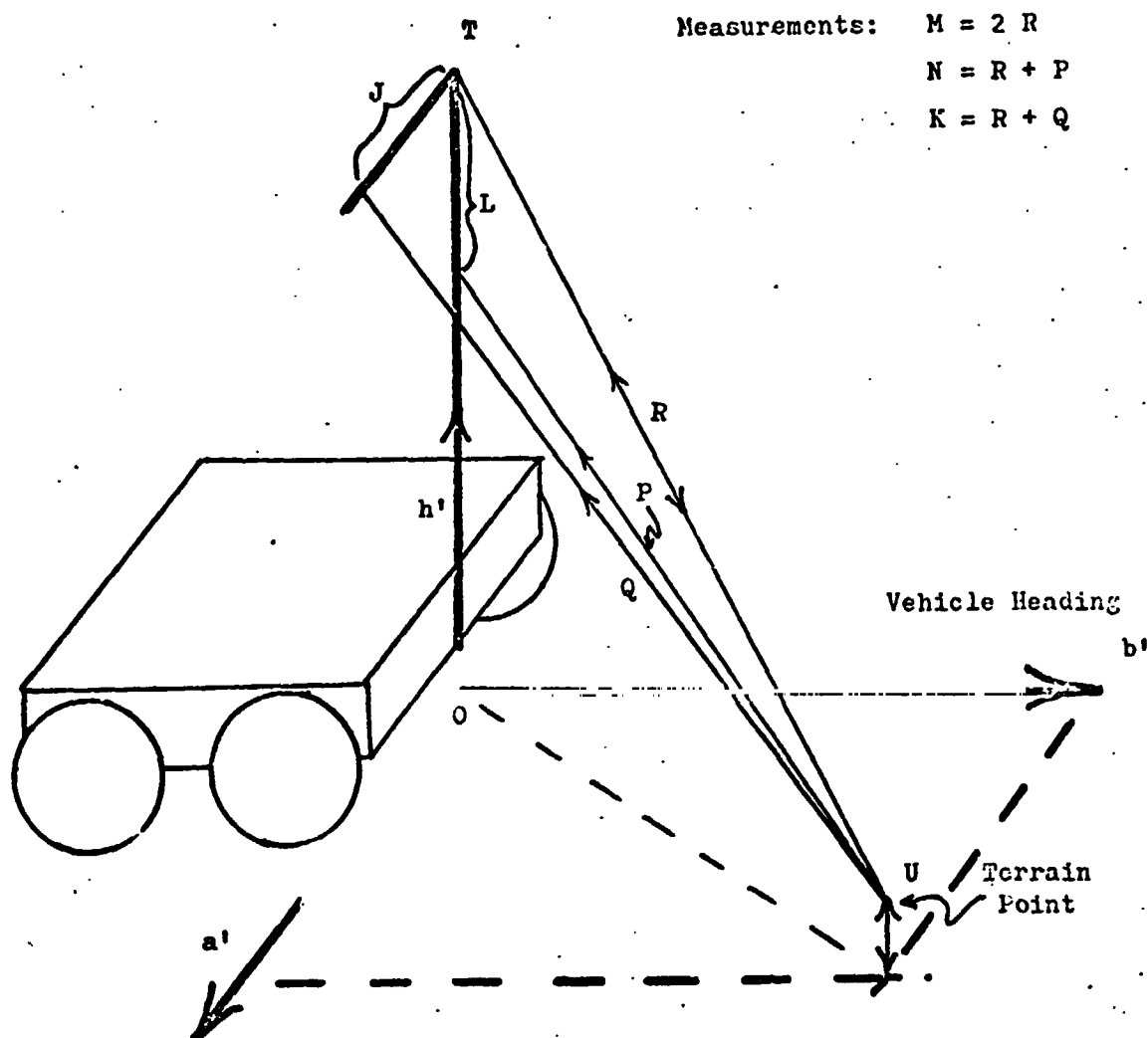


**Figure 67. Stereo Range System Coordinates**

### Analytic Solutions for Estimation

Let the symbol  $\delta$  denote a perturbation. If  $\delta\phi$ ,  $\delta\xi$ ,  $\delta\alpha$ ,  $\delta\beta$ ,  $\delta\theta$  and  $\delta L$  are not correlated the following relation is obtained.

#### a) Stereo Angles System

$$Y_a = D \begin{bmatrix} E(\delta\phi)^2 & 0 \\ 0 & E(\delta\xi)^2 \end{bmatrix} D^T + C B G_a \begin{bmatrix} E(\delta\alpha)^2 & 0 & 0 & 0 \\ 0 & E(\delta\beta)^2 & 0 & 0 \\ 0 & 0 & E(\delta\theta)^2 & 0 \\ 0 & 0 & 0 & E(\delta L)^2 \end{bmatrix} G_a^T B^T C^T \quad (4)$$

The standard deviations of  $h$ ,  $a$  and  $b$  can be computed in terms of those of  $\phi$ ,  $\xi$ ,  $\alpha$ ,  $\beta$ ,  $\theta$  and  $L$  for each point. These are known quantities which depend on the accuracy of the measuring devices.

#### b) Stereo Range System

If  $\delta\phi$ ,  $\delta\xi$ ,  $\delta M$ ,  $\delta N$ ,  $\delta K$ ,  $\delta L$  and  $\delta J$  are uncorrelated, the following is obtained by the same method used to derive equation (4).

$$Y_r = D \begin{bmatrix} E(\delta\phi)^2 & 0 \\ 0 & E(\delta\xi)^2 \end{bmatrix} D^T + C B G_r \begin{bmatrix} E(\delta M)^2 & 0 & 0 & 0 & 0 \\ 0 & E(\delta N)^2 & 0 & 0 & 0 \\ 0 & 0 & E(\delta K)^2 & 0 & 0 \\ 0 & 0 & 0 & E(\delta L)^2 & 0 \\ 0 & 0 & 0 & 0 & E(\delta J)^2 \end{bmatrix} G_r^T B^T C^T \quad (5)$$

The standard deviations of  $h$ ,  $a$ , and  $b$  can be computed in terms of those of  $\phi$ ,  $\xi$ ,  $M$ ,  $N$ ,  $K$ ,  $L$ , and  $J$  for each point. Equations (4) and (5) include the matrix  $G$  which involves all the measured quantities. Therefore, the standard deviations in  $h$ ,  $a$ , and  $b$  depend on the locations of the data points in relation to the vehicle as well as on the accuracies of these measurements.

The slopes and gradient are calculated by the Eqs. (12) - (16) presented under Task C.2.a.

### Numerical Results for Stereo Measurement Systems

#### a) Stereo Angles Systems

It is assumed that the scanning mechanism can provide any desired data point spacing at distances from 3 to 30 meters from the vehicle. Since the data point spacing also

depends on terrain irregularities, a flat terrain is assumed at the start.

The distance  $L$  in Fig. 66 is assumed to be 1.0 meter. This is the most reasonable value for a 3 meter sensor mast height. A larger value of  $L$  can give smaller errors in measurement. But, as  $L$  is increased beyond one meter, the vehicle's ability to observe negative slopes is decreased. Also, if the receiver is lower on the mast there is more chance that the reflected laser beam will be blocked by other vehicle equipment. A rapid scan laser is assumed.

Figure 68 shows a plot of standard deviation in gradient  $\sigma_{sg}$  vs distance,  $b^*$ , from the vehicle for flat terrain with  $0^\circ$  relative slope with  $\sigma_L = 0.01$  m. The dotted lines are for  $\sigma_L = 0.005$  m. Clearly  $\sigma_L$  has an important effect on  $\sigma_{sg}$  for the stereo angles system, especially at close range where decreasing  $\sigma_L$  from 0.01 m to 0.005 m reduces the value of  $\sigma_{sg}$  by fifty percent. As expected, larger data point spacing gives smaller values for the standard deviation in gradient. At close range, data point spacing of 0.66 m or less is required because 0.66 meters is the width of the widest navigable crevice. If  $\sigma_{sg}$  is desired to be less than  $2^\circ$  it appears that  $\sigma_L$  must be about 0.005 meter or less.

The standard deviation in the distance  $L$  ( $\sigma_L$ ) may result from changes in the sensor mast, expansion or contraction due to temperature changes, or from uncertainties caused by the laser equipment.

Figure 69 shows the plot of  $\sigma_{sg}$  versus relative in-path slope from  $-27^\circ$  to  $+50^\circ$  at a distance of 4 meters from the vehicle. The vehicle cannot measure negative in-path slopes of more than  $-27^\circ$  because the terrain obstructs the line of sight. The cross-path slope,  $x_1$ , is set to  $0^\circ$  and the in-path slope,  $x_2$ , is varied from  $-27^\circ$  to  $+50^\circ$ . The standard deviations  $\sigma_L$  and  $\sigma_A$  are varied in Eq. (4) and the results used in Eqs. (15) and (16), Task C.2.a. to calculate the quantity  $\sigma_{sg}$ . In Figure 69 the data point spacing is 0.6 meter as required at the 4 meter distance. The stereo angles system estimate of the standard deviation in gradient  $\sigma_{sg}$  is quite sensitive to the relative in-path slope.

Figure 70 shows the standard deviation in gradient  $\sigma_{sg}$  vs. relative in-path slope from  $-6^\circ$  to  $+50^\circ$  at a distance of 20 meters from the vehicle. The terrain obstructs the view of the in-path slopes for more than  $-6^\circ$  relative slopes at 20 meters. For this graph the data point spacing is 1.2 meters. At 20 meters the standard deviation  $\sigma_{sg}$  increases drastically with increasing relative in-path slope. To obtain the quantity  $\sigma_{sg}$  less than  $3^\circ$  for all relative in-path slopes up to  $50^\circ$  the standard deviations  $\sigma_L$  should be less than 0.001 m and  $\sigma_A$  less than 6".

Figure 71 shows the standard deviation in gradient vs. relative cross-path slopes from  $0^\circ$  to  $+50^\circ$  for distances of 4 and 20 meters with data point spacings of 0.6 meters and 1.2

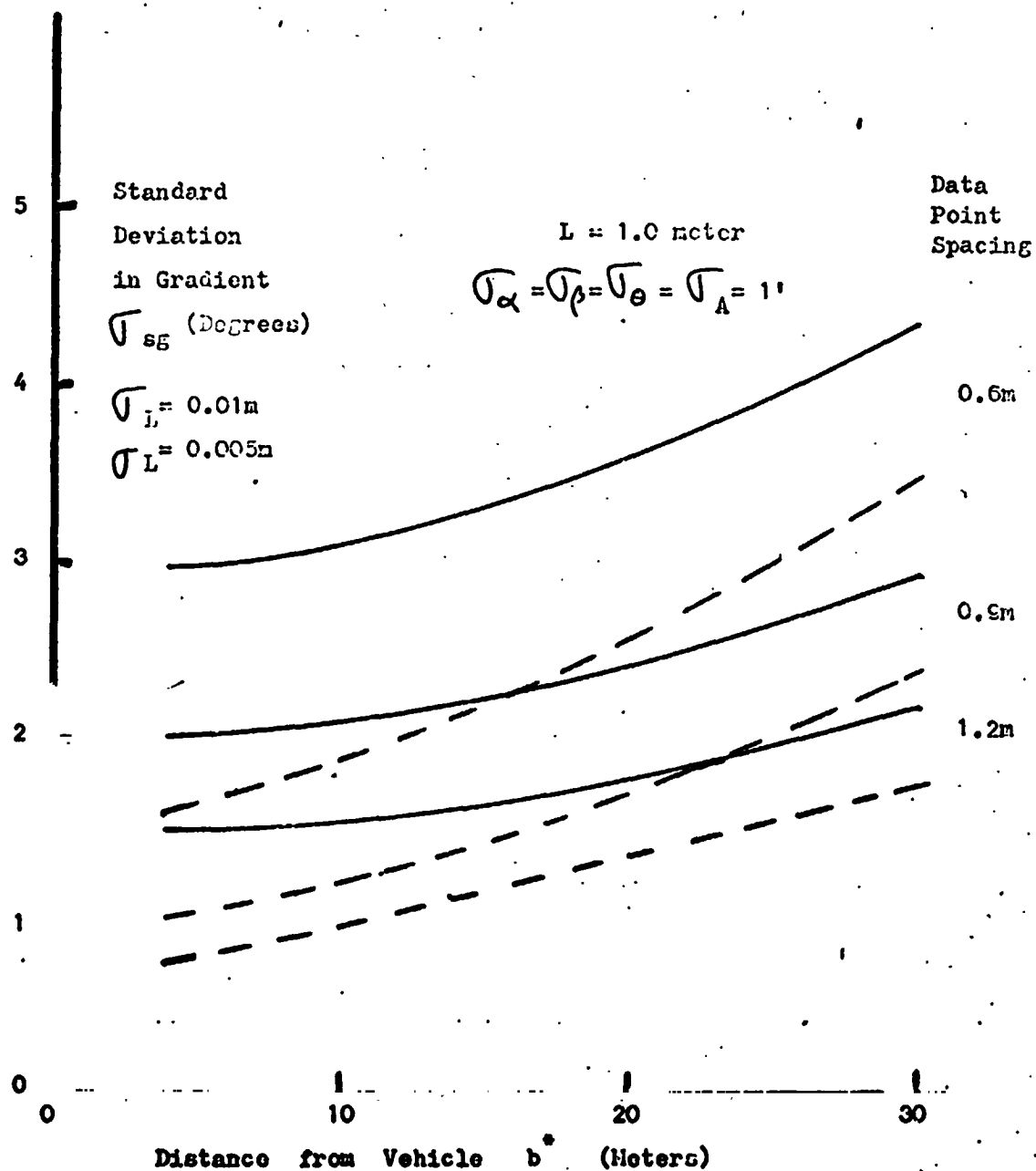


Figure 68. Stereo Angles System: Standard Deviation in Gradient Versus Distance from Vehicle on Flat Terrain with Relative Slope =  $0^\circ$

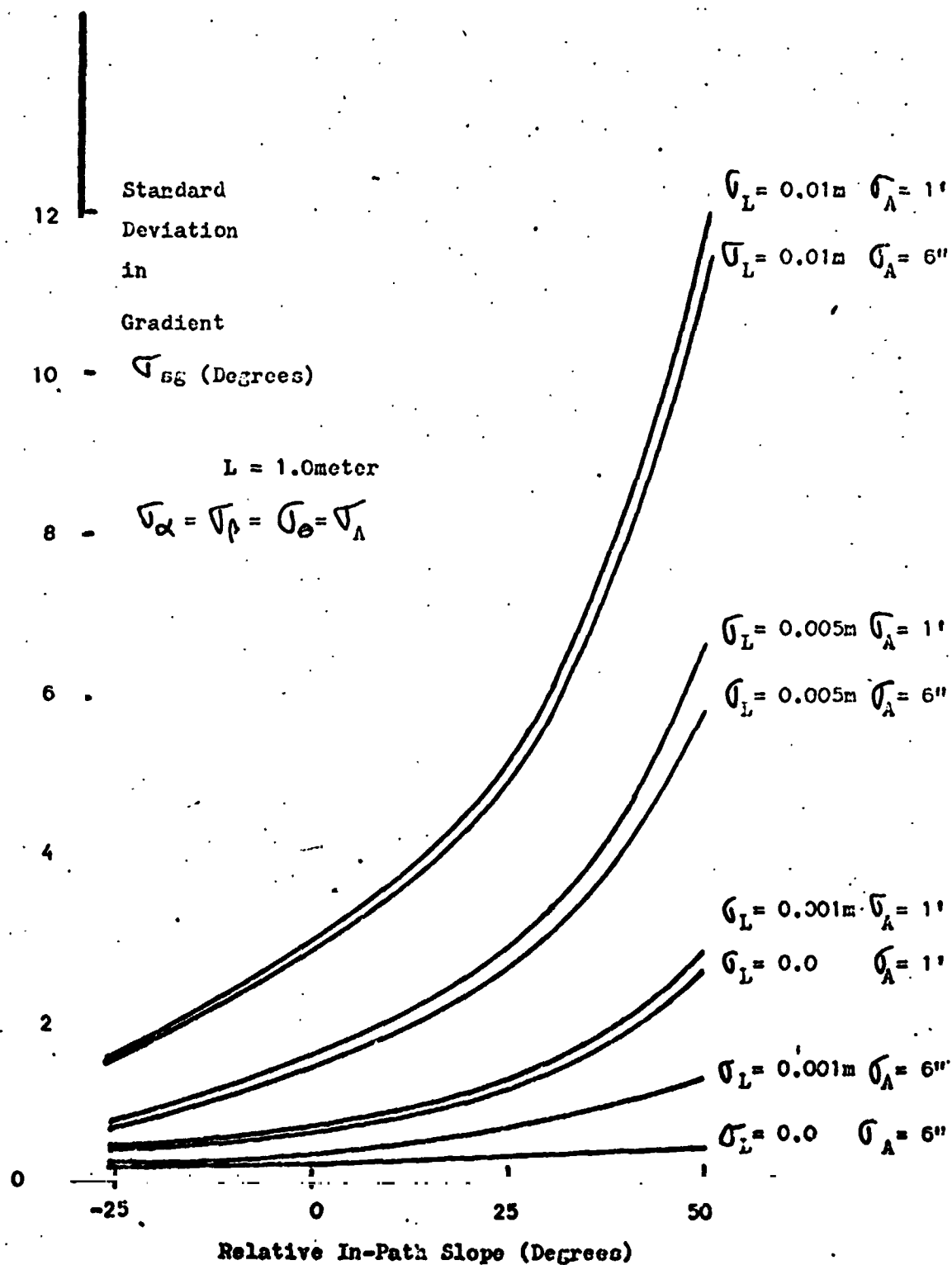


Figure 69. Stereo Angles System: Standard Deviation in Gradient Versus Relative In-Path Slopes for Terrain at 4m with Data Point Spacing=0.6m



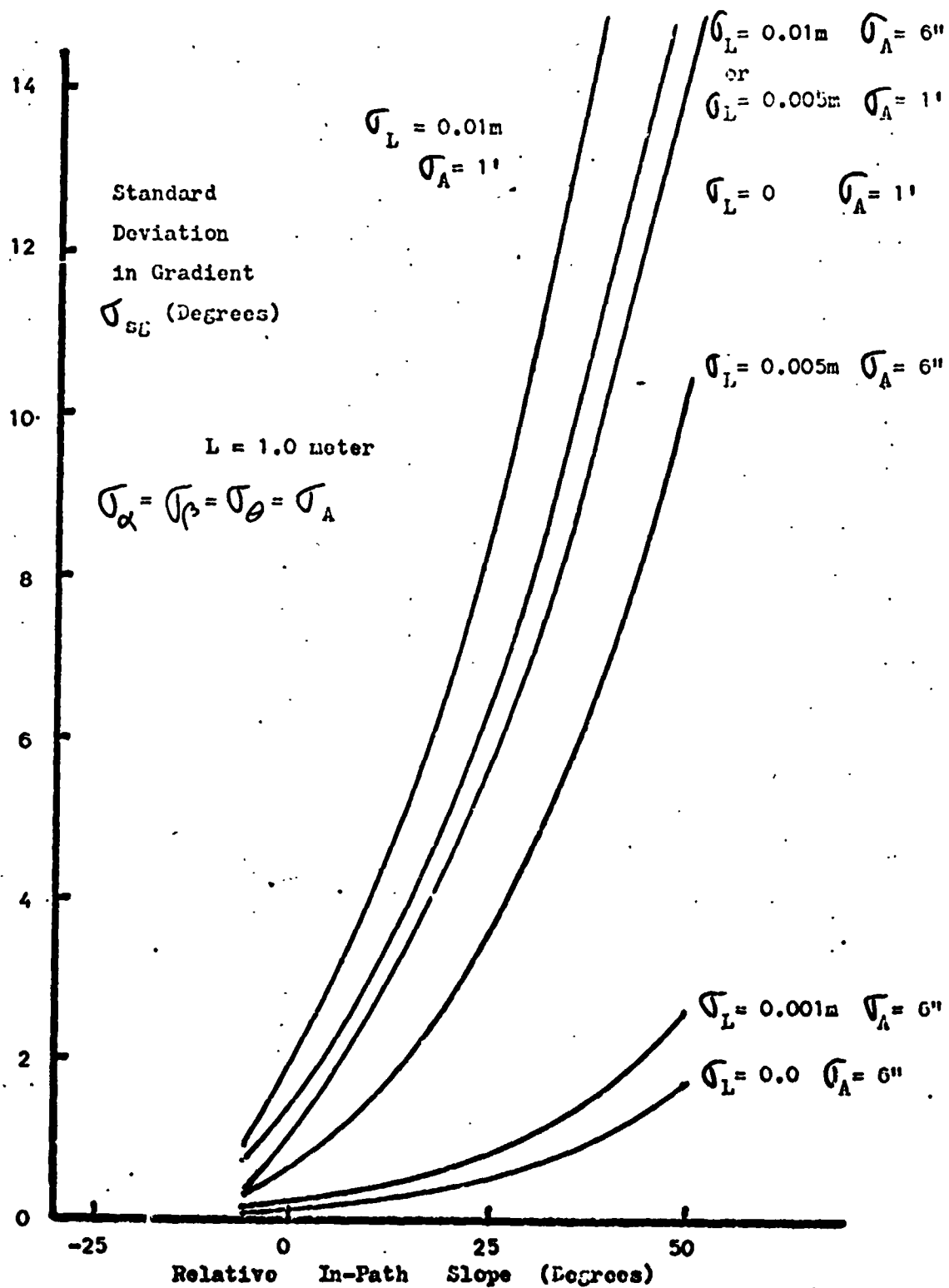


Figure 70. Stereo Angles System: Standard Deviation in Gradient Versus Relative In-Path Slope for Terrain at 20 Meters with Data Point spacing 1.2m

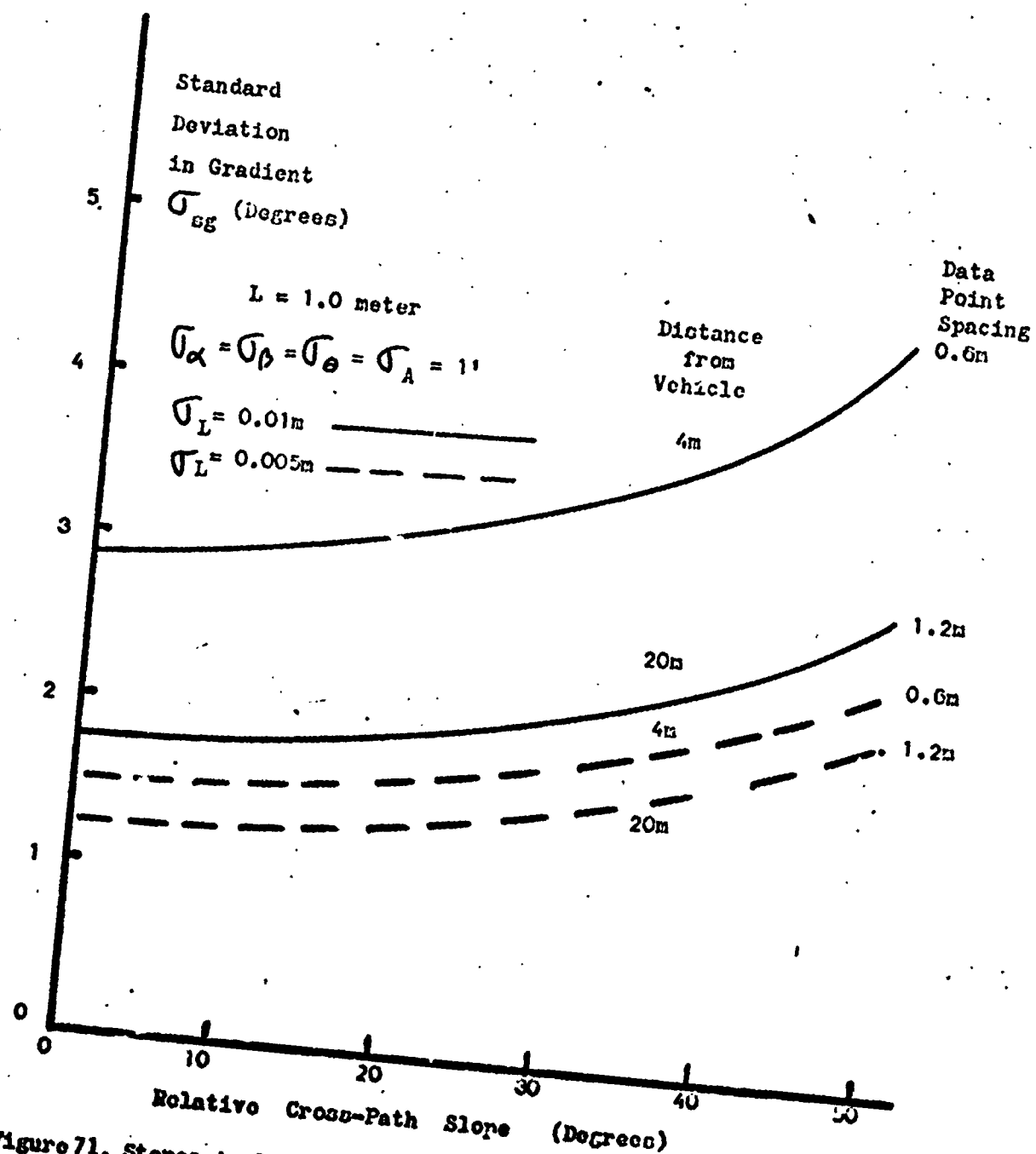


Figure 71. Stereo Angles System: Standard Deviation in Gradient Versus Relative Cross-Path Slope for Terrain at 4 and 20 Meters

meters respectively. If the standard deviations  $\sigma_A = 1'$  and  $\sigma_L = 0.005\text{m}$ , or less, the value of  $\sigma_{sg}$  is less than  $2.5^\circ$  at both distances.

b) Stereo Range System

As in the stereo angles system, it is assumed that the rapid scan transmitter at T, (Fig. 67), can provide the desired data point spacing for flat terrain. The separation distances L and J are both assumed to be equal to one meter. The one meter value is reasonable for the horizontal separation distance J because a larger J will require a more massive support.

It is assumed that the standard deviations in L and J are equal since the system configuration is somewhat symmetric in the horizontal and vertical directions. These uncertainties may result from changes in the support dimensions and from the laser transmitter and its 3 receivers.

The range standard deviations  $\sigma_M$ ,  $\sigma_N$ , and  $\sigma_K$  are all assumed equal to  $2\sigma_R$ . These standard deviations and the data point coordinates are employed to calculate the quantity  $\sigma_{sg}$  in Equation (5), Eqs. (15) and (16), Task C.2.a.

Figure 72 shows  $\sigma_{sg}$  vs. distance,  $b^*$ , from the vehicle for flat terrain with relative slopes  $= 0^\circ$  and  $\sigma_R = 0.001\text{m}$ . The solid lines show the quantity  $\sigma_{sg}$  when the value of  $\sigma_L = \sigma_J$  is  $0.01\text{m}$  and the dotted lines when  $\sigma_L = \sigma_J$  is  $0.005\text{m}$ . The standard deviations in gradient  $\sigma_{sg}$  for the stereo range system are not sensitive to the standard deviations in separation distances  $\sigma_L$  and  $\sigma_J$ .

Figure 73 is a plot of the standard deviation in gradient vs. relative in-path slope at a distance of 4 meters from the vehicle having data point spacing of  $0.6\text{m}$ . In this case  $\sigma_{sg}$  decreases as relative in-path slope increases to  $+50^\circ$ . From the figure it is concluded that to obtain the value of  $\sigma_{sg}$  to be less than  $2^\circ$  for most relative in-path slopes, the magnitude of  $\sigma_R$  must be  $0.001\text{m}$  or less and the magnitude of  $\sigma_L$  must be  $0.005\text{m}$  or less.

In Figure 74 the standard deviation in gradient is plotted against relative in-path slopes at a distance of 20 meters with data point spacing of  $1.2\text{m}$ . In this graph the value of the quantity  $\sigma_{sg}$  increases slightly as relative in-path slope increases to  $+50^\circ$ . To obtain a maximum standard deviation  $\sigma_{sg}$  of  $2^\circ$  when the value of  $\sigma_L$  is  $0.005\text{m}$ , the range standard deviation  $\sigma_R$  must be about  $0.005\text{m}$ .

The results which have been obtained are summarized in Table VIII. On the basis of these calculations and on the presented and projected state of the art relating to rangefinder devices, it is concluded that the non-stereo range angle method studied under Task C.2.a. is superior to both the stereo-range and stereo-angles systems.

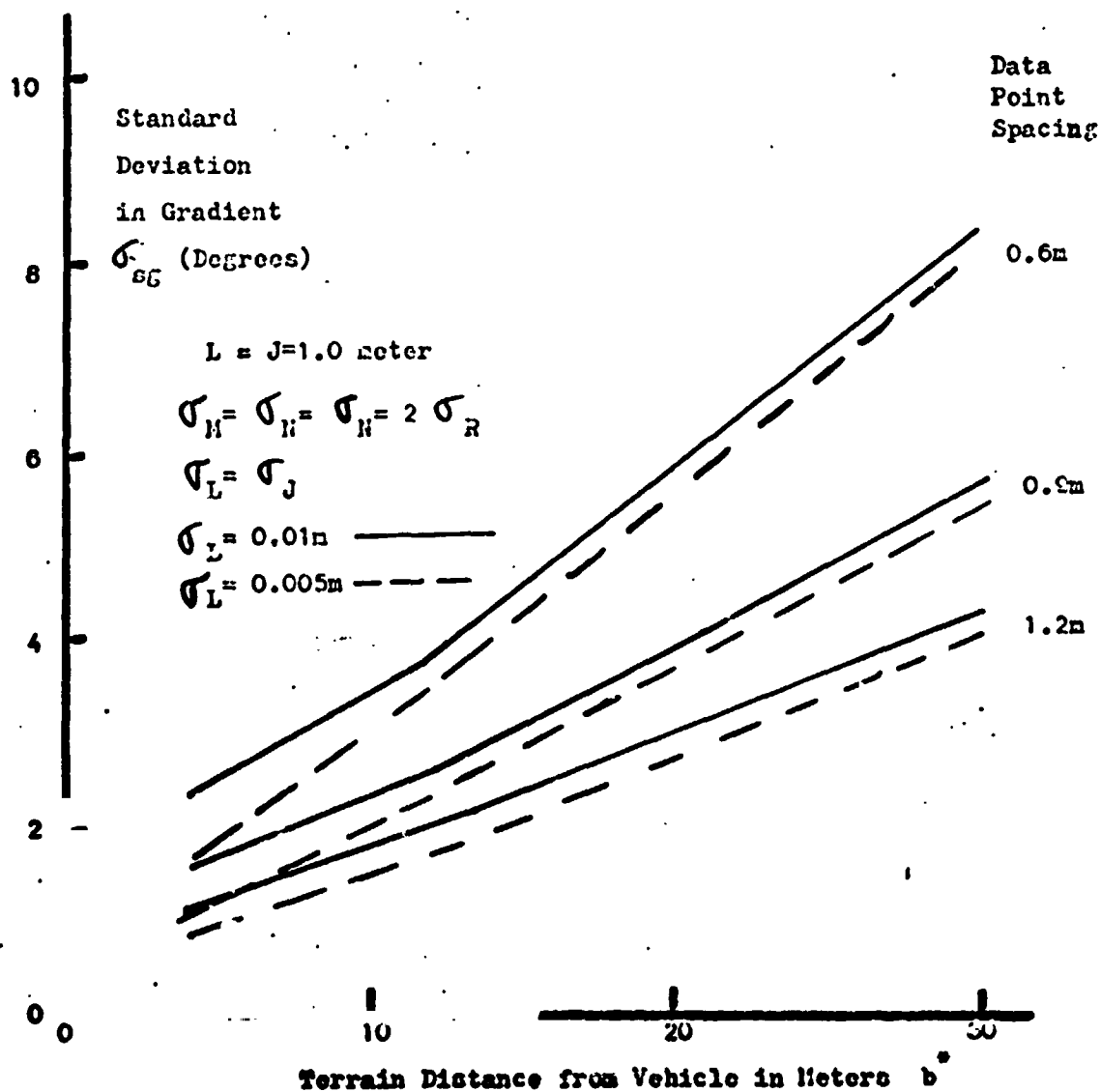


Figure 72. Stereo Range System: Standard Deviation in Gradient Versus Terrain Distance from Vehicle with Relative Slope = 0°

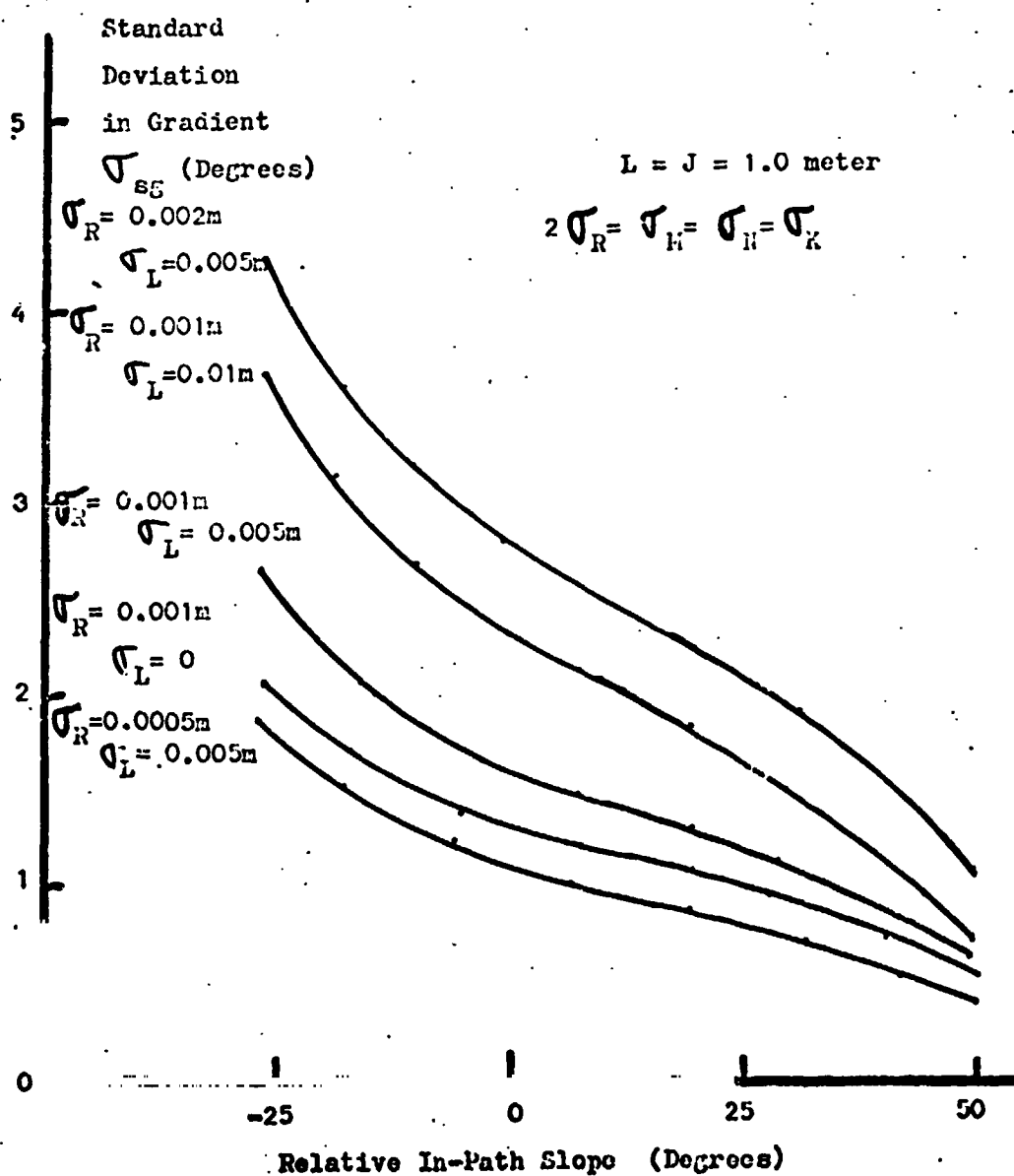


Figure 73. Stereo Range System: Standard Deviation in Gradient Versus  
Relative In-Path Slope for Terrain at 4m with Point Spacing = 0.6m

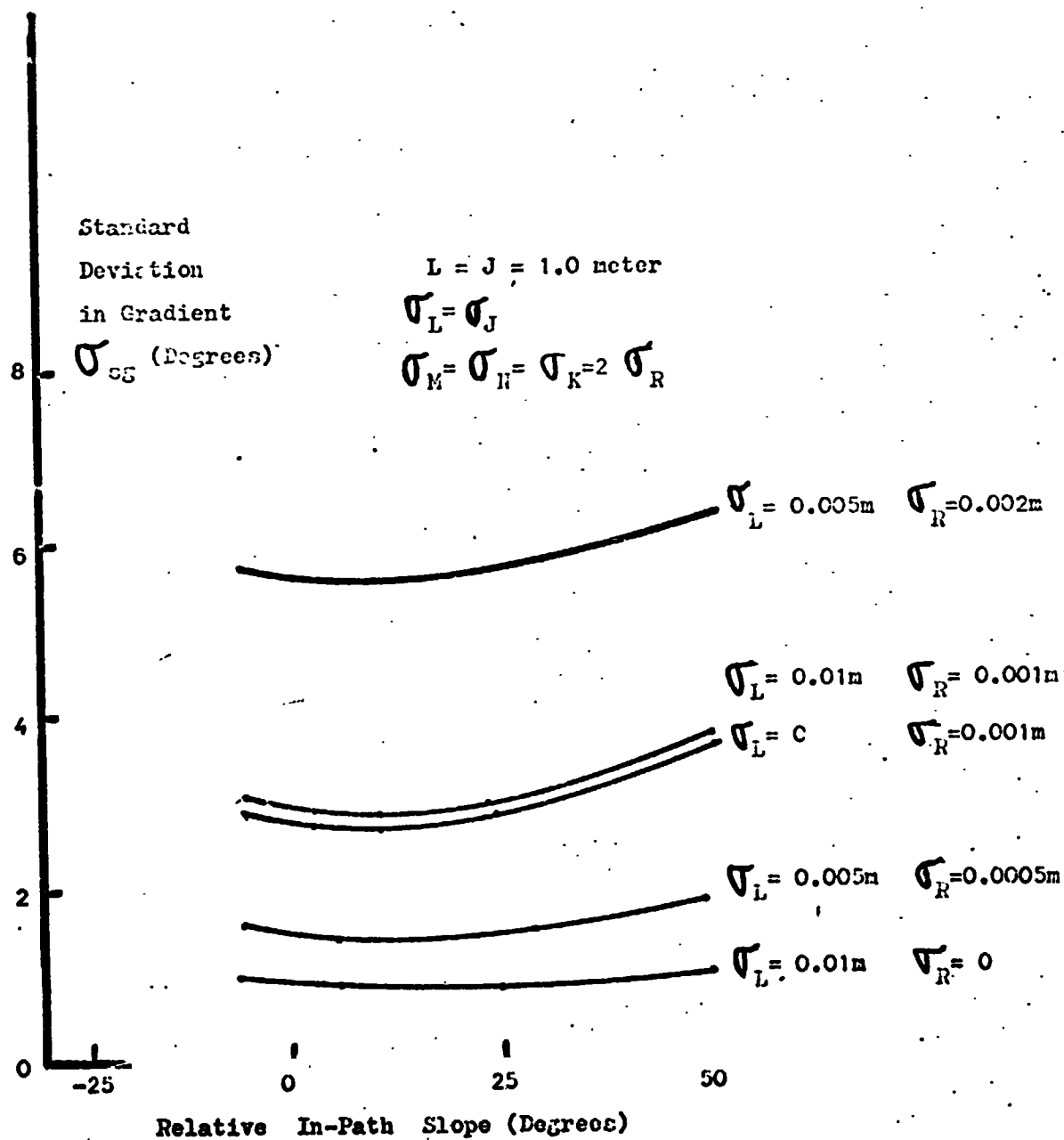


Figure 74. Stereo Range System: Standard Deviation in Gradient Versus Relative In-Path Slope for Terrain at 20m with Point Spacing = 1.2m

TABLE VIII

COMPARISON OF STEREO AND NON-STEREO  
MEASUREMENTS USING FOUR POINT PLANE FITTING

SYSTEM	MAX. RANGE STD. DEV. $\sigma_R$	MAX. ANGLE STD. DEV. $\sigma_A$	MAX. DISTANCE L & J STD. DEV. $\sigma_L = \sigma_J$
At 4 meters from the vehicle:			
Stereo-Range	0.001 meter	-----	0.005 meter
Stereo-Angles	-----	1 minute	0.001 meter
Non-sterco	0.01 meter	1 minute	-----
At 20 meters from the vehicle:			
Stereo-Range	0.0005 meter	-----	0.005 meter
Stereo-Angles	-----	6 arc-sec.	0.001 meter
Non-sterco	0.02-0.03 meter	1 minute	-----

Task C.3.      Path Selection System Evaluation  
                  S. Boheim, M. Szymanski, G. Ditlow, R. Campbell, R. Simonds  
                  Faculty Advisor: Prof. D. K. Frederick

The objectives of the present effort have been threefold: the continued development of a computer package which will provide the capability of dynamically simulating a wide variety of sensor, terrain modelling, and path-selection algorithm combinations; the generation of criteria for the quantitative evaluation and comparison of the system's performance; and the use of these criteria in evaluating proposed systems.

Previous efforts in the area of path-selection system evaluation have concentrated on the development of the major features of the computer simulation package and have been summarized in Reference 18. The progress attained during the past year consists of the following:

- a) Extension of the program to include an emergency backup mode and to incorporate nonzero vehicle dimensions.
- b) Addition of indices for safety and for obstacle detection errors to the quantitative performance measure.
- c) A comparison of the relative merits of vehicle- and vertical-fixed sensor configurations in terms of their effect upon path-selection system performance.

In addition to the above tasks, considerable effort was devoted to the various and sundry chores associated with the enhancement and documentation of a large computer program. Such items included reprogramming for reduced running time and storage requirements and improved output.

After a brief description of the program's structure, the specific accomplishments noted above will be described, followed by a statement of the goals which have been set for the coming year.

#### A. Program Structure

As indicated in Figure 75, the computer program for the simulation and evaluation of proposed path-selection systems has been structured so that each block contains a separate function, thereby allowing substitution of alternate simulation schemes without major reprogramming. Briefly, the entire system operation can be divided into four major portions. These are: 1) terrain characterization, 2) path-selection system, 3) vehicle dynamics, and 4) system evaluation and simulation display.

The terrain characterization portion is used to generate a very general terrain which includes boulders, crevases, craters, and cliffs.

The path-selection system provides the functions of 1) sensor operation simulation, 2) terrain modelling (i.e., determining if an obstacle is present at a particular heading), and 3) path-selection algorithm.

The third major portion of the program is the vehicle dynamics simulation in which the response of the vehicle to the commands of the path-selection system is simulated by determining how the moving vehicle is affected by the terrain and how this in turn may affect the path-selection system.



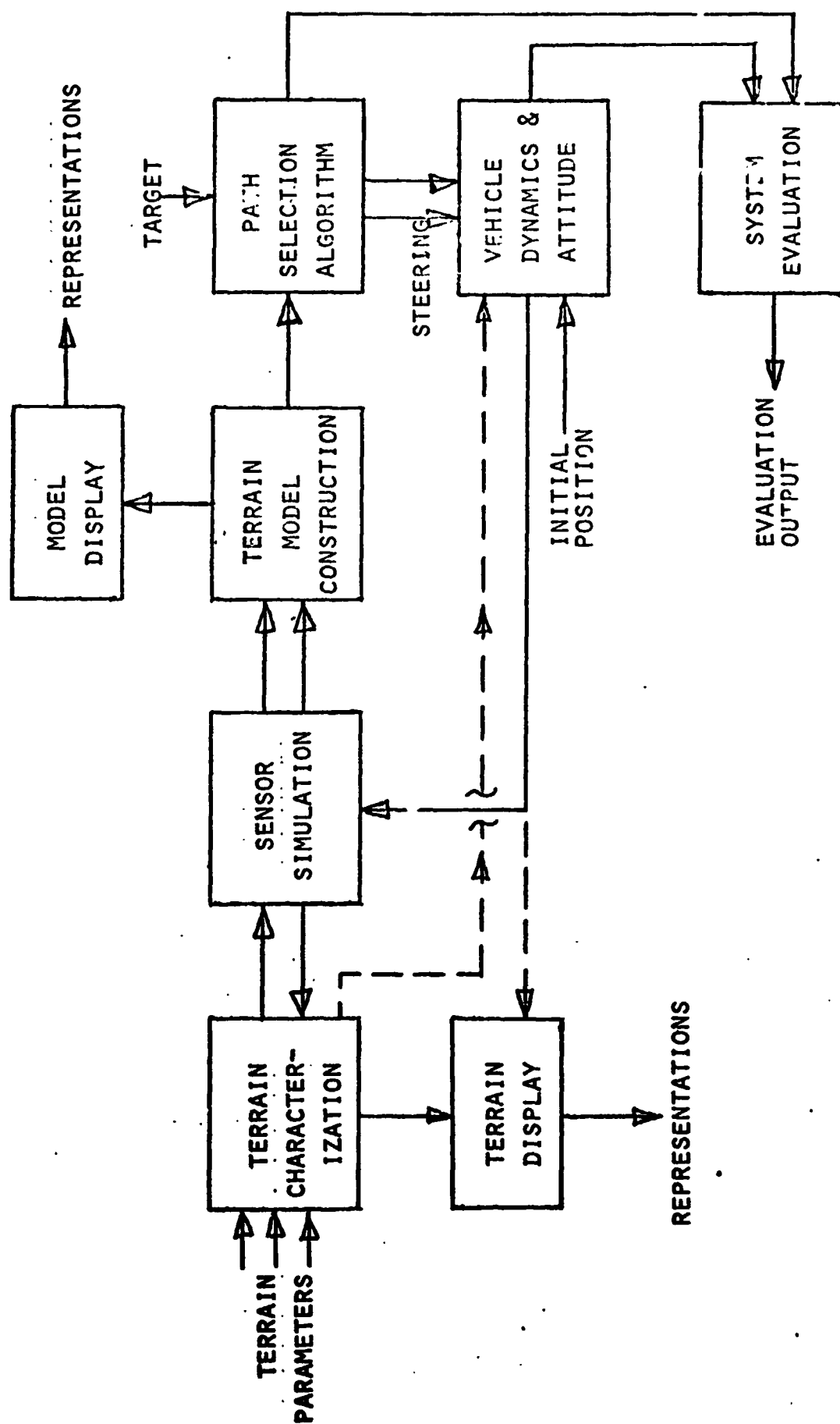


**Figure 75. SIMULATION STRUCTURE**

Finally, the system evaluation and simulation display supplies visual information indicating what the vehicle is doing, and what the terrain looks like. In addition, this portion assigns a numerical value to the system's overall performance.

In the following sections the major refinements to the computer package are described, followed by an evaluation of the effect of sensor gimbaling upon the performance of the path-selection system.

## B. Vehicle Backup Capability

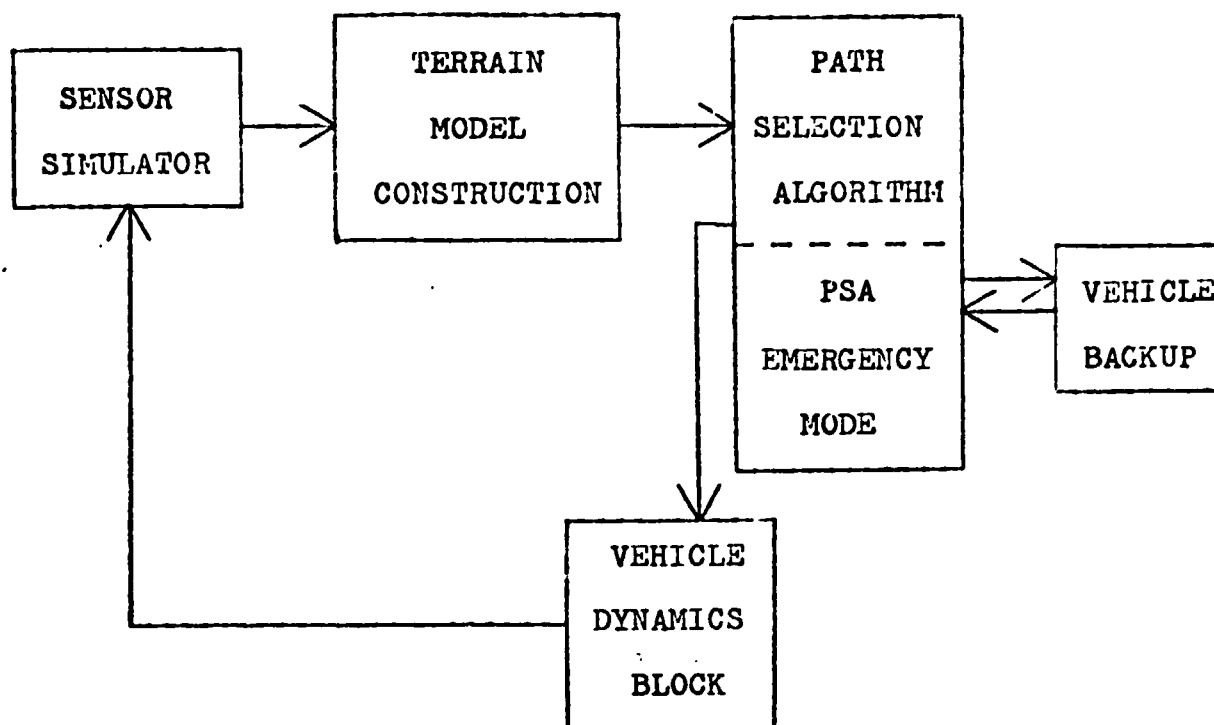
In simulations reported in Ref. 18, no penalties were imposed upon a vehicle which struck an obstacle, thereby giving an unrealistic assessment of its performance. As a means of eliminating this deficiency, an emergency path-selection algorithm with optional backup capability has been incorporated into the simulation package. This subset of the path-selection algorithm is only used when the vehicle encounters an obstacle it cannot negotiate. The vehicle backup function constitutes a separate block, Figure 76, which can be called only by the emergency mode of the path-selection algorithm.

The two major considerations taken into account during the development of the vehicle backup capability were flexibility and realism. Any addition to the overall simulation program must not degrade these considerations. Flexibility is of primary importance because the substitution of alternative path-selection systems must be performed with a minimum of effort for the program to be useful. Realism is necessary to ensure reliable system evaluation.

The backup block requires three parameters to be specified by the user, namely, the heading, speed (assumed to be constant), and distance of the backup maneuver. The program simulates backup motion and then passes the new vehicle location to the path-selection algorithm after the backup is completed. Overall simulation data, such as total elapsed time, total distance traveled, and total battery time used are tabulated, thereby penalizing the quantitative performance evaluation figure computed by the program.

The backup process is performed by the program in step increments of one half meter, unless otherwise requested by the user. The block also includes the option of simulating an ideal mechanical sensor, at each increment. The mechanical sensor checks the safety of each increment by calculating the in-path slope immediately behind the vehicle and comparing this slope with a prescribed limit (commonly chosen as 30 degrees). If the calculated in-path slope exceeds the limit, the vehicle stops and does not traverse this increment. Control is now returned to the emergency mode for the vehicle to receive the next command. Figure 77-A shows the simulation of a safe backup path in which all slopes are within the allowed limit. In Figure 77-B the boulder is detected by the sensor since the angle  $\theta_3$  is sufficiently large to exceed the slope limit.

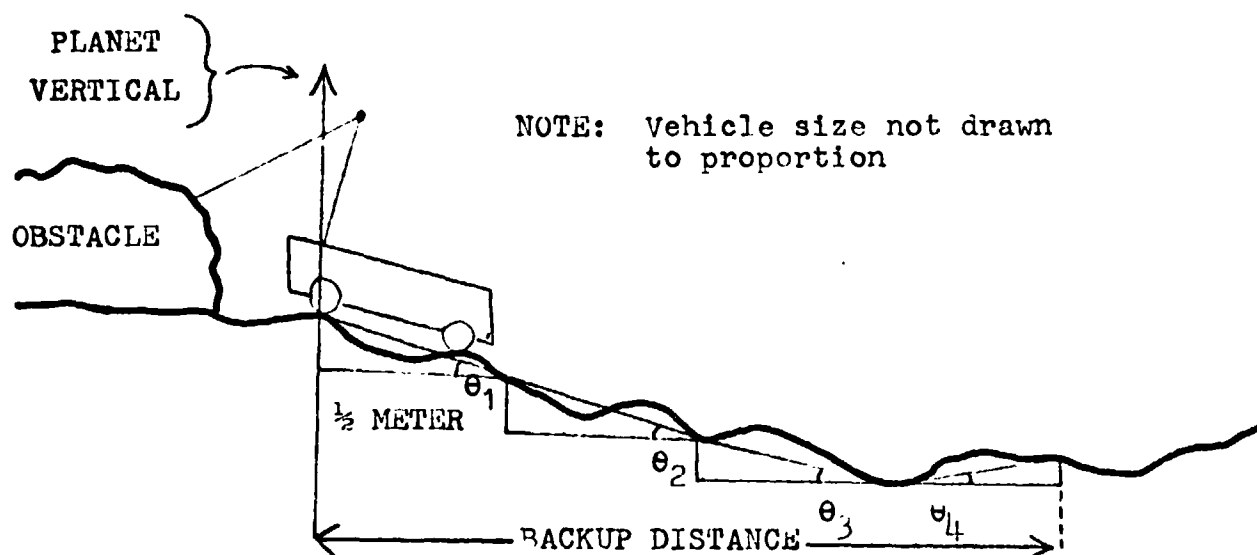
When the control returns from the backup procedure it is up to the emergency mode of the path-selection algorithm to make the next decision



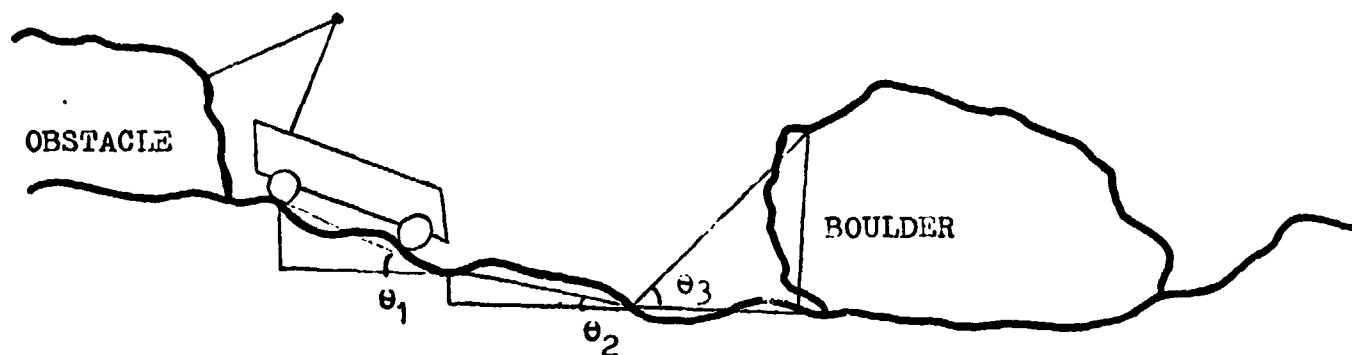
PATH SELECTION SYSTEM WITH

EMERGENCY MODE

Figure 76



(A) A SAFE BACKUP PATH



(B) AN UNSAFE BACKUP PATH

Figure 77. SIMULATION OF VEHICLE BACKUP

as to the vehicle's heading. Such a decision might call for turning the vehicle a certain number of degrees and scanning for a new path to the target or perhaps providing mission control a television picture of the situation and waiting for instructions.

In the area of program refinements, effort has also been devoted to endowing the vehicle with a nonzero width so that it must have sufficient clearance on each side in order to pass by an obstacle. As originally programmed the vehicle was treated as a point mass and in principle could pass between two very closely spaced boulders.

A computer simulation demonstrating a vehicle backup maneuver is shown in Figure 78. When the vehicle fails to successfully negotiate the boulders a backup of six meters is performed. Upon completion of the backup the emergency mode commands the vehicle to turn 45 degrees clockwise and look for a safe path. This procedure allows the vehicle to find a safe path to the target.

#### C. Performance Evaluation

The performance index that had been used to date in the simulation consisted of an equally weighted sum of indices measuring:

- 1) path length
- 2) time taken to arrive at target position
- 3) battery usage time

The minimum values that could be obtained by a three dimensional straight line path from initial position to target were used as a base line for the performance evaluation. Subsequent simulations, Ref. 18, have shown that these measures alone are inadequate to evaluate the performance of a path selection system due to the fact that increases in time and path length that occur when the vehicle strikes an obstacle are generally small and cause only small decreases in the performance index. Using these measures alone near perfect scores were awarded to imperfect systems that failed to detect obstacles and ran into them.

To improve the performance evaluation two additional indices have been added, namely

- 4) safety index
- 5) detection error index

The first new index is an additional measure of path quality, penalizing the system for approaching too close to and striking obstacles. The second penalizes the system for failing to detect any obstacles it may encounter in its path. The manner in which each index has been defined and implemented will be described below.

##### 1. Safety Index

Having decided that a measure of path safety is desirable, the problem of measuring it for any arbitrary path on any arbitrary terrain arises. The solution decided upon consists of

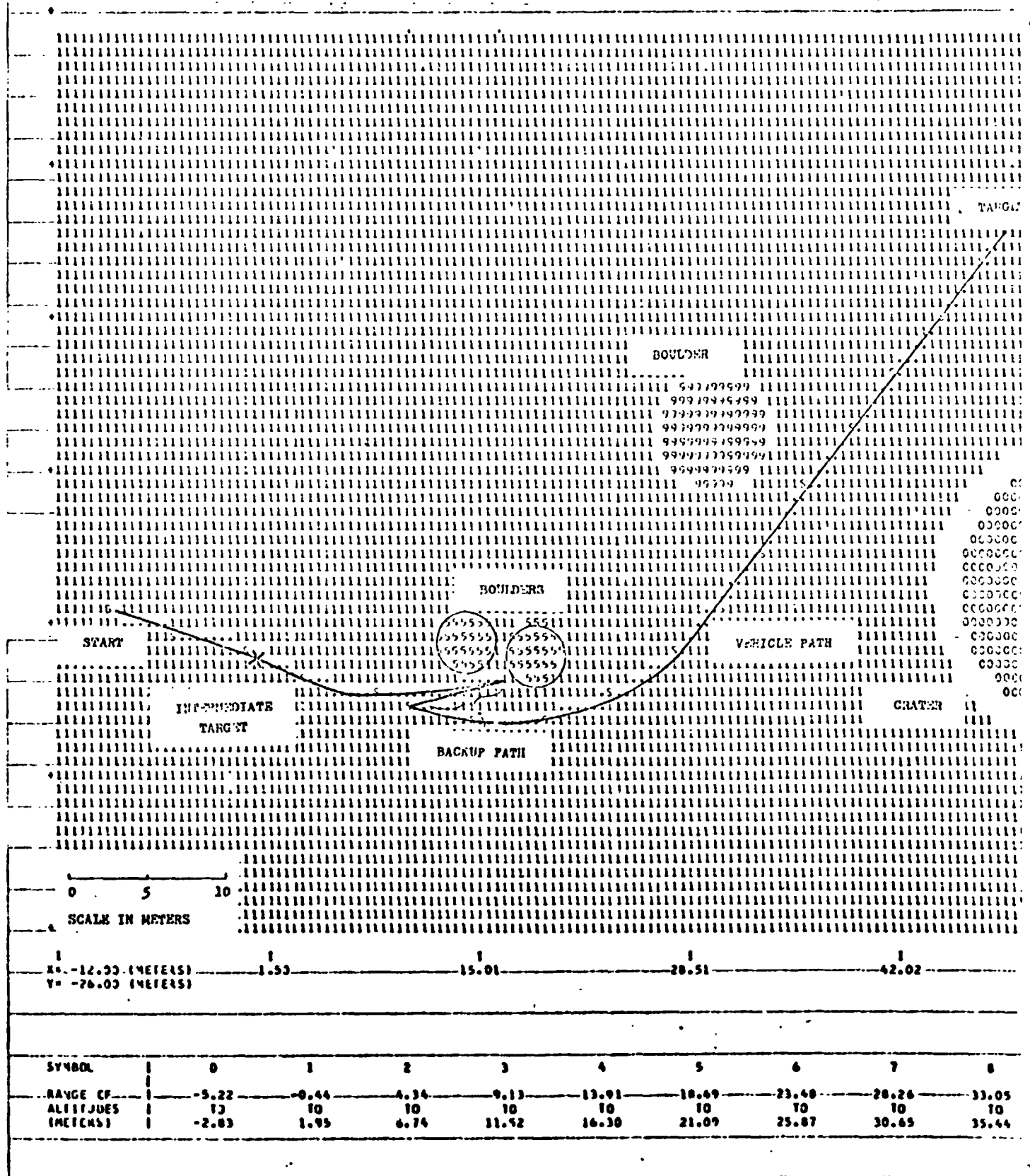


Figure 78. Simulation of Backup Maneuver

characterizing the location of each obstacle by a point in the horizontal (x,y) plane, computing the distance from the vehicle position to this location, then penalizing the system according to the distance between the vehicle position and the assigned obstacle location. The types of obstacles for which the safety index is applicable are boulders, craters, cliffs, and crevasses. For slopes which are too steep for the vehicle to negotiate no specific penalties are imposed by the safety index.

To implement the safety index, the location of each obstacle is characterized by a point in the x,y plane, denoted by the coordinates  $x_0, y_0$ . For a boulder or crater,  $x_0$  and  $y_0$  are at the center of the obstacle's circular profile in the x,y plane. However, since the edges of cliffs and crevasses are second-order polynomials in the x,y plane, their location is characterized by that point on the edge which minimizes the distance in the x,y plane between the vehicle and the edge of the obstacle.

The distance, denoted by  $D$ , in the x,y plane between  $(x_0, y_0)$  and the vehicle's current position is computed for each obstacle at every sensor scan and when the emergency mode is activated. This distance is then converted to a danger cost according to the function sketched in Figure 78, where  $D_1$  is the radius of a crater or boulder, or half of the vehicle's length for a cliff or crevasse and  $D_2$  is the desired pass buffer for the obstacle type. The values of the parameters  $D_1$  and  $D_2$  are specified by the user for each obstacle included in the terrain.

Finally, a running total,  $P_t$ , of the penalties assessed by the program is kept and the value of the safety index is computed according to the formula

$$\text{SAFETY INDEX} = \frac{1}{1 + P_t}$$

Clearly, the value of the safety index will be between 0 and 1, with unity being the maximum attainable.

## 2. Detection Error Index

As indicated above, the purpose of this index is to penalize the path-selection system for failing to detect an obstacle which lies within its scan region during any scan interval. Since the computer program knows the vehicle location and heading and the location of each obstacle in the x,y plane, it can compare this information with the output of the sensor simulation to determine if a specific obstacle has been detected, i.e., has caused the path-selection system to detect the existence of no-go lines of travel within the scan region. Failure to detect the presence of no-go lines of travel in the scan region when

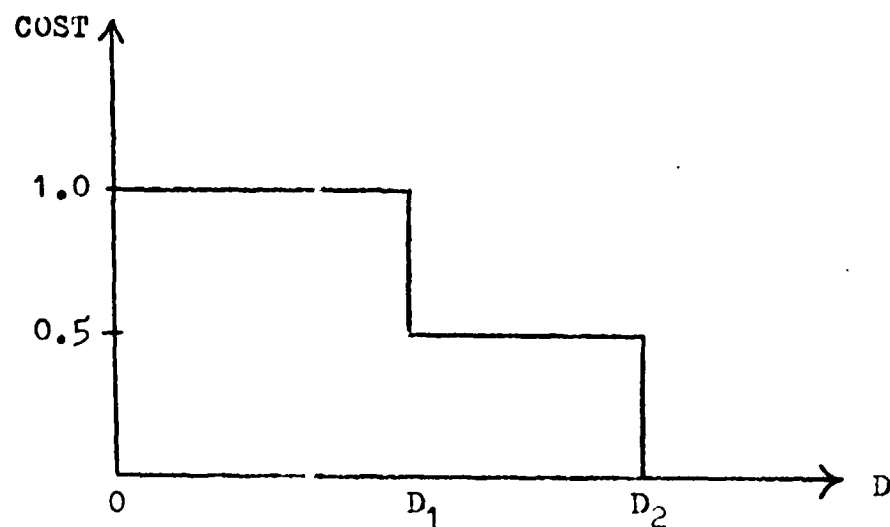


Figure 78. Safety Penalty Function

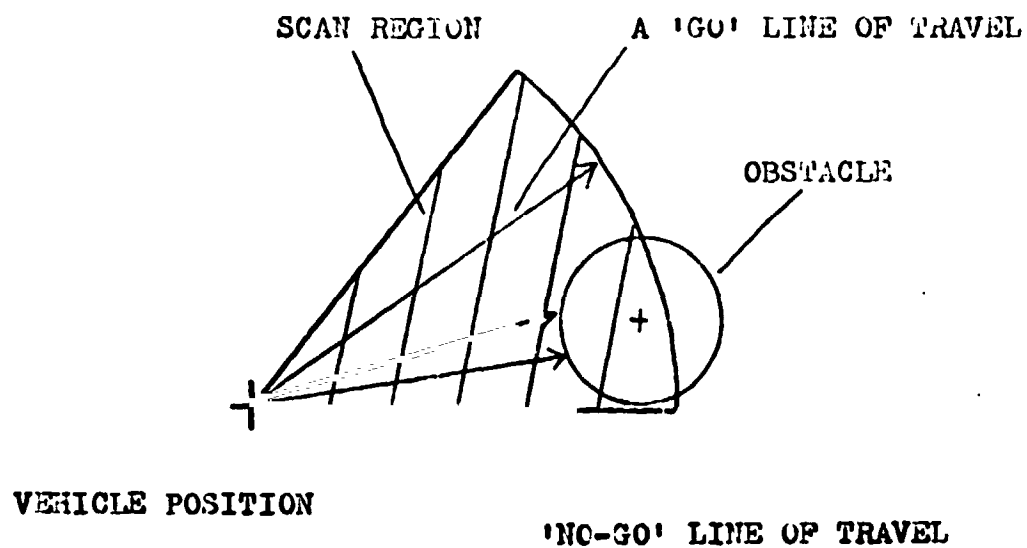


Figure 79. Occurance of a Detection Error



an obstacle exists in the region is counted as a detection error and the system is penalized accordingly.

The implementation of the detection error index is illustrated in Figure 79, where IND is a no-go line of travel indicator provided by the path selection system that has the value 1 when the system detects a no-go line of travel in the scan region and 0 otherwise. In the situation shown in Figure 79, the computer program has determined from the size of the scan region, the vehicle location and heading, and the obstacle location information, that a portion of the obstacle lies within the scan region during the current scan interval. Since the value of the indicator provided by the path selection system is 0 (indicating no detection of no-go lines of travel in the scan region during the present scan interval) the program has counted a detection error against the system.

Finally, a running total,  $N_{DE}$ , of the number of detection errors assessed by the program is kept and the value of the detection error index is computed according to the formula

$$\text{DETECTION ERROR INDEX} = \frac{1}{1 + N_{DE}}$$

Clearly, the value of the detection error index will be between 0 and 1, with unity being the maximum attainable.

The computer simulation shown in Figure 78 was run both with and without the implementation of the safety and detection error indices. The vehicle backup that occurs was initiated by an ideal mechanical sensor that detected the presence of a boulder in the vehicle path after the path selection system failed to do so on the previous sensor scan. Without the implementation of the new indices, the path selection system being used was awarded a performance index of 0.977. This nearly perfect score was awarded even though the system had failed to detect an obstacle in its path on the one occasion that an obstacle avoidance situation arose.

The simulation was then duplicated, but this time the safety and detection error indices were used in the system's performance evaluation. These indices were assigned weights of 0.70 and 0.15 respectively, while the path length, battery drain, and travel time indices were each assigned a weight of 0.05. A safety buffer of 1.5 meters from the edge of each obstacle was specified. The results of the simulation indicate that the system was penalized for three detection errors and for approaching the boulders to less than 1.5 meters on three occasions. With the implementation of the new indices, the same system performance was now awarded a performance index of 0.428.

#### D. Sensor Orientation Comparison

##### 1. System Description

One aspect of this year's work has been a comparison of vehicle-fixed and vertical-fixed sensor systems. In the former system, the

sensor laser beam is maintained at a fixed angle of  $82.4^\circ$  with respect to the vehicle's mast which is itself fixed with respect to the vehicle. In the latter case, the beam is maintained at an angle of  $82.4^\circ$  from the local planet vertical, see Figure 80.

In both cases, 17 equally spaced range measurements are made within  $40^\circ$  scan ahead of the vehicle. For modelling purposes, the terrain is assumed to be linear from a point underneath the vehicle to the impingement point of the laser beam. By comparing the resulting calculated slopes of the lines from the point under the vehicle to the 17 impingement points with acceptable maximum and minimum slopes of  $\pm 30$  degrees, the terrain modeller builds a 17 element go/no-go map corresponding to the 17 possible paths in front of the vehicle. That direction closest to the current target heading is selected for travel.

If the slope is too great for travel in the direction the vehicle is currently heading, the surrounding paths are successively investigated until an unobstructed path is located and a steering command generated. Should all 17 paths indicate obstacles, i.e., slopes which are too great, the vehicle rotates  $30^\circ$  clockwise and repeats its scan. The vehicle is initially pointed toward its target position and the mid-range sensor is used every 3 seconds.

## 2. Terrain Description

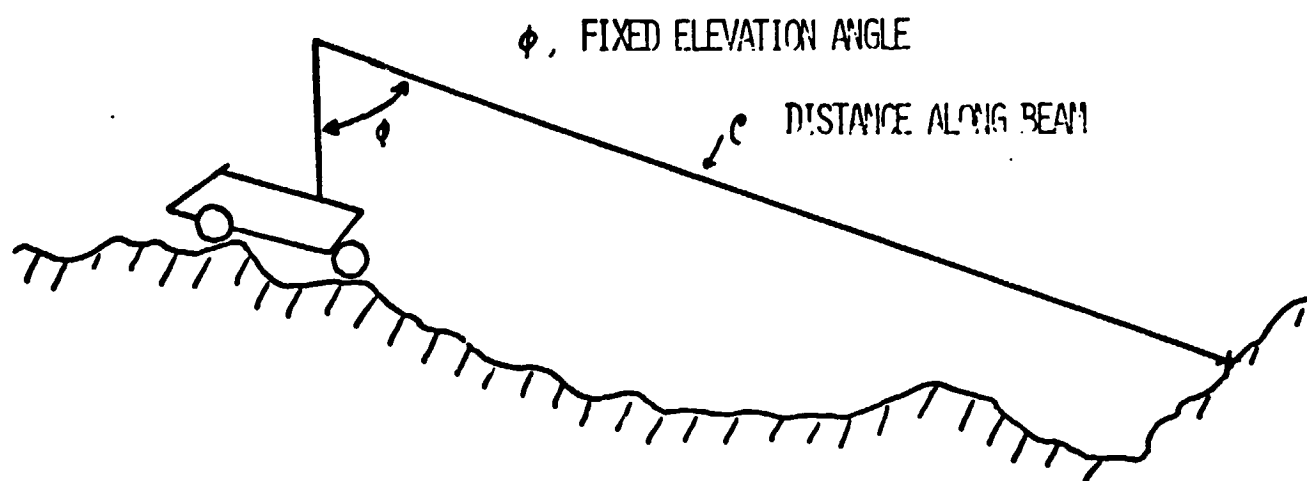
The two sensor systems were compared by using the computer program to simulate their responses over four terrains. In each case the terrain consisted of a sloping plane containing either a boulder or a crater directly between the vehicle's starting point and target. The terrain parameters are summarized in Table IX below.

TABLE IX  
TERRAIN PARAMETERS

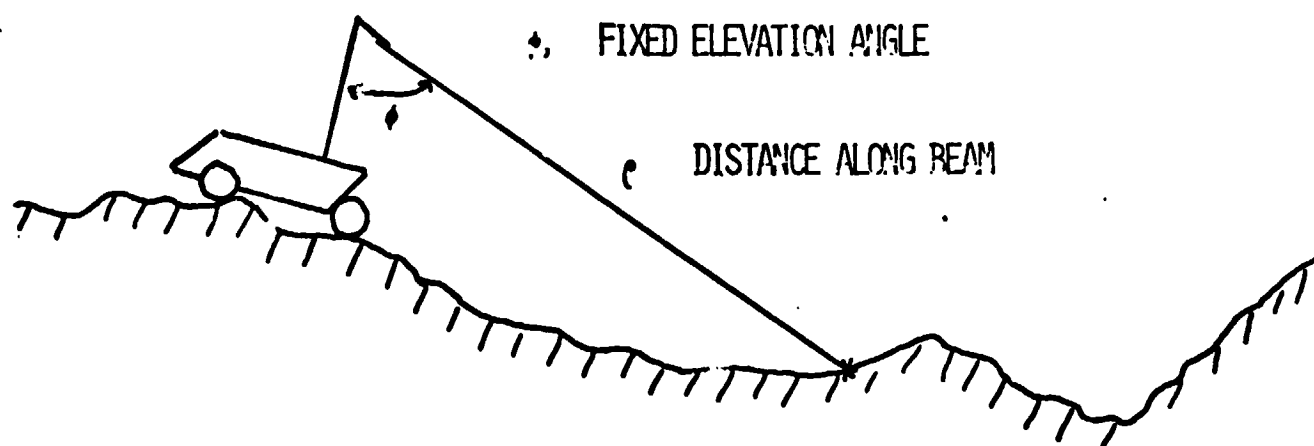
Terrain Number	In-Path Slope (degrees)	Cross-Path Slope (degrees)	Obstacle Type
1	- 25	0	Boulder
2	0	25	Boulder
3	+ 25	0	Crater
4	+ 25	0	Boulder

## 3. System Performance

Cases were first run in the absence of any random effects and then random noise was added to the deterministic values of the vehicle's in-path and cross-path slopes in order to simulate sensor attitude changes caused by passing over an irregular terrain surface, e.g., small rocks and depressions. The terrain map and vehicle path generated by a typical run are shown in Figure 81.



A. Planet-vertical Fixed



B. Vehicle Fixed

Figure 6. Sensor Configurations

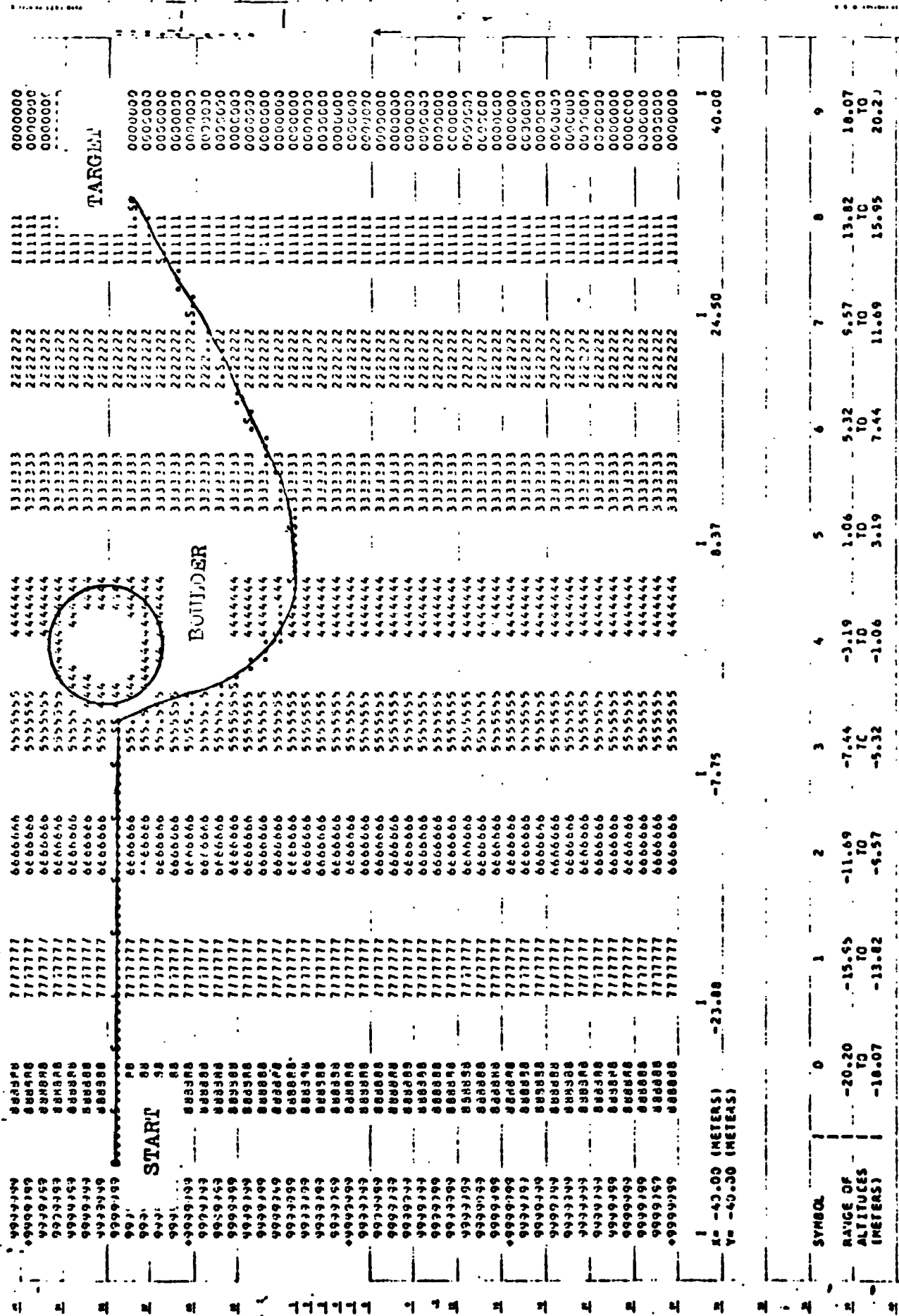


Figure 81. Terrain Map With Vehicle Path

While the terrain modelling subsystem and the path-selection algorithm used in these comparisons are not the most effective which can be designed and the terrains used are certainly not comprehensive, certain conclusions can be drawn from the results.

- a) The vehicle-fixed sensor gave more reliable indications of positive obstacles than the vertical-fixed one.
- b) Both systems are sensitive to cross-path slopes, but the vertical-fixed version more so than the other.
- c) Negative obstacles, e.g., craters, appear to pose more serious detection problems than positive obstacles, e.g., boulders for both types of systems.
- d) Direct range measurements seem to provide a better indication of positive obstacles than the computer slope values used in the simulations.

#### E. Summary

Due to the nature of the computer simulation task which has been undertaken, it is necessary to continue to improve upon the program's efficiency and realism as it is being used to evaluate proposed path-selection systems. Furthermore, as the program grows in size and complexity, the problems of documentation and handling grow.

As more experience is gained in evaluating various path-selection systems, the effectiveness of the present quantitative evaluation criteria must be scrutinized carefully and improved upon where deemed necessary. As a natural consequence of carrying out system evaluations, efforts should be devoted to devising new path-selection systems which hopefully are capable of performing better than those studied to date.

The activities of the coming year will be devoted to the tasks listed below, along with their target dates:

- 1. Refinement of the simulation program:
  - Addition of sideways roll (Dec. 1973)
  - and wheel slippage (May 1974)
- 2. Development of standardized test terrains (Dec. 1973)
- 3. Study of vehicle behavior using only a short range (say 2 meters) sensor (March 1974)
- 4. Simulation and evaluation of the Cornell path-selection system (Dec. 1973)

In addition to the above tasks, there are the ongoing tasks of improving the simulation program and evaluating alternative path-selection systems.

#### Task D. Chemical Analysis of Specimens

One important phase of the initial missions to Mars is the search for organic matter and living organisms on the martian surface. The present concept for attaining this objective consists of subjecting samples of the atmosphere and surface material to certain chemical and biochemical reactions and thereafter analyzing the products produced, probably in a combination gas chromatograph/mass spectrometer (GC/MS). The gas chromatograph is proposed for separating complex mixtures evolved from the experiments into small groups of similar chemical species. Chemical analysis of these groups would be accomplished in the mass spectrometer. It is the objective of this task to provide engineering techniques and criteria for designing such a system.

The overall concept of the chemical analysis system is shown schematically in Figure 82. Most of the previous effort has involved an analysis of the gas chromatograph using simulation, Ref. 19 and 20. This technique uses mathematical models, which incorporate fundamental parameters evaluated from reported experiments, to explore various concepts and to direct further experimental research. The objectives of the task have been extended to include preliminary studies of the entire chemical analysis system. System topics being considered include carrier gas generation and removal, and limitations imposed by and upon the mass spectrometer.

The task problems were attacked by a four-member team, each of whom pursued a specific assignment:

1. GC/MS system concepts
  - a. Mass spectrometer system characteristics
  - b. Carrier gas generation and removal
2. Chromatographic system analysis
  - a. Multicomponent chromatography
  - b. Chromatograph model improvement

#### D.1. GC/MS System Concepts

##### D.1.a. Mass Spectrometer System Characteristics - M. P. Badawy Faculty Advisor: Prof. P. K. Lashmet

It is the function of the mass spectrometer to provide mass spectra for several inputs, Figure 82. This subtask had as its objective the characterization of the major properties of the mass spectrometer, the resulting relations to provide direction in designing an instrument suitable for this space mission. In particular, those characteristics influencing power, weight, and volume requirements of the system were of primary concern, Ref. 21.

Prior work provided a parametric study of the coupling between the magnetic field and electrostatic potential in determining the ion masses to be detected. Instrument resolution and the nature of the ionizing process were investigated during the past year.

Resolution, or the ability of the instrument to differentiate between similar masses at a given time, is estimated for the single

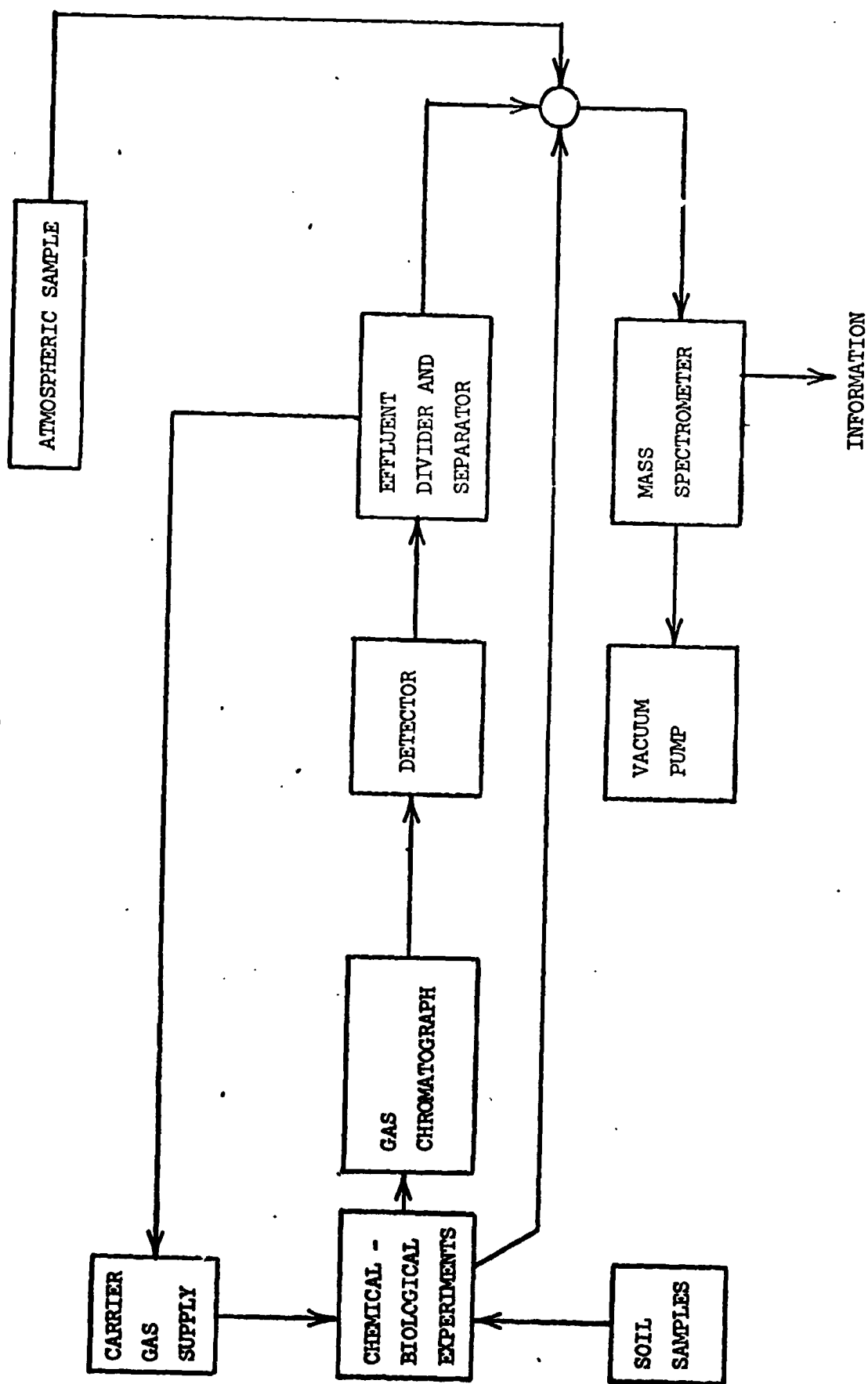


Figure 82. Schematic of Chemical Analysis System

focusing spectrometer as follows, Ref. 22, 23:

$$\Delta M/M = \frac{s' + s''}{a_m} + \left| \frac{\Delta V}{V} \right|$$

where

$s', s''$  = slit widths at the source and detector ends, respectively

$a_m$  = magnetic field radius of curvature

$V$  = voltage used for deflection of mass  $M$

$V$  = voltage equivalent to range of masses emanating from the electrostatic field at different velocities

$M$  = dispersion in mass detected

Similar but more complicated results for the double focusing mass spectrometer have also been developed, Ref. 21. These results emphasize the importance of the slit widths, the radius of curvature of the magnetic spectrum analyzer, and the energy spread of the instrument. Table X summarizes the physical parameters of three mass spectrometers and presents their respective mass resolutions as estimated from the above equations. Higher mass resolution can be achieved with more complicated designs, e.g., the toroidal electric sector field design, Ref. 24. However, for the current preliminary studies, the characteristics of the more simple, single or double focusing designs are satisfactory for representing the basic treatment.

Instrument sensitivity or the minimum concentration level detectable is determined to a great extent by the ionization process. The performance of the ionization chamber, based on an electron impact source is characterized by the following equation, Ref. 25 and 26:

$$I = b N \sigma s I_e$$

where

$I, I_e$  = ion and electron currents, respectively

$b$  = ion extraction efficiency

$N$  = molecular density

$\sigma$  = ionization cross-section

$s$  = effective electron path length

Difficulty in determining the ionization cross-section limited the utility of the equation. Ionization cross-sections for single electron emission were available, Ref. 27. However, because knowledge of the components in the gas to be analyzed was uncertain, and determination of the ionization fragments was complicated, it appeared that theoretical treatment of the ionization process was beyond the scope of this preliminary study.



Table X  
Specific Parameters for Several Mass Spectrometers

	JPL	Hayden and Nier	Voorhies et. al.
Electrostatic field angle	$\phi_e$ 90.°	—	90.°
Magnetic field angle	$\phi_m$ 90.°	—	60.°
Source to electrostatic field length	$l_e$ 1.656 cm	0.8 cm	4.34 cm
Mass dispersion coefficient	$\Delta v/v$ $\pm 0.01$	$\pm 0.02^*$	$\pm 0.02^*$
Magnetic field radius	$a_m$ 3.82 cm	2.54 cm	25.4 cm
Electrostatic field radius	$a_e$ 4.7 cm	4.27 cm	31.5 cm
Entrance slit width	$s'$ 0.00507 cm	0.01 cm	0.00456 cm
Exit slit width	$s''$ .00507 cm	0.038 cm	0.01524 cm
Mass resolution	$M/\Delta M$ SF (41.6) ** DF 180.9	(26.3) ** 47.31	1.25 (1.28) **

\* Assumed

\*\* Estimated resolution if instrument had different type of focusing

Experimental relations between the ion and electron currents will be sought to complete this phase of the task.

Further work was concerned with determining the effect of major design variables upon power consumption of the mass spectrometer. Figure 83 shows schematically the relation between the various power-consuming elements of the instrument. Most recent studies involved estimates of power associated with the filament of the ionization chamber.

In generating an electron emission current for ionizing the chemical specimens, the filament is a power consumer. Filament power, as determined by the filament current and its resistance, is dissipated through three mechanisms:

1. Power associated with the electron emission current which is dependent upon filament temperature and voltage. These effects are demonstrated in Figure 84 which is adapted from Ref. 28.
2. Thermal radiation between the hot filament and the cooler envelope of the ionization chamber. This effect is proportional to the fourth power of the filament temperature.
3. Molecular conduction by gas molecules in the space between the filament and the chamber envelope. This effect is proportional to the gas pressure, Ref. 29 and, because of the low pressures of the mass spectrometer, is generally of secondary importance.

The steady state energy balance, obtained by equating the Joulean heating of the filament to the dissipation terms, was investigated for several voltages and electron emitting areas. Table XI summarizes some of the studies and shows filament power is inefficiently used in producing an emission current. At the high filament temperatures considered, most of the energy is dissipated as thermal radiation. Radiation shields may well improve this energy utilization. These data also show that fine filaments are required.

These studies have determined the essential features of the filament. Future work will involve estimation of emission current ranges required in the mass spectrometer and the physical dimensions and voltage which result in minimum input power. After these studies are completed, the accelerating chamber, the magnet, and the vacuum pumping system will be considered.

D.1.b. Carrier Gas Generation and Removal - C. W. Jarva  
Faculty Advisor: Prof. P. K. Lashmet

Carrier gas, which is relatively inert with respect to the samples being analyzed and which must be in supply for an appreciable part of the mission, is required to propel minute samples through the column of the gas chromatograph. On arriving at the mass spectrometer, which operates at a low pressure ( $\sim 10^{-4}$  torr), the major portion of this

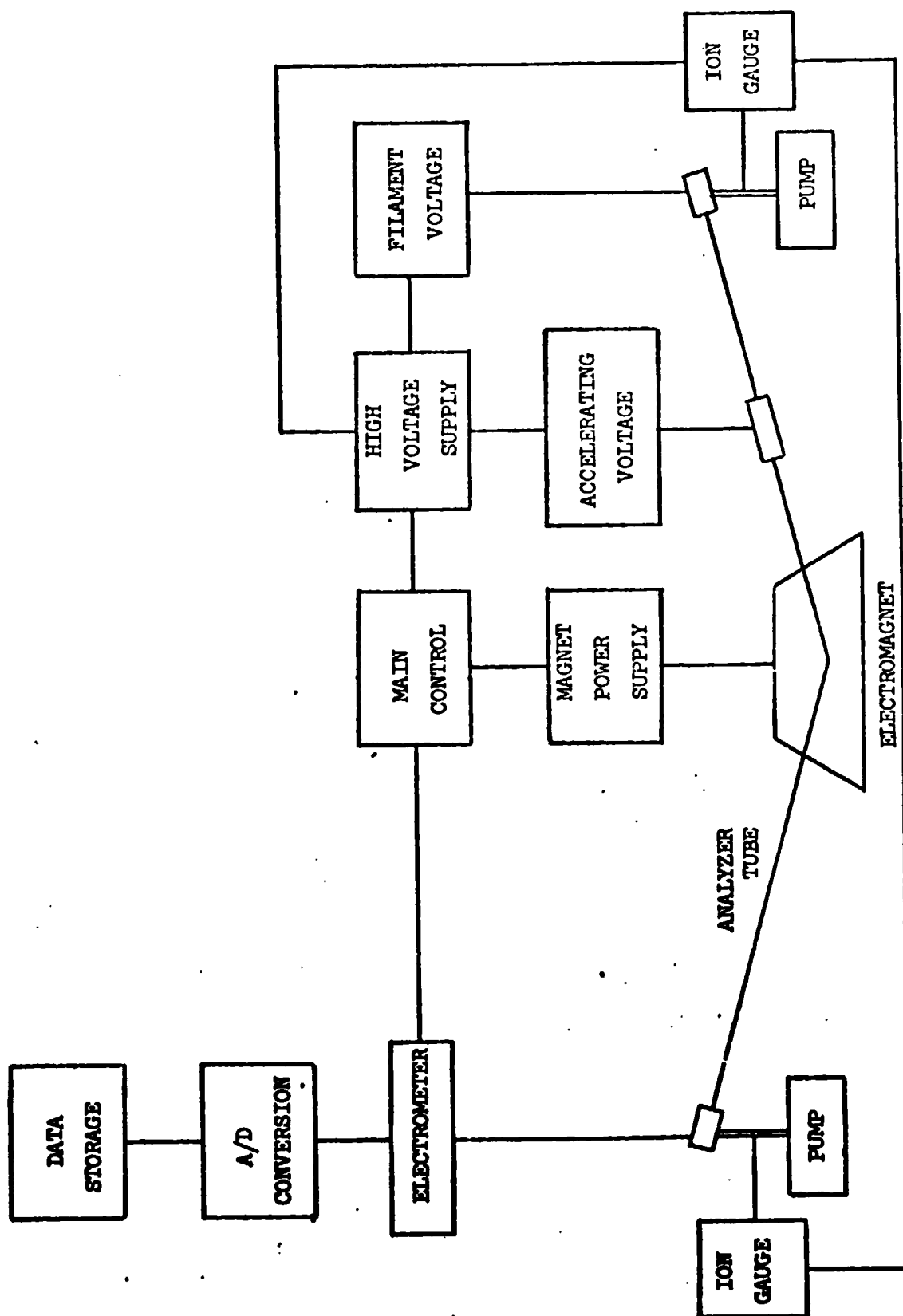


Figure 83. Power-Consuming Components of Mass Spectrometer

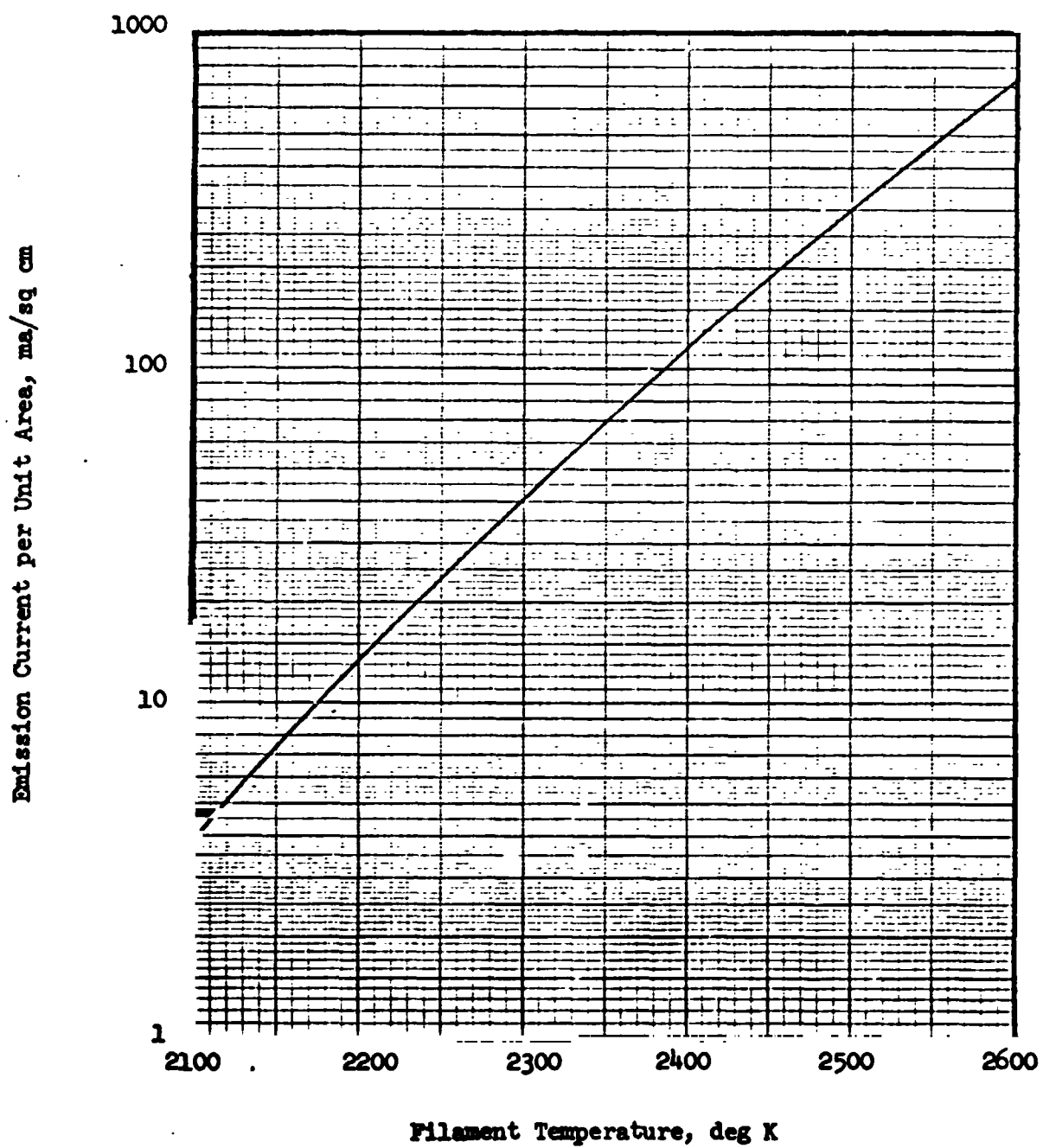


Figure 84. Emission Current for Heated Tungsten Filaments

TABLE XI Estimated Filament Characteristics

Filament temperature - 2100°K  
 Envelop temperature - 300°K  
 Envelop pressure - 10<sup>-4</sup> torr

<u>Filament Dia., cm</u>	<u>Filament Length, cm</u>	<u>Emission Current, mA</u>	<u>Filament Power, w</u>	<u>Emission Power, mw</u>
Filament voltage - 35.0 volts				
0.36 x 10 <sup>-3</sup>	8.75	0.54	0.241	19.
0.58 x 10 <sup>-3</sup>	11.06	1.09	0.478	38.
0.76 x 10 <sup>-3</sup>	12.55	1.63	0.723	57.
0.91 x 10 <sup>-3</sup>	13.95	2.17	0.964	76.
1.00 x 10 <sup>-3</sup>	14.97	2.72	1.20	95.
Filament voltage - 87.5 volts				
0.20 x 10 <sup>-3</sup>	15.55	0.54	0.269	48.
0.32 x 10 <sup>-3</sup>	19.64	1.09	0.534	95.
0.42 x 10 <sup>-3</sup>	22.4	1.63	0.807	143.
0.51 x 10 <sup>-3</sup>	24.7	2.17	1.08	190.
0.60 x 10 <sup>-3</sup>	26.6	2.72	1.35	238.

carrier gas must be separated from the sample and must be removed from the system. Thus the systems for generating, separating, and removing the carrier gas are important to overall system design and operation. It is the objective of this subtask to generate the basic characteristics and limitations of several promising concepts to aid in the design of the final overall system.

A study was undertaken, Ref. 30, to determine, as a function of the initial charge pressure, the physical characteristics of a spherical, high-pressure tank for storing the amount of carrier gas necessary for experimentation. Because of diffusion of the carrier gas, assumed to be hydrogen, through the vessel wall and its leakage through welds, valves, etc., Ref. 31 and 32, the gas storage capacity was greater than the requirement for the experimentation. Diffusion rates were determined from reported data, Ref. 33. To estimate leakage through welds and valves, it was assumed the vessel would be subjected to helium leak detection when charged to a practical pressure taken as 34 atmospheres in this case. The minimum leak detectable by modern leak detectors, about  $10^{-6}$  atm, cm<sup>3</sup>/sec, Ref. 32, was extrapolated to account for hydrogen as the gas and for the actual charge pressure. The vessel wall thickness was estimated from standard equations, Ref. 34.

Estimates of vessel size and weights as affected by charge pressure and operating time are shown in Figures 85 and 86. These estimates are based on the following assumptions:

1. Construction - fiber reinforced stainless steel containing 1/3 metal by volume, Ref. 35.
2. Allowable working stress -  $4.5 \times 10^8$  N/m<sup>2</sup> (66,000 psi), Ref. 35.
3. Gas flow rate for experiments - 2 std cm<sup>3</sup>/min, Ref. 36.
4. Flight time to Mars - six months
5. Maximum temperature - 300°K

Although diffusion and leakage were considered in these studies, these processes contributed only about 1% to the vessel volume. The vessel weights, shown in Fig. 86 to be approximately independent of charge pressure, are for the shell only. The pressure regulator and its mounting boss will contribute an additional one kgm approximately.

It was a major objective of this study to examine the merits of the gas storage vessel especially relative to a water electrolyzing cell proposed earlier, Ref. 37. It is estimated that the gas storage tank will weigh approximately 60% more than a comparable electrolyzing cell system but will occupy about the same space depending upon the charge pressure. It thus appears that if reliable fiber-reinforced vessels having about four times the allowable working stresses of stainless steel, can be fabricated, the concept of the high-pressure storage vessel has promise, especially since the system is simple.

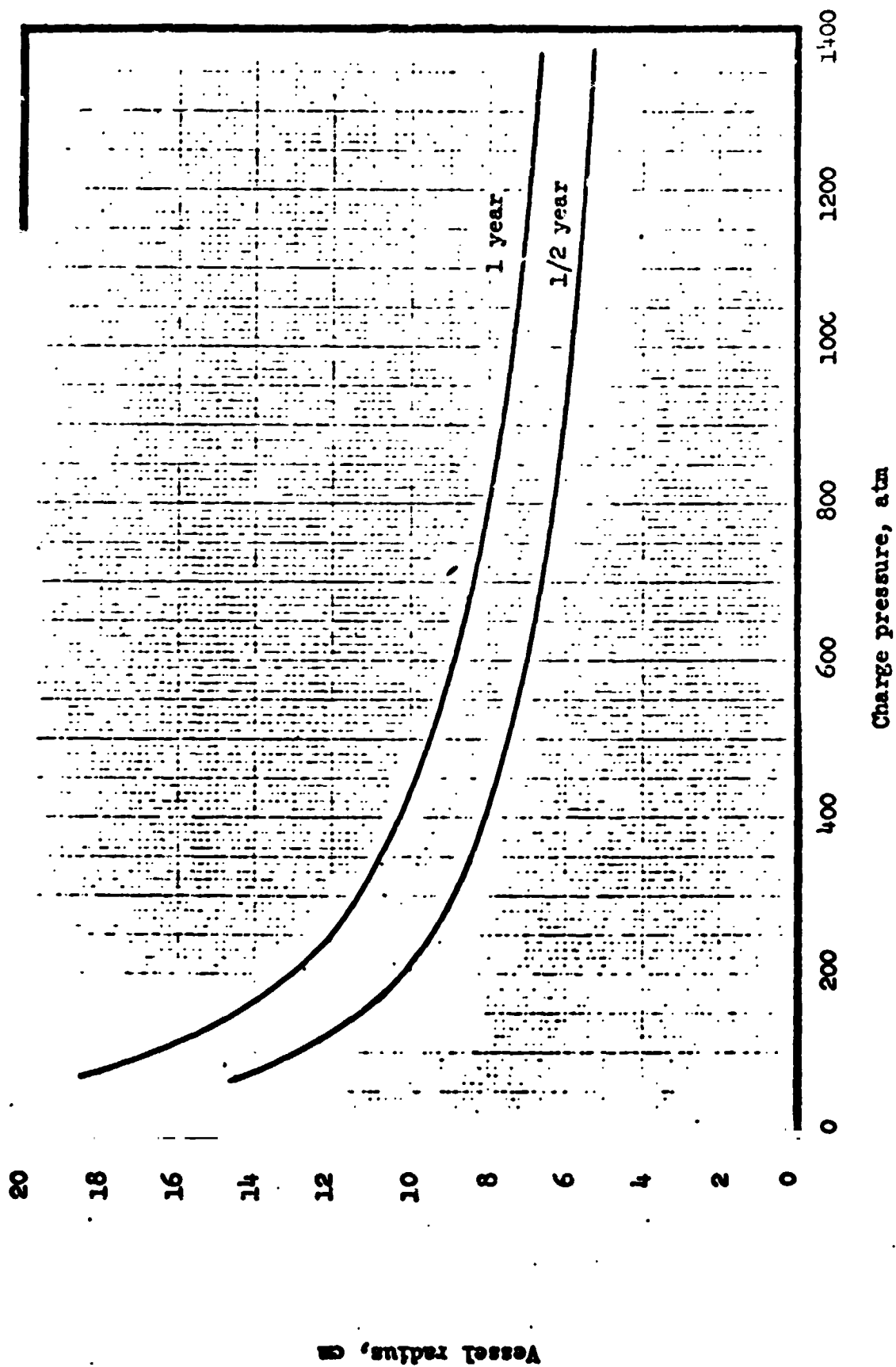


Figure 85. Effect of Charge Pressure and Operation Time on Size of Carrier Gas Sphere.

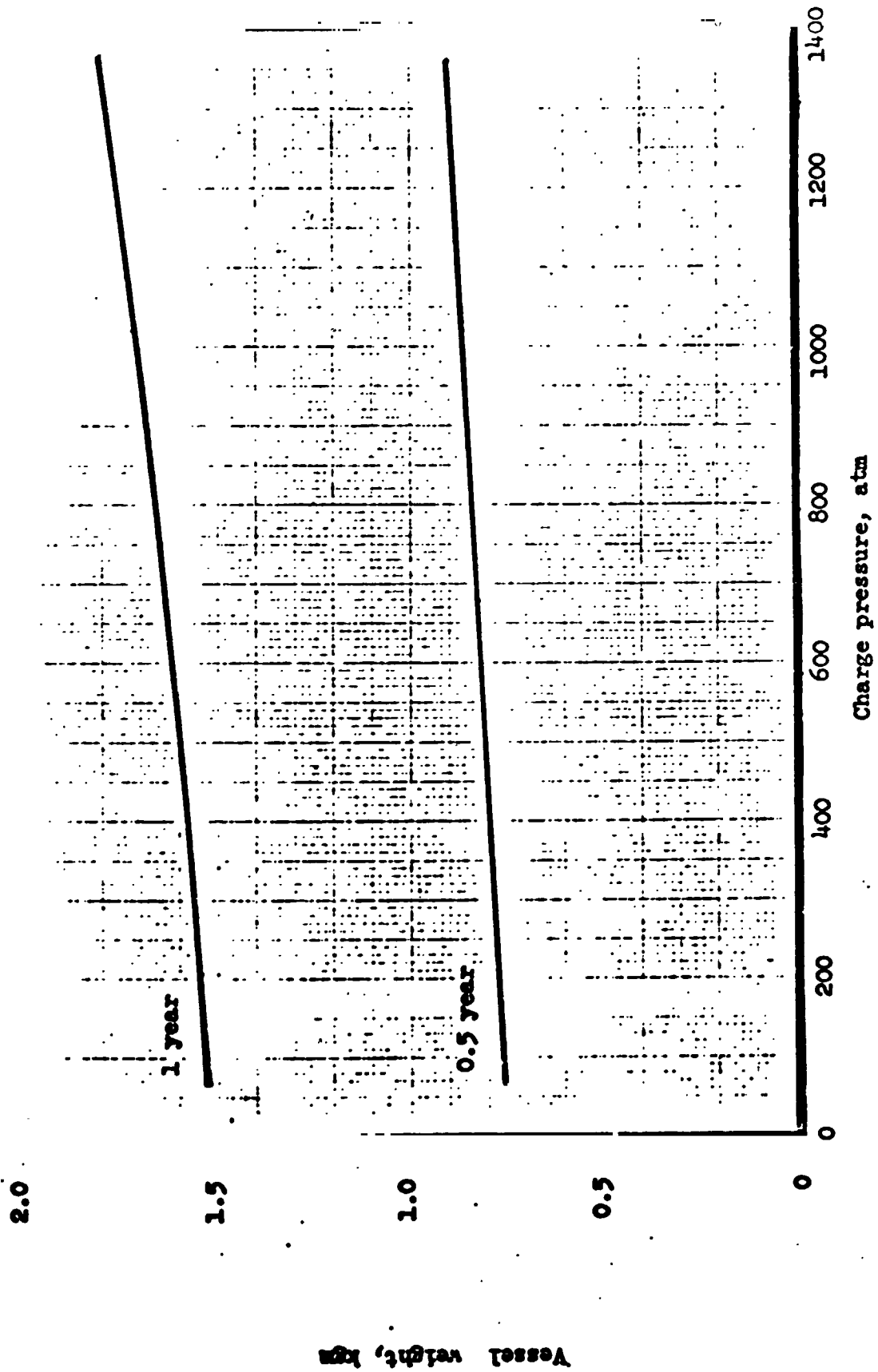


Figure 86. Effect of Charge Pressure and Operation Time on Shell Weight of Carrier Gas Sphere.



Except for possible minor improvements in the calculational procedures, this preliminary study has been completed, and a technical report will be issued in the near future.

A carrier gas removal system must be considered because the operating pressure of the mass spectrometer is about  $10^{-7}$  times the pressure expected in the chromatograph, Ref. 38. The palladium-silver alloy/hydrogen gas separator has been proposed, Ref. 36. In such a system, hydrogen flowing in a palladium tube diffuses rapidly through the heated tubing wall in comparison to other gaseous materials. This subtask is concerned with developing technical procedures suitable for the design of such a unit as well as with assessing its merits.

For the initial studies, the steady state of a system containing only hydrogen was considered, Ref. 30. Hydrogen diffusion rate through a palladium wall is proportional to the difference between the square roots of the hydrogen gas pressures at each face of the wall because of dissociation during diffusion, Ref. 39. From this diffusion rate equation, a first order, nonlinear, differential equation was developed which related the rate of material flowing at any point in the tube to the rate the gas diffused out of the system. Combined with a second order nonlinear momentum balance equation, a describing set of equations for this system was formed which required numerical solution. This analysis assumed a flat velocity profile, pure hydrogen flowing through the palladium tube (no presence of sample), and radial flow of the diffusing gas through the palladium walls.

These first studies showed the hydrogen pressure to be approximately constant over the tubing length, thereby eliminating the need for the momentum balance. The remaining rate equation was integrated directly. Figure 87 shows the estimated hydrogen flow rate as a fraction of the inlet flow rate for such a palladium tube under the following conditions, Ref. 36:

Inside radius of tube -  $7.6 \times 10^{-3}$  cm

Thickness of tube wall -  $7.6 \times 10^{-3}$  cm

Hydrogen pressure within tube - 4 atm

Hydrogen pressure outside tube - 0 atm

Temperature - 47 and 573 deg K.

For this simplified system model, approximately all of the hydrogen would have diffused through a tube 0.27 meter in length. This compares to an experimental value of 0.31 meter, Ref. 36, an indication the model and diffusion coefficients reasonably represent the system.

In an actual system, it is expected that the mass velocity of Figure 87 will approach zero asymptotically because of the presence of samples which essentially do not diffuse through the tubing wall. In the future, equations accounting for the presence of sample will be developed. The present study also considered the hydrogen pressure outside the palladium tube to be approximately zero. Pumping means such as combining the diffused hydrogen with oxygen on the tubing wall, Ref. 36, is a

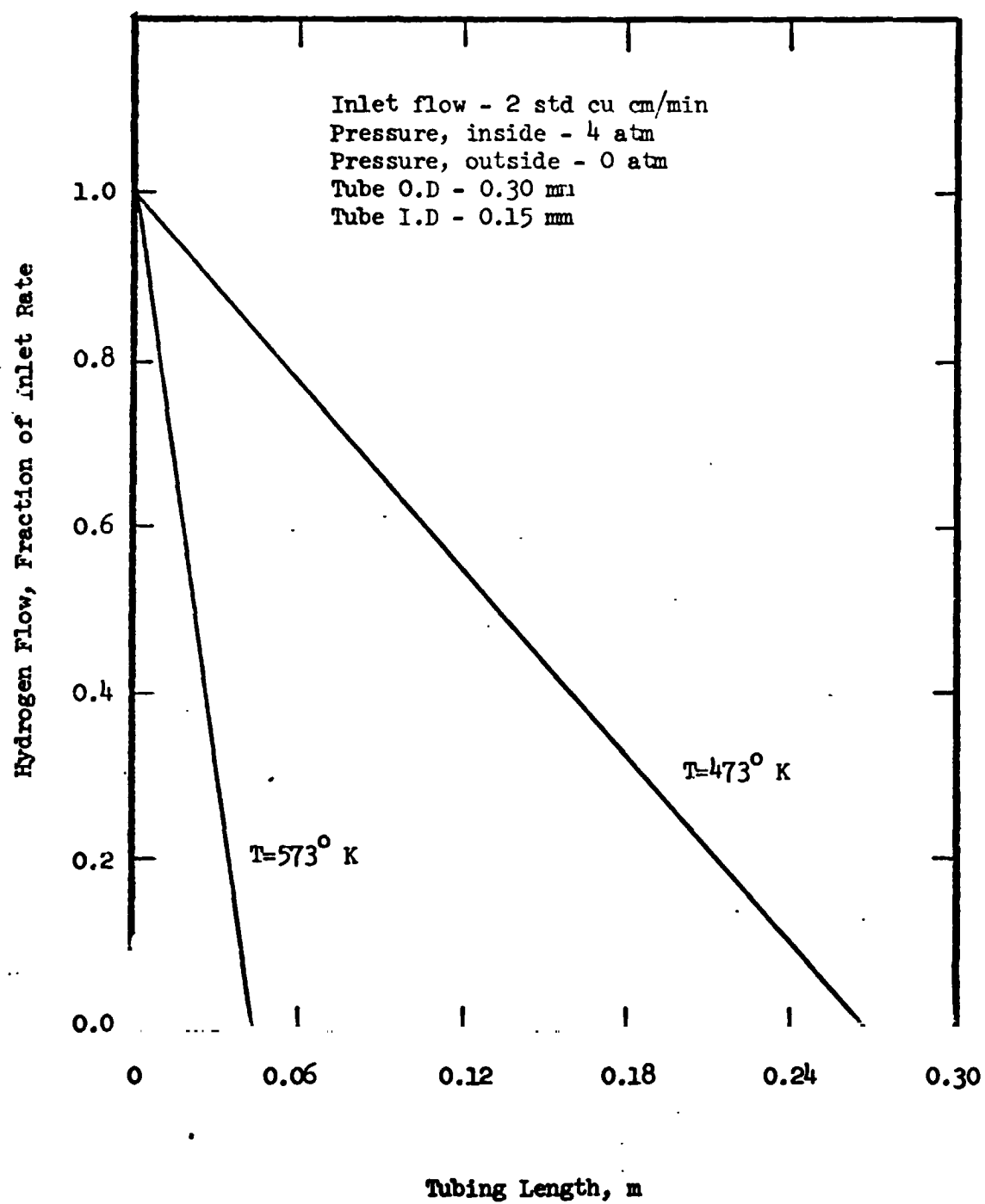


Figure 87. Length-Flow Profile for Palladium Separator

topic of future work. Other topics worthy of consideration include estimations of mechanical breakdown due to temperature and pressure cycling and chemical breakdowns due to contaminants.

D.2. Chromatographic System Analysis

D.2.a. Multicomponent Chromatography - A. J. Meisch  
Faculty Advisor: Prof. P. K. Lashmet

Linear mathematical models of the chromatograph have been developed for single chemical components and have been solved, analytically for an impulse input, Ref. 20, 40 and 41. Other work, Ref. 19, which used data from a chromatographic test facility, has shown that convolution of the actual input data with the theoretical normalized impulse response gives a reasonable representation of the actual chromatogram for a single component.

It was the objective of this subtask to experimentally evaluate the mathematical model for multicomponent chemical systems using superposition of single component data. Specifically the equilibrium adsorption model, Ref. 41, was considered:

$$Y(\theta) = \sqrt{\beta \text{Pe}/4\pi} \theta^3 \exp \left[ -(\text{Pe}/4\beta \theta) (\theta - \beta)^2 \right]$$

where

- $\beta$  =  $1 + (V/mR_0)$
- $\theta$  = dimensionless time -  $vt/L$
- $v$  = carrier gas velocity
- $t$  = time
- $L$  = column length
- $\text{Pe}$  = the Peclet number, a dimensionless measure of sample diffusion in the carrier gas
- $mR_0$  = a thermodynamic parameter, specific to the chemical system considered
- $Y$  = composition response to a unit impulse

This model assumes the gas at each point to be in equilibrium with the solid adsorbent; i.e., the column is very long. The Peclet number is a function of the fluid mechanics and the physical properties of the system and is predictable, Ref. 20. The parameter  $mR_0$  is specific to the system and is determined from the system data using a curve fitting technique, Ref. 19.

Extension of the model to multicomponent chemical systems using superposition of pure component data was proposed. Experimental work reported earlier, Ref. 20 on the binary system n-pentane/n-heptane on a microporous adsorbent Chromosorb 102 column (see Table XII) showed

Table XII  
COLUMN CHARACTERISTICS

	Chromosorb 102	Carbowax 1500
Length (cm)	100	100
Outside Diameter(cm)	0.32	0.32
Inside Diameter(cm)	0.22	0.22
Mesh	60/80	60/80
Particle Size(cm)	0.025/0.0177	0.025/0.0177
Composition	Microporous Styrene-Divinyl Benzene Polymers	Polyethylene Glycol 20% by weight
Temperature Range	Room-250°C	Room-150°C
Application	Separation of low molecular weight, very polar sub- stances such as water, alcohols, amines, acids, esters, ketones, ethers, aldehydes, and to a limited extent, light gases.	Separation of high boiling polar com- pounds. General purpose column for polar samples.

superposition was only a first order approximation and large deviations were noted. This subtask had as its objective the verification of the previously observed discrepancies and the generation of additional multicomponent chromatographic data, Ref. 42.

Chromatographic data for the system n-pentane/heptane on the porous Chromosorb 102 column have been obtained at 150, 175, and 200°C and for mixtures containing zero to 100% n-pentane by weight. As shown in Figure 88, the peak times for the multicomponent system lagged peak times predicted from superposition of the pure component data. This time lag occurred for both compounds for all mixtures considered as shown typically in Table XIII and it increased as the component composition became more dilute.

The peak time is primarily related to the parameter  $mR_0$ , Ref. 41. As the peak time varies with sample composition, it is possible that  $mR_0$  is composition dependent. The component compositions in the helium carrier gas are not small ( $\sim 10^{-2}$  mole fraction), and there may be possible interaction effects at the adsorbent surface. Figure 89 shows the values of  $mR_0$  necessary to superimpose the model upon the data. This is empirical, and future work will consider interactions between the system differential equations.

To determine if these interaction effects were attributable to the porosity of the Chromosorb 102 adsorbent, the chromatographic separation of n-pentane and n-heptane was attempted on a nonporous Carbowax 1500 column described in Table XII. Separation was not effected because of similar adsorption characteristics and large sample dispersion of the input sample. Possible modifications to the injection device to reduce the input pulse width as well as selection of a more favorable adsorbent are being considered.

To improve data handling and consistency, a more automated data processing scheme outlined in Figure 90 was considered. Implementation of the proposal with existing major hardware appeared feasible. However, manual analysis of the stripchart chromatograms yielded about twice the resolution obtainable from the automatic processing system which was limited by the A/D converter of the available minicomputer. The proposal was rejected, and possible changes to the detector control circuits to obtain full scale readings with most samples are being considered.

Experimental studies on the porosity and pore-size distribution of the adsorbents were begun. These data are required for accurate prediction by the improved mathematical models being developed (see Task D.2.b.). Initial data were obtained with a mercury porosimeter using a sample holder more suited to coarse adsorbent particles than to the 60/80 mesh particles of the chromatographic columns. The data appeared qualitatively reasonable, and work will continue upon receipt of a more suitable sample holder.

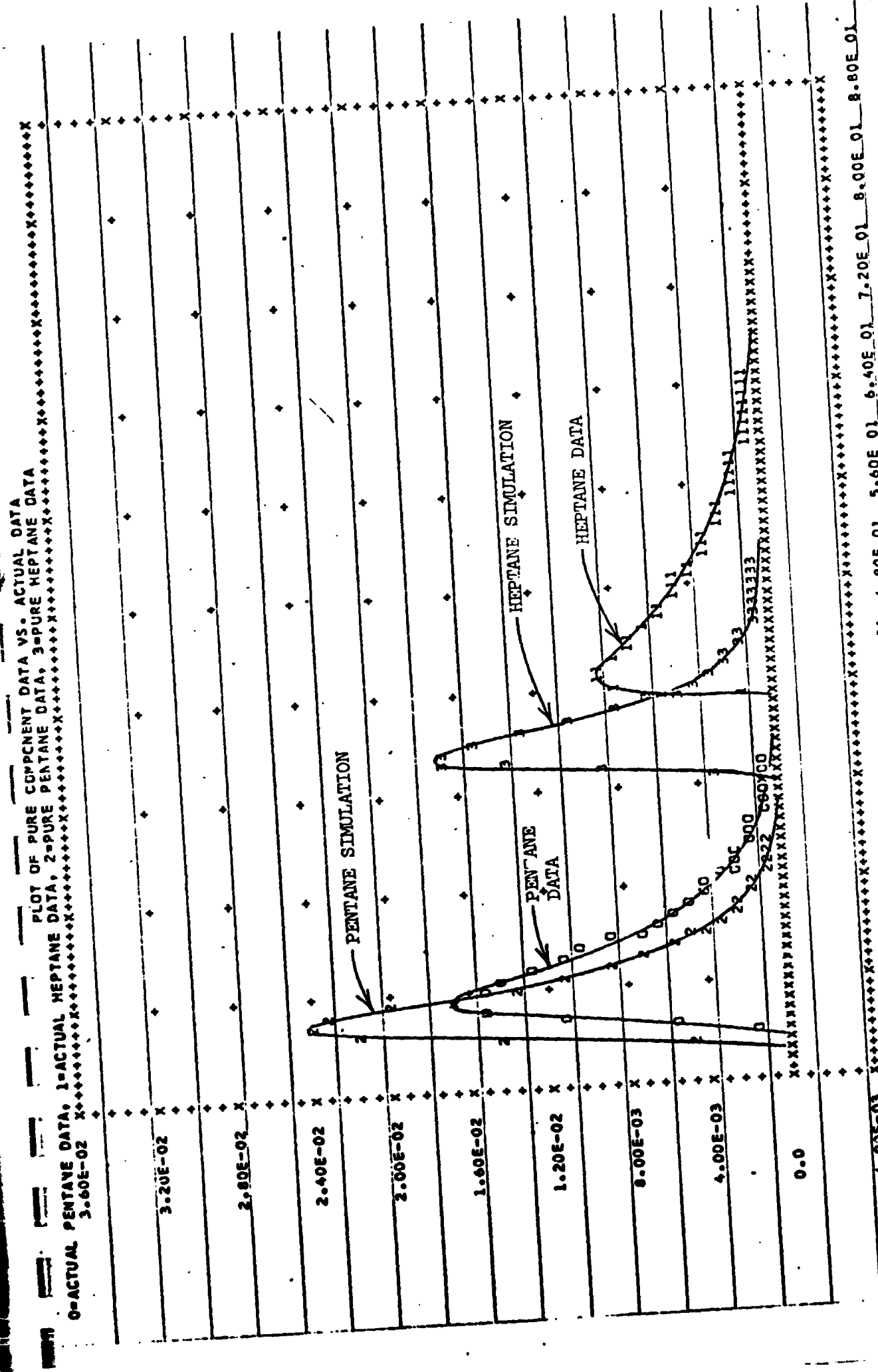


Figure 88. Predicted and Actual Binary Chromatograms for Pentane-Heptane System on C-102 at 175°C

Table XIII  
TIME LAGS IN BINARY DATA

Pentane-Heptane System on C-102  
Flow Rate of 29.4 cc/min at 150°C

Composition weight %	Time of Pentane Peak, sec	Time of Heptane Peak, sec
100 H	-	285.5
99 H - 1 P	95.0	294.0
75 H - 25 P	88.5	307.5
50 H - 50 P	86.0	327.5
25 H - 75 P	84.0	364.0
1 H - 99 P	81.5	432.5
100 P	80.5	

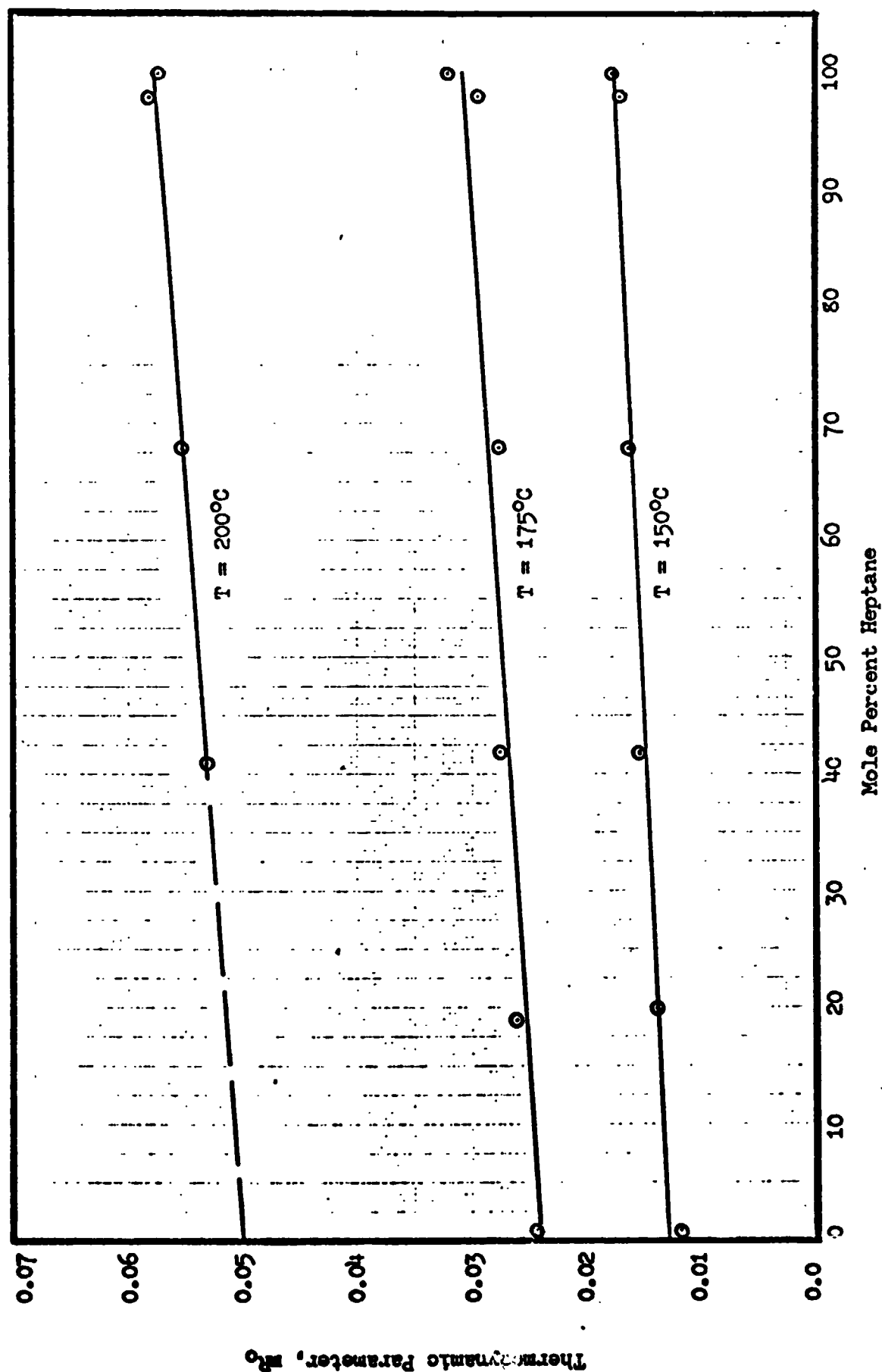


Figure 89. Effect of Composition on Heptane  $mR_0$  for Pentane-Heptane System on C-102



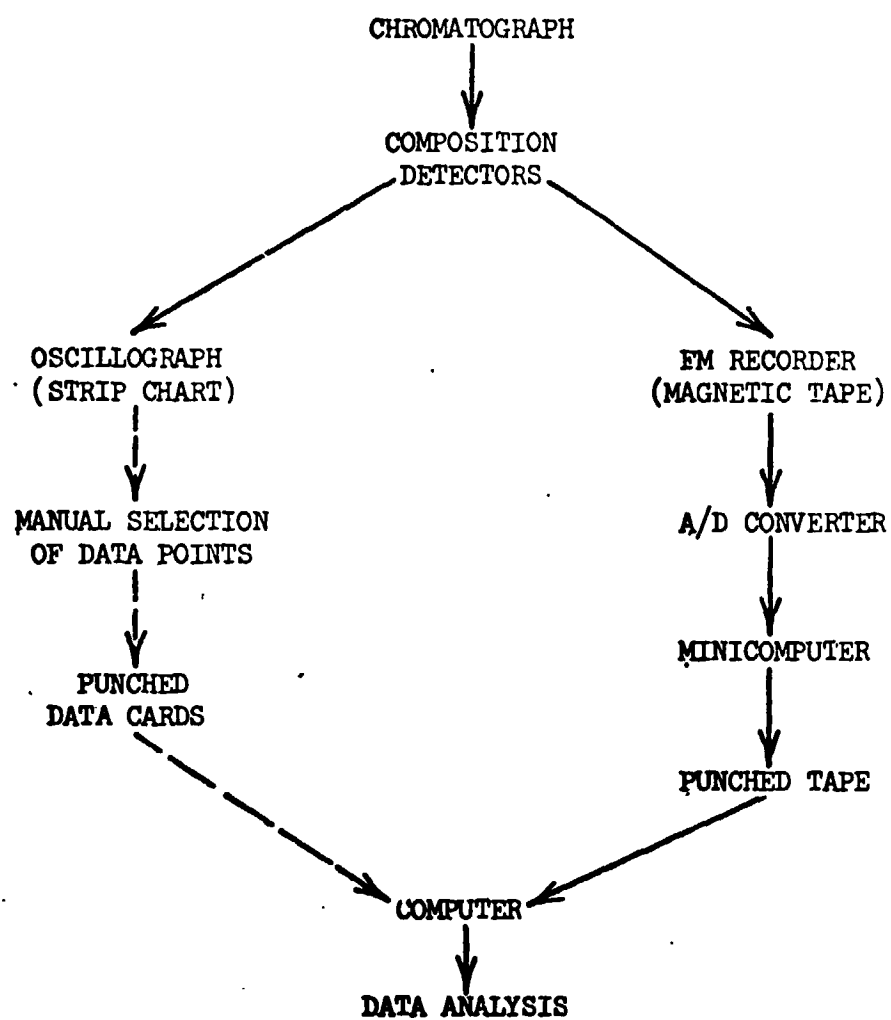


Figure 90. Chromatographic Data Processing

MANUAL PROCESSING - - - - -

AUTOMATIC PROCESSING ———

D.2.b. Chromatograph Model Improvement - P. T. Woodrow  
 Faculty Advisor: Prof. P. K. Lashmet

Prior to July 1972 the mathematical model of the chromatographic column was based on a packing material which either was non-porous or allowed pore diffusion and subsequent adsorption to occur at such a high rate that the resultant system dynamics were not significantly affected. Thus, in modeling the system, only interparticle and adsorbed phase mass balances were considered. The applicable partial differential equations, assumptions, initial conditions, and boundary conditions have been presented elsewhere, Ref. 20. These equations showed the predicted chromatogram to be a function of three variables:

$mK_0$  = a thermodynamic parameter, specific to the chemical system considered

$N_{tOG}$  = the number of transfer units, a dimensionless measure of diffusion rates to the adsorbent surface

$Pe$  = the Peclet number, a dimensionless measure of sample diffusion in the carrier gas.

Solutions to this system of equations have been reported, and cases of equilibrium adsorption ( $N_{tOG} \rightarrow \infty$ ) and non-equilibrium adsorption ( $N_{tOG}$  is finite) have been compared with experimental data, Ref. 20. It was concluded that for the ranges of parameters encountered in typical chromatographs, consideration of a finite rate of mass transfer ( $N_{tOG}$  is finite) yields minor, at best, improvement in output chromatogram predictions. In addition, the predictions of peak height and spreading were inadequate for some experimental conditions and chemical systems. It appeared that another mechanism not considered in the model formulation was responsible for the discrepancies between prediction and experiment. As the adsorbent (Chromosorb 102) was porous, Table XII, the mechanism of intraparticle diffusion warranted investigation.

Consideration of the intraparticle diffusion process as well as the rate of surface adsorption yielded a new system of equations shown in Figure 91 and having the following parameters and variables not defined previously:

$m$  = thermodynamic equilibrium constant

$N_{RU}$  = the number of reactor units, a dimensionless measure of the rate of adsorption

$Pe_A$  = intraparticle Peclet number, a dimensionless measure of diffusion rates within the particle

$Pe_E$  = interparticle Peclet number, a dimensionless measure of diffusion rates in the carrier gas

$L/R$  = ratio of column length to particle radius

$R_1$  = moles of fluid in particle per mole of adsorption sites

$r$  = intraparticle space variable, dimensionless

INTERPARTICLE PHASE MASS BALANCE:

$$\left(\frac{1}{P_{eE}}\right) \frac{\partial^2 y}{\partial z^2} - \frac{\partial y}{\partial z} - N_{tOG} (y - y_1)_{z=1} = \frac{\partial y}{\partial \theta}$$

INTRAPARTICLE PHASE MASS BALANCE:

$$\frac{1}{P_{eA}} \left(\frac{L}{R}\right)^2 \left[ \frac{\partial^2 y_1}{\partial r^2} + \left(\frac{2}{r}\right) \frac{\partial y_1}{\partial r} \right] - N_{RU} (y_1 - y_1^*) = \frac{\partial y_1}{\partial \theta}$$

ADSORBED PHASE MASS BALANCE:

$$\left(\frac{1}{R_I}\right) \frac{\partial x}{\partial \theta} = N_{RU} (y_1 - y_1^*)$$

THERMODYNAMIC RELATIONSHIP:

$$y_1^* = m x$$

Figure 91. System Equations for Inter-Intraparticle Model

- $x$  = adsorbed phase composition, dimensionless
- $y$  = interparticle gas phase composition, dimensionless
- $y_i$  = intraparticle gas phase composition, dimensionless
- $y_i^*$  = equilibrium intraparticle gas phase composition, dimensionless
- $z$  = longitudinal position in column, dimensionless

As an aid to envisioning the various transport processes incorporated in this new chromatograph system formulation, Figure 92 is included. In the interparticle region, material is transported by convection (i.e., by carrier gas flow) and by turbulent and molecular diffusion in the axial direction, which is characterized by the interparticle Peclet group,  $Pe_F$ . The transport from the interparticle region to the intraparticle region is characterized by the dimensionless mass transfer coefficient,  $N_{tOG}$ . Transport by diffusion within the particle - the intraparticle region - is characterized by the intraparticle Peclet group,  $Pe_A$ . The rate of adsorption from the intraparticle gas phase to the adsorbed phase within the particle is characterized by  $N_{RU}$ , the number of reactor units.

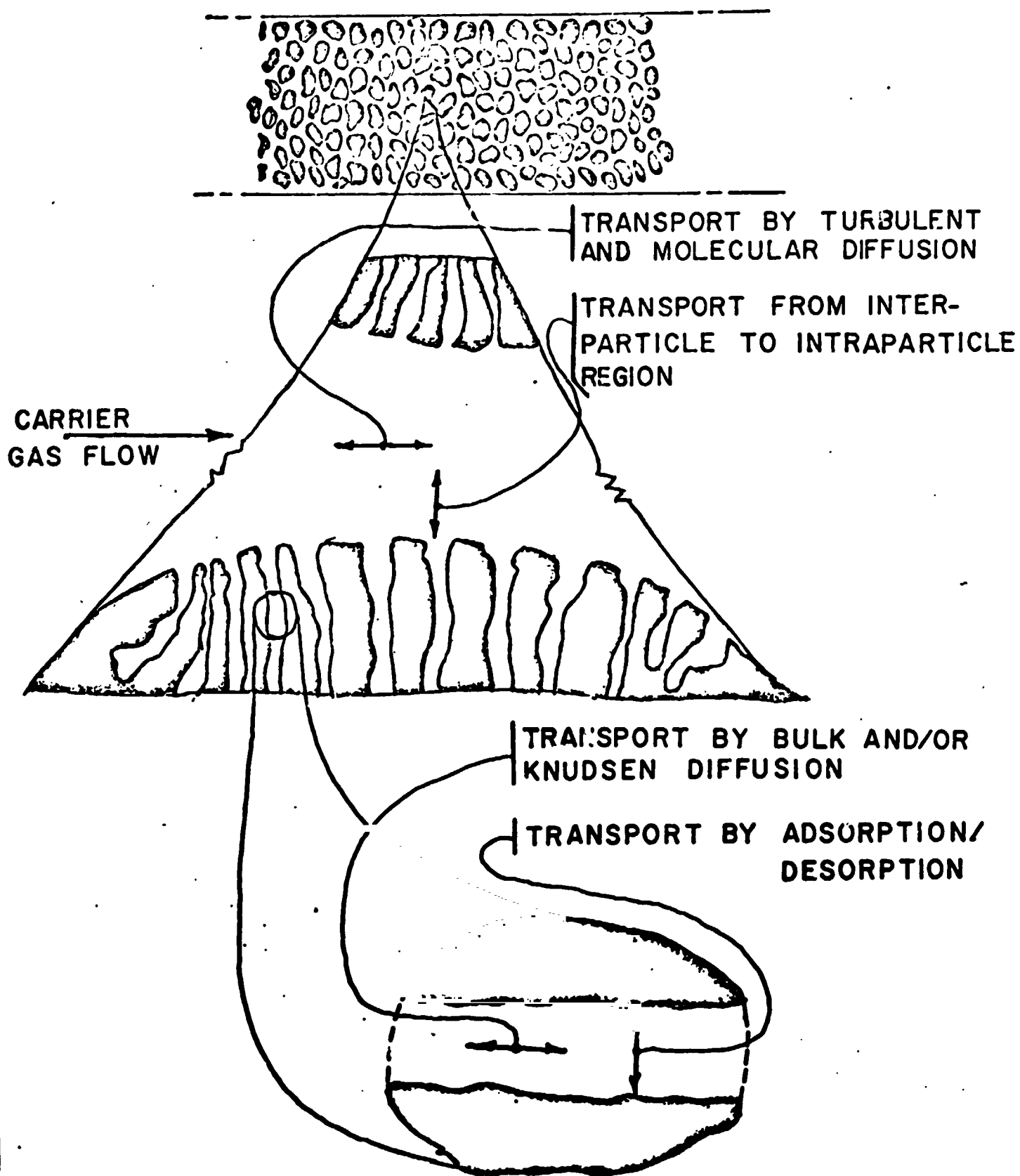
The transfer function of the system of Figure 91 is given in Figure 93. Before attempting an inversion of this equation, a moment analysis of the model hereafter designated as the Inter-Intraparticle Adsorption Model was undertaken to determine gross behavior.

The three moments of a chromatogram, Ref. 41,

$$\begin{aligned}\bar{\mu}_1 &= \int_0^{\infty} y \theta \, d\theta / \int_0^{\infty} y \, d\theta \\ \bar{\mu}_2 &= \int_0^{\infty} y (\theta - \bar{\mu}_1)^2 \, d\theta / \int_0^{\infty} y \, d\theta \\ \bar{\mu}_3 &= \int_0^{\infty} y (\theta - \bar{\mu}_1)^3 \, d\theta / \int_0^{\infty} y \, d\theta\end{aligned}$$

which are derivable directly from the system transfer function and the moments of the input or sample injection pulse, give an indication of the time for peak appearance, the dispersion, and the skew respectively.

# CHROMATOGRAPHIC COLUMN INTER-INTRAPARTICLE MODEL CONCEPTS



$$\begin{aligned}
 Y(L,s) &= \exp \left\{ \frac{Pe_E}{2} - \sqrt{\frac{Pe_E^2}{4} + \gamma(s) Pe_E} \right\} \\
 \text{where: } \gamma(s) &= N_{\text{TOG}} (1 - \lambda(s)) + s \\
 \lambda(s) &= \frac{b \sinh(\sqrt{a_1})}{[(b-1)\sinh(\sqrt{a_1}) + \sqrt{a_1} \cosh(\sqrt{a_1})]} \\
 a_1(s) &= \left\{ \left[ \frac{-N_{\text{RU}}^2}{(s + N_{\text{RU}})} + N_{\text{RU}} + s \right] \left( \frac{R}{L} \right)^2 Pe_A \right\} \\
 b &= \frac{N_{\text{TOG}}}{3 \beta \frac{(1-\epsilon)}{\epsilon} \left( \frac{L}{R} \right)^2 \frac{1}{Pe_A}} \\
 \beta &= \text{Particle porosity} \\
 \epsilon &= \text{Bed void fraction}
 \end{aligned}$$

Figure 73. Transfer Function of Chromatograph

Tables XIV and XV compare chromatograph moments obtained from ethylene and acetone data, Ref. 20, with predictions from the interparticle equilibrium adsorption model, Ref. 41 (see section D.2.a. above) and the new model. A priori calculation of  $(L/R)$ ,  $Pe_A$ ,  $Pe_E$ ,  $N_{tOG}$  was possible from the experimental conditions. The values of  $mR_0$  determined earlier, Ref. 20, were used, and computations were made for several values of  $N_{RU}$ . In both cases the new model more closely predicts the mean  $\bar{\mu}_1$  although differences between the two models and the data are small. More importantly, the new model is capable, in both cases, of better predicting the dispersion  $\bar{\mu}_2$ , and more closely approximates the skew  $\bar{\mu}_3$ . The values of  $N_{RU}$  necessary for matching  $\bar{\mu}_2$  for both systems are of the same order of magnitude and are in reasonable accord with other independent data, Ref. 43. The differences in the gross behaviors of the two systems as represented by the respective moments is primarily a result of the parameter,  $mR_0$  as all other parameters are of the same order of magnitude. As a result of the moment analyses and parametric studies, it appears that the proposed model will yield more adequate chromatogram prediction.

The solution to the equations of Figure 91 is presently being considered. It appears that inversion of the transfer function of Figure 93 is not feasible, and an analytical solution is probably not realizable. The simplified situation of negligible mass transfer resistance ( $N_{tOG} \rightarrow \infty$ ) and equilibrium adsorption ( $N_{RU} \rightarrow \infty$ ) was also investigated. It appeared that the resulting transfer function while considerably less complicated, is also not easily inverted. Thus, the application of an appropriate numerical technique is required for the solution of the system equations.

Prior to obtain the final numerical solution, several preliminary studies were required. The second order equations of Figure 91 require two boundary conditions which prescribe the solution behavior at two points in the space domain, as well as a set of initial conditions. Thus a complete description of the interparticle mass balance of Figure 91 becomes

$$(1/Pe) (\partial^2 y / \partial z^2) - (\partial y / \partial z) - R = (\partial y / \partial \theta) \quad (1)$$

$$y(z, 0) = 0 \quad (2)$$

$$y(0, \theta) = A\theta \quad \theta > 0 \quad (3)$$

$$\lim_{z \rightarrow \infty} y(z, \theta) = \text{finite} \quad \theta > 0 \quad (4)$$

where  $R$  is the rate of adsorption of the samples. Equations 3 and 4 are the boundary conditions that have been previously used for development of the analytical models. However, use of Equation 4 as a terminal boundary condition is impractical for numerical treatment and must be replaced with an appropriate finite terminal boundary condition. It is

TABLE XIV

## MOMENT ANALYSIS AND PARAMETRIC

STUDY - ETHYLENE 50°C.

$mR_0$	$\mu_{1, \text{observed}}$	$\mu_{1, \text{predicted}}^{(1)}$	$\mu_{1, \text{predicted}}^{(2)}$
0.194	26.475	25.986	23.719

$N_{RU}$	$\bar{\mu}_2 \text{ observed}$	$\bar{\mu}_2 \text{ predicted}^{(1)}$	$\bar{\mu}_2 \text{ predicted}^{(2)}$
100	7.024	13.283	0.388
200	↓	6.973	↓
400		3.817	
800		2.240	
1600		1.451	
3200		1.056	
6400		0.859	
12800		0.760	
25600		0.711	

$N_{RU}$	$\bar{\mu}_3 \text{ observed}$	$\bar{\mu}_3 \text{ predicted}^{(1)}$	$\bar{\mu}_3 \text{ predicted}^{(2)}$
100	19.623	13.049	0.191
200	↓	3.519	↓
400		1.058	
800		0.403	
1600		0.219	
3200		0.163	
6400		0.144	
12800		0.137	
25600		0.134	

$$Pe_A = 9744$$

$$N_{t03} = 79750$$

$$(L/R)^2 / Pe_A = 436.2$$

- (1) Inter-Intraparticle Adsorption Model  
 (2) Interparticle Equilibrium Adsorption Model



TABLE XV

## MOMENT ANALYSIS AND PARAMETRIC

STUDY - ACETONE 100°C.

$mR_0$	$\mu_{1, \text{observed}}$	(1) $\mu_{1, \text{predicted}}$	(2) $\mu_{1, \text{predicted}}$
0.029	173.29	158.69	156.49
$N_{RU}$	$\mu_{2, \text{observed}}$	(1) $\mu_{2, \text{predicted}}$	(2) $\mu_{2, \text{predicted}}$
100	815.67	977.55	437.28
200		723.41	
400		686.34	
800		517.80	
1600		483.53	
3200		466.40	
6400		457.83	
12800		453.55	
25600		451.41	
$N_{RU}$	$\mu_{3, \text{observed}}$	(1) $\mu_{3, \text{predicted}}$	(2) $\mu_{3, \text{predicted}}$
100	25404.0	23192.2	19499.2
200		20454.8	
400		19745.3	
800		19555.4	
1600		19511.7	
3200		19485.1	
6400		19480.4	
12800		19477.2	
25600		19476.2	

---


$$Pe_A = 8689$$

$$N_{tOG} = 88960$$

$$(L/R)^2 / Pe_A = 328.2$$

- (1) Inter-Intraparticle Adsorption Model  
 (2) Interparticle Equilibrium Adsorption Model

also desirable that the solution obtained by use of the finite terminal boundary condition possess the same characteristics at the column outlet ( $z = 1$ ) as the infinite column solution, using Equation 4 as the terminal boundary condition.

A possible alternate boundary condition sometimes encountered in similar diffusions problem is the zero-derivative condition

$$\partial y(z_0, \theta) / \partial z = 0; \quad z_0 \geq 1; \quad \theta > 0 \quad (5)$$

To develop guidelines on the use of Equation 5, two cases were compared via moment analysis:

Case I

Equation 1,  $R = 0$

Equations 2, 3, 4

Case II

Equation 1,  $R = 0$

Equations 2, 3, 5

Specifically, parametric studies were made by moment analysis to determine

- 1) errors associated with letting  $z_0$  be 1 as a function of  $Pe$  and
- 2) the smallest  $z_0$ , as a function of  $Pe$  that could be used to approximate infinite column behavior at  $z$  of 1.

These results are summarized in Tab I. Thus criteria have been developed for accurate use of a finite terminal boundary condition which can be accommodated in a numerical procedure.

Considerable effort has been spent in evaluating several numerical methods for solving the partial differential equation set of Figure 91. The implicit Crank-Nicolson method, which is based on finite difference representation of the derivatives, appears impractical for this pulse propagation problem because of restrictions in space and time discretizations to maintain numerical stability. This appears primarily caused by the large Peclet number values (1000 to 10,000) encountered in these systems.

The method of weighted residuals (MWR), Ref. 44, offers promise. In this method, the exact solution is approximated by a trial solution of the form:

$$y \approx y^{(N)}(z, \theta) = \sum_{i=1}^N a_i^{(N)}(\theta) \bar{\phi}_i(z) + \bar{\phi}_0(z)$$

TABLE XVI. CRITERIA FOR USING FINITE BOUNDARY CONDITION

Case I: infinite boundary condition  
 Case II: finite boundary condition

Pe	Safe $z_0$	Safe $z_0$
	$(\mu_{1,I} = \mu_{1,II})^*$	$(\bar{\mu}_{2,I} = \bar{\mu}_{2,II})^{**}$
2	9.791	11.768
4	5.254	6.021
8	3.043	3.328
16	1.978	2.073
32	1.467	1.490
64	1.223	1.222
128	1.106	1.044
254	1.050	1.002
512	1.024	1.0005
1024	1.011	1.0001
2048	1.005	1.0000
4096	1.002	1.0000
8192	1.001	1.0000

$$* \quad \mu_{1,I} - \mu_{1,II} \leq 10^{-8}$$

$$** \quad \bar{\mu}_{2,I} - \bar{\mu}_{2,II} \leq 10^{-8}$$

where  $\bar{\Phi}_i(z)$  are a set of trial functions and  $\Phi_0(z)$  satisfies the boundary conditions. If the trial solution is substituted into the partial differential equation, a residual,  $R$ , is formed. In MWR the weighted integrals of the residual are set to zero:

$$\int_V w_j R dV = 0, \quad j = 1, 2, \dots, N$$

where  $w_j$  is a weighting function. In the orthogonal collocation version of the method, the weighting functions are families of orthogonal polynomials. This method has been shown applicable to similar diffusion-type problems, Ref. 44. The application of orthogonal collocation to the system models under consideration is the present area of endeavor. It is anticipated that a technical report dealing with this subtask from July, 1972 through August, 1973 will be issued during September, 1973.

## REFERENCES

1. Frederick, D.K., Lashmet, P.K., Sandor, G.N., Shen, C.N., Smith, E.J., and Yerazunis, S.W., "Progress Report for July 1, 1972 to December 31, 1972," RPI Technical Report MP-30, Rensselaer Polytechnic Institute, Troy, New York, January 1973.
2. Moore, J.W. and Burke, J.D., "An Exploratory Investigation of a 1979 Mars Roving Vehicle Mission," Jet Propulsion Laboratory, December 1970.
3. Pavarini, C., Baker, J. and Goldberg, A., "An Optimal System Design Process for a Mars Roving Vehicle," NASA CR-125616, November 1971.
4. Zuraski, J., "Laser Range Measurement for a Satellite Navigation Scheme and Mid-Range Path Selection and Obstacle Avoidance," Rensselaer Polytechnic Institute, Troy, New York, June 1972.
5. Kuriger, W.K., "A Proposed Obstacle Sensor for a Mars Rover," Journal Spacecraft, 10, p. 1043, October 1971.
6. DeVilbiss, W.F., and Klunk, S.L., "A High Speed Pulser for Injection-Laser Diodes," RCA Application Note #AN-4741, September 1971.
7. RCA, Application Notes #AN-4469, June 1972.
8. Sprague Engineering Bulletin, #27111, 1970.
9. Herb, G.T., "Laser Scanning Methods and a Phase Comparison, Modulated Laser Range Finder for Terrain Sensing on a Mars Roving Vehicle," RPI Technical Report MP-34, Rensselaer Polytechnic Institute, Troy, New York, May 1973.
10. Fox, E.A., Mechanics, Harper & Row, New York, 1967, p. 237.
11. Pavarini, C. and Chrysler, J.H., "Terrain Modeling and Path Selection by an Autonomous Martian Exploratory Vehicle," RPI Technical Report MP-14, Rensselaer Polytechnic Institute, Troy, New York, June 1970.
12. Rautio, A., "An Analysis of the Effect of Sensor Errors on a Long Range Terrain Modeling System and a Study of Short Range Terrain Modeling for an Autonomous Roving Vehicle," Rensselaer Polytechnic Institute Masters Project Report, June 1971.
13. DeRusso, P., Roy, R., and Close, C., State Variables for Engineers, John Wiley & Sons, Inc., New York, 1965, p. 457.
14. Bryson, A.E. and Ho, Y.C., Applied Optimal Control, Ginn-Blaisdell Publishing Co., 1969, Chapter 12.
15. Shen, C.N., "Random Variables, Gauss-Markov Random Sequences and Linear Discrete Optimal Filtering," unpublished notes, Rensselaer Polytechnic Institute, Troy, New York.

16. Burger, P.A., "Stochastic Estimates of Gradient from Laser Measurements for an Autonomous Martian Roving Vehicle," RPI Technical Report MP-33, Rensselaer Polytechnic Institute, Troy, New York, May 1973.
17. Shen, C.N. and Burger, P., "Stochastic Estimates of Gradient from Laser Measurements for an Autonomous Martian Roving Vehicle," Proceedings of the Third IFAC Symposium on the "Identification and System Parameter Estimation" at the Hague, The Netherlands, June 12-15, 1973.
18. Boheim, S. and Purdon, W., "Path Selection System Evaluation for a Martian Roving Vehicle," RPI Technical Report MP-29, Rensselaer Polytechnic Institute, Troy, New York, December 1972.
19. Benoit, G.L., "Reduction of Chromatographic Data and Evaluation of a GC Model," RPI Technical Report MP-22, Rensselaer Polytechnic Institute, Troy, New York, June 1971.
20. Keba, P.S., and Woodrow, P.T., "A Comparison of Two Gas Chromatograph Models and Analysis of Binary Data," RPI Technical Report MP-27, Rensselaer Polytechnic Institute, Troy, New York, July 1972.
21. Badawy, M.P., "System Analysis of a Mass Spectrometer," M. Eng. Project Report, Rensselaer Polytechnic Institute, Troy, New York, May 1973.
22. Mattuch, J., and Herzog, R., "Über einen neuen Massen-spektrographen," Z. Phys., 89, 786-795 (1934).
23. Herzog, R., "Ionen-und elektronenoptische Zylinderlinsen und Prismen, I.," Ibid, 89, 447-473 (1934).
24. Matsuda, H., Fukumoto, S., and Matsuo, T., "New Ion Optical System for a High-Resolution Mass Spectrometer," "Recent Developments in Mass Spectroscopy," (K. Ogata and T. Hayakawa, ed.), University Park Press, Baltimore, 1970, pp. 175-180.
25. Nier, A.O., "A Mass Spectrometer for Isotope and Gas Analysis," Rev. Sci. Instr., 18, 398-411 (1947).
26. Nier, A.O., "A Mass Spectrometer for Routine Isotope Abundance Measurements," Ibid., 11, 212-216 (1940).
27. Cooper, J.L., Pressley, G.A., and Stafford, F.E., "Electron Impact Ionization Cross-sections for Atoms," J. Chem. Phys., 44, 3946-3949 (1966).
28. Dushman, S., "Determination of e/m from Measurements of Thermionic Currents," Phys. Rev., 4, 123-134 (1914).
29. Corruccini, R.J., "Gaseous Heat Conduction at Low Pressures and Temperatures," Vacuum, VII-VIII, 19-29 (1957-1958).
30. Jarva, C.W., "A Study of Carrier Gas Generation and Removal Systems for Remote Gas Chromatograph - Mass Spectrometer Operation," M. Eng. Project Report, Rensselaer Polytechnic Institute, Troy, New York, May 1973.
31. Kubaschewski, O., Cibula, A., and Moore, D., "Gases and Metals," American Elsevier, New York, 1970, p. 94.

32. Burmeister, L., Loser, J., and Sneegas, E., "Advanced Valve Technology," Report NASA SP-5019, Natl. Aeronaut. Space Admin., Washington, D. C., 1967.
33. Dushman, S., "Scientific Foundations of Vacuum Technique," 2nd ed., (J.M. Lafferty, ed.), Wiley, New York, 1962, pp. 570-574.
34. Siemon, K., "Pressure Vessel Manual," Edwards Brothers, Ann Arbor, Mich., 1958, pp. 37-52.
35. Morris, E.E., "Glass-Fiber-Reinforced Metallic Tanks for Cryogenic Service," in "Advances in Structural Composites," Sci. Adv. Mater. Process Eng., 12, Paper No. AS-4, 1967.
36. "Engineering Model GC/MS Design Review: Gas Chromatograph Subsystem," pp. 6-1 to 6-29, Jet Propulsion Lab., Pasadena, Cal., Jan. 28, 1971.
37. Ibid., pp. 2-1 to 2-8.
38. "Dynamic Response of a Gas Chromatograph - Mass Spectrometer Combination," JPL Space Programs Summary 37-62, v. I, pp. 28-33, Jet Propulsion Lab., Pasadena, Cal., March 31, 1970.
39. Crank, J., "The Mathematics of Diffusion," Clarendon Press, Oxford, 1956, pp. 62-64.
40. Sliva, T.F., "Chromatographic Systems Analysis: First-Order Model Evaluation," RPI Technical Report MP-1, Rensselaer Polytechnic Institute, Troy, New York, September 1968.
41. Voytus, W.A., "Chromatographic Systems Analysis: Moment Analysis of the Equilibrium Adsorption Model," RPI Technical Report MP-9, Rensselaer Polytechnic Institute, Troy, New York, August 1969.
42. Meisch, A. J., "Binary Chromatographic Data and Estimation of Adsorbent Porosities," RPI Technical Report MP-31, Rensselaer Polytechnic Institute, Troy, New York, May 1973.
43. Schneider, P., and Smith, J.M., "Adsorption Rate Constants from Chromatography," AIChE J., 14, 762-771 (1968).
44. Finlayson, B.A., "The Method of Weighted Residuals and Variational Principles," Academic Press, New York, 1972.

## V. Educational Considerations

In addition to the technical goals outlined earlier, this project has the objective of promoting the education of engineering students in directions and dimensions not normally encountered in formal programs of study. In brief, the project activity provides real problems of substance whose solutions are obtained not by the application of expedient simplifications to make them manageable but rather according to the technical needs that realistically apply to the situation. Accordingly, the students learn to accommodate to trade-offs between competing values and to work with boundary conditions and constraints originating with the factual situations and which may be compounded by the interfacing of tasks. In this type of environment, the student perceives that his role in professional practice will normally involve a significant amount of interaction with other individuals and that his work cannot proceed independently and without consideration of and impingement by the work of others. Furthermore, he is forced to obtain, understand and utilize knowledge which is on occasion far removed from his own speciality field and to undertake research when necessary to obtain the required information. Although the very nature of the problems and the faculty perspective emphasize the relevance and importance of the technical goals, the periodic visits of Dr. Garrett Paine of Jet Propulsion, and on occasion of other NASA representatives, to review progress reinforce these concepts dramatically.

From an educational point of view, the project has proven to be an unqualified success. Large numbers of students (approximately 100 in five years) have had the unique experience of a real-life involvement in engineering problems within the context of their formal education. Although the majority of participating students have been candidates for the Master of Engineering degree, a significant number have pursued the doctoral degree



and a substantial number of undergraduates have been involved. While a fraction of the students receive financial support from the project, the majority have elected to participate in order to receive academic credit. The latter students are self-supporting, hold fellowships or are retained as teaching assistants. The fact that so many of them have elected to work on the project to gain academic credit indicates the interest which the project has generated and the educational value that the participating students perceive to be related with this activity.

During the past year from July 1, 1972 to June 30, 1973, a total of 34 students have been involved in the project. Of this group, 3 are following a doctoral program, 18 are, or were, candidates for a master's degree and the remaining 13 were undergraduates. A number of the undergraduates intend to continue their involvement in the project.

This substantial interest by the students indicates that the NASA support is contributing significantly and meaningfully to their education. Furthermore, the effort to resolve crucial problems related to an unmanned mission to Mars has been amplified by the technical contributions of students who are receiving no or very little financial support from the project. Thus, this NASA project has the unique benefits of providing technical support to national goals in space exploration and of enhancing engineering education at Rensselaer.